FACULTY OF SCIENCES
DEPARTMENT OF GEOGRAPHY

Total Electron Content reconstruction using triple frequency GNSS signals

PhD. thesis submitted in partial fulfillment of the requirements for the degree of Doctor in Sciences

Justine Spits

Academic Year 2011-2012

Supervisor:	Dr. R. Warnant (ULg)
Examining committee:	Dr. R. Arnould (ULg)
	Dr. R. Billen (ULg)
	Dr.-Ir. J.-C. Jodogne (RMI – Belgium)
	Dr. S. Stankov (RMI – Belgium)
	Dr.-Ir. H. van der Marel (TU Delft – Nederland)

Abstract

Nowadays, Global Navigation Satellite System (GNSS) provide accurate three dimensional positioning and navigation anywhere and anytime on the Earth's surface and are being utilized in numerous civilian and military applications. The US Global Positioning System (GPS) is currently being modernized to transmit radio signals on an additional third frequency, while the European Galileo is a newly developed system which will transmit on three civil frequency bands.

One of the major error sources affecting GNSS is the delay caused when the signals pass through the ionosphere on their way to the Earth's surface. This delay is inversely proportional to the square of the carrier frequency, and directly proportional to the Total Electron Content (TEC) of the ionosphere. In the last 20 years, several techniques using dual frequency GNSS measurements have been developed to estimate the TEC. With these techniques, systematic errors are confined to at least -2.5 and 2.5 TECU for a mid-latitude site, and to at least -5.5 and 5 TECU for a low-latitude location.

In the last decades, knowledge about the ionosphere has grown considerably thanks to the use of GNSS measurements, and in turn the GNSS have highly benefited from this improved knowledge. Nowadays the availability of triple frequency GNSS signals enables the development of new processing techniques. We have therefore dedicated this work to developing a TEC reconstruction methodology based on triple frequency GNSS measurements and aimed at improving the accuracy of the final TEC values with regards to existing techniques.

The structure of this study is as follows. Firstly, we provide information about GNSS, focusing on concepts, definitions and assumptions which will be used throughout this study. Then, we introduce the concepts of ionospheric propagation of radio signals and give a review of the literature on existing techniques used to extract the TEC with dual frequency GNSS measurements. We further present the complete design of the triple frequency TEC reconstruction methodology. We start by giving the set of combinations which allows us to resolve the original integer ambiguities, then we address the principles of TEC reconstruction, and finally we give an accuracy assessment of the computed TEC values. We also present an innovative technique to calibrate the satellite and receiver code hardware delays. We continue with testing the features developed on a simulated GPS and Galileo observation dataset, as well as on a real GIOVE observation dataset. Finally, we conclude this work by providing a critical overview of our investigations and suggesting various improvements of the current limitations.

Resumé

De nos jours, les systèmes globaux de positionnement par satellites (GNSS) fournissent une couverture globale de positionnement et de navigation tri-dimensionnelle à la surface de la Terre, et sont utilisés dans de nombreuses applications civiles et militaires. Le système américain GPS est actuellement en cours de modernisation, et ce notamment dans l'optique de transmettre des signaux dans une bande de fréquence supplémentaire. Le système européen Galileo est quant à lui en plein développement et transmettra ses signaux dans trois bandes de fréquence civiles.

Une des principales sources d'erreur affectant les GNSS est le délai engendré lorsque les signaux traversent l'ionosphère en direction de la Terre. Ce délai est inversement proportionnel au carré de la fréquence du signal, et directement proportionnel au Contenu Électronique Total (TEC) de l'ionosphère. Jusqu'à présent, les techniques utilisées pour calculer le TEC étaient basées sur l'utilisation de mesures GNSS double fréquence. L'exactitude du TEC obtenu est de ce fait limitée par la présence d'erreurs systématiques à -2.5 et 2.5 TECU aux latitudes moyennes, et à -5.5 et 5 TECU aux basses latitudes.

Durant les dernières décennies, les GNSS ont largement contribué à améliorer les connaissances concernant la distribution des électrons libres dans l'ionosphère. De la même manière, les GNSS ont fortement bénéficié de cet accroissement du savoir ionosphérique. La disponibilité de signaux GNSS triple fréquence permet le développement de diverses techniques nouvelles. Nous avons choisi de consacrer nos recherches au développement d'une nouvelle technique de reconstruction du TEC basée sur l'utilisation de mesures GNSS triple fréquence, et ce dans le but d'améliorer l'exactitude du TEC obtenu par rapport aux techniques existantes.

Ce travail aborde la problématique comme suit. Tout d'abord, nous présentons des informations générales à propos des GNSS, en se concentrant sur les concepts, définitions et hypothèses qui seront nécessaires tout au long du travail. Ensuite, nous expliquons les concepts concernant la propagation des signaux radios dans l'ionosphère, et nous réalisons un état de l'art des techniques existantes de calcul du TEC. Par la suite, nous présentons en détail la conception de la technique de calcul du TEC triple fréquence. Pour cela, nous présentons les combinaisons qui permettent de résoudre les ambiguités entières, nous exposons les principes de calcul du TEC et nous procédons à une étude détaillée des erreurs affectant les valeurs du TEC. En aval de la méthode de calcul du TEC, nous présentons également une technique innovatrice qui permet de calibrer les délais de codes dans l'électronique du satellite et du récepteur. Nous procédons ensuite à la validation des méthodologies développées à l'aide de données simulées GPS et Galileo, ainsi que de données réelles provenant des satellites GIOVE. Pour conclure ce travail, nous portons un avis critique sur nos recherches et suggérons diverses améliorations possibles.

Once upon a time, je commence une thèse de doctorat...le temps est à présent venu d'adresser mes remerciements.

Je remercie mes parents, mes frère et soeur et toute ma famille pour le soutien et la confiance qu'ils m'ont toujours accordée.

Je tiens à remercier mon promoteur, M. Warnant, de m'avoir lancée dans cette aventure, merci pour son aide et ses conseils toujours judicieux. Un merci spécial à M. Donnay pour son soutien lors des dernières étapes de ce travail. I would also like to thank M. Langley for the help provided during and after the meeting in Copenhagen. Thanks a lot to M. Santos for the support and good advice in the last few months.

Ces années de thèse n'auraient pas été pareilles sans la présence de tous mes collègues de l'Observatoire Royal de Belgique. Merci à Sandrine pour sa présence et son perpétuel soutien. Merci à elle d'avoir partagé bureau et de nombreuses discussions... Merci à Tillio et Antony pour toutes les longueurs nagées côte à côte. Merci à Grégor pour son enthousiasme. Merci à Pascal d'avoir notamment partagé quelques samedis et dimanches midis. Merci à Quentin et à Marie-Carmen pour les agréables moments passés ensemble à Copenhague, mais aussi pour les discussions intéressantes et cruciales à quelques semaines de la fin de mon travail. Merci à Marie, Laurence et Nicolas d'avoir entretenu mon envie d'évasion. Merci à Ronny pour le support technique.

De la même manière, je me dois de remercier mes collègues de l'Institut Royal Météorologique de Belgique qui ont cotoyé la deuxième partie de mes années de thèse. Merci à Alessandro pour son fichier–modèle en LaTeX, sa relecture attentive*, ses conseils et son aide indispensable tout au long de mon travail. Merci à Almudena† et Ilse pour leur amitié sans limite. Merci à Annette pour sa patience et l'aide qu'elle procure sans compter. Merci à Cédric de m'avoir fait découvrir les Cowboys Fringants, le Canada, l'Ultimate‡, mais aussi pour tous les moments passés ensemble§. Merci à Edward pour son aide lors de la finalisation de ce manuscrit. Merci à Koen pour son dévouement et son oreille attentive qui furent indispensables à l'aboutissement de ce travail. Merci à Nadia pour sa douceur et le cadre de travail qu'elle nous offre. Merci à Nico de m'avoir conduit à Liège un jour de novembre... Merci à Sabri de m'avoir fait découvrir une autre façon de voir la vie et tous ses moments. Merci à Stijn pour les échanges de mots et de produits locaux.

Je voudrais à présent remercier tous mes amis qui, parfois sans trop comprendre où tout cela menait, m'ont soutenue coûte que coûte. I would like to thank Alex, for making some of my days 5 hours longer and giving me a lot of things to look forward to. Merci à Alexis de m'avoir supportée pendant les jours difficiles. Merci à Amélie de m'avoir si bien comprise dans les derniers mois (histoire similaire ?). Merci à Anabel-Lise qui, malgré son arrivée tardive, a su m'apporter un réconfort et une écoute incomparables. Merci à Anna pour son immense gentillesse et disponibilité, mais aussi pour les innombrables moments de détente, de stretching, les vacances passé(e)s ensemble. Merci à Annelies pour ses conseils toujours avisés à tous les niveaux (...), sa capacité à comprendre mes états d'âmes, son talent de coiffeuse¶, mais aussi pour tous les moments d'évasion. Merci à Arne pour m'avoir appris un des derniers soirs que ce qui est rond est rond... Merci à Christine pour ses relectures indispensables. Merci à eux deux pour leur compagnie toujours agréable, leur capacité à me faire aller de l'avant. Et c'est peu dire. Merci à Del & Fred pour leur soutien et leur enthousiasme face à mes projets. Gracias a Esti y Litus por su amabilidad, apoyo y acogida en el equipo. Merci à

*Il parait que certains passages ont même été relus à lueur d'une lampe de poche.

†Un grand merci à Sofiene de nous avoir nourries lors d'une mémorable nocturne.

‡Un soir de l'été 2008 dans les contrées quebécoises, ce fut le *Love at first flight*.

§I am thinking about the skyline...

¶que ça soit sur le thème du chic-choc, du hip-hop ou de la colère

Fabien pour son amitié, sa gentillesse, mais aussi pour les purs moments de détente[‖]. Merci à Gilles pour tout ce qu'il a fait pour moi. Merci à Gwen pour sa bonne humeur et sa disponibilité un jour d'été où j'en avais vraimen besoin. Merci à Julie pour sa paisible amitié. Merci à Lio pour son enthousiasme, son réconfort toujours bienvenu. Merci à Manu de m'avoir soutenue à chaque occasion. Merci à Nathan de m'avoir permis de relativiser en ces jours de septembre. Merci à Pascal de m'avoir accompagnée lors d'une longue soirée d'octobre... Merci à Steph pour son soutien, pour la détente apportée par le Shiatsu, pour tous les moments passés ensemble. Merci à Sophie & Sophie, deux rayons de soleil arrivés au bon moment. Merci à Tof pour son agréable compagnie lors de soirées ensoleillées de mai, mais aussi pour son soutien toujours bienvenu.

Puis, je n'en serais sans doute pas là sans ce disque volant qui permet un tel échappement à la réalité. Je voudrais remercier les Ouf(ette)s, Mubidisk[**] No Limit[††], mes buddys du TTB Dave, Didier & Julien, Volando Voy[‡‡] et tous mes coéquipiers d'un jour[§§] ou de toujours[¶¶].

Enfin l'aboutissement de ce travail n'aurait pas été pareil sans Lotus[***], Glee, Glee customisé par Christine, les 5 heures de PureFM[†††], the National, Jack Johnson, le bain salé de Frederiksberg, les laits russes du Belga, les cafés *leche–leche* de Lanzarote, et j'en passe.

[‖] Je pense en particulier à un samedi soir de la fin du mois d'août.

[**] Spécial dédicace à Alexis & Fontes

[††] Spécial dédicace à Jaymeen, Ringhio & Matteo Fiammingo !

[‡‡] Spécial dédicace à Esti & Litus, Fayna & Sosa

[§§] Spécial dédicace à Arnaud au Yes But Nau, Diego à Padova, Frank au XL Hat.

[¶¶] Merci Frédé d'avoir toujours cru en moi.

[***] en particulier lors de la Nuit Blanche de Bruxelles un jour d'octobre

[†††] mais au fait qui va garder Milou ?

A Nathan…

Contents

Chapter 1

Introduction

1.1 Once upon a time

SINCE the dawn of humankind, as a species, we have been curious about the world that surrounds us. This curiosity led to exploring and an effort to push back the frontiers around the known territory. At first, all exploration was limited to the surrounding land. Then, with the advent of ships, the seas were conquered as well, which led to better maps and tremendous improvements in navigation. Navigation is defined as the science of monitoring and controlling the movement of a craft or a vehicle compared to a reference. Navigation techniques have evolved significantly during history. Initially, maritime navigation was based on celestial navigation systems, which rely on the observation of the sun, moon, planets and stars coupled with the use of marine chronometers.

A more complex navigation technique called radionavigation was developed in the 1930s. Radionavigation is based on the transmission of ground-based or space-based electronic signals which enable users to compute their position. During World War II, major advances were made in ground-based radionavigation. Then, with the space age, humankind took the spirit of exploration to the skies. Developed by the US Department of Defense (DoD) and operational since the mid-1990s, the Global Positioning System (GPS) was the first Global Navigation Satellite System (GNSS), or satellite-based system providing accurate three dimensional positioning and navigation anywhere and anytime on the Earth's surface. Nowadays, there are four existing GNSS: the US GPS, the Russian Global'naya Navigatsionnaya Sputnikkovaya Sistema (GLONASS), the European Galileo and the Chinese Compass. While the GPS and GLONASS are currently being modernized, Galileo and Compass are newly developed systems. GPS satellites transmit radio signals on two frequencies (L1, L2) and will, after completion of the modernization, transmit on a third frequency called L5. It was initially developed exclusively for military purposes, but opened to civilian use later on. Galileo satellites transmit on three civil frequency bands (L1, E5b, E5a*). Nowadays, GNSS systems are being utilized in numerous civilian and military applications, like air/maritime/land navigation, surveying, spacecraft guidance, etc.

There are two types of GNSS observables of interest to users: the pseudorange (or code)

*identical to GPS L5

and the carrier phase. The pseudorange is a measure of the transmission time (and therefore of the distance) between the receiver – generally on or near the Earth's surface – and simultaneously observed satellites. A set of a least four code measurements is actually required to determine the user latitude, longitude, height and receiver clock error*. The carrier phase is the phase difference between the received signal and a copy generated in the receiver. Since it can be tracked with millimeter accuracy, a significantly higher positioning accuracy can be achieved with the carrier phase than with the code. However, the carrier phase requires the resolution of an integer ambiguity parameter for each satellite.

In a perfect world, if the position of at least four satellites is known, multiplying the transmission time by the velocity of light would allow us to obtain the exact position of the receiver. However, in reality, the code and phase observables are affected by systematic and random errors which can be divided into three groups: satellite, signal and receiver related errors. Some of these errors can be modeled or eliminated by using appropriate combinations of observables. One of the major error sources affecting GNSS systems is the delay caused when the signals pass through the ionosphere on their way to the Earth's surface. During the propagation, the signals interact with the charged particles contained in the ionosphere, resulting in a change in wave velocity which depends on the refractive index. The refractive index of the ionosphere is a rather complicated expression given by the *Appleton-Hartree* formula [26]. For GNSS signals, however, the expression can be simplified: the delay caused by the ionosphere is inversely proportional to the square of the carrier frequency, and directly proportional to the integrated density of electrons in the ionosphere. The latter is well-known as the Total Electron Content (TEC) of the ionosphere. Taking advantage of the ionosphere's dispersive nature†, dual frequency GNSS measurements can be used to estimate or alternatively to eliminate the ionospheric delays.

1.2 Scope and objectives of the thesis

Nowadays, GNSS constitute a very useful tool to investigate the Earth's ionosphere. The computation of ionospheric delays is based on dual frequency GNSS measurements and the basic information retrieved from the observations is the Total Electron Content (TEC) of the ionosphere along the satellite-to-receiver path. Further, if a global network of GNSS receivers is used, the three dimensional distribution (latitude, longitude, time) of the vertical TEC‡ can be determined.

The calibration of TEC is based on the use of the Geometric-Free (GF) phase combination and requires the computation of its non-integer ambiguity. To extract the TEC with dual frequency GNSS measurements, one generally performs the carrier-to-code levelling process (code/phase) or the unlevelled carrier phase process (phase only). In both techniques, the TEC needs to be modeled, which induces non-negligible model errors in the calibrated TEC values. Moreover, in the code/phase technique, levelling errors are caused by the temporal variation of satellite and receiver code Inter-Frequency Biases (IFB) as well as by the non-zero average of code multipath delays. In total, these systematic errors limit the accuracy of the calibrated TEC values to a few TECU§. For a mid-latitude site, the error effects are confined

*The receiver clock is not synchronized to the satellite clock.
†The wave velocity is a function of the carrier frequency.
‡which is the TEC along the vertical from the Earth's surface to a given height in the ionosphere
§with 1 TECU being 10^{16} electrons per 1-square meter column

to -4.6 and 3.6 TECU for the code/phase technique, and to -2.5 and 2.5 TECU for the phase only technique. For a low-latitude site, the performance deteriorates: the error effects are confined to -5.5 and 5 TECU for the code/phase technique, and to -5.5 and 7.5 TECU for the phase only technique.

In the last decades, knowledge about the ionosphere has grown considerably thanks to the use of GNSS measurements, and at the same time the GNSS have highly benefited from this improved knowledge. An accurate understanding of the distribution of free electrons can improve GNSS techniques at different levels, such as higher-order ionospheric effects, real-time GNSS meteorology, etc. The recent modernization and development of GNSS systems has resulted in additional frequencies and new signals. This enables the development of new processing techniques which may further improve the mitigation of ionospheric delays, and thus the benefit for GNSS techniques. We have therefore dedicated this work to developing a TEC reconstruction methodology based on triple frequency GNSS measurements and aimed at improving the accuracy of the final TEC values with regards to existing techniques. The main research questions are the following:

- how would it possible to improve the accuracy of the TEC with triple frequency GNSS?
- which level of accuracy would it be possible to reach?

For this purpose, we investigate the various combinations which can be formed from triple frequency code and phase measurements in the aim of improving the computation of the GF ambiguity and therefore the accuracy of the TEC.

1.3 Outline of the thesis

The work presented in this thesis focuses exclusively on the development and validation of a TEC reconstruction methodology using triple frequency GNSS signals. It follows a two step approach:

- the conceptual development and theoretical accuracy assessment of the new TEC reconstruction methodology,
- the validation of this method by using simulated GPS and Galileo data, as well as real Galileo In-Orbit Validation Element (GIOVE) data.

The structure of this manuscript is as follows.

In chapter 2, we introduce the concepts and definitions of GNSS which will be used throughout the text. We first present the composition of GPS and Galileo systems and describe the different signals which can be provided. Then we recall the basic principles of GNSS code and phase observables and give a detailed description of their error sources. Finally, we derive the mathematical model of GNSS measurements.

Chapter 3 briefly presents the composition, formation and variability of the ionosphere, and introduces the concepts of ionospheric propagation of radio signals. It then gives a review of the literature on existing techniques used to extract the TEC with dual frequency

GNSS measurements. We investigate the characteristics and accuracy of the various methods. Their strengths and weaknesses will drive our choice of the adopted triple frequency TEC reconstruction methodology.

Chapter 4 is dedicated to the development of the triple frequency TEC reconstruction methodology. We start by introducing some useful concepts, especially regarding linear combinations of GNSS data. We then investigate several types and schemes of linear combinations of measurements on the basis of their interesting characteristics (large wavelength, elimination of the ionosphere and geometry) to suggest a promising set of combinations which allows us to resolve the original integer ambiguities and therefore reconstruct the GF ambiguities. We further address the principles of TEC reconstruction and give an accuracy assessment of the computed TEC values. Finally, we present an innovative method to calibrate the satellite and receiver code hardware delays.

In chapter 5, we aim to validate the triple frequency TEC reconstruction methodology by using triple frequency GPS and Galileo simulated data. We first describe the simulation software, which was designed to provide realistic triple frequency code and phase measurements. Then, we present the results of the ambiguity resolution procedure and TEC reconstruction based on a simulated observation dataset.

Chapter 6 is dedicated to triple frequency TEC reconstruction based on real triple frequency GIOVE measurements. We first describe the preprocessing of observation and navigation data which is a prerequisite to any data processing. Then we present the results of the ambiguity resolution procedure, TEC reconstruction and code hardware delay calibration based on the available GIOVE observation dataset.

Finally we summarize the work performed in this thesis in chapter 7. Suggested improvements and outlook of the methodologies developed are also presented.

Chapter 2

Global Navigation Satellite Systems

THIS chapter provides a summary of GPS and Galileo systems, giving their composition and signals (section 3.1). Following the basic principles of GNSS code and phase observables (section 2.2.1), their error sources are exposed in detail (section 2.2.2). Finally, the mathematical model of GNSS measurements is given in section 2.2.3.

2.1 Description

Global Navigation Satellite System (GNSS) are satellite-based systems providing accurate positioning and navigation anywhere and anytime on the Earth's surface. The computation of a location relies on the measurement of the range between the receiver and several simultaneously observed satellites. Currently, there are four existing GNSS: the US Global Positioning System (GPS), the Russian Global'naya Navigatsionnaya Sputnikkovaya Sistema (GLONASS), the European Galileo and the Chinese Compass. While the GPS and GLONASS are currently being modernized, Galileo and Compass are newly developed systems. As we exclusively deal with GPS and Galileo systems in the rest of this thesis, the other GNSS will not be described.

2.1.1 GPS

The GPS system was designed by the US Department of Defense (DoD) as a dual frequency (L1/L2) system with the aim of meeting the military's needs for positioning. Over the past decade, the number of civilian applications has increased considerably, and the system is undergoing a major modernization. This includes the transmission of a third civil frequency called L5.

2.1.1.1 Composition

The GPS system is divided into three segments: the space, control and user segments.

- Space segment

  The space segment consists of a least 24 Medium Earth Orbit (MEO) satellites deployed in six orbital planes with an inclination of about 55°, with the ascending nodes of the orbital planes equally spaced by 60°. Each satellite has a nearly circular orbit with a semi-major axis of about 26600 km and a period of about 12 hours. The satellite time frame is defined by the onboard four atomic clocks of each satellite. Those clocks produce the fundamental frequency of 10.23 MHz, from which all satellite transmissions are derived coherently. The built-up of the GPS satellite constellation was accomplished successively with the series of Block I satellites, Block II/IIA satellites and Block IIR satellites. The modernization began with the launch of Block IIR-M satellites, transmitting new civil codes on L2 (L2C). Currently, the build-up of Block IIF is ongoing. The satellites of Block IIF transmit a third civil frequency (L5).

- Control segment

  The control segment consists of six monitoring stations distributed worldwide. The master control station is located in Colorado Springs, Colorado. This segment is responsible for the control of the satellite constellation, as well as for the determination and transmission of the satellite ephemerides and clock corrections.

- User segment

  The user segment is formed by the GPS receivers. Their main function is to receive the signal transmitted by the satellites and convert it into useful measurements (observables). There are several types of receivers, mainly differing with regards to the capability to lock one, two or three frequencies (multi-frequency receivers), as well as other features, e.g. the capability to get signals from other GNSS (multi-GNSS receivers).

2.1.1.2 Signal

Each GPS satellite transmits signals on two or three frequencies: L1 (1575.42 MHz), L2 (1227.60 MHz) and L5 (1176.45 MHz). The L1, L2 and L5 carrier frequencies are generated by multiplying the fundamental frequency (10.23 MHz) by 154, 120 and 115, respectively. Their corresponding wavelength (λ) is given by dividing the velocity of light (c) by the frequency (f). Pseudorandom Noise (PRN) codes and navigation data – including satellite ephemerides, satellite clock bias and ionospheric model – are superimposed onto the carrier frequency. The Coarse Acquisition (C/A) code is modulated onto the L1 carrier, while the Precise (P) code is modulated on the L1, L2 carrier frequencies. The former constitutes the Standard Positioning Service (SPS), whereas the latter is associated with the Precise Positioning System (PPS). Moreover, modernized GPS satellites will transmit new civil signals using improved code modulation schemes. The first new civil signal is L2C, where C states for *civilian*. It was designed specifically to meet commercial needs. Even if L2C code constitutes an improvement with regards to the current GPS L2, its multipath and noise characteristics are similar to those of the C/A code. The second new civil signal is L5. It was designed to meet the requirements of high precision applications, and therefore has improved noise and multipath characteristics. Each GPS observable is actually a set of four measurements: a code observable, a phase observable, a Doppler shift and the signal strength or Carrier-to-Noise density ratio (C/N_0). Table 2.1 summarizes the characteristics of GPS signals.

Table 2.1 *– GPS carrier frequencies and wavelengths.*

Signal	Frequency [MHz]	λ [m]
L1	1575.42	0.1903
L2	1227.60	0.2442
L5	1176.45	0.2548

2.1.2 Galileo

The Galileo system is developed by the European Commission (EC) and the European Space Agency (ESA) to provide a highly accurate global positioning service available to civilian users.

2.1.2.1 Composition

The Galileo system is divided into three main parts: the global component, the regional and local components and the user segment.

- Global component

  The global component is the core of the system, comprising the space segment and the ground segment.

  The space segment consists of 30 MEO satellites deployed in three orbital planes with an inclination of 56°, with the ascending nodes of the orbital planes equally spaced by 120°. In every orbital plane, there are nine equally spaced operational satellites, plus one inactive spare satellite. Each satellite has a nearly circular orbit with a semi-major axis of about 29600 km and a period of about 14 hours. The satellite time frame is defined by the atomic clocks of each satellite. There are two types of clocks onboard each spacecraft: two passive hydrogen maser clocks and two rubidium clocks.

  The ground segment consists of two Ground Control Centers (GCCs) combined with the Ground Control Segment (GCS) and the Ground Mission Segment (GMS). The mission of the GCS is to handle spacecraft operation and constellation maintenance via a network of five telemetry, tracking and command (TTC) stations. The GMS will use a network of 30 Galileo Sensor Stations (GSSs) to handle mission navigation system control. It communicates with the Galileo satellites through a global network of up-link stations.

- Regional and local components

  The regional component of Galileo may comprise a number of systems that will independently provide the integrity of the Galileo services. Moreover, since some positioning and navigation applications require a very high level of accuracy, local components may be deployed for improving the performance of Galileo locally, e.g. by means of existing communications networks.

- User segment

  The user segment is formed by the Galileo receivers. As for GPS, there are several types of receivers: single, multi-frequency and multi-GNSS receivers. Dual frequency receivers will track L1 and the high performance E5-AltBOC signal (see section 2.1.2.2).

2.1.2.2 Signal and services

Galileo transmits signals on four frequency bands: E5a (1176.45 MHz), E5b (1207.14 MHz), E6 (1278.75 MHz) and E2-L1-E1* (1575.42 MHz). Figure 2.1 shows the general view of the Galileo spectrum. The signal structure design of Galileo offers significant advantages in comparison with the GPS:

- The power of Galileo signals is greater by factor two, resulting in a reduction of code measurement noise with regards to GPS L1/L2 code measurements.
- Novel modulation schemes have been developed, resulting in important reduction of code multipath delays and measurement noise compared to GPS L1/L2 code measurements. The Alternative Binary Offset Carrier (AltBOC) modulation is a new modulation scheme used in the Galileo E5 frequency band. The AltBOC offers the advantage that E5a and E5b can be tracked as two independent Binary Phase Shift Keying (BPSK)(10) modulation at center frequencies of 1176.45 MHz and 1207.14 MHz, or coherently as one signal centered at 1191.795 MHz. The latter leads to the E5-AltBOC observable (or E5a+b observable) which has exceptional characteristics in terms of code tracking noise and code multipath, as well as phase multipath [113, 116].
- There is a distinction between signals containing navigation data ("data channels") and signals carrying no data ("pilot channels"). The pilot channel is in quadraphase with the usual data channels (see figure 2.1). As pilot dataless components can be acquired independently without the need for decoding data, this will significantly enhance the carrier phase tracking in terms of reliability and sensitivity. As a matter of fact, the phase tracking will be more robust and measurements will be possible at lower C/N_0 that would otherwise be possible [58].

In comparison with GPS, Galileo offers a much greater variety of signals and services [113]. The complex signal structure includes 10 signal components that will be used for four different services [113] (see figure 2.1):

- the Open Service (OS), covering mass-market applications,
- the Commercial Service (CS), covering market applications and requiring higher performance,
- the Public Regulated Service (PRS), designed for governmental applications,
- the Safety-of-Life Service (SoL), used for transport applications where lives could be endangered if the performance is degraded without real-time notice.

*For more convenience, the E2-L1-E1 will be denoted as L1.

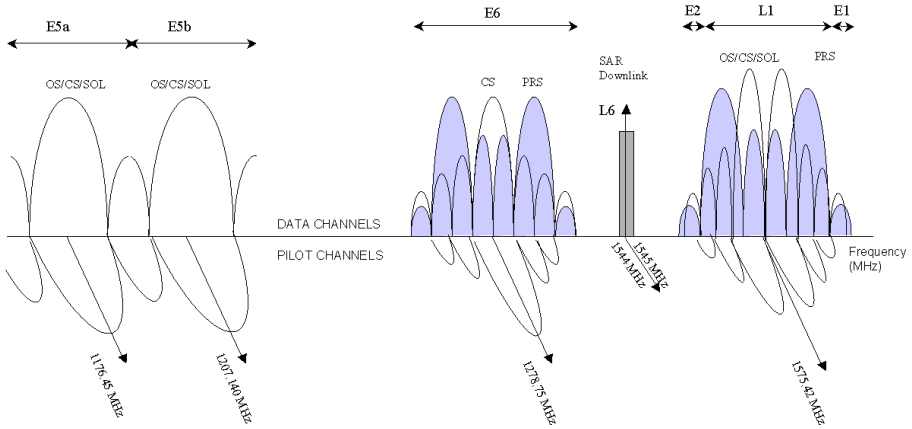

Figure 2.1 *– Galileo signals and frequencies. From [30].*

Table 2.2 summarizes the characteristics of the Galileo signals. Similarly to the GPS, each Galileo observable is a set of four measurements (code, phase, Doppler, signal strength). The OSs are achieved through the use of L1 and E5 observables (whether data or pilot), while the CSs are realized through the E6 signals. In single frequency OS, it is therefore possible to use L1, E5b, E5a or E5a+b together with an ionospheric model. Dual frequency OS are generally realized with L1/E5a and make it possible to cancel the first-order ionospheric delays, as will be explained in section 2.2.2.5. The whole signal (L1, E5b, E5a) can also be exploited for very precise applications.

Table 2.2 *– Galileo carrier frequencies and wavelengths.*

Signal	Frequency [MHz]	λ [m]
L1	1575.42	0.1903
E6	1278.75	0.2345
E5b	1207.14	0.2483
E5a	1176.45	0.2548
E5a+b	1191.795	0.2515

It is worth noting that the interoperability and compatibility of Galileo and GPS has been ensured by three means. Firstly, GPS and Galileo signals use two common frequencies (L1 and L5/E5a). Secondly, an independent coordinate reference frame is adopted for Galileo, while the World Geodetic System of 1984 (WGS84) is used for GPS. This Galileo Terrestrial Reference Frame (GTRF) is also realization of the International Terrestrial Reference System (ITRS). The differences between both reference frames are expected to be a few centimeters [44]. Finally, the Galileo System Time (GST) is a continuous atomic time scale, and the offset between GST and GPS time is monitored by the ground segment.

2.1.2.3 In-Orbit Validation phase

Once the definition of the Galileo system was completed, development and In-Orbit Validation (IOV) phase began with the Galileo In-Orbit Validation Element (GIOVE) mission. The objectives of the GIOVE mission are the following:

- secure access to the Galileo frequencies allocated by the International Telecommunications Union (ITU),
- test the critical onboard instruments and technologies (e.g. rubidium clock),
- characterize the novel features of the Galileo signal design; improve signal transmission capabilities using two or three channels in parallel,
- characterize the radiation environment in MEO using several radiation monitoring instruments.

The GIOVE mission uses two satellites (GIOVE-A and GIOVE-B) working together with their ground segment. These two satellites were launched in December 2005 and April 2008, respectively. The ground segment includes a worldwide network of 13 sensor stations, referred to as Galileo Experimental Sensor Stations (GESS) and of a processing center located in ESA–ESTEC. The IOV phase will be completed by the launch of four additional satellites. The first two satellites were launched in October 2011, with two more following them by mid-2012.

2.2 Observables

Code and phase measurements are the most important GNSS observables, used for positioning (point, differential or relative), time transfer or for estimating ionospheric and tropospheric delays. Some applications can use only code, phase, or both types of observations [69]. This section deals with the basic principles of code and phase measurements (section 2.2.1), and explains all error sources that affect them in detail (section 2.2.2). In addition to this, we will give the corresponding mathematical model (section 2.2.3).

Throughout this and subsequent sections and chapters, the superscript i identifies the satellite, and the subscript p identifies the receiver. Moreover, the subscript g or Φ identifies that the term relates respectively to code or phase measurements. Finally, the subscripts k, m, n indicate the dependency on the carrier wave frequency.

2.2.1 Basic principles

2.2.1.1 Code measurements

The code measurement refers to the distance between the satellite and the receiver. The measure itself consists of estimating the transmission time of the codes by correlating the PRN generated by the satellite with the internal replica generated by the receiver.

The code observable (in vacuum) can be written as:

$$P^i_{p,k} = c\left(t_p - t^i\right) \tag{2.1}$$

where
$P^i_{p,k}$ is the code observable [m]
c is the velocity of light [m/s]
t_p is the time of observation in the receiver time frame [s]
t^i is the time of transmission in the satellite time frame [s]

As the satellite and receiver time frames are not synchronized, it is necessary to use a common reference time frame – the GPS time frame* – so that we can write:

$$t_p = \widehat{t}_p + \Delta t_p \tag{2.2}$$
$$t^i = \widehat{t}^i + \Delta t^i \tag{2.3}$$

where
$\widehat{t}_p$ is the time of observation in the GPS time frame [s]
$\widehat{t}^i$ is the time of transmission in the GPS time frame [s]
Δt_p is the receiver clock bias [s]
Δt^i is the satellite clock bias [s]

Equation (2.1) then becomes:

$$\begin{aligned} P^i_{p,k} &= c\left(\widehat{t}_p - \widehat{t}^i\right) + c\,\Delta t_p - c\,\Delta t^i \\ &= c\,\tau^i_{p,g,k} + c\,\Delta t_p - c\,\Delta t^i \end{aligned} \tag{2.4}$$

where $\tau^i_{p,g,k} = \widehat{t}_p - \widehat{t}^i$ is the code travel time [s]

Multiplying the code travel time $\tau^i_{p,g,k}$ with the velocity of light c is not equal to the geometric distance between the satellite and receiver (ρ^i_p). This is due to signal propagation in the atmosphere and to other systematic (e.g. hardware delays), random (measurement noise) and non-random (e.g. multipath delays) biases. In practice, equation (2.4) will have to be modified to account for all those effects, as explained in sections 2.2.2 and 2.2.3.

2.2.1.2 Phase measurements

The phase measurement is a measure of the phase difference between the received signal and a copy generated in the receiver. As only the fractional phase can be measured in this way, an integer constant representing an integer number of cycles is still unknown. This integer phase ambiguity refers to the first epoch of observation and remains constant during the satellite pass (assuming that no cycle slip† occurs).

In vacuum, the phase of the signal emitted by the satellite at the time of transmission is equal to the phase of the signal received from the satellite by the receiver at the time of

*The same statements can be derived for Galileo.

†A cycle slip can be defined as a sudden jump in the phase measurement that is always an integer number of cycles. More details about cycle slips are given in section 6.3.1.1.

observation. We can thus write:

$$\varphi^i_{p,k} = \varphi_{p,k}(t_p) - \varphi^i_k(t^i) - N^i_{p,k} \tag{2.5}$$

where
$\varphi^i_{p,k}$ is the phase observable [cycles]
$\varphi_{p,k}(t_p)$ is the phase in the receiver at t_p [cycles]
$\varphi^i_k(t^i)$ is the phase in the satellite at t^i [cycles]
$N^i_{p,k}$ is the integer phase ambiguity [cycles]

Following [52] and using equations (2.2) and (2.3), equation (2.5) becomes:

$$\begin{aligned}
\varphi^i_{p,k} &= f_k\, t_p + \varphi_{p,k}(t_0) - \left(f_k\, t^i + \varphi^i_k(t_0)\right) - N^i_{p,k} \\
&= f_k\, (\widehat{t}_p + \Delta t_p) + \varphi_{p,k}(t_0) - f_k\, \left(\widehat{t}^i + \Delta t^i\right) - \varphi^i_k(t_0) - N^i_{p,k} \\
&= \varphi_{p,k}(t_0) - \varphi^i_k(t_0) + f_k\, \left(\widehat{t}_p - \widehat{t}^i\right) + f_k\, \Delta t_p - f_k\, \Delta t^i - N^i_{p,k} \\
&= \varphi_{p,k}(t_0) - \varphi^i_k(t_0) + f_k\, \tau^i_{p,\Phi,k} + f_k\, \Delta t_p - f_k\, \Delta t^i - N^i_{p,k}
\end{aligned} \tag{2.6}$$

where
f_k is the frequency of the carrier wave k [Hz]
t_0 is the first epoch of measurement [s]
$\varphi_{p,k}(t_0)$ is the initial phase bias in the receiver [cycles]
$\varphi^i_k(t_0)$ is the initial phase bias in the satellite [cycles]
$\tau^i_{p,\Phi,k}$ is the phase travel time [s]

The phase observable can be scaled to unit of distance if we multiply equation (2.6) by the carrier wavelength $\lambda_k = c/f_k$:

$$\Phi^i_{p,k} = \Phi_{p,k}(t_0) - \Phi^i_k(t_0) + c\, \tau^i_{p,\Phi,k} + c\, \Delta t_p - c\, \Delta t^i - \lambda_k\, N^i_{p,k} \tag{2.7}$$

where
$\Phi^i_{p,k}$ is the phase observable [m]
$\Phi_{p,k}(t_0)$ is the initial phase bias in the receiver [m]
$\Phi^i_k(t_0)$ is the initial phase bias in the satellite [m]

The initial phase biases are non-integer biases caused by the non-synchronization of the satellite and receiver clocks at the first epoch of measurement (t_0). These biases corrupt the ambiguity term, and the resulting ambiguity is not an integer anymore. It is worth noticing that only the fractional part of the phase delays is critical, whereas the integer part is in any case not separable from the integer ambiguities [37]. Since they cancel out in Double Differences (DDs), these biases are not critical in relative positioning applications. However, their determination constitute a challenge for Precise Point Positioning (PPP) applications.

The satellite and receiver initial phase biases are actually strongly correlated with the phase hardware delays generated by the electronic of the satellite and receiver [67]. For this reason, the initial phase biases will be considered together with the phase hardware delays, and will from now on be dropped from the phase observable equation. We refer to section 2.2.2.9 for a more detailed discussion.

As for code observables, multiplying the phase travel time $\tau^i_{p,\Phi,k}$ with the velocity of light c is not equal to the geometric distance between the satellite and receiver (ρ^i_p). In practice, equations (2.6) and (2.7) will have to be modified, as explained in sections 2.2.2 and 2.2.3.

It has to be stressed that the geometric distance between the satellite and the receiver (ρ^i_p) is evaluated at the transmission time $\widehat{t}^i$, which is computed by subtracting the code or phase signal travel time ($\tau^i_{p,g,k}$ ou $\tau^i_{p,\Phi,k}$) to the observation time ($\widehat{t}_p$). As the difference between $\tau^i_{p,g,k}$ and $\tau^i_{p,\Phi,k}$ ($\simeq 10^{-7}$ s) is negligible with regards to the signal travel time ($\simeq$ 0.08 s), we can write:

$$\widehat{t}^i = \widehat{t}_p - \tau^i_{p,k} \tag{2.8}$$

where $\tau^i_{p,k}$ is the signal travel time [s]
As a consequence, it is assumed that ρ^i_p is equal for code and phase measurement [81] so that the transmission time $\widehat{t}^i$ can be computed by:

$$\widehat{t}^i = \widehat{t}_p - \frac{\rho^i_p}{c} \tag{2.9}$$

In the Earth-Centered-Earth-Fixed (ECEF) coordinate system, the geometric distance between the satellite and the receiver is computed as follows:

$$\rho^i_p \quad = \quad \|\mathbf{X^i} - \mathbf{X_p}\| \tag{2.10}$$

where
$\mathbf{X^i}$ is the position vector of the satellite in the ECEF coordinate system
$\mathbf{X_p}$ is the position vector of the receiver in the ECEF coordinate system

2.2.2 Error sources

As already mentioned in section 2.2.1, multiplying the travel time with the velocity of light is not equal to the geometric distance between the satellite and the receiver. This is due the following effects:

- atmospheric (ionospheric and tropospheric) refraction (sections 2.2.2.5 and 2.2.2.6),
- multipath delays (section 2.2.2.7),
- hardware or instrumental delays (section 2.2.2.9),
- antenna phase center offset and variations (section 2.2.2.10),
- phase wind-up effect (only for phase) (section 2.2.2.12).

Furthermore, as we use the geocentric ECEF coordinate system, it is necessary to correct the satellite coordinates for the Earth rotation effect (section 2.2.2.4). As the Newtonian mechanics are not strictly applicable, we have to correct the satellite clocks for relativistic effects (section 2.2.2.3). Finally, since GNSS observables are stochastic, we have to account for measurement noise in the equations (section 2.2.2.11).

All errors sources can be divided into three groups [52]: satellite, signal and receiver related errors (see table 2.3). In the next section, we will describe each error source in detail. In the meantime, we will mention the possibilities of reducing their impact – modeling or correction of the effect –, allowing us to obtain the error budget for undifferenced measurements.

Table 2.3 *– Classification of GNSS error sources.*

Source	Error
Satellite	Orbital bias
	Clock bias
	Relativistic effects
	Earth rotation effect
	Hardware delays
	Antenna phase center offset and variations
Signal	Ionospheric delays
	Tropospheric delays
	Multipath delays
Receiver	Clock bias
	Hardware delays
	Antenna phase center offset and variations
	Measurement noise
	Phase wind-up effect

2.2.2.1 Orbital bias

The orbital bias is the difference between the expected position of the satellite – given by the ephemerides – and its actual position.

Satellite ephemeris – a set of Keplerian elements with additional perturbation parameters for a given reference epoch – are broadcast in the navigation message and used in a standard algorithm [23, 69] to estimate real-time satellite positions. The accuracy of broadcast ephemeris is around 1 meter.

For precise applications, broadcast ephemeris are not accurate enough. Therefore, the International GNSS Service (IGS) produces precise ephemeris based on observations from globally distributed tracking stations. Table 2.4 gives the accuracy, latency and sample interval of the IGS precise orbit products. Broadcast ephemeris have been included for comparison. The accuracy values obtained are based on comparison with independent Satellite Laser Ranging (SLR) measurements [56].

Since the orbital bias induces an error in the geometric distance between the satellite and the receiver (ρ_p^j), there is no need to add a specific term in the mathematical model. The magnitude of this error mainly depends on the relative position between the satellite and the receiver, and more specifically on the distribution of the orbital bias between the along-track (satellite's direction of motion), cross-track (perpendicular to along-track and radial) and radial (from Earth's center to satellite) components.

Table 2.4 *– GPS orbit products. From [56].*

Orbit product	Accuracy [cm]	Latency	Sample interval
Broadcast	~ 100	real time	daily
Ultra-rapid (predicted)	~ 5	real time	15 min
Ultra-rapid (observed)	~ 3	3-9 hours	15 min
Rapid	~ 2.5	17-41 hours	15 min
Final	~ 2.5	12-18 days	15 min

Figure 2.2 shows the along-track, cross-track and radial components of broadcast orbital bias for November 1 1997, PRN 22, which were computed with respect to the IGS final orbit. It can be observed that along-track and cross-track components of the orbital bias tend to have approximately the same range, while it is four time smaller for the radial bias. This can be explained by the fact that the revolution time (and thus the semi-major axis) can be very accurately determined, as well as by the fact that GNSS measurements are more sensitive to changes in the radial direction [95].

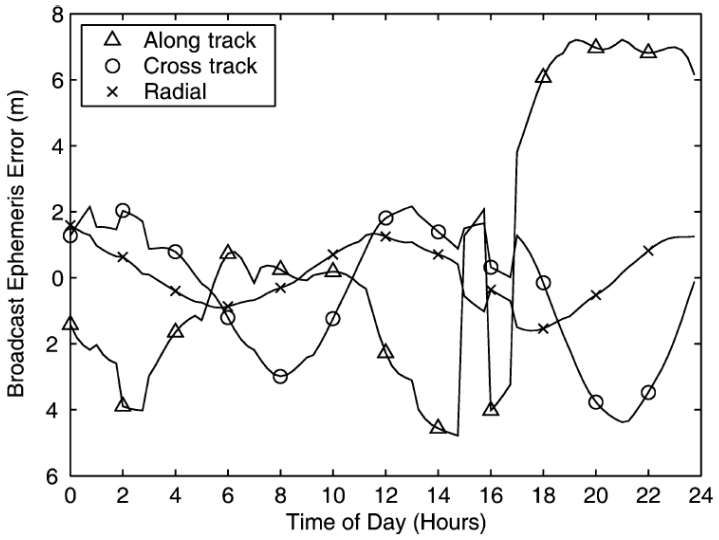

Figure 2.2 *– Along-track, cross-track and radial components of broadcast orbital bias (reference: IGS final orbit) for November 1 1997, PRN 22. From [127].*

A realistic approximation of the error on geometric distance due to satellite orbital bias is given by [127]:

$$SISRE_{orb} = \sqrt{R^2 + \frac{1}{49}\left(A^2 + C^2\right)} \tag{2.11}$$

where
$SISRE_{orb}$ is the "orbit only" Signal-In-Space-Range-Error (SISRE) [m]
R [m], A [m], C [m] are the radial, along-track and cross-track components of the orbital bias

Equation (2.11) takes into account that an error on the radial component has a major impact. By considering precise orbits to be the truth, any difference with other orbit products can be attributed to the orbital bias. Using this, $SISRE_{orb}$ of ultra-rapid products was found to be around 2 cm [77] and $SISRE_{orb}$ of broadcast ephemeris around 1 m [127].

From table 2.4, one can note that the sample interval of orbit products is generally 15 min. Therefore the satellite positions and velocities need to be interpolated to match the observation epochs (1 s or 30 s sample interval). Most of the polynomial methods used result in accurate millimeter interpolation of satellite positions [103]. More details about the interpolation method used in this work will be given in section 6.3.2.

2.2.2.2 Satellite clock bias

The satellite clock bias Δt^i [s] is the difference between the time of transmission in the satellite time frame (satellite clock reading) and the time of transmission in the GPS time frame, as shown in equation (2.3). As both code and phase measurements are directly linked to the time measurement, this bias has to be taken into account, as already done in equations (2.4), (2.6) and (2.7).

The satellite clock biases of the GPS satellites are monitored by the GPS control segment and predicted in the form of a second-order polynomial. All parameters are included in the first parameter group of the broadcast ephemerides. The satellite clock bias can thus be modeled as follows [23]:

$$\Delta t^i = a_0 + a_1 \left(\widehat{t}^i - t_{0c}\right) + a_2 \left(\widehat{t}^i - t_{0c}\right)^2 \tag{2.12}$$

where
t_{0c} is the reference time for the clock model [s]
a_0, a_1, a_2 are the polynomial coefficients, respectively given in [s], [s/s] and $\left[\mathrm{s/s^2}\right]$

These satellite clock biases are used for real-time applications and have a precision of about 5 ns or 1.5 m, which is not sufficient for precise applications. Thus, similarly to orbits, IGS computes precise satellite clock biases by using their global network of stations. Table 2.5 shows all GPS satellite clock products available and their corresponding accuracy [56].

Table 2.5 *– GPS satellite clock products.*

Clock product	Accuracy [ns]	Latency	Sample interval
Broadcast	~ 5	real time	daily
Ultra-rapid (predicted)	~ 3	real time	15 min
Ultra-rapid (observed)	~ 0.15	3-9 hours	15 min
Rapid	~ 0.075	17-41 hours	5 min
Final	~ 0.075	12-18 days	30 s

In contrast to orbital data, high-order polynomial interpolation is not suitable for clocks due to their random behavior. Linear interpolation should therefore be preferred. This causes non negligible interpolation errors depending on the clock type (cesium or rubidium) and on the product used (sample interval). The error associated with the interpolation of different

clock data sets has been assessed in [77]. The results are presented in figure 2.3. A Root Mean Square (RMS) interpolation error of 10 cm is obtained for cesium clocks at the 15 min sample interval, while at 5 min intervals it decreases to a few centimeters regardless of the clock type. Moreover, at 30 s intervals the RMS interpolation error decreases to 4 mm [136].

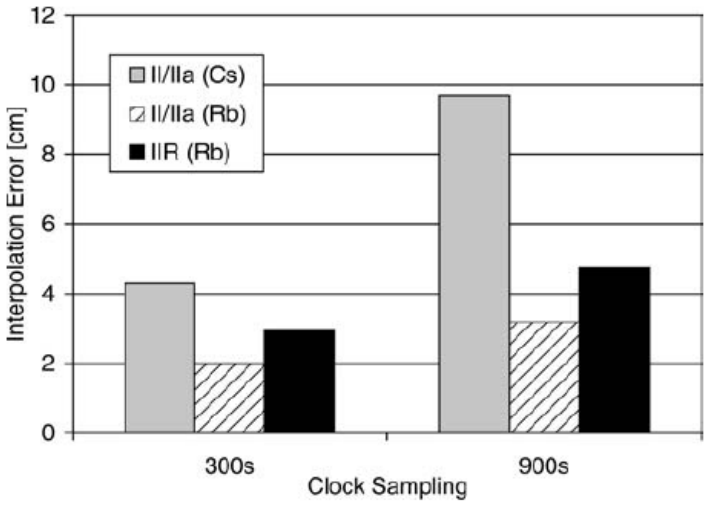

Figure 2.3 *– RMS interpolation error of GPS clocks at 5 min and 15 min sample intervals. From [77].*

2.2.2.3 Relativistic effects

The satellite clocks undergo relativistic effects. This is due to the satellite's velocity (special relativity) and also to gravitational potential differences between the satellite and Earth's surface (general relativity). The main part of those relativistic effects is a constant and appears as a frequency shift in the satellite clocks. This is compensated by slightly reducing the nominal frequency (0.0045 Hz at 10.23 MHz). The remaining part is a periodic component that is mainly caused by the orbital eccentricity e. Thus, for exact circular orbits, this correction is zero (e.g. for Galileo).

Conventionally, relativistic effects are removed from all GPS clocks – either broadcast or precise – in order to facilitate their maintenance, synchronization and prediction (linear behaviour). Thus, all users must apply the conventional correction to the satellite clock bias as follows [23]:

$$\Delta t^i + \Delta t^i_{rel} \tag{2.13}$$

where Δt^i_{rel} are the relativistic effects [s]

While using broadcast ephemerides (both orbits and clocks), relativistic effects can be computed as follows [23]:

$$\Delta t^i_{rel} = -\frac{2}{c^2}\sqrt{aGM}\, e \sin E \tag{2.14}$$

where
a is the semi-major axis of the satellite orbit [m]

G is the universal gravitational constant $\left[\mathrm{m}^3 \cdot \mathrm{kg}^{-1} \cdot \mathrm{s}^{-2}\right]$
M is the Earth's mass [kg]
e is the eccentricity of the orbit $[-]$
E is the eccentric (angular) anomaly of the orbit [rad]

More details about those parameters will be given in section 5.2.1.1.

For precise ephemerides, an equivalent but more convenient formulation is used [62]:

$$\Delta t^i_{rel} = -2\frac{\mathbf{X^i} \cdot \mathbf{v^i}}{c^2} \tag{2.15}$$

where $\mathbf{X^i}$ and $\mathbf{v^i}$ are the position and velocity vector of the satellite, respectively.

The magnitude of relativistic effects generally varies between 0 and 45 ns ($\sim$ 14 m) for $e = 0.02$, but can reach 70 ns ($\sim$ 20 m).

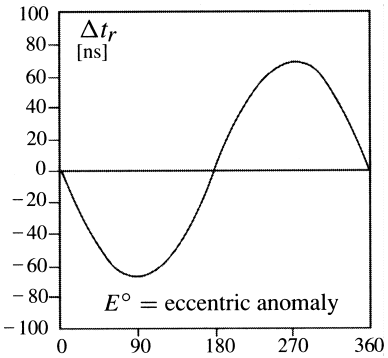

Figure 2.4 *– Relativistic effects for one satellite revolution (E from 0° to 360°). From [107].*

The relativistic clock correction obtained by equations (2.14) and (2.15) are affected by small periodic errors with amplitude of about 0.1 ns ($\sim$ 3 cm) [62], which is about the same precision level as the final IGS clock products (table 2.5). Therefore, an improved relativistic correction has been developed in [63] which makes it possible to reach a precision of 0.015 ns.

2.2.2.4 Earth rotation effect

The satellite coordinates are computed in the ECEF coordinate system at the time of transmission $\widehat{t}_i$. As this system rotates with respect to the satellite during the signal propagation, this causes a change of the satellite coordinates – rotation around the Z-axis –, transferred in the geometric distance ρ^i_p as the so-called Earth rotation effect, also known as *Sagnac* effect [135].

Therefore, a correction of the satellite coordinates – and implicitly ρ^i_p – is necessary. Thus, the original satellite coordinates must be rotated around the Z-axis (in counterclockwise direction) by an angle α given by [107]:

$$\alpha = \omega_e \, \tau^i_p \tag{2.16}$$

where ω_e [rad/s] is the Earth's rotational velocity and τ_p^i [s] is the signal travel time.

If X^{i2}, Y^{i2}, Z^{i2} are the original satellite coordinates, the satellite coordinates corrected for the Earth rotation effect are given by:

$$X^i = X^{i2}\cos\alpha + Y^{i2}\sin\alpha \quad (2.17)$$

$$Y^i = Y^{i2}\cos\alpha - X^{i2}\sin\alpha \quad (2.18)$$

$$Z^i = Z^{i2} \quad (2.19)$$

Thus, the geometric distance ρ_p^i is computed with the corrected satellite coordinates X^i, Y^i, Z^i. Note that it would be equivalent to correct the receiver coordinates as in [7] or directly the geometric distance as explained in [135]. Using equation (2.9), we can write:

$$\alpha = \omega_e \frac{\rho_p^i}{c} \quad (2.20)$$

Equations (2.20) and (2.10) imply that α is a function of ρ_p^i. An iterative process could be used; however, as the improvement is negligible, one generally stops at the first iteration.

As the signal travel time τ_p^i is approximately equal to 0.08 s, α is smaller than $1.5''$ or $7.27 \cdot 10^{-6}$ rad. For a user located at the equator, the effect can reach about 30 meters [135]. Figure 2.5 shows the Earth rotation effect for five GNSS satellites on a given day. The effect is positive (negative) when the relative distance between the satellite and the station is increasing (decreasing).

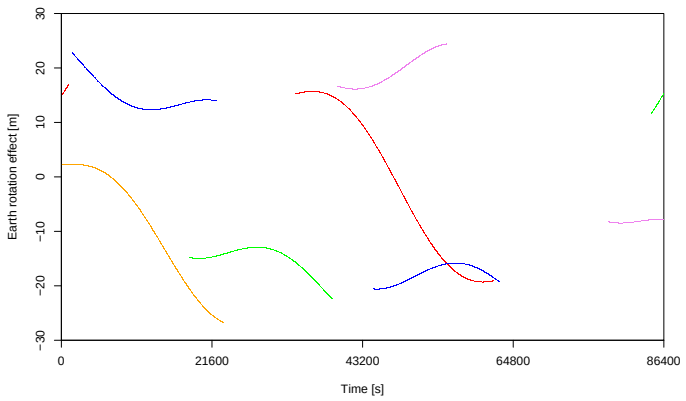

***Figure* 2.5** – *Illustration of the Earth rotation effect.*

2.2.2.5 Ionospheric delays

A more exhaustive description of the ionosphere will be given in chapter 3. However, we will present the information relative to the general GNSS point of view here.

The ionosphere can be defined as the part of the upper atmosphere in which sufficient ionization exists to influence the propagation of radio waves [29]; it is characterized by the

electron density N_e $\left[\text{electrons}/\text{m}^3\right]$ that strongly depends on solar radiation. These free electrons of the ionosphere affect the propagation of GNSS radio signals: there is a change in wave velocity which depends on the ionospheric index of refraction. As the ionosphere is an heterogeneous, anisotropic and dispersive medium, this index is not a constant. Considering GNSS frequency range, the phase and group index of refraction are respectively given by:

$$n_{\Phi,k} = 1 - \frac{1}{2}\frac{f_p^2}{f_k^2} - \frac{1}{2}\frac{f_p^2 f_g |\cos\Theta|}{f_k^3} - \frac{1}{8}\frac{f_p^4}{f_k^4} \tag{2.21}$$

$$n_{g,k} = 1 + \frac{1}{2}\frac{f_p^2}{f_k^2} + \frac{f_p^2 f_g |\cos\Theta|}{f_k^3} + \frac{3}{8}\frac{f_p^4}{f_k^4} \tag{2.22}$$

where
f_p is the electron plasma frequency [Hz]
f_g is the electron gyrofrequency [Hz]
Θ is the angle between the wave direction of propagation and the Earth's magnetic field vector [rad]

These equations will be detailed in section 3.1.4.1. As $n_{\Phi,k} < 1$ and $n_{g,k} > 1$ there is a phase advance and a group delay in the ionosphere. However, for more convenience, the term of ionospheric *delays* will be used for both phase and code measurements.

By integrating the index of refraction along the satellite-to-receiver path while neglecting the *bending effect** we obtain the phase and group ionospheric delays $I^i_{p,\Phi,k}$ and $I^i_{p,g,k}$ in unit of distance, which will be detailed in section 3.1.4.2. The ionospheric delay consists of the first and higher-order (second, third) terms of expansion. As the first-order term contains the main part of the delay (99.9 %), very small higher-order terms are usually ignored. Thus we may write:

$$I^i_{p,\Phi,k} = -\frac{40.3}{f_k^2}\,\text{TEC} \tag{2.23}$$

$$I^i_{p,g,k} = \frac{40.3}{f_k^2}\,\text{TEC} \tag{2.24}$$

where

$$\text{TEC} = \int N_e\, ds \tag{2.25}$$

The Total Electron Content (TEC) is the integral of the electron density N_e along the satellite-to-receiver path. It represents the number of free electrons in a 1-square meter column along the satellite-to-receiver path. It is generally expressed in TECU, with 1 TECU being 10^{16} electrons per 1-square meter column ($1\,\text{TECU} = 10^{16}$ electrons$/\text{m}^2$).

As phase and group delays are equal but have opposite sign, their notation can be contracted in the code and phase mathematical model without specifying the subscript of the observable type:

$$I^i_{p,k} = I^i_{p,g,k} = -I^i_{p,\Phi,k} \tag{2.26}$$

Thus the $-I^i_{p,k}$ term designates the phase advance and the $+I^i_{p,k}$ term the code delay.

*The bending effect is the change in the signal propagation direction due to the change of index of refraction along the propagation path.

The ionospheric delay is actually the most important error source in GNSS. Ionospheric delays can vary from 1 meter to more than 100 meters. Taking advantage that GNSS systems work on several frequencies, it is possible to correct (eliminate) or measure ionospheric delays. For a single frequency user, however, ionospheric modeling is the only solution.

Elimination

The use of simultaneous GNSS measurements in both frequencies (dual frequency user) makes the elimination of the first-order ionospheric delays possible. The so-called Ionospheric-Free (IF) code $P_{IF,km}$ [m] and phase combinations $\Phi_{IF,km}$ [m] are given by [69]:

$$P_{IF,km} = \frac{f_k^2 P^i_{p,k} - f_m^2 P^i_{p,m}}{f_k^2 - f_m^2} \tag{2.27}$$

$$\Phi_{IF,km} = \frac{f_k^2 \Phi^i_{p,k} - f_m^2 \Phi^i_{p,m}}{f_k^2 - f_m^2} \tag{2.28}$$

This combination has the advantage to make first-order ionospheric delays disappear while keeping other terms (geometric distance, clocks, etc.) identical. However, the combined ambiguity (IF ambiguity) is not an integer anymore, and the measurement noise has increased. Those combinations are used in precise positioning [69]. If millimeter level accuracy is needed, higher-order terms cannot be ignored anymore. Correction formulae have been derived by several authors [9, 49, 55]. This will be explained in details in section 3.1.4.3. The availability of a third frequency makes it possible to eliminate the first- and second-order ionospheric delays by using the second-order IF code and phase combinations defined in [125, 135]. For a triple frequency user, this is another option for reaching millimeter level accuracy.

Measurement

For a dual frequency user, it is also possible to use the so-called Geometric-Free (GF) code and phase combinations in order to reconstruct the TEC. This technique – which is described in detail in section 3.2 – is used for example to compute numerical TEC maps (section 3.2.3). Moreover, the core of our research is the development of a triple frequency TEC reconstruction technique which is explained in chapter 4.

Modeling

For a single frequency user, or if one needs to keep the integer nature of the ambiguities, ionospheric modeling is required. Several types of ionospheric models are available: empirical models, GPS data driven models, analytical and physical models.

- *Empirical models based on ionospheric measurements*
  The Klobuchar model is a broadcast model that gives the vertical ionospheric delay at a given time and location [61]. A description will be given in section 5.2.2.4.
  The NeQuick model describes the spatial and temporal variation of the electron density [51, 89]. This profiler calculates the electron density at a given location and time in the ionosphere. Different formulations are used for the bottomside or topside ionosphere. NeQuick is used to provide a real-time ionospheric correction for Galileo single frequency users.
  The International Reference Ionosphere (IRI) model is an international standard for the

specification of ionospheric parameters. For a given location and time, IRI provides monthly averages of several parameters (electron density, ion temperature, ion composition, etc.) in the altitude range from 50 to 2000 km [14].

- *GPS data driven models*, or numerical maps are computed on a global or local scale and provide the value of an ionospheric parameter in a grid, e.g. the vertical TEC (vTEC) in a TEC map. This example is detailed in section 3.2.3. The value of the parameter at a given location and time can then be retrieved through interpolation in the grid, as explained in section 3.2.3.2.
- *Analytical and physical models* which are not used in GNSS positioning applications. Examples of analytical models are CCIR maps of foF2 computed from ionosonde measurements [1]. Physical models are based on the theory of ionospheric formation.

2.2.2.6 Tropospheric delays

The troposphere is the lower part of the Earth's atmosphere which extends from the surface to about 9 km at poles and 16 km at the equator where the daily weather takes place and where sufficient neutral particles (atoms and molecules) are present to affect the propagation of radio waves [75, 107]. The effect of the neutral atmosphere is called tropospheric refraction, even if it includes the effect of the stratosphere (up to 40 km). However, the contribution of the troposphere is dominant.

Unlike the ionosphere, the troposphere behaves as a non dispersive medium for GNSS frequencies. The tropospheric index of refraction n is thus frequency-independent, implying that the effect is equal for phase and code. Besides, as $n > 1$ the tropospheric effect is a delay (positive). The integration of the index of refraction along the satellite-to-receiver path – neglecting the *bending effect* – gives the tropospheric delay T_p^i [m]:

$$T_p^i = \int (n-1)\, ds \tag{2.29}$$

As n is numerically close to 1, one rather uses the refractivity of the troposphere N_T [69]:

$$N_T = 10^6 (n-1) \tag{2.30}$$

Substituting equation (2.30) in equation (2.29) gives:

$$T_p^i = 10^{-6} \int N_T\, ds \tag{2.31}$$

The refractivity N_T can be described as a function of meteorological parameters with the following empirical formula, giving the separation into a dry (hydrostatic) N_d and a wet component N_w [107]:

$$N_T = C_1 \frac{P}{T} + C_4 \frac{e}{T^2} = N_d + N_w \tag{2.32}$$

where
T is the temperature [K]
P is the atmospheric pressure [hPa]
e is the partial pressure of water vapor [hPa]
C_1 and C_4 are empirical coefficients, resp. in $\left[\mathrm{K} \cdot \mathrm{hPa}^{-1}\right]$ and $\left[\mathrm{K}^2 \cdot \mathrm{hPa}^{-1}\right]$

From this, equation (2.31) can be written as:

$$T_p^i = 10^{-6} \int (N_d + N_w)\, ds = T_{p,d}^i + T_{p,w}^i \tag{2.33}$$

where $T_{p,d}$, $T_{p,w}$ are respectively the dry and wet tropospheric delay [m], representing respectively $\pm$ 90 % and $\pm$ 10 % of the total delay.

The integral in equation (2.33) can be solved if we know the behavior of the refractivity along the signal path. Direct measurements of N_d and N_w are generally not feasible. This is why several models of the zenithal delay were developed in the literature. The most frequently used ones are the Hopfield [53] and Saastamoinen [97] models. The dry and wet components of Saastamoinen's model are given by [76]:

$$vT_{p,d}^i = 0.0022777\,(1 + 0.0026\,\cos 2\varphi + 0.00028\,H)\,P_0 \tag{2.34}$$

$$vT_{p,w}^i = 0.0022777\left(\frac{1255}{T_0} + 0.05\right) e_0 \tag{2.35}$$

where
$vT_{p,d}^i$ is the dry zenithal tropospheric delay [m]
$vT_{p,w}^i$ is the wet zenithal tropospheric delay [m]
φ is the latitude of the station [rad]
H is the orthometric height of the station* of the station [m]
P_0 is the atmospheric pressure at the station [hPa]
T_0 is the temperature at the station [K]
e_0 is the partial pressure of water vapor at the station [hPa]

At sea-level, $vT_{p,d}^i$ generally varies between 2.30 and 2.60 m, while $vT_{p,w}^i$ ranges from 0 to 0.40 m. Those models require the knowledge of meteorological parameters. When using so-called standard meteorological data (P, T, e), the precision of the total zenithal tropospheric delay is about 5-10 cm. However, when using measured parameters, the precision changes to the millimeter for the dry component, but only to 1-2 cm for the wet component that is more difficult to model from ground meteorological measurements [7].

A mapping function is needed to convert the dry/wet zenithal tropospheric delay to the dry/wet tropospheric delay along the satellite-to-receiver path. The dry and wet mapping functions (MF_d, MF_w) can be defined as:

$$\frac{T_{p,d}^i}{vT_{p,d}^i} = MF_d \tag{2.36}$$

$$\frac{T_{p,w}^i}{vT_{p,w}^i} = MF_w \tag{2.37}$$

The total tropospheric delay T_p^i is obtained by:

$$T_p^i = MF_d \cdot vT_{p,d}^i + MF_w \cdot vT_{p,w}^i \tag{2.38}$$

*The orthometric height of a point is the distance along a plumb line from the geoid to this point [69].

As the tropospheric delay increases when the satellite zenith angle χ increases (the air mass path length increases), the mapping function depends on χ. Due to the spatial and temporal variability of the troposphere, the modeling of the mapping function is not straightforward. There are several models but Niell's function is generally used [80]. It consists of one expression whose coefficients – given in tables as a function of the latitude of the station – differ for MF_d and MF_w. This function is accurate, independent of the surface meteorology and requires only the satellite zenith angle (χ), the latitude of the station (φ) and the Day of Year (DOY) as input [69]. Nevertheless, its precision depends on the satellite zenith angle. Table 2.6 gives the accuracy of the Niell dry and wet mapping functions as a function of χ. Those values were obtained by comparison with ray tracing computations [75].

Table 2.6 *– Accuracy of Niell's mapping function. From [7, 75].*

χ (°)	Accuracy [mm]	
	MF_d	MF_w
60	0.2	0.1
70	0.7	0.2
75	1.4	0.4
80	4.4	1.2
84	15.5	5.8
87	70.0	28.6

The error on the modeled zenithal tropospheric delay is amplified by the mapping function, itself also associated with an error. The tropospheric delay, and in particular the wet component, is therefore considered an important error source in point positioning.

2.2.2.7 Multipath delays

The signal emitted by the satellite can reach the receiver through more than one path – due to the reflection on objects near the receiver such as buildings, ground and water, trees, hills. When it does, direct and indirect (reflected) signals interfere at the receiver, causing multipath delays. This is illustrated in figure 2.6.

Multipath delays constitute an almost random periodic effect that affects code and phase measurements differently. The effect on code measurements is generally two orders of magnitude larger than on phase measurements. For phase measurements, the maximal value is about one fourth of the signal wavelength (about 5-6 cm) [69]. Moreover, multipath delays depend on the carrier wave frequency and on the satellite elevation. It implies that multipath delays are written $M^i_{p,g,k}$ and $M^i_{p,\Phi,k}$, respectively for code and phase measurements, both in units of meters.

Because of the arbitrarily different geometric situations, and since a lot of parameters can influence the magnitude of multipath delays (reflection coefficient, orientation, inclination of the surface), there is no general model able to correct those effects. However, several strategies are able to mitigate their impact, e.g. [69, 107]:

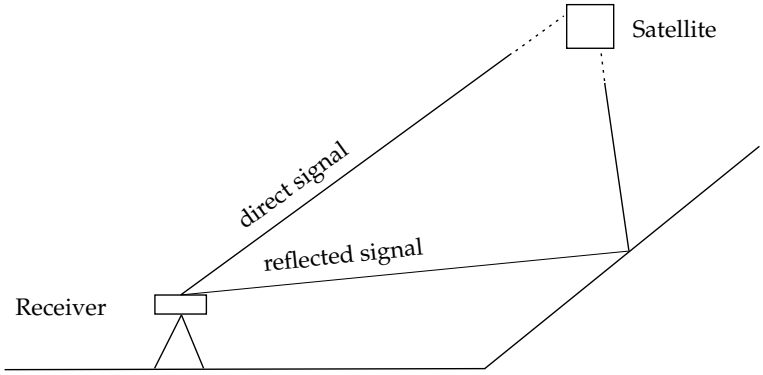

Figure 2.6 *– Geometry of multipath delays.*

- observe over a longer time period (valid for static positioning),
- choose a location away from reflecting objects,
- use an antenna taking the polarization of the signal into account – as reflection changes the way of polarization – or use a choke ring antenna, consisting of several concentric metallic circular fins above a metallic base,
- calibrate stations (reference stations): first, the multipath is detected by using DD over short baselines or Signal-to-Noise Ratio (SNR); then a moving station is used to cancel out multipath effects through the controlled motion of a robot; finally, the DD are used to model the multipath effects of the fixed station,
- analyze the repeatability pattern: since multipath delays depend on the geometry between the satellite, the receiver and the reflecting objects, they show the same pattern between consecutive sidereal days; this day-to-day repeatability can be used to reduce multipath in a permanent station,
- in practical situations, it is recommended to avoid observing satellite close to the horizon in order to reduce multipath; this is done by applying an elevation mask.

The influence of multipath delays can be estimated by using combinations of GNSS code and/or phase measurements. A dual frequency combination of code and phase measurements MP_k [m] is used to assess the influence of code multipath delays [69, 115] :

$$MP_k = P^i_{p,k} - \Phi^i_{p,k} + \frac{2}{1 - \frac{f_k^2}{f_m^2}} \left(\Phi^i_{p,k} - \Phi^i_{p,m} \right) \tag{2.39}$$

For phase multipath delays, no combination of undifferenced dual frequency measurements is available. Nevertheless, some information can be extracted from Single Difference (SD) or DD phase measurements processing. If a third frequency is available, a triple frequency phase multipath combination $\Phi^3_{M,125}$ $\left[\mathrm{m}^3\right]$ can be formed [111]:

$$\Phi^3_{M,125} = \lambda^2_{\mathrm{L5}} \left(\Phi_{\mathrm{L1}} - \Phi_{\mathrm{L2}} \right) + \lambda^2_{\mathrm{L2}} \left(\Phi_{\mathrm{L5}} - \Phi_{\mathrm{L1}} \right) + \lambda^2_{\mathrm{L1}} \left(\Phi_{\mathrm{L2}} - \Phi_{\mathrm{L5}} \right) \tag{2.40}$$

This combination provides an indication of phase multipath delays, but can also be used to improve multi-frequency ambiguity resolution algorithms in precise positioning [111]. This combination will also be used in the ambiguity resolution procedure of the TEC reconstruction methodology (see section 4.3.2). Besides, a triple frequency code multipath combination $P^3_{M,125}\ \left[\mathrm{m}^3\right]$ can be formed [111]:

$$P^3_{M,125} = \lambda^2_{\mathrm{L5}}\left(P_{\mathrm{L1}} - P_{\mathrm{L2}}\right) + \lambda^2_{\mathrm{L2}}\left(P_{\mathrm{L5}} - P_{\mathrm{L1}}\right) + \lambda^2_{\mathrm{L1}}\left(P_{\mathrm{L2}} - P_{\mathrm{L5}}\right) \tag{2.41}$$

This combination provides an estimation of code multipath delays. However, it only gives information about the mixed effect on the three frequencies. Moreover, this combination can also be used as a relationship between code hardware delays.

As multipath is modulation-dependent, it is possible to improve code multipath performance by changing the signal definition [114]. In this context, advanced Galileo code modulation schemes were developed in the aim to significantly reduce code multipath delays [113]. A common tool to study resistance to multipath of a given signal/receiver/environment combination is to compute the multipath error envelope by simulating the tracking process. A multipath error envelope represents the resulting code multipath delays $M^i_{p,g,k}$ as a function of geometric path delays under idealized conditions: one multipath signal, specific relative amplitude (generally 0.5) [32, 57]. This can be done in several multipath environments, characterized by their Signal-to-Multipath Ratio (SMR), i.e. 27.5 dB, 13.5 dB and 6 dB respectively for open, rural and urban environments [32].

Figure 2.7 compares the multipath error envelopes for GPS C/A with all Galileo code modulation schemes at SMR=6 dB. It shows that all Galileo code modulations should be more multipath resistant than the GPS C/A code. Moreover, it can be pointed out that one advantage of Galileo is the suppression of long-delay multipath. The exceptional resistance to multipath of E5-AltBOC is also illustrated. It is worth noticing that the multipath performance of GPS P, L2C and L5 codes is identical to the performance of Galileo E5a, GPS C/A and Galileo E5a, respectively. This improvement of Galileo multipath performance has also been confirmed by applying equation (2.39) to experimental GPS and GIOVE-A data [112, 114]. In that analysis, statistics of multipath code delays were computed, e.g. standard deviation values that will be used later on, and particularly in chapter 4.

Table 2.7 *– Standard deviation of code and phase multipath delays for GPS and Galileo L1, L2 and L5 measurements [112, 114].*

Signal	$\sigma_{M_{g,k}}$ [m]		$\sigma_{M_{\Phi,k}}$ [mm]	
	GPS	Galileo	GPS	Galileo
L1	0.6	0.4	3	3
L2	0.6	0.2	3	3
L5	0.2	0.2	3	3

Similarly to measurement noise (see section 2.2.2.11), the code and phase multipath delays can generally be assumed to be white Gaussian, i.e. to have a normal distribution with a zero-mean. However, the white Gaussian behavior is not exactly true for code multipath delays. As a matter a fact, code multipath delays are not totally random effects. Moreover, contrary to phase multipath delays, code multipath delays do not have a zero-mean [115]

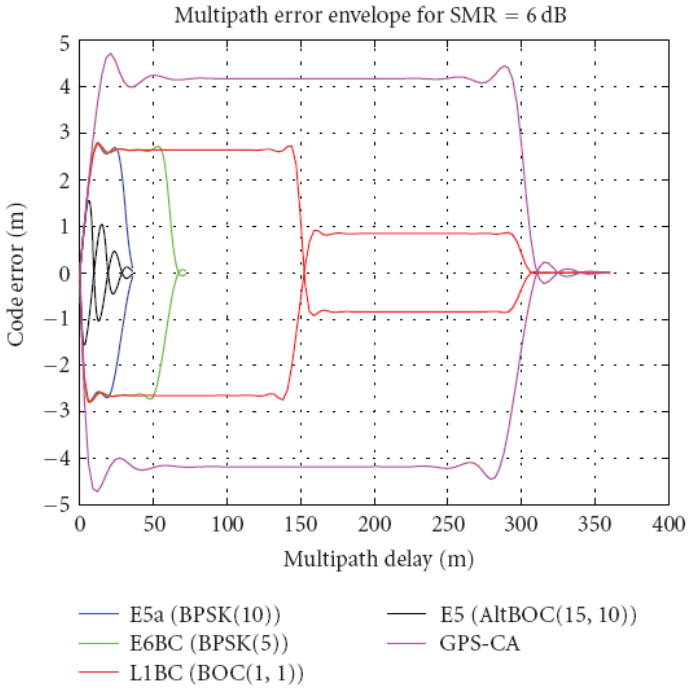

Figure 2.7 *– Multipath error envelopes of GNSS code modulations at SMR of 6 dB: GPS C/A (magenta), Galileo L1BC (red), E6BC (green), E5a (blue), E5-AltBOC (black). From [114].*

and should therefore rather be considered as a systematic error. Nevertheless, the use of an appropriate period length keeps the remaining code multipath delays relatively low, while phase multipath delays cancel out [115]. In chapter 4, code multipath delays will be assumed to be white Gaussian.

Table 2.7 summarizes the theoretical standard deviation of code and phase multipath delays for GPS and Galileo triple frequency measurements which will be used for TEC reconstruction. These frequencies are L1, L2 and L5 for GPS, and L1, E5b and E5a* for Galileo. The frequency choice is justified in chapter 4. The standard deviation values are valid for a satellite elevation angle greater than 10°.

In conclusion, even if multipath delays remain one dominant error source in GNSS, their influence can be mitigated significantly.

2.2.2.8 Receiver clock bias

The receiver clock bias Δt_p [s] is the difference between time of observation in the receiver time frame (receiver clock reading) and the time of observation in the GPS time frame, as

*These are more conveniently named L1, L2 and L5, respectively.

shown in equation (2.2). As both code and phase measurements are directly linked to time measurement, this bias has to be taken into account, as already done in equations (2.4), (2.6) and (2.7).

The requirements of the receiver clock are not very high, which means that it generally only consists of a quartz oscillator, whose stability is lower than that of the satellite [107]. In other words, the behavior of a receiver clock cannot be predicted. Consequently, for point positioning, the usual approach is to solve for an extra receiver clock bias parameter (one per epoch) along with the receiver coordinates. This bias is assumed to be independent at each measurement epoch. In relative positioning the receiver clock bias is eliminated by means of between-satellite SD or DD measurements.

Note that in some cases (e.g. receiver used for satellite orbit determination) the receiver is linked to a precise external clock, whose polynomial modeling is then possible [107]. In particular, for the realization of the IGS/BIPM timing project, many receivers of the IGS network were equipped with an atomic standard external reference. This has led to the development of the new IGS clock format (clock Receiver Independent Exchange (format) (RINEX), [56]), which provides the satellite and receiver clock bias at a 30 seconds sampling interval.

2.2.2.9 Satellite and receiver hardware delays

The satellite and receiver hardware delays are generated by the electronics of the satellite and receiver. The satellite hardware delay is the travel time between the generation and transmission in the satellite, whereas the receiver hardware delay can be defined as the travel time between reception and correlation in the receiver [81].

These satellite and hardware delays are different for each observable type (code/phase) and are mainly temperature and frequency dependent. Nevertheless, the exact relationship between temperature and frequency is not known [98]. The stability of receiver hardware delays is supposed to be better than 0.1 mm/s, and even better for satellite hardware delays [121]. While different techniques are developed to calibrate intra- and inter-frequency biases, the absolute hardware delays associated with a particular observable on a given frequency is much more difficult to determine. This is due to linearity of many parameters in the mathematical model, such as the clock biases, hardware delays and ambiguity parameters [8].

Satellite and receiver code hardware delays

In the satellite, the signals on each carrier frequencies (e.g. C/A and P1) and among frequencies are not synchronized because of the different digital and analog signal paths which correspond to each signal.

According to [23], the timing bias between GPS L1 and L2 code measurements is the *transmitter group delay* or T_{GD} [s]. This offset is available to users through the navigation message. Before 1999, the T_{GD} values were calibrated by the satellite manufacturer before launch during factory testing, with an accuracy of 15 ns ($\sim$ 4.5 m). Since April 1999, the T_{GD} values are estimated and provided by the Jet Propulsion Laboratory (JPL) with an accuracy of 0.5 ns ($\sim$ 0.15 m) [59]. This effort was made to answer the demand for ever greater accuracy in various applications, like point positioning or time transfer [131]. Since the satellite clock biases are determined by using the IF code combination, this timing bias is inconsequential in

PPP applications which are based on the same linear combination. However, single frequency users must adequately correct the clock biases as follows:

$$\Delta t^i - T_{GD} \qquad \text{for L1} \tag{2.42}$$

$$\Delta t^i - \frac{f_{\mathrm{L1}}^2}{f_{\mathrm{L2}}^2} T_{GD} \quad \text{for L2} \tag{2.43}$$

For L5 users, it will be necessary to use T_{GD} together with the *Inter-Signal Correction* (ISC_{L5}) as follows [24]:

$$\Delta t^i - T_{GD} + ISC_{\mathrm{L5}} \quad \text{for L5} \tag{2.44}$$

The satellite code hardware delays in units of meters will be denoted as $+\, d_{g,k}^i$ [m] in the mathematical model. We can thus write:

$$d_{g,\mathrm{L1}}^i = c \cdot T_{GD} \tag{2.45}$$

$$d_{g,\mathrm{L2}}^i = c \cdot \frac{f_{\mathrm{L1}}^2}{f_{\mathrm{L2}}^2} \cdot T_{GD} \tag{2.46}$$

In parallel, satellite Differential Code Biases (DCB) are estimated by the Center for Orbit Determination in Europe (CODE) as constant values for each day as a by-product of Global Ionospheric Maps (GIMs) [71, 100, 130]. The satellite DCB are related to T_{GD} by a simple linear relationship [7, 101]:

$$DCB_{km}^i = \frac{1}{c} \left(d_{g,\mathrm{L1}}^i - d_{g,\mathrm{L2}}^i \right) \tag{2.47}$$

$$= \frac{f_{\mathrm{L2}}^2 - f_{\mathrm{L1}}^2}{f_{\mathrm{L2}}^2} T_{GD} \tag{2.48}$$

where DCB_{km}^i are the satellite DCB [s]
In practice, T_{GD} or DCB_{km}^i are expressed in [ns].

In the receiver, the signals are delayed as they travel through the antenna, analog hardware and digital processing units until the physical point where the measurements are made [59]. For most applications, the receiver code hardware delays do not need to be calibrated, since they merge with the estimated clock biases parameters. However, the calibration of these delays is important for timing applications and for TEC computation. In this context, the receiver DCB are also estimated by CODE as an ancillary product of GIMs. They can be defined as:

$$DCB_{p,km} = \frac{1}{c} \left(d_{p,g,\mathrm{L1}} - d_{p,g,\mathrm{L2}} \right) \tag{2.49}$$

where
$DCB_{p,km}$ are the receiver DCB [s]
$d_{p,g,k}$ are the receiver code hardware delays for k frequency [m]

In the mathematical model, a $+\, d_{p,g,k}$ [m] term will be added.

The magnitude of DCB is found to be ± 3 ns for satellites and ± 10 ns for receivers, with an uncertainty of 0.5 ns and 0.2 ns, respectively [130]. Moreover, the stability of these DCB is about 0.5 ns for satellites, and 1 ns for receivers [4, 130].

Satellite and receiver phase hardware delays

Since the initial phase biases and the phase hardware delays are strongly correlated with each other [67], they cannot be separated from each other and will be considered together (see section 2.2.1.2). Nevertheless, they constitute two different effects with two different causes:

- the phase hardware delays are generated by the electronics of the satellite and receiver,
- the satellite and receiver initial phase biases are caused by the non-synchronization of the satellite and receiver clocks at t_0 and corrupt the integer ambiguity term of phase measurements (which is not an integer anymore).

We know that these phase delays are frequency-dependent. Thus, for satellite a $+ d^i_{\Phi,k}$ [m] term will be added in the mathematical model, whereas the receiver phase delays will be denoted as $+ d_{p,\Phi,k}$ [m]. Even if there is a certain lack of knowledge on the properties of the phase delays, some investigations have been driven lately to characterize and determine them [7, 8, 36, 37, 67, 68, 124]. From all these studies, it results that:

- The phase delays should be relatively stable over a few days. Nevertheless, this assumption is not entirely true: part of these biases are hardware-dependent and could have some variability.
- It is rather difficult to find information about their amplitude on undifferenced measurements. As a matter of fact, most methods estimated them for SD measurements (receiver-receiver SD for receiver biases, satellite-satellite SD for satellite biases). Moreover, in the method presented by [8], the determination of phase delays is biased by the code hardware delays.
- As the calibration procedures are still in development, we do not know much about the accuracy of the computed biases.

The determination of the receiver and satellite phase hardware delays is thus still a challenge, especially for the needs of carrier phase positioning.

2.2.2.10 Satellite and receiver antenna phase center offset and variations

The electrical Phase Center (PC) of an antenna can be defined as the point at which the electromagnetic signal is actually emitted (satellite) or received (receiver). In particular for GNSS, the antenna instantaneous phase centers of both satellite and receiver serve as the end points of the measured distance between the satellite and the receiver. In other words, it is the point which the code and phase measurements refer to. Since their position cannot be accessed directly, it can be modeled by a consistent set of antenna Phase Center Offset (PCO) and Phase Center Variation (PCV) values. The Phase Center Offset (PCO) is, for the satellite and receiver respectively:

- the distance from the satellite Center of Mass (CM) to the antenna mean phase center

  The satellite CM is actually the point to which precise orbits refers to, while broadcast orbits refer to the mean phase center.

- the distance from the Antenna Reference Point (ARP) to the antenna mean phase center

  The ARP is an external point on the antenna that can be physically determined. It is defined as the center of the bottom surface of the preamplifier [39]. This geometric point is used to link the measured positions to the geodetic point (ground marker) above which each antenna is installed; the distance from the marker to the ARP is called the antenna height (h_{ant}).

The deviations of the antenna mean phase center from the antenna instantaneous phase center are the Phase Center Variations (PCVs). The location of the instantaneous phase center actually varies with the orientation of the satellite-to-receiver vector, and more specifically with the satellite zenith and azimuth angles.

Satellite antenna PCO

A correction of the satellite antenna PCO has to be applied to the satellite coordinates to ensure the compatibility with the use of precise ephemeris. The PCO is given in the satellite-fixed coordinate system whose origin is the satellite's center of mass. This coordinate system is shown in figure 2.8. The z-axis is pointed towards the Earth's center of mass, and is thus parallel to the antenna pointing direction. The y-axis is parallel to the solar panel axis, and is kept perpendicular to the solar vector* during the motion of the satellite. The x-axis completes the right-hand coordinate system.

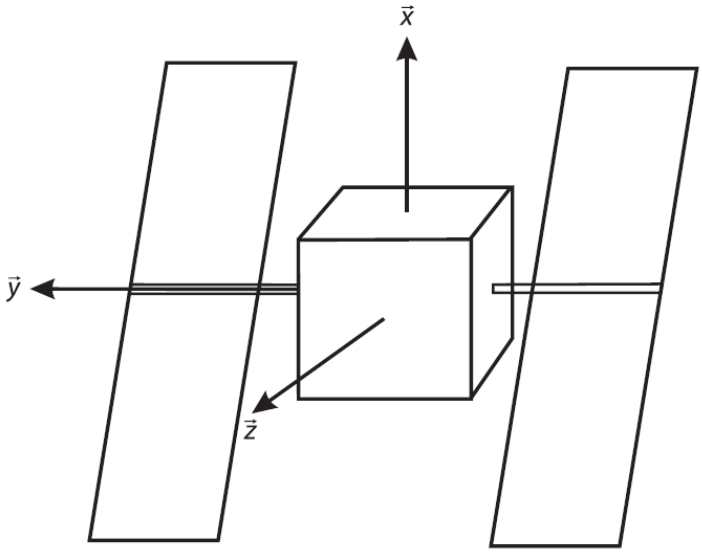

Figure 2.8 *– Satellite-fixed coordinate system. From [135].*

If $\mathbf{x_o^i}\,(\Delta x, \Delta y, \Delta z)$ is the satellite PCO vector in the satellite-fixed coordinate system, the position of the satellite antenna mean phase center in the ECEF coordinate system is given by

*The solar vector is the vector from the satellite to the Sun.

[69, 135]:

$$\mathbf{X^i_{mPC}} = \mathbf{X^i_{CM}} + \left[\widehat{\mathbf{e}}_\mathbf{x}\, \widehat{\mathbf{e}}_\mathbf{y}\, \widehat{\mathbf{e}}_\mathbf{z}\right] \mathbf{x^i_o} \tag{2.50}$$

where
$\mathbf{X^i_{mPC}}$ is the position vector of the satellite antenna mean phase center (ECEF)
$\mathbf{X^i_{CM}}$ is the position vector of the satellite's center of mass (ECEF)
$\widehat{\mathbf{e}}_\mathbf{x}, \widehat{\mathbf{e}}_\mathbf{y}, \widehat{\mathbf{e}}_\mathbf{z}$ are the unit vectors of the satellite-fixed coordinate system, expressed as a function of satellite position vector and solar vector ($\mathbf{n_{sun}}$) in the ECEF coordinate system, given by:

$$\widehat{\mathbf{e}}_\mathbf{z} = \frac{-\mathbf{X^i}}{\|\mathbf{X^i}\|} \tag{2.51}$$

$$\widehat{\mathbf{e}}_\mathbf{y} = \frac{\widehat{\mathbf{e}}_\mathbf{z} \times \mathbf{n_{sun}}}{\|\widehat{\mathbf{e}}_\mathbf{z} \times \mathbf{n_{sun}}\|} \tag{2.52}$$

$$\widehat{\mathbf{e}}_\mathbf{x} = \widehat{\mathbf{e}}_\mathbf{y} \times \widehat{\mathbf{e}}_\mathbf{z} \tag{2.53}$$

In the past, IGS adopted block-specific antenna PCO [64]. However, several authors pointed out that, as there are significant differences between individual satellites, it is necessary to provide satellite-specific corrections, for both antenna PCO and PCV corrections [106]. These corrections are given in the IGS antenna files in Antenna Exchange format (ANTEX) [94] for each satellite. The current model is the *igs08.atx*, to be used with the International Terrestrial Reference Frame of 2008 (ITRF08). For PCO corrections, satellite-specific z-offsets (Δz) are provided, while x- and y-offsets (Δx, Δy) are still manufacturers' values [105].

If pco^i is the satellite PCO, the IGS convention sign allows us to add a $+pco^i$ term in the code and phase mathematical model [94].

Satellite antenna PCV

There are some variations of the satellite antenna phase center with the satellite zenith and azimuth angles. The current IGS model provides nadir-dependent antenna PCV corrections. Although present, azimuth-dependent PCV corrections are still not considered for the actual IGS model [105]. Satellite antenna PCV corrections are provided in the IGS antenna files for each satellite [94] and are given as a scalar that depends on the nadir angle at the satellite as well as on the frequency. However, the current antenna PCV corrections are given for the IF linear combination and not for L1 and L2 observables separately [134]. The nadir angle at the satellite ($\chi^{'}$) is related to the satellite zenith angle at the receiver (χ) by (see figure 2.9):

$$\sin \chi^{'} = \frac{R_E}{r} \sin \chi \tag{2.54}$$

where R_E is the Earth radius and r the geocentric distance from the center of the Earth to the satellite

If pcv^i_k is the satellite antenna PCV correction, the IGS sign convention allows us to add a $+pcv^i_k$ term in the code and phase mathematical model [94].

Receiver antenna PCO and PCV

As far as the receiver is concerned, a correction of the receiver antenna phase center offset and variations is also necessary. Since 2006, IGS provides absolute receiver antenna calibrated PCO and PCV values. Before that, the calibration was relative to a reference antenna. The absolute

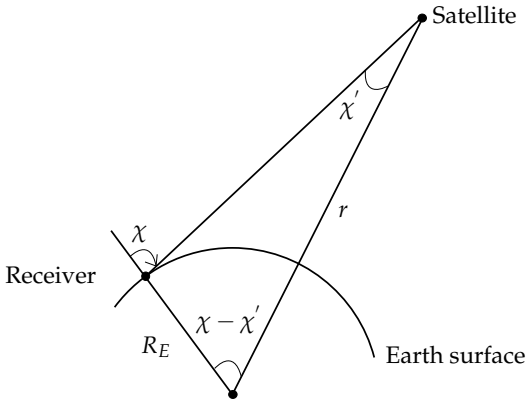

Figure 2.9 *– Relation between the nadir angle at the satellite (χ') and the satellite zenith angle at the receiver (χ).*

calibration can either be done in an anechoic chamber or from field calibration, i.e. using a robot. Both absolute antenna PCO and PCV corrections are referred to the local coordinate system (see figure 2.10), whose origin is the local point (O). The z'-axis is perpendicular to Earth's ellipsoid, the x'-axis is pointed to the North and the y'-axis is pointed to the East. The x'- and y'-axis define the local horizon.

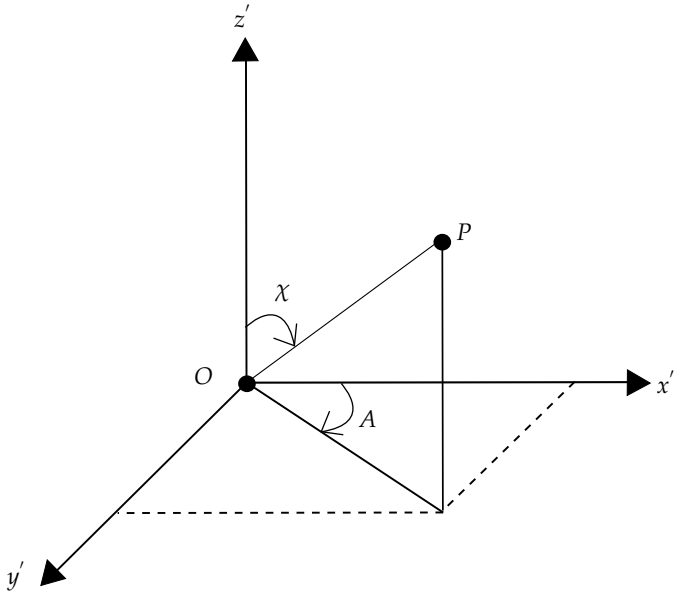

Figure 2.10 *– Local coordinate system.*

Receiver PCO corrections are given as a vector in the local coordinate system for each carrier frequency, denoted as $\mathbf{x_{p,o,k}}\,(\Delta n,\, \Delta e,\, \Delta h)$. Following the IGS sign convention, we can write [94]:

$$\mathbf{x_{p,ARP}} = \mathbf{x_{p,mPC}} - \mathbf{x_{p,o,k}} \tag{2.55}$$

where $\mathbf{x_{p,ARP}}$ and $\mathbf{x_{p,mPC}}$ are the position vectors of the receiver antenna reference point and of the receiver antenna mean phase center (local coordinate system).
Therefore, this sign convention allows us to add a $+pco_{p,k}$ term in the code and phase mathematical model, with:

$$pco_{p,k} = \left[l_x\, l_y\, l_z\right] \mathbf{x_{p,o,k}} \tag{2.56}$$

where l_x, l_y, l_z are the components of the satellite-to-receiver unit vector in the local reference frame, given by [69]:

$$l_x = \cos A \sin \chi \tag{2.57}$$
$$l_y = \sin A \sin \chi \tag{2.58}$$
$$l_z = \cos \chi \tag{2.59}$$

Receiver antenna PCV corrections are given as a scalar number that depends on the elevation and azimuth angle, as well as on the frequency. If $pcv_{p,k}$ is the PCV correction, the IGS sign convention allows us to add a $+pcv_{p,k}$ term in the code and phase mathematical model [94].

Both absolute receiver antenna PCO and PCV corrections are provided in the IGS antenna files (following the *igs08.atx* model) for each antenna and radome type. They constitute empirical corrections, whose accuracy is supposed to be sub-centimetric [106]. Additionally, more accurate individual receiver antenna calibrations are performed for EUREF Permanent Network (EPN) stations [31].

2.2.2.11 Measurement noise

As GNSS code and phase observations are stochastic by nature, they cannot be measured perfectly and are subject to random measurement errors (measurement resolution) [107], called measurement noise. Those random errors are caused by disturbances in the antenna, cables and receiver itself. For example, the movement of electrons in resistances and semi-conductors of the receiver causes a thermal noise.

The measurement noise is a function of the signal wavelength as well as of the Carrier-to-Noise density ratio (C/N_0), and thus of the satellite elevation, receiver hardware and antenna cables. The standard deviation of code (σ_{DLL}) and phase (σ_{PLL}) locked loop thermal noise is given in [66]. For a $C/N_0 > 35$ dB-Hz (high performance receiver), the formulation of σ_{DLL} and σ_{PLL} [m] is simplified to:

$$\sigma_{DLL} = \sqrt{\frac{\alpha\, B_L}{c/n_0}}\lambda_c \tag{2.60}$$

$$\sigma_{PLL} = \sqrt{\frac{B_P}{c/n_0}}\lambda_k \tag{2.61}$$

where
c/n_0 is the C/N_0 expressed as a ratio:

$$c/n_0 = 10^{(C/N_0)/10} \tag{2.62}$$

α is the DLL discriminator correlator factor $[-]$, which is equal to 1 or 0.5 depending on the correlator type
B_L is the equivalent code loop bandwidth [Hz]
B_P is the carrier loop bandwidth [Hz]
λ_c is the wavelength of the PRN code [m]
λ_k is the wavelength of the carrier [m]

The measurement noise is supposed to be white Gaussian, i.e. to have a normal distribution with a zero-mean [115]. It is considered to be about (or below) 1 % of the signal wavelength [107], i.e. about 3 m for GPS C/A-code, 0.3 m for GPS P-code and Galileo code measurements and 2 mm for phase measurements. Moreover, it is worth noticing that, together with the novel modulation schemes, the power of Galileo signals – which is greater by factor 2 – results in a reduction of the code measurement noise compared to GPS L1/L2 [113]. Nevertheless, Galileo L1 code measurement is less precise than L2/L5 ones, while GPS L5 code measurements have the same level of noise as the latter.

Equations (2.60) and (2.61) allow us to obtain the expected (theoretical) standard deviation of code and phase measurement noise. With the availability of real GPS and Galileo triple frequency data, some studies have been performed on the characteristics of the code and phase measurements. In [27, 28, 121, 123], the authors use specific linear combinations of code and phase measurements in order to retrieve their stochastic properties. This method is applied to dual frequency GPS and Galileo measurements (L1/L5) and uses several GF combinations on Short Baseline (SB) and Zero Baseline (ZB).

For code measurements, the combinations used are the SD, DD and Time Difference (TD) of the code-phase combination $r_{CP,k} = P^i_{p,k} - \Phi^i_{p,k}$ and of the multipath combination MP_k (equation (2.39)). For SB cases, the use of the TD combinations is necessary to reduce the effects of code multipath delays. For a ZB setup, multipath delays already cancel out using SD. Thus, it is possible to obtain the standard deviations of the combinations measured at different C/N_0 – normalized to undifferenced level – and estimate the average standard deviation of code measurement noise for a C/N_0 of 45 dB-Hz. Those values are found to be very close to the theoretical values.
To retrieve the standard deviation of phase measurements noise, DD phase combinations are used. For the SB set-up, the use of a second-order polynomial is needed to remove the geometry. Similarly, it makes it possible to estimate the average standard deviation of phase measurement noise for a C/N_0 of 45 dB-Hz, which is also found to be coherent with the theory. As expected, those values are almost equal for GPS and Galileo. Moreover, due to larger wavelength but also to the lower receiver signal power (i.e. higher C/N_0), the L5 phase measurements are noisier than the L1 phase measurements.

Table 2.8 summarizes the theoretical standard deviation of code and phase measurement noise for GPS and Galileo triple frequency measurements that will be used for TEC reconstruction. Those values were coherently chosen with the results given in [27, 28, 121, 123] and are valid for a C/N_0 of 45 dB-Hz, which corresponds to a satellite elevation angle of approximately $30 - 40^\circ$.

Finally, these random errors – which are inherent in the nature of measurements – cannot

Table 2.8 *– Standard deviation of code and phase measurement noise for GPS and Galileo L1, L2 and L5 measurements [27, 28, 45, 121, 123].*

Signal	$\sigma_{\varepsilon_{g,k}}$ [m]		$\sigma_{\varepsilon_{\Phi,k}}$ [mm]	
	GPS	Galileo	GPS	Galileo
L1	0.25	0.18	0.5	0.5
L2	0.25	0.05	0.7	0.7
L5	0.07	0.05	0.7	0.7

be modelled and, even though they can be minimized, cannot be totally overcome.

2.2.2.12 Phase wind-up effect

The phase wind-up effect is a geometric effect related to the emission/reception of right-hand circularly polarized electromagnetic waves, which is the case of GNSS radio waves. The electromagnetic wave may be visualized as a rotating electric field vector which propagates from the satellite antenna to the receiver antenna, and the measured carrier phase may be seen as the geometric angle between the instantaneous electric field vector at the receiving antenna and a reference direction on the antenna [132]. Therefore, the measured carrier phase depends on the orientation of the receiver and satellite antenna as well as on the direction of the line-of-sight to the satellite. The latter varies along the orbital movement. As their solar panels are being oriented towards the Sun, the satellite antennae undergo slow rotations. the orientation of the satellite antenna is constantly changing along the orbit. However, unless in dynamic mode, the receiver antenna does not rotate and is oriented towards a reference direction (usually North) [64].

This change induced in the carrier phase observable is the phase wind-up effect ω_p^i [cycles]. The phase wind-up effect has an identical effect on each carrier wave frequency in cycles and does not affect code observables. It can reach up to 1 cycle, which corresponds to one complete revolution of either the satellite or the receiver antenna around its axis [50]. As it is quite small, the phase wind-up effect has been generally neglected in GNSS applications, especially in SB positioning. Nevertheless, for precise applications like point positioning or long-baseline differential positioning, it needs to be taken into account [64]. The phase wind-up correction expression considering crossed dipole antennae is given by [132]:

$$\delta\omega_p^i = \text{sign}\left[\widehat{\mathbf{k}}\cdot\left(\mathbf{d}\times\mathbf{d}'\right)\right]\cos^{-1}\left(\frac{\mathbf{d}\cdot\mathbf{d}'}{||\mathbf{d}||\,||\mathbf{d}'||}\right) \tag{2.63}$$

$$\omega_p^i = 2N\pi + \delta\omega_p^i \tag{2.64}$$

with

$$\mathbf{d} = \widehat{\mathbf{x}} - \widehat{\mathbf{k}}\left(\widehat{\mathbf{k}}\cdot\widehat{\mathbf{x}}\right) + \widehat{\mathbf{k}}\times\widehat{\mathbf{y}} \tag{2.65}$$

$$\mathbf{d}' = \widehat{\mathbf{x}}' - \widehat{\mathbf{k}}\left(\widehat{\mathbf{k}}\cdot\widehat{\mathbf{x}}'\right) + \widehat{\mathbf{k}}\times\widehat{\mathbf{y}}' \tag{2.66}$$

where
$\delta\omega_p^i$ is the fractional part of the phase wind-up effect [cycles]

ω_p^i is the phase wind-up effect [cycles]
$\mathbf{d}, \mathbf{d}'$ are the effective dipole vectors of the satellite and receiver antenna, respectively
$\widehat{\mathbf{x}}$, $\widehat{\mathbf{y}}$ are the unit vectors in the direction of the two-dipole elements in the satellite antenna
$\widehat{\mathbf{x}}'$, $\widehat{\mathbf{y}}'$ are the unit vectors in the direction of the two-dipole elements in the receiver antenna
$\widehat{\mathbf{k}}$ is the unit vector pointing from the satellite to the antenna
N is an integer which is arbitrarily set to 0 at the beginning of an observation period and then updated to ensure the continuity within a satellite path [64, 132].

In practical, it is more convenient to use the satellite-fixed coordinate system (figure 2.8) and the local coordinate system (figure 2.10) for the satellite and receiver antenna orientation, respectively [69, 132]. It means that $\mathbf{d}, \mathbf{d}'$ are the effective dipole vectors of the satellite and receiver antenna computed from the satellite-fixed coordinate unit vectors ($\widehat{\mathbf{x}}$, $\widehat{\mathbf{y}}$, $\widehat{\mathbf{z}}$) and the local coordinate unit vectors (i.e. North, East, Up) denoted by $\widehat{\mathbf{x}}'$, $\widehat{\mathbf{y}}'$, $\widehat{\mathbf{z}}'$. This redefinition will cause an additional initial (integer) wind-up effect that cannot be separated from the undifferenced ambiguities in any case.

If it is not taken into account, the phase wind-up effect has a non-negligible influence on undifferenced carrier phase measurements. Nevertheless, the algorithm described here allows us to correct the phase wind-up effect to cm-level accuracy [19].

2.2.3 Mathematical model of GNSS measurements

In section 2.2.2 we have described all error sources which affect code and phase GNSS measurements. Taking all those effects into account, the code and phase travel time from equations (2.4), (2.6) and (2.7) can now be developed as follows:

$$\begin{aligned}\tau_{p,g,k}^i &= \frac{1}{c}\Big(\rho_p^i + I_{p,g,k}^i + T_p^i + d_{g,k}^i + d_{p,g,k} + pco^i + pcv_k^i + pco_{p,k} + pcv_{p,k} \\ &\quad + M_{p,g,k}^i + \varepsilon_{p,g,k}^i\Big) \qquad (2.67)\\ \tau_{p,\Phi,k}^i &= \frac{1}{c}\Big(\rho_p^i + I_{p,\Phi,k}^i + T_p^i + d_{\Phi,k}^i + d_{p,\Phi,k} + pco^i + pcv_k^i + pco_{p,k} + pcv_{p,k} \\ &\quad + \lambda_k\,\omega_p^i + M_{p,\Phi,k}^i + \varepsilon_{p,\Phi,k}^i\Big) \qquad (2.68)\end{aligned}$$

Including the relativistic effects (section 2.2.2.3) and using the simplified notation for iono-

spheric delays (section 2.2.2.5), equations (2.4),(2.6),(2.7) can be written as:

$$\begin{aligned} P^i_{p,k} &= \rho^i_p + c\,\Delta t_p - c\left(\Delta t^i + \Delta t^i_{rel}\right) + I^i_{p,k} + T^i_p + d^i_{g,k} + d_{p,g,k} + pco^i + pcv^i_k + pco_{p,k} + pcv_{p,k} \\ &\quad + M^i_{p,g,k} + \varepsilon^i_{p,g,k} \end{aligned} \tag{2.69}$$

$$\begin{aligned} \varphi^i_{p,k} &= \frac{f_k}{c}\rho^i_p + f_k\,\Delta t_p - f_k\left(\Delta t^i + \Delta t^i_{rel}\right) \\ &\quad + \frac{f_k}{c}\left(-I^i_{p,k} + T^i_p + d^i_{\Phi,k} + d_{p,\Phi,k} + pco^i + pcv^i_k + pco_{p,k} + pcv_{p,k} + M^i_{p,\Phi,k} + \varepsilon^i_{p,\Phi,k}\right) \\ &\quad + \omega^i_p - N^i_{p,k} \end{aligned} \tag{2.70}$$

$$\begin{aligned} \Phi^i_{p,k} &= \rho^i_p + c\,\Delta t_p - c\left(\Delta t^i + \Delta t^i_{rel}\right) \\ &\quad - I^i_{p,k} + T^i_p + d^i_{\Phi,k} + d_{p,\Phi,k} + pco^i + pcv^i_k + pco_{p,k} + pcv_{p,k} + M^i_{p,\Phi,k} + \varepsilon^i_{p,\Phi,k} \\ &\quad + \lambda_k\,\omega^i_p - \lambda_k\,N^i_{p,k} \end{aligned} \tag{2.71}$$

These equations constitute the mathematical model of GNSS measurements. They will be used as basis for some developments of the next chapters, especially to explain the extraction of the TEC with dual frequency GNSS in section 3.2 and to develop the triple frequency TEC reconstruction technique in chapter 4.

Chapter 3

The Earth's ionosphere

THIS chapter deals with the Earth's ionosphere. The first section (3.1) describes the composition, formation and variability of the ionosphere, and briefly introduces the main concepts of ionospheric propagation of radio signals. The second section (3.2) explains how to extract the total electron content with dual frequency Global Navigation Satellite System (GNSS) measurements.

3.1 Description

3.1.1 Definition

The Earth's atmosphere is a layer of gases and dust surrounding the Earth. Each part of the atmosphere has its own physical and chemical properties: composition, temperature, ionization, propagation, etc. as shown in figure 3.1. According to the presence of ionized particles, the atmosphere can be divided into two parts: the non-ionized part or neutral atmosphere (neutrosphere) and the ionized part, which consists of the ionosphere (between approximately 50 and 1000 km) and the plasmasphere (above 1000 km). The ionosphere can be defined as the part of the upper atmosphere in which sufficient ionization exists to influence the propagation of radio waves [29].

3.1.2 Composition and formation

The charged particles of ionosphere are produced by a broad spectrum of solar radiation (UV, EUV and X-ray) which dissociates and ionizes the mixture of gases by absorption of energy. This process is called photo-ionization and can be summarized as:

$$X + \{\text{photon}\} \rightarrow X^{+} + e^{-} \tag{3.1}$$

At the same time, two other processes occur in which electrons disappear: recombination (radiative or dissociative) and attachment. Altogether these processes cause a permanent

Altitude (km)	Temperature	Ionization	Magnetic field	Propagation
10000	Thermo-sphere	Protono-sphere	Magneto-sphere	Ionosphere
1000		Ionosphere		
100	Mesosphere		Dynamo-sphere	Troposphere
	Stratosphere	Neutrosphere		
10	Troposphere			

Figure 3.1 *– Possible subdivisions of the Earth's atmosphere. From [107].*

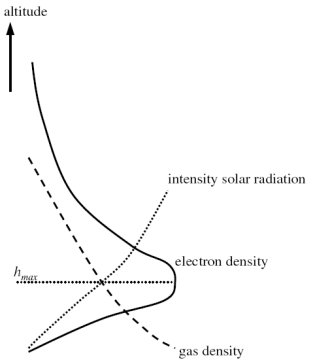

Figure 3.2 *– Global profile of electron density and intensity of solar radiation with altitude. From [81].*

change of the electron density N_e (electrons/m^3). Moreover, considering the absorption characteristics of the atmosphere and its composition dependency on the altitude, the ionosphere tends to be horizontally stratified. The regions differ not only from their ion composition but also from their formation mechanism. Since the intensity of solar radiation increases with altitude, the electron density first increases till $h_{\max}$, often denoted as hmF2. It then begins to decrease since the gas density, thus the amount of possibly ionized particles decreases. This is illustrated in figure 3.2. Not all particles in the ionosphere are charged. As a matter of fact, the degree of ionization is very low. Nevertheless, only the charged particles – and mainly the free electrons – influence the propagation of radio signals. This will be detailed in section 3.1.4.

The main regions are respectively called D-, E-and F-region in order of increasing altitude (figure 3.3). As there is a gradual change from one region to the other, the boundary heights cannot be clearly determined.

- The D-Region is the lower layer. It completely disappears during the night and its electron density (during daytime) is about 10^{10} electrons/m^3.

- The E-Region is the middle layer. It remains during the night, though it is considerably diminished; its electron density is about 10^{11} electrons/m^3 (during daytime). It is dominated by O_2^+ and NO^+ ions. Although the density of O_2 and NO is negligible, the following reactions can explain the production of those ions:

$$N_2 + \{\text{photon}\} \rightarrow N_2^+ + e^- \tag{3.2}$$
$$N_2^+ + O \rightarrow NO^+ + N \tag{3.3}$$
$$N_2^+ + O_2 \rightarrow O_2^+ + N_2 \tag{3.4}$$

  During nighttime, there is no solar radiation anymore and a rapid destruction by dissociative recombination occurs:

$$NO^+ + e^- \rightarrow N + O \tag{3.5}$$
$$O_2^+ + e^- \rightarrow O + O \tag{3.6}$$

- The F-Region is the upper layer. As O is the major component at this altitude, the largest species of atomic ion is O^+:

$$O + \{\text{photon}\} \rightarrow O^+ + e^+ \tag{3.7}$$

  The loss of ions is caused by charge transfer and then dissociative recombination as:

$$O^+ + N_2 \rightarrow NO^+ + N \tag{3.8}$$
$$O^+ + O_2 \rightarrow O_2^+ + O \tag{3.9}$$
$$NO^+ + e^- \rightarrow N + O \tag{3.10}$$
$$O_2^+ + e^- \rightarrow O + O \tag{3.11}$$

  The F-Region can actually be divided into an F1- and F2- layer. As the charge transfer is efficient in F1-layer, it disappears during nighttime. Since the recombination process is very slow in F2-layer (low neutral particles concentration), it remains during the night. This is the region that has the greatest concentration of electrons (about 10^{12} electrons/m^3 during the day), and where the maximum peak of electron density NmF2 is reached at peak height hmF2 (see figure 3.4).

  It results that the formation mechanism is governed by the *photochemical equilibrium* in the D- and E-Regions, since in the F-Region the transport process becomes predominant (*diffusive equilibrium*).

- The topside ionosphere is the region above F2. The transport process is dominant and O^+ ion is the major constituent. Progressively, O^+ ions are replaced by lighter ions He^+ and H^+. The plasmasphere – which is a fully ionized region – begins when H^+ becomes the dominant ion specy (around 1000 km).

3.1.3 Variability

As the electron density strongly depends on solar radiation, it exhibits a wide range of variability both in space and time. These variations are mainly due to solar activity, season, time of the day and latitude. Furthermore, other variations can occur more suddenly like Travelling Ionospheric Disturbances (TIDs) and scintillations.

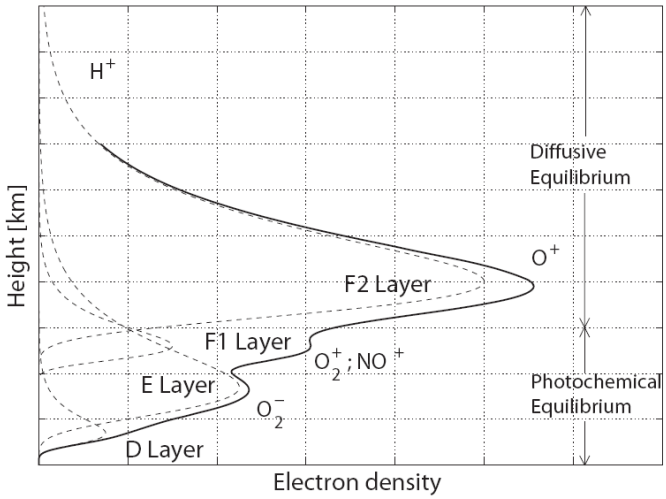

Figure 3.3 *– A typical vertical ionospheric electron density profile during daytime in mid-latitude regions. From [74].*

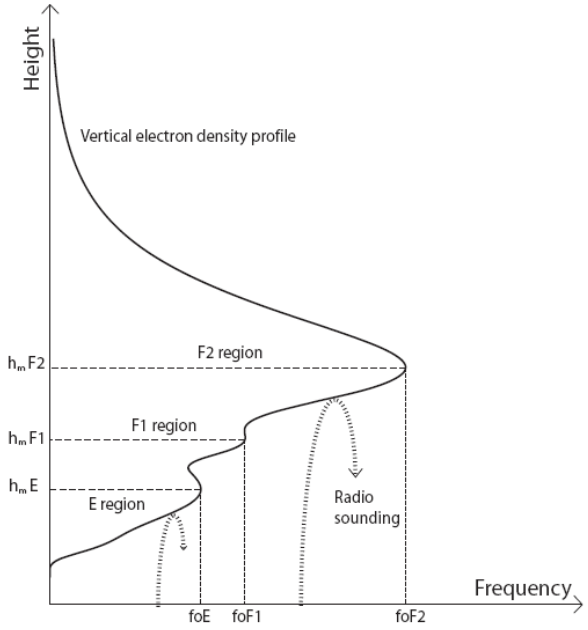

Figure 3.4 *– Illustration of the peak plasma frequency and the peak height of the ionospheric regions. From [74].*

3.1.3.1 Solar activity

Solar activity is modulated by the 11-year solar cycle. It is associated with a variation of solar radiation, and therefore of the ionospheric electron density. Several indices are used to characterize the solar activity level:

- Firstly, the *Wolf sunspot number* (R), using the number of sunspot as indicator for solar activity, is defined as:

$$R = k\ (10\,g + f) \tag{3.12}$$

  where g is the number of sunspot groups, f the total number of sunspots and k a normalization constant.

  Figure 3.5 shows the yearly (up to 1750) and monthly Wolf sunspot numbers (from 1750), while figure 3.6 shows the daily, monthly and monthly smoothed sunspots numbers since 2000, as well as predictions for 12 months ahead.

- Secondly, the $F_{10.7}$ *index*, or solar flux on the radio wavelength of 10.7 cm, is measured daily since 1948 in Ottawa. The solar flux unit is $10^{-22}\,\mathrm{W \cdot m^2 \cdot Hz^{-1}}$. As it is correlated with X-ray and EUV fluxes, it constitutes an excellent indicator for solar activity.

3.1.3.2 Seasonal variation

Since the rotation axis of the Earth has an inclination of 23.5° over the orbital plane, the incident angle of the sun's rays varies depending on the season. According to the position of the Earth along its orbit, there is a variation of the solar radiation intensity and therefore of the ionization (electron density).

3.1.3.3 Diurnal variation

The ionization also shows a strong correlation with the local sun zenith angle, reaching a maximum around local noon and a minimum during nighttime.

3.1.3.4 Latitudinal variation

As the free electrons in the ionosphere are influenced by the Earth's magnetic field, the electron density shows a large dependence on the geomagnetic latitude. Three geomagnetic zones can be distinguished: equatorial, mid-latitude and auroral (polar). These three zones are illustrated in figure 3.7. The electron density is the largest in the equatorial region ($\pm 20°$) and the smallest (with high variability) in the polar regions (above 60°). This can be explained by equatorial anomalies – horizontal magnetic field combined with an eastward electric field – and by the precipitation of solar particles producing aurorae.

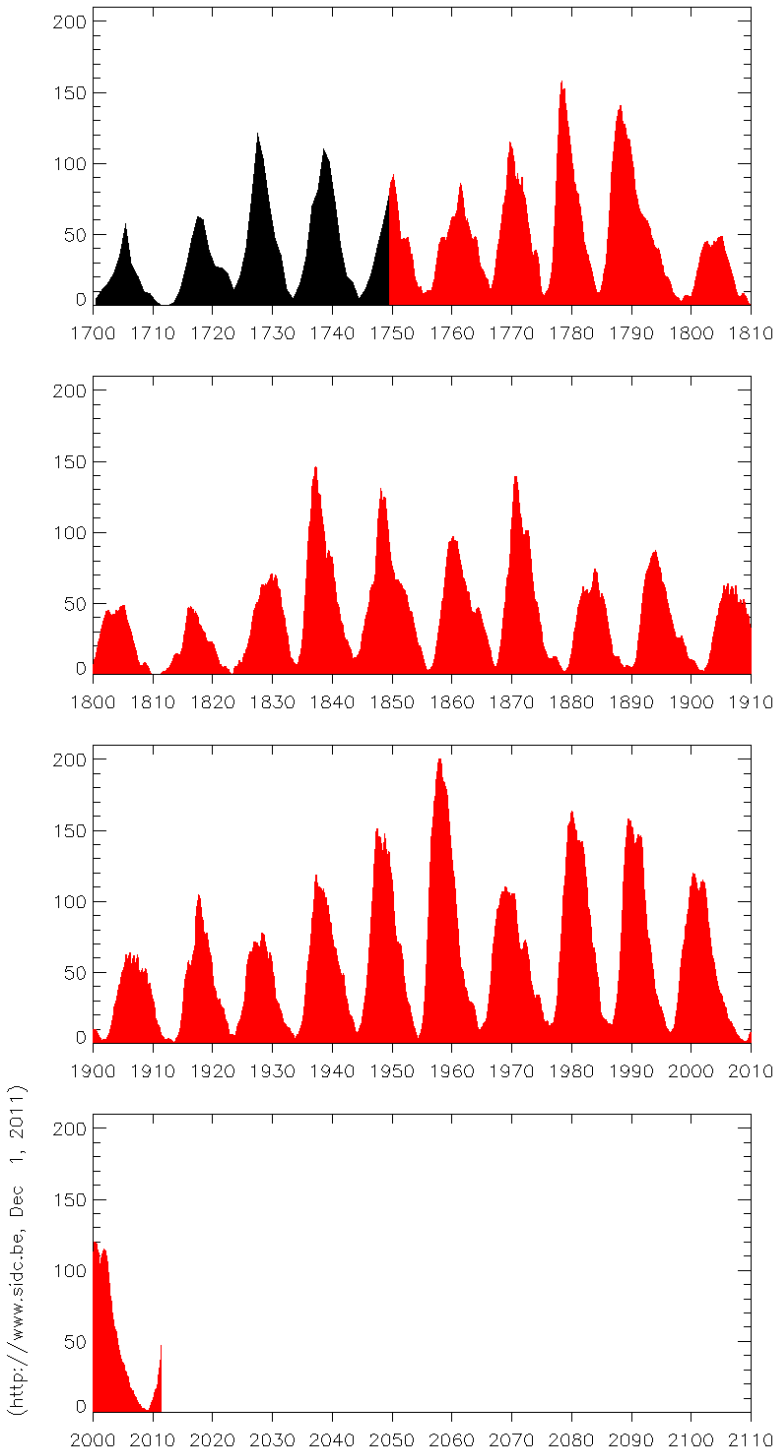

Figure 3.5 *– Yearly (black, up to 1750) and monthly (red, from 1750 up to now) Wolf sunspot numbers. From [109].*

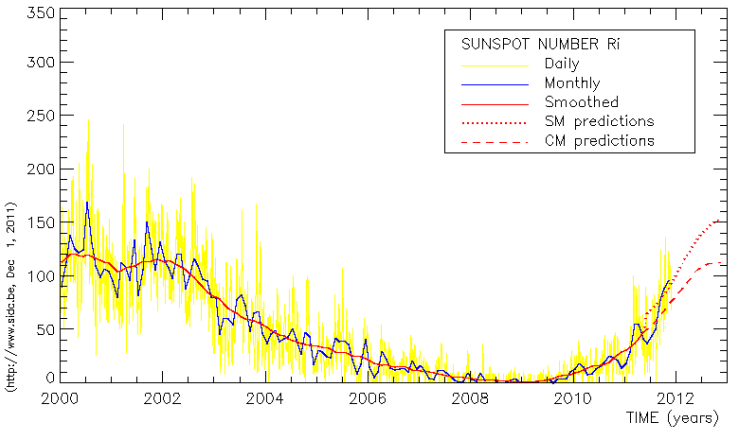

Figure 3.6 *– Daily (yellow), monthly (blue) and monthly smoothed (red) sunspot numbers since 2000, together with predictions for 12 months ahead. From [109].*

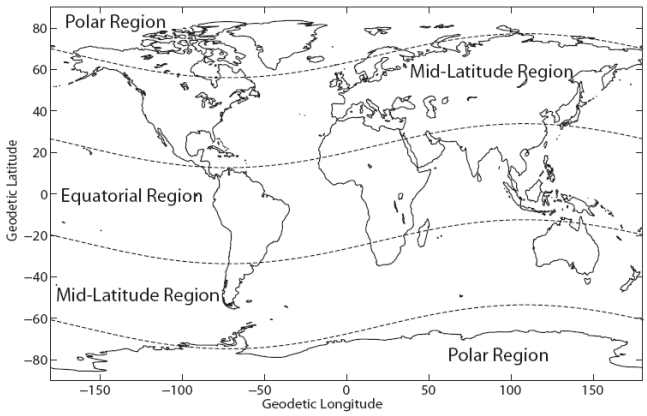

Figure 3.7 *– Division of the Earth into geomagnetic regions. The geomagnetic parallel lines* $66.5^\circ N/S$ *and* $23.5^\circ N/S$ *are plotted in the geodetic reference frame. From [74].*

3.1.3.5 Irregular variability

Geomagnetic storms

The sun continuously emits a stream of energized charged particles called the solar wind. When the solar activity increases, the number of Coronal Mass Ejections (CMEs) also increases. CMEs are often related to solar flares – explosions on the sun's surface – and constitute huge bubbles of gas threaded with the magnetic field lines that are ejected from the sun. When a CME is directed towards the Earth, this causes a worldwide disturbance of the Earth's magnetic field, which is known as a *geomagnetic storm*. Such geomagnetic storms may result in ionospheric disturbances, called *ionospheric storms*. Those phenomena generally occur at high-latitude, creating the well-known *aurora borealis*, but sometimes they also penetrate into mid- and equatorial latitudes regions [65].

The most severe geomagnetic storms of the past decade occurred in 2003, on October 29-30 and November 20. Three times during those periods, the *planetary Kp index** was observed equal to its maximal possible value ($Kp = 9$). Those events were associated with ionospheric storms: in mid-latitude regions, Total Electron Content (TEC) values of 50 TECU were observed, and TEC temporal gradients reached 9 TECU/min [70].

Travelling Ionospheric Disturbances

TIDs are considered to be plasma density variations that propagate through the ionosphere at a open range of velocities and wavelengths [48]. Those fluctuations can be detected in the TEC measurements computed from GNSS data. There are three types of TIDs, differing from period and propagation velocity [48]:

- the large-scale TIDs (LSTIDs) propagate faster than 300 m/s with a period greater than one hour,
- the medium-scale TIDs (MSTIDs) move around 50-300 m/s with a period that varies from 10 minutes to one hour,
- the small-scale TIDs (SSTIDs) propagate slower than 100 m/s with a period of only several minutes.

The origin of LSTIDs is considered to be linked with geomagnetic disturbances (e.g. auroras, ionospheric storms, etc.), while the origin of MSTIDs seems to be more related with the solar terminator – the moving border that separates the day from the night side of the ionosphere – that produces Atmospheric Gravity Waves (AGWs). A more exhaustive study has shown common properties of MSTIDs happening mostly in winter during daytime and in summer during nighttime, and propagating, respectively, towards the equator and towards the west.

Scintillations

Scintillations can be defined as rapid amplitude and phase fluctuations of radio signals that propagate through the ionosphere. They are produced by random fluctuations of the index of

*The planetary *Kp* index is a 3-hourly planetary geomagnetic index of activity generated in Göttingen, Germany, based on the K INDEX from 12 or 13 stations distributed around the world [110].

refraction, caused by ionospheric plasma density irregularities. Scintillations are more intense during high solar activity, and are likely to occur in equatorial and auroral regions.

Two indexes are widely used to characterize scintillations. Amplitude scintillations are quantified by the S_4 index, which is the standard deviation of the received power or intensity (I) normalized by its mean value (generally over 60 seconds):

$$S_4 = \sqrt{\frac{\langle I^2 \rangle - \langle I \rangle^2}{\langle I \rangle^2}} \tag{3.13}$$

where S_4 $[-]$ varies from 0 to 1.

Phase scintillations are described by σ_φ [rad], which is the standard deviation of the received carrier phase signal. The S_4 and σ_φ quantities are correlated and depend on solar activity, and thus on the Wolf sunspot number R.

Short-term variations in the signal amplitude and phase may represent problems for the carrier tracking loop in a receiver. Amplitude scintillations increase the S_4 value and therefore the thermal noise [12], which degrades the Signal-to-Noise Ratio (SNR) of the receiver. A receiver is able to tolerate scintillation conditions if the SNR remains above a minimal value. Otherwise this leads to loss of lock of the signal, causing a phase discontinuity or cycle slip. This value is linked to S_4 and σ_φ, which makes it possible to evaluate the probability of loss of lock. Phase scintillations may also lead to loss of lock, and consequently to cycle slips. This explains why the Global Ionospheric Scintillation Model (GISM) has been developed to estimate the scintillation characteristics and the receiver performance in a scintillation regime [11].

3.1.4 Ionospheric propagation of radio signals

3.1.4.1 Ionospheric refraction

The free electrons of the ionosphere affect the propagation of GNSS radio signals. The main effect which affects GNSS signal propagation in the ionosphere is a change in the wave velocity, which can be quantified thanks to the *index of refraction* of the medium. This index is the ratio of the velocity of light in free space (c) and the velocity of the wave in a medium (v):

$$n = c/v \tag{3.14}$$

As the ionosphere is an heterogeneous, anisotropic and dispersive medium, the index of refraction is not a constant in space and time.

First, as the ionosphere is a dispersive medium, we have to distinguish between the *phase velocity* v_ϕ and the *group velocity* v_g; hence the index of refraction is defined for phase and group, respectively (with $v_g \leq v_\Phi$):

$$n_\Phi = c/v_\Phi \tag{3.15}$$

$$n_g = c/v_g \tag{3.16}$$

The relation between v_g and v_Φ is given by the *Rayleigh equation*:

$$v_g = v_\Phi + f_k \frac{\partial v_\Phi}{\partial f_k} \tag{3.17}$$

with f_k the frequency of the carrier wave k.

Acting as a dispersive medium not only means that the group and phase indices of refraction are different, but also that they depend on the frequency of the signal. The ionospheric index of refraction can be derived from the *Appleton-Hartree* formula [26]:

$$n_{\Phi,k}^2 = 1 - \frac{X}{1 - iZ - \frac{(Y|\sin\Theta|)^2}{2(1-X-iZ)} \pm \sqrt{\frac{(Y|\sin\Theta|)^4}{4(1-X-iZ)^2} + (Y|\cos\Theta|)^2}} \tag{3.18}$$

with

$$X = \frac{f_p^2}{f_k^2} = \frac{N_e\, e^2}{4\pi^2 \varepsilon_0 m_e f_k^2} \simeq \frac{80.6 N_e}{f_k^2} \tag{3.19}$$

$$Y = \frac{f_g}{f_k} = \frac{eB}{2\pi m_e f_k} \tag{3.20}$$

$$Z = \frac{\nu}{f_k} \tag{3.21}$$

where
f_p is the electron plasma frequency [Hz]
f_g is the electron gyrofrequency [Hz]
ν is the electron collision frequency [Hz]
N_e is the electron density $\left[\text{electrons}/\text{m}^3\right]$ e is the electron charge $[\text{A}\cdot\text{s}]$
ε_0 is the electric permittivity of free space $\left[\text{A}\cdot\text{s}\cdot\text{V}^{-1}\cdot\text{m}^{-1}\right]$
m_e is the electron mass [Kg]
B is the magnetic induction of the Earth's magnetic field $\left[\text{V}\cdot\text{s}\cdot\text{m}^{-2}\right]$
Θ is the angle between the propagation of the wave and the Earth's magnetic field vector [rad]

The three properties of the ionosphere are present in equation (3.18). As already mentioned earlier, the dispersive property is reflected in the dependence on f_k. The heterogeneity can be recognized in N_e which is function of space and time. The anisotropy, i.e. the dependence on the propagation direction of the wave, is expressed in the terms depending on B and Θ.

Since we only consider the ionospheric propagation of GNSS signals, we can neglect absorption due to collisions between the electrons. Therefore, as the imaginary part of $n_{\Phi,k}^2$ quantifies the absorption, we can set it to 0 ($f_k \gg \nu \rightarrow Z = 0$) so that $n_{\Phi,k}^2$ becomes a real number:

$$n_{\Phi,k}^2 = 1 - \frac{X}{1 - \frac{(Y|\sin\Theta|)^2}{2(1-X)} \pm \sqrt{\frac{(Y|\sin\Theta|)^4}{4(1-X)^2} + (Y|\cos\Theta|)^2}} \tag{3.22}$$

Considering high frequencies ($f_k > 100$ MHz), equation (3.22) can be expressed as [40]:

$$n_{\Phi,k}^2 = 1 - \frac{f_p^2}{f_k^2 \pm f_k f_g |\cos\Theta|} \tag{3.23}$$

The minus sign corresponds to right-hand circularly polarized electromagnetic waves (ordinary wave), whereas the plus sign corresponds to left-hand circularly polarized electromagnetic waves (extraordinary wave) [40]. Since GNSS signals are right-hand circularly polarized electromagnetic waves [54], only the minus sign of equation (3.23) will be considered from now on.

Since f_p and $f_g \ll f_k$, it is allowed to expand the phase index of refraction $n_{\Phi,k}$ from equation (3.23) into the following Taylor-series:

$$n_{\Phi,k} = 1 - \frac{1}{2}\frac{f_p^2}{f_k^2} - \frac{1}{2}\frac{f_p^2 f_g |\cos\Theta|}{f_k^3} - \frac{1}{8}\frac{f_p^4}{f_k^4} \tag{3.24}$$

Using equations (3.24) and (3.17), we obtain the group index of refraction n_g:

$$n_{g,k} = 1 + \frac{1}{2}\frac{f_p^2}{f_k^2} + \frac{f_p^2 f_g |\cos\Theta|}{f_k^3} + \frac{3}{8}\frac{f_p^4}{f_k^4} \tag{3.25}$$

One may notice that the phase index of refraction $n_{\Phi,k}$ is smaller than 1 implying that $v_\Phi > c$ and that the group index of refraction $n_{g,k}$ is larger than 1 resulting in $v_g < c$. This means that there is a *phase advance* but a *group delay* in the ionosphere. However, we will use the terminology *delay* for both phase and code measurements.

3.1.4.2 First and higher-order ionospheric terms

To obtain the phase ionospheric delay $I^i_{p,\phi,k}$ in unit of distance, the difference between the measured range (s') and the geometric range (s) from the receiver (subscript p) to the satellite (superscript i) has to be computed:

$$I^i_{p,\phi,k} = s' - s = \int n_{\Phi,k}\, ds' - \int ds \tag{3.26}$$

When a wave passes through an heterogeneous refractive medium like the ionosphere, there is a *bending effect*, i.e. a change in the signal propagation direction due to the change of n_Φ along the propagation path. If we neglect this *bending* effect and take only the *propagation effect* into account, $ds' = ds$ and equation (3.26) becomes:

$$I^i_{p,\phi,k} = \int (n_{\Phi,k} - 1)\, ds \tag{3.27}$$

Identically for the group ionospheric delay $I^i_{p,g,k}$ [m]:

$$I^i_{p,g,k} = \int (n_{g,k} - 1)\, ds \tag{3.28}$$

Usually, as $f_k > 1$ GHz higher-order terms are neglected and we use the first-order ionospheric delays, denoted by the superscript (1). Substituting (3.24) in (3.27) and (3.25) in (3.28) we obtain:

$$I^{i,(1)}_{p,\Phi,k} = -\frac{1}{2f_k^2}\int f_p^2\, ds = -\frac{40.3}{f_k^2}\int N_e\, ds \tag{3.29}$$

$$I^{i,(1)}_{p,g,k} = \frac{1}{2f_k^2}\int f_p^2\, ds = \frac{40.3}{f_k^2}\int N_e\, ds \tag{3.30}$$

As defined in equation (2.25), the integral of the electron density N_e along the satellite-to-receiver path is the Total Electron Content (TEC). Equations (3.29) and (3.30) thus become:

$$I^{i,(1)}_{p,\Phi,k} = -\frac{40.3}{f_k^2}\,\mathrm{TEC} \tag{3.31}$$

$$I^{i,(1)}_{p,g,k} = \frac{40.3}{f_k^2}\,\mathrm{TEC} \tag{3.32}$$

The first-order ionospheric delay contributes to 99.9 % of the ionospheric effect.
For precise applications however, higher-order ionospheric terms have to be considered. Following the same procedure, we can find the second- and third- order ionospheric phase and group delays, denoted by the superscripts (2) and (3):

$$I^{i,(2)}_{p,\Phi,k} = -\frac{1}{2f_k^3}\int f_p^2\, f_g\, |\cos\Theta|\, ds = -\frac{40.3}{f_k^3}\int f_g\, |\cos\Theta|\, N_e\, ds \tag{3.33}$$

$$I^{i,(2)}_{p,g,k} = \frac{1}{f_k^3}\int f_p^2\, f_g\, |\cos\Theta|\, ds = \frac{80.6}{f_k^3}\int f_g\, |\cos\Theta|\, N_e\, ds \tag{3.34}$$

$$I^{i,(3)}_{p,\Phi,k} = -\frac{1}{8f_k^4}\int f_p^4\, ds = -\frac{1}{8}\frac{80.6^2}{f_k^4}\int N_e^2\, ds \tag{3.35}$$

$$I^{i,(3)}_{p,g,k} = \frac{3}{8f_k^4}\int f_p^4\, ds = \frac{3}{8}\frac{80.6^2}{f_k^4}\int N_e^2\, ds \tag{3.36}$$

The first-order phase and code delays are equal but do not have the same sign. The second- and third-order delays have opposite signs but are not equal: the second-order phase delay represents half of the respective group delay, while the third-order phase delay represents a third of the respective group delay.

3.1.4.3 Approximation and correction of the higher-order terms

First, using the thin 1-layer model of the ionosphere given in section 3.1.4.4, it may be assumed that the product $f_g|\cos\Theta|$ is constant along the signal path [49], so that equations (3.33) and (3.34) become:

$$I^{i,(2)}_{p,\Phi,k} = -\frac{40.3}{f_k^3} f_g\, |\cos\Theta|\, \mathrm{TEC} \tag{3.37}$$

$$I^{i,(2)}_{p,g,k} = \frac{80.6}{f_k^3} f_g\, |\cos\Theta|\, \mathrm{TEC} \tag{3.38}$$

In order to quantify the influence of higher-order ionospheric terms, we will assume "worst-case" values of the different parameters. According to [40], we will consider $f_g = 1.74$ MHz and $\cos\Theta = 1$. Furthermore, as it is difficult to evaluate $\int N_e^2\, ds$, it can be rewritten in terms of TEC so that equations (3.35) and (3.36) become [40]:

$$I^{i,(3)}_{p,\Phi,k} = -\frac{1}{8}\frac{80.6^2}{f_k^4}\,\mathrm{TEC}^2\,\frac{y}{\tau} \tag{3.39}$$

$$I^{i,(3)}_{p,g,k} = \frac{3}{8}\frac{80.6^2}{f_k^4}\,\mathrm{TEC}^2\,\frac{y}{\tau} \tag{3.40}$$

where τ [m] is the equivalent slab thickness and y $[-]$ is the shape factor, defined as [40]:

$$\tau = \frac{\int N_e\, ds}{N_{e,max}} \tag{3.41}$$

$$y = \frac{1}{\tau}\int (N_e/N_{e,max})^2\, ds \tag{3.42}$$

where $N_{e,max}$ is the maximal electron density (NmF2).

To match with the "worst-case" scenario, we will consider a slab of constant electron density with a thickness τ of 200 km and a shape factor y of 1. Note that now both second- and third-order ionospheric delays can be evaluated as a function of TEC.

Figures 3.8 and 3.9 show the magnitude of second- and third-order phase ionospheric delays, evaluated for GPS L1, L2 and L5 frequencies and Galileo L1, E5b and E5a frequencies in the "worst-case" scenario for vertical incidence. For TEC values smaller than 100 TECU, the second- and third-order phase ionospheric delays are smaller than 4 cm and 2 mm, respectively.

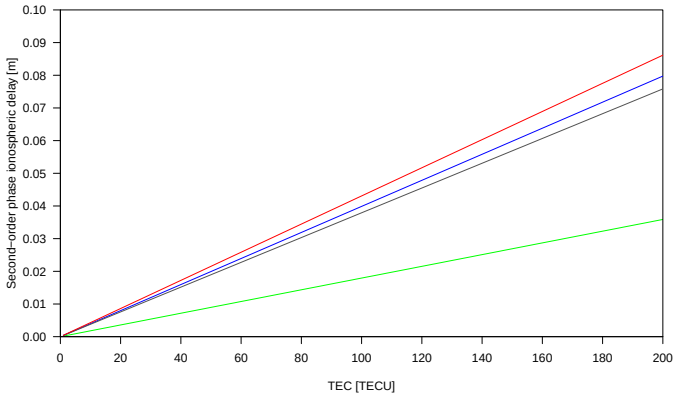

Figure 3.8 *– Second-order phase ionospheric delays for GPS and Galileo frequencies in the "worst-case" scenario (green = L1, grey = L2, blue = E5b, red = L5/E5a).*

Generally, we can consider that the second- and third-order ionospheric delays vary respectively around 0–2 cm and 0–2 mm at zenith [9]. Therefore, if a high level accuracy is needed (e.g. in Precise Point Positioning (PPP)), higher-order terms have to be taken into account. For this purpose, several formulae have been implemented in order to correct second-order ionospheric delay [9, 49, 55]. Based on simulation studies, [55] has derived a formula that computes the average value of the Earth's magnetic field component ($f_g|\cos\Theta|$) as a function of geographic latitude and longitude of the receiver, and of the satellite elevation and azimuth angles. Using this formula together with TEC values makes it possible to correct the second-order ionospheric delay in real-time.

3.1.4.4 Ionospheric model

The TEC and thus the ionospheric delay depends on the satellite zenith angle due to the fact that the propagation path is larger when the former increases. Therefore one has to convert slant TEC values into vertical TEC values *, that can be more easily compared or modelled. This conversion is done through the so-called ionospheric mapping function or obliquity fac-

*In the equations, TEC are the slant TEC values and vTEC constitute the vertical TEC values.

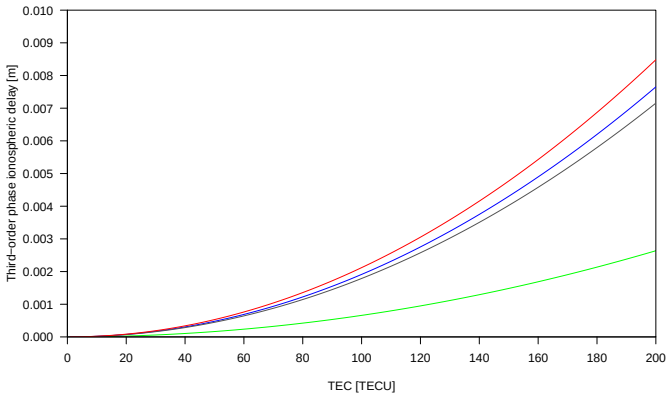

Figure 3.9 *– Third-order phase ionospheric delays for GPS and Galileo frequencies in the "worst-case" scenario (green = L1, grey = L2, blue = E5b, red = L5/E5a).*

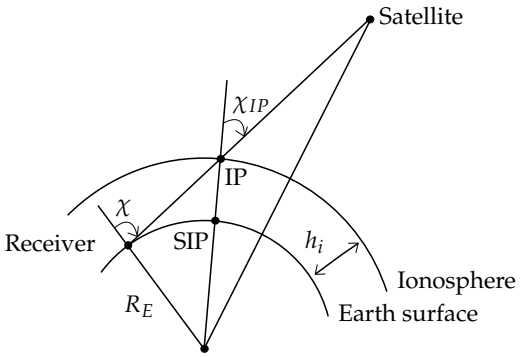

Figure 3.10 *– Representation of the thin 1-layer ionospheric model.*

tor MF $[-]$:

$$\frac{\text{TEC}}{\text{vTEC}} = MF \tag{3.43}$$

For this purpose, different kinds of ionospheric models exist: the thin 1-layer model, the thick 1-layer model, the 2-layer voxel model [82]. We will focus on the thin 1-layer model*, which is the most commonly used. It assumes that all free electrons of the ionosphere are concentrated in a spherical shell of infinitesimal thickness at a fixed height (h_i of effective height), so that equation (3.43) becomes:

$$\frac{\text{TEC}}{\text{vTEC}} = \frac{1}{\cos \chi_{IP}} \tag{3.44}$$

with χ_{IP} [rad] the satellite zenith angle at the Ionospheric (Piercing) Point (IP), which is the intersection of the line of sight with the 1-layer ionosphere (figure 3.10). The vertical projection

*From now on, if we mention the 1-layer model, it refers to the thin 1-layer model.

of IP on the Earth's surface is called Sub-Ionospheric Point (SIP). The relation between the satellite zenith angle at the receiver (χ) and at the IP (χ_{IP}) can be geometrically defined as:

$$\sin \chi_{IP} = \frac{R_E}{R_E + h_i} sin\chi \tag{3.45}$$

where R_E [m] is the Earth radius.

Such a model – depending only on χ and h_i – can produce some discrepancies [82], depending on several parameters, e.g. satellite elevation and azimuth, solar activity, seasonal, local time and latitudinal variations. For example, in the presence of horizontal electron density gradients, equation (3.44) can lead to important mapping function (TEC conversion) errors. In [79], the authors have used the "coinciding pierce point" technique to study the mapping function errors induced by electron density gradients. It follows that a suitable effective height that minimizes the mapping function errors can be determined. For mid-latitude regions, it is fixed at 400 km in quiet geomagnetic conditions and at 500 km in disturbed conditions; for low latitude regions the suitable h_i is 400 km (independently of the conditions).

3.1.4.5 Mathematical model of vertical TEC

Modeling the vertical TEC values requires the use of a spatio-temporal coordinate system in which the ionospheric variability is as smooth as possible in space and time [5]. For this purpose, this is always a sun-fixed coordinate system, using either the geomagnetic latitude (φ_m) or the modified dip latitude (modip or μ); the temporal variability of vTEC is usually considered to be a function of the local time. The modip μ is given by [91]:

$$\tan(\mu) = \frac{I}{\sqrt{\cos(\varphi)}} \tag{3.46}$$

where I is the true magnetic dipole and φ the geographic latitude. The modip sun-fixed coordinate system is adapted to the real magnetic inclination, and is more suitable than the geomagnetic latitude in order to represent the vTEC [5].

The simplest vTEC representation consists of a second-order polynomial which is a function of the local time h and modip latitude μ at the IP [17, 126]:

$$\text{vTEC}_{model}(h, \mu) = a_0 + a_1\, h + a_2\, \mu + a_3\, h^2 + a_4\, h\, \mu + a_5\, \mu^2 \tag{3.47}$$

More elaborated models make use of a fourth-order polynomial [99] and even of spherical harmonic expansion [18].

3.2 Extracting the TEC with GNSS

This section explains how it is possible to extract the TEC with dual frequency GNSS measurements: first we give the main principles and equations (section 3.2.1), then we describe two different methodologies (section 3.2.2) and finally we deal with the generation, interpolation and performance of TEC maps (section 3.2.3).

3.2.1 Principles

Dual frequency GNSS measurements make it possible to reconstruct the Total Electron Content by using the so-called Geometric-Free (GF) combinations of one-way code and/or phase measurements $P_{GF,km}$ and $\Phi_{GF,km}$ [m]:

$$P_{GF,km} = P^i_{p,k} - P^i_{p,m} \tag{3.48}$$

$$\Phi_{GF,km} = \Phi^i_{p,m} - \Phi^i_{p,k} \tag{3.49}$$

In such GF combinations, all frequency-independent effects (such as ρ^i_p, clocks errors, tropospheric delays, etc.) are eliminated, so that only frequency-dependent effects ($k-, m-$ subscripts) remain, i.e.:

- ionospheric delays,
- satellite and receiver hardware delays (code/phase),
- satellite and receiver antenna phase center offset and variations (code/phase),
- multipath delays (code/phase),
- measurement noise (code/phase),
- phase wind-up effect (phase only),
- integer ambiguity (phase only).

Note that the influence of satellite and receiver antenna phase center offsets and variations is negligible with respect to the other errors affecting the TEC values reconstructed with dual frequency measurements (see section 3.2.2.3). Moreover, since the maximum phase wind-up effect is 1 cycle [50], it will be shown in section 4.4.2.1 that it causes an error of maximum half a TECU on the reconstructed TEC values. Therefore, those effects will not be considered in the following development. It results that equations (3.48) and (3.49) can be developed from equations (2.69) and (2.71) as follows:

$$\begin{aligned} P_{GF,km} = {} & I^i_{p,k} - I^i_{p,m} + d^i_{g,k} - d^i_{g,m} + d_{p,g,k} - d_{p,g,m} \\ & + M^i_{p,g,k} - M^i_{p,g,m} + \varepsilon^i_{p,g,k} - \varepsilon^i_{p,g,m} \end{aligned} \tag{3.50}$$

$$\begin{aligned} \Phi_{GF,km} = {} & I^i_{p,k} - I^i_{p,m} + d^i_{\Phi,m} - d^i_{\Phi,k} + d_{p,\Phi,m} - d_{p,\Phi,k} \\ & + M^i_{p,\Phi,m} - M^i_{p,\Phi,k} + \varepsilon^i_{p,\Phi,m} - \varepsilon^i_{p,\Phi,k} - \lambda_m N^i_{p,m} + \lambda_k N^i_{p,k} \end{aligned} \tag{3.51}$$

If we neglect higher-order ionospheric terms, the ionospheric term of equations (3.50) and (3.51) can be developed as follows using equations (2.23),(2.24) and (2.26):

$$I^i_{p,k} - I^i_{p,m} = 40.3 \cdot 10^{16} \cdot \left(\frac{1}{f_k^2} - \frac{1}{f_m^2} \right) \text{TEC} = \alpha_{km} \, \text{TEC} \tag{3.52}$$

where α_{km} $\left[\text{m} \cdot \text{TECU}^{-1}\right]$ is used to convert TECU to length units.

In the first-order approximation, the ionospheric term is directly proportional to the TEC. It is

therefore straightforward to compute the TEC by using the GF code and/or phase combination. However, higher-order ionospheric terms have an influence on the computed TEC. This effect is not considered here but will be studied in section 4.4.2.

We can group the satellite and receiver code hardware delays:

$$IFB_{g,km} = d^i_{g,k} - d^i_{g,m} + d_{p,g,k} - d_{p,g,m} \tag{3.53}$$

where $IFB_{g,km}$ [m] are the so-called code Inter-Frequency Biases (IFB), also referred to as Differential Code Biases (DCB) DCB_{km} [s] (see section 2.2.2.9).

Similarly for satellite and receiver phase hardware delays:

$$IFB_{\Phi,km} = d^i_{\Phi,m} - d^i_{\Phi,k} + d_{p,\Phi,m} - d_{p,\Phi,k} \tag{3.54}$$

where $IFB_{\Phi,km}$ [m] are the so-called phase IFB.

Moreover, if we group the ambiguities in one term as follows:

$$\begin{aligned} -\lambda_m N^i_{p,m} + \lambda_k N^i_{p,k} &= -\lambda_k \left(\frac{\lambda_m}{\lambda_k} N^i_{p,m} - N^i_{p,k} \right) && (3.55)\\ &= -\lambda_k \left(\frac{f_k}{f_m} N^i_{p,m} - N^i_{p,k} \right) && (3.56)\\ &= -\lambda_k N_{GF,km} && (3.57) \end{aligned}$$

where the GF ambiguity $N_{GF,km}$ [cycles] is defined as:

$$N_{GF,km} = -N^i_{p,k} + \frac{f_k}{f_m} N^i_{p,m} \tag{3.58}$$

For more convenience, we group the effects of multipath delays and measurement noise in $E_{g,km}$ and $E_{\Phi,km}$ [m]:

$$\begin{aligned} E_{g,km} &= M^i_{p,g,k} - M^i_{p,g,m} + \varepsilon^i_{p,g,k} - \varepsilon^i_{p,g,m} && (3.59)\\ E_{\Phi,km} &= M^i_{p,\Phi,m} - M^i_{p,\Phi,k} + \varepsilon^i_{p,\Phi,m} - \varepsilon^i_{p,\Phi,k} && (3.60) \end{aligned}$$

From all this, equations (3.50) and (3.51) become:

$$\begin{aligned} P_{GF,km} &= \alpha_{km}\,\mathrm{TEC} + IFB_{g,km} + E_{g,km} && (3.61)\\ \Phi_{GF,km} &= \alpha_{km}\,\mathrm{TEC} + IFB_{\Phi,km} - \lambda_k N_{GF,km} + E_{\Phi,km} && (3.62) \end{aligned}$$

As phase measurements are much less affected by measurement noise and multipath delays than code measurements (see sections 2.2.2.7 and 2.2.2.11), TEC is computed from the GF phase combination $\Phi_{GF,km}$ [20]. However, as phase measurements are biased by the unknown ambiguities $N_{GF,km}$, one has to apply a procedure to compute those ambiguities. Two kinds of approaches exist for dual frequency TEC reconstruction: (1) the carrier-to-code levelling process (section 3.2.2.1) and (2) the unlevelled carrier phase process (section 3.2.2.2). In the two following sections, we will briefly describe the methodology used in each approach, with their common and specific principles. Section 3.2.2.3 summarizes the accuracy assessment of the reconstructed TEC values for both techniques. Actually, there is an alternative to the first TEC reconstruction approach: it consists of levelling phase measurements with TEC values coming from TEC maps. This will be explained in section 3.2.3.4.

3.2.2 Methodology

3.2.2.1 The carrier-to-code levelling process

This technique involves the use of the GF code combination $P_{GF,km}$ to level the GF phase combination $\Phi_{GF,km}$. The main steps of this carrier-to-code levelling process are [17, 20]:

- The mean value of the difference between the GF phase combination $\Phi_{GF,km}$ and the GF code combination $P_{GF,km}$ ($\langle \Phi_{GF,km} - P_{GF,km} \rangle$) is computed for each satellite pass and then subtracted from $\Phi_{GF,km}$ in order to remove the GF ambiguity. We obtain the so-called "levelled" GF phase combination $\Phi_{GF,km,l}$ [m]:

$$\Phi_{GF,km,l} = \Phi_{GF,km} - \langle \Phi_{GF,km} - P_{GF,km} \rangle \tag{3.63}$$
$$= \alpha_{km}\,\mathrm{TEC} + IFB_{g,km} + \langle E_{g,km} \rangle + \langle \delta\, IFB_{g,km} \rangle + E_{\Phi,km} \tag{3.64}$$

  The $E_{\Phi,km}$ term is the observational error due to phase multipath delays and phase measurement noise (see equation (3.60)). It has to be noted that equation (3.64) neglects the mean of combined phase multipath delays and phase measurement noise ($\langle E_{\Phi,km} \rangle$ term), which is assumed to be zero as stated in sections 2.2.2.7 and 2.2.2.11.
  Moreover, the "levelled" GF phase combination may be affected by code multipath delays if they do not average to zero over a satellite pass. This is represented by the $\langle E_{g,km} \rangle$ term.
  Finally, in this technique the code IFB are assumed to be constant over a given period. However, the receiver code IFB undergo temporal variations that would be related to the environmental conditions around the antenna/receiver [17]. The temporal variation of code IFB is reprensented by the $\langle \delta\, IFB_{g,km} \rangle$ term.
  The two latter effects constitute the so-called levelling errors $\Delta\Phi_{GF,km,l}$ [m]:

$$\Delta\Phi_{GF,km,l} = \langle E_{g,km} \rangle + \langle \delta\, IFB_{g,km} \rangle \tag{3.65}$$

- As in equation (3.64), the code IFB remain unknown, they have to be estimated and removed from (3.64). To solve for $IFB_{g,km}$, one represents the TEC with a simple model:

$$\mathrm{TEC} = \frac{\mathrm{vTEC}_{model}}{\cos\chi_{IP}} + \Delta\,\mathrm{TEC}_{model} \tag{3.66}$$

  where $\Delta\,\mathrm{TEC}_{model}$ are the model errors on TEC [TECU]

  These model errors have two origins: the mapping function given by equation (3.44) (see section 3.1.4.4) and the mathematical expansion used to represent the spatial and temporal variability of the vertical TEC (see section 3.1.4.5).
  Equation (3.64) can now be written as follows:

$$\Phi_{GF,km,l} = \alpha_{km}\,\frac{\mathrm{vTEC}_{model}}{\cos\chi_{IP}} + IFB_{g,km} + \Delta\Phi_{GF,km,l} + \alpha_{km}\,\Delta\,\mathrm{TEC}_{model} + E_{\Phi,km} \tag{3.67}$$

- Using a given number of observations, a linear system of equations of observations is constituted: $\Phi_{GF,km,l}$ are the observations, while $IFB_{g,km}$ and the model coefficients (a_i) from equation (3.47) are the unknowns. The system can then be solved by using a least-square adjustment, in which the code IFB are considered to be constant for a given period (3 days in [17]). As a result, we obtain an estimation of the code IFB, denoted as

$\widehat{IFB}_{g,km}$. It has to be stressed that the levelling, model and observational errors will be translated to the estimation of IFB and therefore of TEC values. Therefore, their notation will be adapted.

- By removing $\widehat{IFB}_{g,km}$ from $\Phi_{GF,km,l}$ and dividing by α_{km} to convert in TECU, we obtain the "levelled" calibrated TEC values TEC_l [TECU]:

$$\text{TEC}_l = \frac{1}{\alpha_{km}} \left(\Phi_{GF,km,l} - \widehat{IFB}_{g,km} \right) \tag{3.68}$$

$$= \text{TEC} + \Delta\text{TEC}_l + \Delta\text{TEC}_{l,model} + E_l \tag{3.69}$$

where
ΔTEC_l are the levelling errors on TEC_l [TECU]
$\Delta\text{TEC}_{l,model}$ are the model errors on TEC_l [TECU]
E_l is the observational error on TEC_l [TECU]

It has to be stressed that this technique is a satellite-by-satellite calibration technique, as there is one $IFB_{g,km}$ unknown per satellite/receiver.

Equation (3.68) implies that the precision of the "levelled" calibrated TEC values is determined by the observational error (E_l), which is a function of phase multipath delays and measurement noise. This term can be considered as a quasi-random error with a standard deviation of a few hundredths of TECU [17], which is rather precise. However, the "levelled" calibrated TEC values are biased by systematic errors. As a matter of fact, the accuracy of the "levelled" calibrated TEC values depends on the aforementioned levelling errors (ΔTEC_l) and model errors ($\Delta\text{TEC}_{l,model}$). The magnitude of these levelling and model errors has been assessed in [17]. A brief summary will be given in section 3.2.2.3.

3.2.2.2 The unlevelled carrier phase process

This technique only relies on the GF phase combination $\Phi_{GF,km}$ given by equation (3.62). The main steps of this unlevelled carrier phase process are [17]:

- We substitute equation (3.66) into equation (3.62), which gives $\Phi_{GF,km}$ [m]:

$$\Phi_{GF,km} = \alpha_{km} \frac{\text{vTEC}_{model}}{\cos\chi_{IP}} + \left(IFB_{\Phi,km} - \lambda_k N_{GF,km} \right) + \alpha_{km} \Delta\text{TEC}_{model} + E_{\Phi,km} \tag{3.70}$$

- Using a given number of observations, a linear system of equations of observations can be constituted: $\Phi_{GF,km}$ are the observations, while $x = \left(IFB_{\Phi,km} - \lambda_k N_{GF,km} \right)$ and the model coefficients (a_i) from equation (3.47) are the unknowns. The system can then be solved using a least-square adjustment. As a result, we obtain an estimation of the x quantity, denoted $\widehat{x}$. It has to be stressed that the model and observational errors will be translated to the estimation of IFB and therefore of TEC values. Therefore, their notation will be adapted.

- By removing $\widehat{x}$ from $\Phi_{GF,km}$ of equation (3.62) and dividing by α_{km} to convert in TECU, we obtain the "unlevelled" calibrated TEC values TEC_u [TECU]:

$$\text{TEC}_u = \frac{1}{\alpha_{km}} \left(\Phi_{GF,km} - \widehat{x} \right) \tag{3.71}$$

$$= \text{TEC} + \Delta\text{TEC}_{u,model} + E_u \tag{3.72}$$

where
$\Delta\,\mathrm{TEC}_{u,model}$ are the model errors on TEC_u [TECU]
E_u is the observational error on TEC_u [TECU]

It is worth noticing that this is an arc-by-arc calibration technique, as this requires the estimation of one $\left(IFB_{\Phi,km} - \lambda_k\, N_{GF,km}\right)$ per satellite pass. This increases the number of unknowns that have to be estimated, which constitutes a disadvantage in comparison with the previous technique [17].

Equation (3.72) implies that the precision of the "unlevelled" calibrated TEC values is determined by the observational error (E_u), which is a function of phase multipath delays and measurement noise, with a standard deviation of a few hundredths of TECU. Moreover, the "unlevelled" calibrated TEC values are affected by model errors $\Delta\,\mathrm{TEC}_{u,model}$. However, by comparison with "levelled" calibrated TEC values, "unlevelled" calibrated values are free from levelling errors. The accuracy assessment of TEC_u is given in the next section.

3.2.2.3 Accuracy assessment of calibrated TEC values

Even if the levelled (TEC_l) and unlevelled (TEC_u) calibrated TEC values are very precise, their accuracy depends on the levelling ($\Delta\,\mathrm{TEC}_l$) and on the model errors ($\Delta\,\mathrm{TEC}_{l,model}$) for the former, and on the model errors ($\Delta\,\mathrm{TEC}_{u,model}$) for the latter. Based on the use of dual frequency Global Positioning System (GPS) measurements (L1/L2), [17] has assessed the magnitude of those levelling and model errors, and thus the accuracy of the levelled and unlevelled calibrated TEC values. The authors used experimental and synthetic datasets corresponding to two co-located Global Positioning System (GPS) receivers in two differents places (mid-latitude, low-latitude) and for three continuous days in May 2006, which constitutes a period of low solar activity and quiet geomagnetic conditions. The experiments performed in this study lead to levelling errors smaller than $\pm\,1.6$ TECU for mid-latitudes, and smaller than $\pm\,0.5$ TECU for low-latitudes. This study also shows that the model given by equation (3.66) performs relatively well in the mid-latitude ionospheric region, and deteriorates when getting closer to the equatorial region. It has been shown that, if the model errors are large, the arc-by-arc calibration technique propagates them more strongly than the satellite-to-satellite calibration technique. It results from those experiments that:

- for a mid-latitude site, $\Delta\,\mathrm{TEC}_{l,model}$ is ranging from -3 to 2 TECU, whereas $\Delta\,\mathrm{TEC}_{u,model}$ is ranging from -2.5 to 2.5 TECU (95 % confidence interval),
- for a low-latitude site: $\Delta\,\mathrm{TEC}_{l,model}$ is varying from -5 to 4.5 TECU, while $\Delta\,\mathrm{TEC}_{u,model}$ is varying from -5.5 to 7.5 TECU for the unlevelled calibrated TEC values (95 % confidence interval).

In total, as for the "levelled" calibrated TEC values both levelling and model errors act together, the accuracy of TEC_l is smaller than the accuracy of TEC_u for mid-latitude regions, while this is the opposite for equatorial regions. Table 3.1 summarizes the accuracy assessment of both calibration techniques for mid- and low-latitudes. It is clear that the accuracy of TEC values is mostly determined by model errors. Moreover, the part of model errors due to the modeling of vertical TEC is predominant.

Table 3.1 *– Accuracy of levelled (TEC_l) and unlevelled (TEC_u) calibrated TEC values: levelling errors, model errors and combined errors for mid- and low-latitudes (95 % confidence interval). From [17].*

Accuracy	TEC_l		TEC_u	
[TECU]	mid-lat	low-lat	mid-lat	low-lat
levelling errors	$[-1.6, 1.6]$	$[-0.5, 0.5]$	$[-]$	$[-]$
model errors	$[-3.0, 2.0]$	$[-5.0, 4.5]$	$[-2.5, 2.5]$	$[-5.5, 7.5]$
$\sum$	$[-4.6, 3.6]$	$[-5.5, 5.0]$	$[-2.5, 2.5]$	$[-5.5, 7.5]$

3.2.3 TEC maps

Thanks to the availability of a worldwide network of dual frequency GPS receivers, global and continuous ionospheric monitoring is achievable. In this context, International GNSS Service (IGS) started in 1998 to produce Global Ionospheric Maps (GIMs). The GIM products of several Ionosphere Associate Analysis Centers (IAAC) are combined to provide the final IGS GIMs in Ionosphere Map Exchange (format) (IONEX) [101] on a daily basis using grids, with a resolution of $2^h \times 5^\circ \times 2.5^\circ$ in universal time, longitude and latitude [33].

3.2.3.1 Generation of GIMs

The first step is to compute the TEC using all available GPS stations. As seen in section 3.2.2 this can be done either using the carrier-to-code levelling process – used by the Center for Orbit Determination in Europe (CODE), European Space Agency (ESA) and Jet Propulsion Laboratory (JPL) – or the unlevelled carrier phase process. Furthermore, Universitat Politècnica de Catalunya (UPC) uses the tomographic approach [47]. The conversion of TEC into vTEC over each IP is done using the mapping function given by equation (3.44). Generally, $h_i = 450$ km in the standard IGS product. Finally vTEC values are interpolated using spline functions [129] over each grid point, i.e. $5^\circ \times 2.5^\circ$ in geocentric longitude and latitude, and then smoothed in time and space with Gaussian radial basis functions.

3.2.3.2 Interpolating TEC in GIMs

Once GIMs are available, users may be interested in retrieving TEC values at a given location and time (λ_{IP} , φ_{IP} , t). which can be different from the provided grid values. This requires time interpolation, space interpolation and a mapping function conversion.

- Considering that we have TEC maps at T_n ($n = 1, 2, ..., m$), there are three different procedures to perform the time interpolation [102]: select the nearest TEC map (where $|t - T_n| = \min$), interpolate linearly between consecutive maps (where $T_n \leq t \leq T_{n+1}$) or interpolate linearly between consecutive *rotated* maps at T_n and T_{n+1} (same condition) The latter is the most accurate one, as it makes it possible to partially compensate the correlation between the ionosphere and the position of the sun. It can be done as follows:

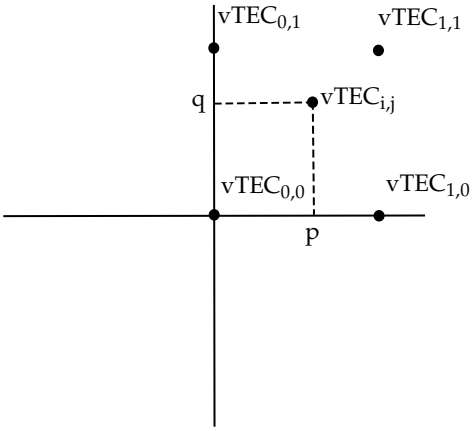

Figure 3.11 *– Bivariate interpolation scheme based on the four nearest* vTEC *values*

$$\text{vTEC}(\lambda_{IP}, \varphi_{IP}, t) = \frac{T_{n+1} - t}{T_{n+1} - T_n} \cdot \text{vTEC}(\lambda_n^{'}, \varphi_{IP}) + \frac{t - T_n}{T_{n+1} - T_n} \cdot \text{vTEC}(\lambda_{n+1}^{'}, \varphi_{IP}) \quad (3.73)$$

where $\lambda_n^{'} = \lambda_{IP} + (t - T_n) \cdot 15$ and $\lambda_{n+1}^{'} = \lambda_{IP} + (T_{n+1} - t) \cdot 15$. The factor "15" converts the time given in hours to degrees.

- The space interpolation (longitude, latitude) is done using the bivariate interpolation algorithm based on the four nearest vTEC values as illustrated in figure 3.11:

$$\begin{aligned} \text{vTEC}(i,j) \quad = \quad & (1-p)(1-q)\,\text{vTEC}_{0,0} + p\,(1-q)\,\text{vTEC}_{1,0} \\ & + q\,(1-p)\,\text{vTEC}_{0,1} + p\,q\,\text{vTEC}_{1,1} \end{aligned} \quad (3.74)$$

  where $i = \lambda_0 + p\,\Delta\lambda$ and $j = \varphi_0 + q\,\Delta\varphi$ correspond to the coordinates of the unknown point, knowing that $p, q \in [0, 1]$ and that $\Delta\lambda, \Delta\varphi$ are the grid widths. Equation (3.73) actually requires twice the use of equation (3.74) to proceed space interpolation.

- Once we have obtained vertical TEC values $\text{vTEC}(\lambda_{IP}, \varphi_{IP}, t)$, we can use the mapping function given by (3.44) to obtain slant TEC values $\text{TEC}(\lambda_{IP}, \varphi_{IP}, t)$.

3.2.3.3 Performance of the GIMs

The performance of GIMs has been tested in different ways and conditions in [82–84]. These tests are done on the different GIMs – CODE, ESA, JPL, UPC, final IGS, etc. – either using GPS data, providing relative accuracy of the GIM model, or external data, giving absolute accuracy of the GIM model.

Let us briefly summarize the results of the GPS data tests and external data tests [82–84]. The relative accuracy depends on latitude, and is better in the Northern hemisphere (esp. mid-latitude) than in the Souther hemisphere. The lower accuracy level at low latitudes (N/S) can be related to the lack of GPS receivers available and to the existence of high total

electron content gradients. The performance seems to also depend on the mean TEC value for both hemispheres. Furthermore, there is a degradation of Root Mean Square (RMS) in function of the elevation. The absolute accuracy depends on the mean TEC value, with worse performance at low latitude, especially during the solar maximum period.

As explained in [83], the performance of GIMs is limited by two aspects: firstly, the use of a 1-layer model with a fixed height limits the modeling of total electron content gradients ; secondly, due the lack of GPS receivers in the Southern hemisphere and oceans, TEC computations are affected by the interpolation procedure. For those reasons, UPC has decided to use a 2-layer voxel model of the ionosphere (tomographic approach, see [47] for details) and to proceed the time and space interpolation with the help of the theoretical ionospheric model called International Reference Ionosphere (IRI) [14, 83]. The latter explains the decrease of the UPC GIM bias in the equatorial region since 2000 [83].

The accuracy specified by IGS for their final GIM products is about 2 to 8 TECU [56].

3.2.3.4 The carrier-to-GIM levelling process

This technique is an alternative to the carrier-to-code levelling process given section 3.2.2.1 and involves the use of GIMs to level the GF combination $\Phi_{GF,km}$. The main steps of this carrier-to-GIM levelling process are [13, 84]:

- The interpolation technique described in section 3.2.3.2 is used to interpolate vertical TEC values in available GIMs at $(\lambda_{IP}, \varphi_{IP}, t)$ corresponding to (λ, φ, t) of the measurement. Then vertical TEC values (vTEC_{GIM}) are converted into slant TEC values (TEC_{GIM}) by using the mapping function given by equation (3.44).
- The mean value between $\Phi_{GF,km}$ and $\alpha_{km}\,\mathrm{TEC}_{GIM}$ ($\langle \Phi_{GF,km} - \alpha_{km}\,\mathrm{TEC}_{GIM} \rangle$) is computed for each satellite pass, and then subtracted from $\Phi_{GF,km}$ to remove the GF ambiguity. Dividing by α_{km}, we obtain the "GIM-levelled" calibrated TEC values $\mathrm{TEC}_{l,GIM}$ [TECU]:

$$\mathrm{TEC}_{l,GIM} = \frac{1}{\alpha_{km}} \left(\Phi_{GF,km} - \langle \Phi_{GF,km} - \alpha_{km}\,\mathrm{TEC}_{GIM} \rangle \right) \tag{3.75}$$

$$= \mathrm{TEC} + \Delta\mathrm{TEC}_{l,GIM} + \Delta\mathrm{TEC}_{l,GIM,model} + E_{l,GIM} \tag{3.76}$$

  Note that the $\langle E_{\Phi,km} \rangle$ term can be neglected as in the carrier-to-code levelling process. This carrier-to-GIM levelling process also causes levelling errors ($\Delta\mathrm{TEC}_{l,GIM}$) that are related to the accuracy of vTEC_{GIM}. Moreover, model errors ($\Delta\mathrm{TEC}_{l,GIM,model}$) come from the mapping function conversion.

Equation (3.76) implies that the precision of the "GIM-levelled" calibrated TEC values is determined by the observational error ($E_{l,GIM}$), which is a function of phase multipath delays and measurement noise and has a standard deviation of a few hundredths of TECU. The accuracy of $\mathrm{TEC}_{l,GIM}$ is determined by levelling and model errors:

- the levelling errors ($\Delta\mathrm{TEC}_{l,GIM}$) depend on the accuracy of GIMs,
- the model errors ($\Delta\mathrm{TEC}_{l,GIM,model}$) are only caused by the mapping function in this case.

As stated in section 3.2.2.3, the errors cause by the mapping function are a minor part of the model errors, which are more important for low-latitudes than for mid-latitudes. We can thus assume that the accuracy of "GIM-levelled" calibrated TEC values is comparable to the accuracy of GIMs [84].

Chapter 4

Triple frequency TEC reconstruction methodology

THIS chapter introduces the concepts required for the development of the TEC reconstruction technique before getting to the core of the method itself. The first section (4.1) introduces the transition from dual frequency to triple frequency TEC reconstruction techniques. The second section (4.2) gives the principles and characteristics of GNSS linear combinations. It also deals with linear transformation and covariance propagation. Then, it analyzes optimal phase linear combinations. The third section (4.3) describes the ambiguity resolution step of the technique. For each combination used, we analyze its characteristics in detail and we assess the influence of the residual term on the ambiguity resolution. The fourth section (4.4) explains how the ambiguities are used for TEC reconstruction and gives an accuracy assessment of triple frequency TEC reconstructed values. The fifth section (4.5) presents an innovative method for calibrating the satellite and receiver code hardware delays. Finally, we provide the conclusions of the chapter in section 4.6.

4.1 Introduction

In the last decades, Global Navigation Satellite Systems (GNSSs) has become a very useful tool to investigate the Earth's ionosphere, making it possible to increase knowledge about the ionosphere. Since the delay caused by the ionosphere is one of the major GNSS error sources, GNSS have in turn highly benefited from this improved knowledge. For the last 20 years, Total Electron Content (TEC) reconstruction using GNSS has been based on dual frequency measurements. The recent modernization of the Global Positioning System (GPS) and the development of the Galileo system have resulted in additional frequencies, offering the possibility to develop new techniques.

We have therefore dedicated this work to developing a TEC reconstruction methodology based on triple frequency GNSS measurements and aimed at improving the accuracy of the final TEC values with regards to existing techniques. The main research questions are the following:

- how would it possible to improve the accuracy of the TEC with triple frequency GNSS?
- which level of accuracy would it be possible to reach?

In this context, we will recall the basics of dual frequency techniques, and explain the conceptual development of the triple frequency TEC reconstruction technique.

4.1.1 From dual frequency...

The calibration of TEC is based on the use of the Geometric-Free (GF) phase combination ($\Phi_{GF,km}$) and requires the computation of its non-integer ambiguity ($N_{GF,km}$). With dual frequency GNSS measurements, this can be achieved by the carrier-to-code levelling process (see section 3.2.2.1), the unlevelled carrier phase process (see section 3.2.2.2) or the carrier-to-GIM levelling process (see section 3.2.3.4). In all of those methods, the slant TEC (TEC) needs to be modeled by means of a mathematical expansion using the vertical TEC (VTEC) and/or a mapping function to convert VTEC into TEC. As a consequence, model errors affect the accuracy of the TEC values. Moreover, in the carrier-to-code levelling process, levelling errors are induced by the non-zero average of code multipath delays as well as by the temporal variation of receiver code hardware delays or code Inter-Frequency Biases (IFB). In total, even if the calibrated TEC values are very precise, their accuracy depends on systematic errors and is limited to a few TECU. For a mid-latitude site, the error effects are confined to -4.6 and 3.6 TECU for the carrier-to-code levelling process, and to -2.5 and 2.5 TECU for the unlevelled carrier phase process. For a low-latitude site, the performance deteriorates: the error effects are confined to -5.5 and 5 TECU for the carrier-to-code levelling process, and to -5.5 and 7.5 TECU for the unlevelled carrier phase process (see section 3.2.2.3).

4.1.2 ...to triple frequency

Taking into account the strengths and weaknesses of dual frequency techniques, and considering the new available triple frequency GNSS signals, we have driven the conceptual development of the triple frequency TEC reconstruction methodology as follows:

- The need for TEC modeling is the main cause of errors (model errors) in the dual frequency techniques and is intrinsically linked to the availablity of only two frequencies. The latter determines the way of dealing with the non-integer GF ambiguities, which have to be either levelled (carrier-to-code levelling process) or estimated (unlevelled carrier phase process). Therefore, we have to take advantage of the availability of triple frequency signals to develop a method allowing us to resolve the GF ambiguities without the need for TEC modeling.
- The availability of triple frequency measurements increases the number of linear combinations which may be useful for ambiguity resolution. Since by definition the main unknown – the slant TEC – is related to one satellite-receiver link, we have to work with equations of undifferenced measurements (1 receiver – 1 satellite) and consider one satellite at a time. The TEC reconstruction requires that the GF ambiguities are estimated for each satellite/receiver, and especially for each satellite pass (arc-by-arc). It has also to be stressed that the combinations used have to be GF so that the ambiguity

resolution can be done on a satellite-by-satellite basis and without the need for Precise Point Positioning (PPP), following the so-called GF approach [43].

- We put a special emphasis on searching for linear combinations that improve the ambiguity resolution process. More specifically, we choose a set of combination on the basis of their interesting characteristics (large wavelength, elimination of the ionosphere and of the geometry), making it possible to resolve the original integer ambiguities on each carrier frequency. By doing so, the GF ambiguity can thus be reconstructed from the original integer ambiguities without the need for TEC modeling. The TEC values are then obtained from the usual dual-frequency GF phase combination.

The TEC reconstruction technique which is developed here uses the three carrier frequencies of the GPS system (L1, L2, L5). For Galileo, it uses L1, E5b and E5a, which are more conveniently named L1, L2 and L5, respectively. The choice of the Galileo frequencies was based on several elements. Firstly, it would not make sense to use the E6 signal which is not dedicated to open services (see section 2.1.2.2). Moreover, using E6 would not have lead to so large a wavelength (see equation (4.53)). Table 4.1 summarizes GPS and Galileo frequencies used for triple frequency TEC reconstruction.

Table 4.1 *– GPS and Galileo frequencies for triple frequency TEC reconstruction.*

Signal	Frequency [MHz]	
	GPS	Galileo
L1	1575.42	1575.42
L2	1227.60	1207.14
L5	1176.45	1176.45

4.2 Linear combinations of GNSS data

Before getting into the core of the method itself, we introduce some essential concepts regarding linear combinations of GNSS data.

4.2.1 Principles

As the dominant correlation source between GNSS is found between measurements from the same receiver/satellite/epoch, it is advantageous to create linear combinations of different frequencies of the same type. It is also possible to take advantage of differencing measurements between satellite and/or receiver (Single Difference (SD), Double Difference (DD)). However, here we will only deal with undifferenced measurements, as will be the case in the TEC reconstruction technique.

It is well known that linear combinations of dual frequency GPS measurements have been used for many applications. With the introduction of a third frequency on GPS satellites and the implementation of the Galileo system, there will be three frequencies available in both

systems, increasing the number of GNSS combinations that may be useful. With regards to their precision, combinations of phase measurements are much more often utilized, in order to specifically enhance applications where high precision is required.

There are three main reasons for using linear combinations [92, 93]:

- The first is to eliminate or mitigate individual error sources (unwanted terms), like ionospheric delays, multipath delays or measurement noise.
- The second is to alleviate the computational burden of processing multi-frequency GNSS data, generally by aiding in phase integer ambiguity resolution. This can be done using the Least-Squares Ambiguity Decorrelation Adjustment (LAMBDA) method [120] or a widelane combination [43] – i.e. with a wavelength greater than L5 (see section 4.2.4.1). Both techniques help to decorrelate the ambiguities and reduce the necessary search space (and thus search time). Contrary to the former method, the latter prevents from the resolution of the original L1, L2 and L5 ambiguities. However, the ambiguities of the combined observation can be fixed instead.
- The third motivation is to reduce the communication bandwidth needed for the transmission of GNSS observations: it is possible to transmit a combined observation using the bandwidth required for a single frequency observation. This motivation is of a rather practical nature and will not be mentioned anymore later on in this text.

Besides the chosen purpose (advantage), there could be a considerable increase of the noise level in the combined observation. It is therefore important to study the effect of linear combinations of GNSS data in the parameter estimation process. After providing several characteristics of the linear combinations in section 4.2.2, we will give in section 4.2.3 the mathematical framework that explains how the measurement model and therefore the precision of the estimated parameters are affected by such combinations. Finally, optimal phase linear combinations will be given on the basis of three criteria (section 4.2.4).

It has to be stressed that we will only consider the GPS and Galileo frequencies which will be used for triple frequency TEC reconstruction.

4.2.2 Characteristics

Linear combinations between observations of the same receiver/satellite/epoch can be formed between code or phase measurements. A linear combination (LC) of the three code measurements can be formed as follows *:

$$P_{LC} = \begin{bmatrix} a & b & c \end{bmatrix} \begin{bmatrix} P_{\mathrm{L1}} \\ P_{\mathrm{L2}} \\ P_{\mathrm{L5}} \end{bmatrix} \tag{4.1}$$

P_{LC} is the combined code measurement [m]
a, b, c are the combination coefficients $[-]$
$P_{\mathrm{L1}}, P_{\mathrm{L2}}, P_{\mathrm{L5}}$ are the original code measurements [m]

*The notations are simplified compared to chapter 2: the i and p subscripts are removed and the k subsripts are substituted by L1, L2 or L5.

Similarly, a linear combination of the three phase measurements can be formed as follows:

$$\varphi_{LC} = \begin{bmatrix} \alpha & \beta & \gamma \end{bmatrix} \begin{bmatrix} \varphi_{\mathrm{L1}} \\ \varphi_{\mathrm{L2}} \\ \varphi_{\mathrm{L5}} \end{bmatrix} \tag{4.2}$$

where
φ_{LC} is the combined phase measurement [cycles]
α, β, γ are the combination coefficients $[-]$
$\varphi_{\mathrm{L1}}, \varphi_{\mathrm{L2}}, \varphi_{\mathrm{L5}}$ are the original phase measurements [cycles]

The ambiguity of the combined phase measurement N_{LC} [cycles] can be expressed as:

$$N_{LC} = -\alpha\, N_{\mathrm{L1}} - \beta\, N_{\mathrm{L2}} - \gamma\, N_{\mathrm{L5}} \tag{4.3}$$

Ideally if we wish to keep the integer nature of the carrier phase ambiguity of the combined measurement, the coefficients of the phase combination (α, β, γ) should be a set of integers. As mentioned earlier, the fact that all observations are combined into a single one usually prevents us from resolving the original ambiguities $N_{\mathrm{L1}}, N_{\mathrm{L2}}, N_{\mathrm{L5}}$. The problem is just reparametrized so that it is possible to fix the ambiguity of the combined measurement instead.

The frequency of the combined observation f_{LC} can be expressed as follows:

$$f_{LC} = \alpha\, f_{\mathrm{L1}} + \beta\, f_{\mathrm{L2}} + \gamma\, f_{\mathrm{L5}} \tag{4.4}$$

It results that the wavelength of the combined observation λ_{LC} [m] is given by:

$$\lambda_{LC} = \frac{c}{f_{LC}} = \frac{c}{\alpha\, f_{\mathrm{L1}} + \beta\, f_{\mathrm{L2}} + \gamma\, f_{\mathrm{L5}}} = \frac{\lambda_{\mathrm{L1}}\lambda_{\mathrm{L2}}\lambda_{\mathrm{L5}}}{\alpha\lambda_{\mathrm{L2}}\lambda_{\mathrm{L5}} + \beta\lambda_{\mathrm{L1}}\lambda_{\mathrm{L5}} + \gamma\lambda_{\mathrm{L1}}\lambda_{\mathrm{L2}}} \tag{4.5}$$

The linear combination of phase measurements can also be expressed in meters:

$$\Phi_{LC} = \lambda_{LC}\, \varphi_{LC} = \begin{bmatrix} d & e & f \end{bmatrix} \begin{bmatrix} \Phi_{\mathrm{L1}} \\ \Phi_{\mathrm{L2}} \\ \Phi_{\mathrm{L5}} \end{bmatrix} \tag{4.6}$$

where
Φ_{LC} is the combined phase measurement [m]
d, e, f are the combination coefficients $[-]$
$\Phi_{\mathrm{L1}}, \Phi_{\mathrm{L2}}, \Phi_{\mathrm{L5}}$ are the original phase measurements [m]

The geometric distance of Φ_{LC} is given by $\rho^i_{p,LC}$ [m]:

$$\rho^i_{p,LC} = \lambda_{LC} \left(\alpha\, \frac{f_{\mathrm{L1}}}{c} + \beta\, \frac{f_{\mathrm{L2}}}{c} + \gamma\, \frac{f_{\mathrm{L5}}}{c} \right) \rho^i_p \tag{4.7}$$

Therefore, by constraining the geometric distance term to be unchanged, equation (4.7) gives the expressions of d, e, f as a function of α, β, γ:

$$d = \frac{\alpha\lambda_{LC}}{\lambda_{\mathrm{L1}}} \qquad e = \frac{\beta\lambda_{LC}}{\lambda_{\mathrm{L2}}} \qquad f = \frac{\gamma\lambda_{LC}}{\lambda_{\mathrm{L5}}} \tag{4.8}$$

Substituting equation (4.8) in (4.3) gives:

$$N_{LC} = \frac{-1}{\lambda_{LC}} \left(d\, \lambda_{\mathrm{L1}}\, N_{\mathrm{L1}} + e\, \lambda_{\mathrm{L2}}\, N_{\mathrm{L2}} + f\, \lambda_{\mathrm{L5}}\, N_{\mathrm{L5}} \right) \tag{4.9}$$

4.2.3 Linear transformation and covariance propagation

In this section we will study how the covariance matrix of the measurement is affected by linear combinations. Applying the law of error propagation to equation (4.1), (4.2) and (4.6) gives the variance of the combined (code or phase) measurement:

$$\sigma^2_{P_{LC}} = \begin{bmatrix} a & b & c \end{bmatrix} \begin{bmatrix} \sigma^2_{P_{L1}} & \sigma_{P_{L1},P_{L2}} & \sigma_{P_{L1},P_{L5}} \\ \sigma_{P_{L2},P_{L1}} & \sigma^2_{P_{L2}} & \sigma_{P_{L2},P_{L5}} \\ \sigma_{P_{L5},P_{L1}} & \sigma_{P_{L5},P_{L2}} & \sigma^2_{P_{L5}} \end{bmatrix} \begin{bmatrix} a \\ b \\ c \end{bmatrix} \tag{4.10}$$

where
$\sigma^2_{P_{LC}}$ is the variance of the combined code measurement $\left[\mathrm{m}^2\right]$
$\sigma^2_{P_k}$ is the variance of the original code measurement $\left[\mathrm{m}^2\right]$
σ_{P_k,P_m} is the covariance of the original code measurements $\left[\mathrm{m}^2\right]$

$$\sigma^2_{\varphi_{LC}} = \begin{bmatrix} \alpha & \beta & \gamma \end{bmatrix} \begin{bmatrix} \sigma^2_{\varphi_{L1}} & \sigma_{\varphi_{L1},\varphi_{L2}} & \sigma_{\varphi_{L1},\varphi_{L5}} \\ \sigma_{\varphi_{L2},\varphi_{L1}} & \sigma^2_{\varphi_{L2}} & \sigma_{\varphi_{L2},\varphi_{L5}} \\ \sigma_{\varphi_{L5},\varphi_{L1}} & \sigma_{\varphi_{L5},\varphi_{L2}} & \sigma^2_{\varphi_{L5}} \end{bmatrix} \begin{bmatrix} \alpha \\ \beta \\ \gamma \end{bmatrix} \tag{4.11}$$

where
$\sigma^2_{\varphi_{LC}}$ is the variance of the combined phase measurement $\left[\mathrm{cycles}^2\right]$
$\sigma^2_{\varphi_k}$ is the variance of the original phase measurement $\left[\mathrm{cycles}^2\right]$
$\sigma_{\varphi_k,\varphi_m}$ is the covariance of the original phase measurements $\left[\mathrm{cycles}^2\right]$

$$\sigma^2_{\Phi_{LC}} = \lambda^2_{LC}\,\sigma^2_{\varphi_{LC}} = \begin{bmatrix} d & e & f \end{bmatrix} \begin{bmatrix} \sigma^2_{\Phi_{L1}} & \sigma_{\Phi_{L1},\Phi_{L2}} & \sigma_{\Phi_{L1},\Phi_{L5}} \\ \sigma_{\Phi_{L2},\Phi_{L1}} & \sigma^2_{\Phi_{L2}} & \sigma_{\Phi_{L2},\Phi_{L5}} \\ \sigma_{\Phi_{L5},\Phi_{L1}} & \sigma_{\Phi_{L5},\Phi_{L2}} & \sigma^2_{\Phi_{L5}} \end{bmatrix} \begin{bmatrix} d \\ e \\ f \end{bmatrix} \tag{4.12}$$

where
$\sigma^2_{\Phi_{LC}}$ is the variance of the combined phase measurement $\left[\mathrm{m}^2\right]$
$\sigma^2_{\Phi_k}$ is the variance of the original phase measurement $\left[\mathrm{m}^2\right]$
σ_{Φ_k,Φ_m} is the covariance of the original phase measurements $\left[\mathrm{m}^2\right]$

Let us focus on the influence of the measurement noise in the combined measurement. As stated in section 2.2.2.11, the measurement noise is a stochastic error. Assuming that there is no correlation between frequencies (the matrix becomes diagonal), equations (4.10), (4.11) and (4.12) can be used to provide the variance of measurement noise for a combined code measurement:

$$\sigma^2_{\varepsilon_{g,LC}} = a^2\,\sigma^2_{\varepsilon_{g,L1}} + b^2\,\sigma^2_{\varepsilon_{g,L2}} + c^2\,\sigma^2_{\varepsilon_{g,L5}} \tag{4.13}$$

where
$\sigma^2_{\varepsilon_{g,LC}}$ is the variance of code measurement noise for a combined code measurement $\left[\mathrm{m}^2\right]$
$\sigma^2_{\varepsilon_{g,k}}$ is the variance of code measurement noise for k code measurement $\left[\mathrm{m}^2\right]$
Similarly for a combined phase measurement:

$$\sigma^2_{\varepsilon_{\varphi,LC}} = \alpha^2\,\sigma^2_{\varepsilon_{\varphi,L1}} + \beta^2\,\sigma^2_{\varepsilon_{\varphi,L2}} + \gamma^2\,\sigma^2_{\varepsilon_{\varphi,L5}} \tag{4.14}$$

where
$\sigma^2_{\varepsilon_{\varphi,LC}}$ is the variance of phase measurement noise for a combined phase measurement $\left[\text{cycles}^2\right]$
$\sigma^2_{\varepsilon_{\varphi,k}}$ is the variance of phase measurement noise for k phase measurement $\left[\text{cycles}^2\right]$

$$\sigma^2_{\varepsilon_{\Phi,LC}} = d^2\,\sigma^2_{\varepsilon_{\Phi,\text{L1}}} + e^2\,\sigma^2_{\varepsilon_{\Phi,\text{L2}}} + f^2\,\sigma^2_{\varepsilon_{\Phi,\text{L5}}} \tag{4.15}$$

where
$\sigma^2_{\varepsilon_{\Phi,LC}}$ is the variance of phase measurement noise for a combined phase measurement $\left[\text{m}^2\right]$
$\sigma^2_{\varepsilon_{\Phi,k}}$ is the variance of phase measurement noise for k phase measurement $\left[\text{m}^2\right]$

It is worth noticing that multiplying equation (4.14) by λ^2_{LC} gives equation (4.15).

As seen in section 2.2.2.7, multipath delays can be considered an almost random error. Therefore, equations (4.13), (4.14) and (4.15) can be adapted to compute the influence of multipath delays for a combined code measurement:

$$\sigma^2_{M_{g,LC}} = a^2\,\sigma^2_{M_{g,\text{L1}}} + b^2\,\sigma^2_{M_{g,\text{L2}}} + c^2\,\sigma^2_{M_{g,\text{L5}}} \tag{4.16}$$

where
$\sigma^2_{M_{g,LC}}$ is the variance of code multipath delays for a combined code measurement $\left[\text{m}^2\right]$
$\sigma^2_{M_{g,k}}$ is the variance of code multipath delays for k code measurement $\left[\text{m}^2\right]$
Identically for a combined phase measurement:

$$\sigma^2_{M_{\varphi,LC}} = \alpha^2\,\sigma^2_{M_{\varphi,\text{L1}}} + \beta^2\,\sigma^2_{M_{\varphi,\text{L2}}} + \gamma^2\,\sigma^2_{M_{\varphi,\text{L5}}} \tag{4.17}$$

where
$\sigma^2_{M_{g,LC}}$ is the variance of phase multipath delays for a combined phase measurement $\left[\text{cycles}^2\right]$
$\sigma^2_{M_{\varphi,k}}$ is the variance of phase multipath delays for k phase measurement $\left[\text{cycles}^2\right]$

$$\sigma^2_{M_{\Phi,LC}} = d^2\,\sigma^2_{M_{\Phi,\text{L1}}} + e^2\,\sigma^2_{M_{\Phi,\text{L2}}} + f^2\,\sigma^2_{M_{\Phi,\text{L5}}} \tag{4.18}$$

where
$\sigma^2_{M_{\Phi,LC}}$ is the variance of phase multipath delays for a combined phase measurement $\left[\text{m}^2\right]$
$\sigma^2_{M_{\Phi,k}}$ is the variance of phase multipath delays for k phase measurement $\left[\text{m}^2\right]$

4.2.4 Optimal phase linear combinations

This section will exclusively analyze linear combinations of phase measurements. From section 4.2.1 we can distinguish three purposes for using a combined phase measurement:

1. to increase the wavelength
2. to reduce or eliminate unwanted terms (e.g. ionospheric delays)
3. to reduce the measurement noise/multipath delays

There is no combination that is ideal on all counts. For example, reducing noise or eliminating ionospheric delays reduces the wavelength of the combination, which makes the ambiguity resolution more challenging. Therefore the optimal combination has to be chosen as a function of the desired characteristics. We will briefly describe the three criteria, and for each one we will give the optimal combinations, i.e. combinations that satisfy the chosen criterion without completely unsatisfying the other criteria [122]. We will also give the optimal combinations for the three criteria altogether. It has to be stressed that in the present section all combinations have integer coefficients ($\alpha, \beta, \gamma \in \mathbb{Z}$).

4.2.4.1 Widelane criterion

By definition, a widelane combination has a wavelength greater than the wavelength of GPS or Galileo L5 carrier frequency [122]. The criterion can be written as follows:

$$\lambda_{LC} > \lambda_{\mathrm{L5}} \tag{4.19}$$

By using equation (4.5), this condition becomes:

$$\frac{\lambda_{\mathrm{L1}}\lambda_{\mathrm{L2}}}{\alpha\lambda_{\mathrm{L2}}\lambda_{\mathrm{L5}} + \beta\lambda_{\mathrm{L1}}\lambda_{\mathrm{L5}} + \gamma\lambda_{\mathrm{L1}}\lambda_{\mathrm{L2}}} > 1 \tag{4.20}$$

By rearranging equation (4.20) we can find [122]:

$$\gamma = \mathrm{ceil}(-c_{15}\,\alpha - c_{25}\,\beta) \tag{4.21}$$

where
$c_{15} = \frac{f_{\mathrm{L1}}}{f_{\mathrm{L5}}}$ and $c_{25} = \frac{f_{\mathrm{L2}}}{f_{\mathrm{L5}}}$
$\mathrm{ceil}(x)$ is the smallest integer value that is not less than x

Following the approach used in [22, 46], α and β can be constrained to the following ranges:

$$\alpha \in [-57, 57] \tag{4.22}$$
$$\beta \in [-11, 11] \tag{4.23}$$

Equations (4.22), (4.23) and (4.21) determine all possible widelane combinations.

As there are a lot of widelane combinations that can be formed with three frequencies, we will only show the optimal ones, which either have an extremely large wavelength or minimize noise and ionospheric delays [122]. Tables 4.2 and 4.3 show the optimal widelane combinations for GPS and Galileo, respectively. Each table is giving:

- the letter code describing the linear combination (LC, optional),
- the coefficients of φ_{LC} [cycles] combination (α, β and γ),
- the wavelength of the combination (λ_{LC}),
- the ionosphere amplification factor $[-]$ of φ_{LC} [cycles] and of Φ_{LC} [m] with respect to L1 (see section 4.2.4.2)
- the noise amplification factor $[-]$ of φ_{LC} [cycles] and of Φ_{LC} [m] with respect to L1 (see section 4.2.4.3).

Table 4.2 *– Several optimal widelane combinations for GPS.*

LC	α	β	γ	λ_{LC} [m]	Iono amplification		Noise amplification	
					φ_{LC}	Φ_{LC}	φ_{LC}	Φ_{LC}
ML	1	0	-1	0.7514	-0.3391	-1.3391	1.4142	5.5843
WL	1	-1	0	0.8619	-0.2833	-1.2833	1.4142	6.4056
EWL	0	1	-1	5.8610	-0.0558	-1.7186	1.4142	43.5578
	1	-5	4	2.0932	-0.0601	-0.6616	6.4807	71.2881
	4	-8	3	29.3052	-2.2493	-346.3881	9.4340	1452.8331

Table 4.3 *– Several optimal widelane combinations for Galileo.*

LC	α	β	γ	λ_{LC} [m]	Iono amplification		Noise amplification	
					φ_{LC}	Φ_{LC}	φ_{LC}	Φ_{LC}
ML	1	0	-1	0.7514	-0.3391	-1.3391	1.4142	5.5843
WL	1	-1	0	0.8140	-0.3051	-1.3051	1.4142	6.0497
EWL	0	1	-1	9.7684	-0.0340	-1.7477	1.4142	72.5963
	-3	1	3	29.3052	2.3225	357.6613	4.3589	671.2704

In both GNSS systems, the maximal wavelength is 29.3052 m. The most popular widelane combinations are the extra–widelane (EWL), widelane (WL) and middlelane (ML) combinations, which will be identified as φ_{EWL} , φ_{WL} and φ_{ML} [cycles]. They constitute dual-frequency widelane combinations whose coefficients equal 1 with opposite signs (see tables 4.2 and 4.3):

$$\varphi_{EWL} = \varphi_{\mathrm{L2}} - \varphi_{\mathrm{L5}} \tag{4.24}$$

$$\varphi_{WL} = \varphi_{\mathrm{L1}} - \varphi_{\mathrm{L2}} \tag{4.25}$$

$$\varphi_{ML} = \varphi_{\mathrm{L1}} - \varphi_{\mathrm{L5}} \tag{4.26}$$

The wavelength of those widelane combinations – which is computed by equation (4.5) – is given by:

$$\lambda_{EWL} = \frac{c}{f_{\mathrm{L2}} - f_{\mathrm{L5}}} \tag{4.27}$$

$$\lambda_{WL} = \frac{c}{f_{\mathrm{L1}} - f_{\mathrm{L2}}} \tag{4.28}$$

$$\lambda_{ML} = \frac{c}{f_{\mathrm{L1}} - f_{\mathrm{L5}}} \tag{4.29}$$

Table 4.4 summarizes the values of those wavelengths, respectively for GPS and Galileo. We can observe that λ_{EWL} is larger by a factor of 1.66 for Galileo than for GPS, while λ_{WL} have the same order of magnitude and λ_{ML} are exactly the same. This will have an importance for the ambiguity resolution process explained in section 4.3.1.1. The ambiguities of those combinations are called the EWL, WL and ML ambiguities, which will be identified as N_{EWL} , N_{WL}

and N_{ML}:

$$N_{EWL} = N_{\mathrm{L5}} - N_{\mathrm{L2}} \tag{4.30}$$
$$N_{WL} = N_{\mathrm{L2}} - N_{\mathrm{L1}} \tag{4.31}$$
$$N_{ML} = N_{\mathrm{L5}} - N_{\mathrm{L1}} \tag{4.32}$$

Table 4.4 *– Wavelength of the EWL, WL and ML combinations.*

LC	λ_{LC} [m]	
	GPS	Galileo
EWL	5.861	9.768
WL	0.862	0.814
ML	0.751	0.751

4.2.4.2 Ionosphere-reduced criterion

By definition, an ionosphere-reduced combination is a combination in which the ionospheric delays are reduced compared to those on the L1 frequency. Once again, we will only consider first-order ionospheric delays. The first-order ionospheric delay of the combined measurement Φ_{LC} [m], denoted as $I_{\Phi,LC}$ [m], can be derived from equation (4.6):

$$I_{\Phi,LC} = -d\, I_{\mathrm{L1}} - e\, I_{\mathrm{L2}} - f\, I_{\mathrm{L5}} \tag{4.33}$$

Then using equation (3.31) we can express $I_{\Phi,LC}$ as a function of I_{L1}:

$$I_{\Phi,LC} = -I_{\mathrm{L1}} \left(d + e\, \frac{f_{\mathrm{L1}}^2}{f_{\mathrm{L2}}^2} + f\, \frac{f_{\mathrm{L1}}^2}{f_{\mathrm{L5}}^2} \right) \tag{4.34}$$

The ionosphere-reduced criterion (in meters) is satisfied if

$$\left| d + e\, \frac{f_{\mathrm{L1}}^2}{f_{\mathrm{L2}}^2} + f\, \frac{f_{\mathrm{L1}}^2}{f_{\mathrm{L5}}^2} \right| < 1 \tag{4.35}$$

Similarly, the first-order ionospheric delay of the combined measurement φ_{LC} [cycles], denoted as $I_{\varphi,LC}$ [cycles] can be derived from equation (4.2) and expressed as a function of $I_{p,\mathrm{L1}}^i$:

$$I_{\varphi,LC} = \frac{f_{\mathrm{L1}}}{c}\, I_{\mathrm{L1}} \left(\alpha + \beta\, \frac{f_{\mathrm{L1}}}{f_{\mathrm{L2}}} + \gamma\, \frac{f_{\mathrm{L1}}}{f_{\mathrm{L5}}} \right) \tag{4.36}$$

The ionosphere-reduced criterion (in cycles) is satisfied if

$$\left| \alpha + \beta\, \frac{f_{\mathrm{L1}}}{f_{\mathrm{L2}}} + \gamma\, \frac{f_{\mathrm{L1}}}{f_{\mathrm{L5}}} \right| < 1 \tag{4.37}$$

In order to completely eliminate the first-order ionospheric delays, the following condition must be satisfied, respectively in meters or cycles:

$$d + e\,\frac{f_{\mathrm{L1}}^2}{f_{\mathrm{L2}}^2} + f\,\frac{f_{\mathrm{L1}}^2}{f_{\mathrm{L5}}^2} = 0 \tag{4.38}$$

$$\alpha + \beta\,\frac{f_{\mathrm{L1}}}{f_{\mathrm{L2}}} + \gamma\,\frac{f_{\mathrm{L1}}}{f_{\mathrm{L5}}} = 0 \tag{4.39}$$

This constitutes the Ionospheric-Free (IF) criterion. The ionosphere amplification factor of the combination in meters (Φ_{LC}) with respect to L1 is the left-hand side of equation (4.38), while the ionosphere amplification factor of the combination in cycles (φ_{LC}) with respect to L1 is the left-hand side of equation (4.39). Those factors are unitless.

As for the widelane case, there is a huge number of possible ionosphere-reduced combinations. Thus only the optimal ionosphere-reduced combinations will be shown [122]. Tables 4.5 and 4.6 show the optimal ionosphere-reduced combinations for GPS and Galileo, respectively, following the same scheme as in table 4.2.

Table 4.5 *– Several optimal ionosphere-reduced combinations for GPS.*

LC	α	β	γ	λ_{LC} [m]	Iono amplification		Noise amplification	
					φ_{LC}	Φ_{LC}	φ_{LC}	Φ_{LC}
IF	0	24	-23	0.1247	0.0000	0.0000	33.2415	21.7838
c1	1	-6	5	3.2561	-0.0043	-0.0744	7.8740	134.7330
c2	13	-7	-3	0.0359	-0.0007	-0.0001	15.0665	2.8400
IF	77	-60	0	0.0063	0.0000	0.0000	97.6166	3.2273
IF	154	0	-115	0.0028	0.0000	0.0000	192.2004	2.8214

Table 4.6 *– Several optimal ionosphere-reduced combinations for Galileo.*

LC	α	β	γ	λ_{LC} [m]	Iono amplification		Noise amplification	
					φ_{LC}	Φ_{LC}	φ_{LC}	Φ_{LC}
IF	0	118	-115	0.0419	0.0000	0.0000	164.7695	36.3012
c1	1	-10	9	3.2561	0.0013	0.0227	13.4907	230.8415
c3	26	-23	3	0.0179	0.0004	0.0000	34.8425	3.2818
IF	77	-59	0	0.0060	0.0000	0.0000	97.0052	3.0512
IF	154	0	-115	0.0028	0.0000	0.0000	192.2004	2.8214

The combinations marked IF satisfy the IF criterion. Their noise amplification factor is quite high. While almost eliminating the first-order ionospheric delays, the combination marked c1 in both systems is a widelane ($\lambda = 3.2561$ m). However, its noise amplification factor is the highest of all ionosphere-reduced combinations. The GPS combination marked c2 combines a low ionosphere amplification factor with a low noise amplification factor.

4.2.4.3 Noise-reduced criterion

By definition, a noise-reduced combination is a combination in which the measurement noise is reduced compared to those on the L1 frequency. Note that, as multipath delays constitute an almost random effect, it can be assumed that the combinations that reduce the measurement noise also reduce multipath delays. For this reason, we will only talk about measurement noise, even if the procedure and results are also valid for multipath delays.
According to equation (4.14), the standard deviation of the combined phase measurement due to measurement noise $\sigma_{\varepsilon_{\varphi,LC}}$ [cycles] is given by:

$$\sigma_{\varepsilon_{\varphi,LC}} = \sqrt{\alpha^2\,\sigma^2_{\varepsilon_{\varphi,\mathrm{L1}}} + \beta^2\,\sigma^2_{\varepsilon_{\varphi,\mathrm{L2}}} + \gamma^2\,\sigma^2_{\varepsilon_{\varphi,\mathrm{L5}}}} \tag{4.40}$$

From section 2.2.2.11, it comes that the standard deviation of the noise measurement is proportional to the wavelength. Therefore, in units of cycles, we can reasonably assume that $\sigma_{\varepsilon_{\varphi,\mathrm{L1}}} = \sigma_{\varepsilon_{\varphi,\mathrm{L2}}} = \sigma_{\varepsilon_{\varphi,\mathrm{L5}}}$, so that equation (4.40) becomes:

$$\sigma_{\varepsilon_{\varphi,LC}} = \sigma_{\varepsilon_{\varphi,\mathrm{L1}}}\sqrt{\alpha^2 + \beta^2 + \gamma^2} \tag{4.41}$$

From this, the noise-reduced criterion (in cycles) is satisfied if

$$\sqrt{\alpha^2 + \beta^2 + \gamma^2} < 1 \tag{4.42}$$

As $\alpha, \beta, \gamma \in \mathbb{Z}$, this criterion will never be satisfied. In other words, it is not possible to reduce the effect of measurement noise in units of cycles, and $\sigma_{\varepsilon_{\varphi,LC}}$ will always be greater than $\sigma_{\varepsilon_{\varphi,\mathrm{L1}}}$.

According to equation (4.15), the standard deviation of the combined phase measurement due to measurement noise $\sigma_{\varepsilon_{\Phi,LC}}$ [m] is given by:

$$\sigma_{\varepsilon_{\Phi,LC}} = \sqrt{d^2\,\sigma^2_{\varepsilon_{\Phi,\mathrm{L1}}} + e^2\,\sigma^2_{\varepsilon_{\Phi,\mathrm{L2}}} + f^2\,\sigma^2_{\varepsilon_{\Phi,\mathrm{L5}}}} \tag{4.43}$$

Since multiplying a quantity in cycles by the wavelength gives the quantity in meters ($\sigma_{\varepsilon_{\Phi,k}} = \lambda_k\,\sigma_{\varepsilon_{\varphi,k}}$), and assuming that $\sigma_{\varepsilon_{\varphi,\mathrm{L1}}} = \sigma_{\varepsilon_{\varphi,\mathrm{L2}}} = \sigma_{\varepsilon_{\varphi,\mathrm{L5}}}$, equation (4.43) becomes:

$$\sigma_{\varepsilon_{\Phi,LC}} = \sigma_{\varepsilon_{\Phi,\mathrm{L1}}}\sqrt{d^2 + e^2\,\frac{\lambda^2_{\mathrm{L2}}}{\lambda^2_{\mathrm{L1}}} + f^2\,\frac{\lambda^2_{\mathrm{L5}}}{\lambda^2_{\mathrm{L1}}}} \tag{4.44}$$

Thus the noise-reduced criterion in meters is the following:

$$\sqrt{d^2 + e^2\,\frac{\lambda^2_{\mathrm{L2}}}{\lambda^2_{\mathrm{L1}}} + f^2\,\frac{\lambda^2_{\mathrm{L5}}}{\lambda^2_{\mathrm{L1}}}} < 1 \tag{4.45}$$

The noise amplification factor of the combination in cycles (φ_{LC}) with respect to L1 is the left-hand side of equation (4.42), while the noise amplification factor of to the combination in meters (Φ_{LC}) with respect to L1 is the left-hand side of equation (4.45). Those factors are unitless.

Tables 4.7 and 4.8 show the optimal noise-reduced combinations for GPS and Galileo, respectively, following the same scheme as in table 4.2.

Table 4.7 *– Several optimal noise-reduced combinations for GPS.*

LC	α	β	γ	λ_{LC} [m]	Iono amplification		Noise amplification	
					φ_{LC}	Φ_{LC}	φ_{LC}	Φ_{LC}
NL	1	1	0	0.1070	2.2833	1.2833	1.4142	0.7948
NL	0	1	1	0.1247	2.6225	1.7186	1.4142	0.9268
NL	1	0	1	0.1089	2.3391	1.3391	1.4242	0.8096
c1	1	1	1	0.0753	3.6225	1.4341	1.7321	0.6857

Table 4.8 *– Several optimal noise-reduced combinations for Galileo.*

LC	α	β	γ	λ_{LC} [m]	Iono amplification		Noise amplification	
					φ_{LC}	Φ_{LC}	φ_{LC}	Φ_{LC}
NL	1	1	0	0.1077	2.3051	1.3051	1.4142	0.8007
NL	0	1	1	0.1258	2.6442	1.7477	1.4142	0.9347
NL	1	0	1	0.1089	2.3391	1.3391	1.4142	0.8096
c1	1	1	1	0.0757	3.6442	1.4502	1.7321	0.6892

The best noise-reduced combination is c1, because it has the lowest noise amplification factor in meters. The most popular noise-reduced combinations are the so-called narrowlane combinations, marked NL in tables 4.7 and 4.8. They constitute dual-frequency combinations whose coefficients are equal to 1 and have equal signs. Their general expression is the following:

$$\varphi_{nl,km} = \varphi^i_{p,k} + \varphi^i_{p,m} \tag{4.46}$$

Their wavelength, which is computed by equation (4.5), is given by

$$\lambda_{nl} = \frac{c}{f_k + f_m} \tag{4.47}$$

4.2.4.4 Optimal combinations

It is also possible to select optimal combinations for all three criteria together. Those combinations have to minimize the noise and ionosphere amplification, while keeping a reasonable wavelength so that ambiguity resolution is possible. It has been shown that the lower limit for this is 0.10 m [93]. Tables 4.9 and 4.10 show the optimal combinations for GPS and Galileo, respectively, following the same scheme as in table 4.2. In both systems, all wavelengths are around 0.10 m and the ionospheric delays are greatly reduced.

4.3 Ambiguity resolution

The availability of triple frequency GNSS measurements increases the number of linear combinations which are useful for ambiguity resolution in the aim of TEC reconstruction. Especially,

Table 4.9 *– Optimal combinations for GPS.*

α	β	γ	λ_{LC} [m]	Iono amplification		Noise amplification	
				φ_{LC}	Φ_{LC}	φ_{LC}	Φ_{LC}
4	1	-4	0.1062	-0.0732	-0.0408	5.7446	3.2053
4	0	-3	0.1081	-0.0174	-0.0099	5.0000	2.8413
4	-1	-2	0.1102	0.0384	0.0222	4.5826	2.6531
5	-5	1	0.1028	-0.0775	-0.0419	7.1414	3.8589

Table 4.10 *– Optimal combinations for Galileo.*

α	β	γ	λ_{LC} [m]	Iono amplification		Noise amplification	
				φ_{LC}	Φ_{LC}	φ_{LC}	Φ_{LC}
4	-3	0	0.1119	0.0847	0.0498	5.0000	2.9389
4	-2	-1	0.1106	0.0507	0.0295	4.5826	2.6631
4	-1	-2	0.1093	0.0167	0.0096	4.5826	2.6333
4	0	-3	0.1081	-0.0174	-0.0099	5.0000	2.8413
4	1	-4	0.1070	-0.0514	-0.0289	5.7446	3.2287
4	2	-5	0.1058	-0.0855	-0.0475	6.7082	3.7295

the combinations which are used make the resolution of original integer ambiguities feasible. Instead of being estimated by the carrier-to-code (or carrier-to-GIM) levelling process, or computed by a least-square adjustment in the unlevelled carrier phase process, the GF ambiguity is thus reconstructed from the original ambiguities. The TEC values are then reconstructed from the usual GF phase combination.

The ambiguity resolution procedure follows two main steps:

1. First, the large wavelength of the widelane-narrowlane combinations is exploited to resolve the widelane ambiguities. Only two of the three widelane-narrowlane combinations which are formed are independent. Therefore, it makes sense to use the combinations which have the largest wavelength, i.e. to resolve the EWL and WL ambiguities. Nevertheless, the resolution of ML ambiguities will also be studied. Besides the widelane-narrowlane combinations, the differenced widelane combinations are considered as an alternative to resolve the WL or ML ambiguities (see section 4.3.1).

2. Secondly, the EWL and WL ambiguities are substituted in the triple frequency phase multipath combination, which makes it possible to resolve the original integer ambiguities on L1, L2 and L5 (see section 4.3.2).

As aforementioned in section 4.1, the combinations used are all Geometric-Free (GF) combinations. By definition, GF means that all frequency-independent effects cancel out so that only frequency-dependent effects remain. These frequency-dependent effects – which are given in section 3.2.1 – have an influence on the ambiguity resolution. In the ambiguity resolution procedure, we only consider the influence of the following effects:

- ionospheric delays*,
- satellite and receiver hardware delays (code/phase),
- multipath delays (code/phase),
- measurement noise (code/phase).

This means that we neglect the influence of the following effects:

- satellite and receiver antenna Phase Center Offsets (PCOs) and Phase Center Variations (PCVs) (code/phase),
- phase wind-up effect (phase only).

Nevertheless, as stated in sections 2.2.2.10 and 2.2.2.12, these effects can be removed by applying an adequate correction. The influence of the uncorrected effects on the reconstructed TEC values will be studied in section 4.4.2.1.

4.3.1 Widelane ambiguity resolution

4.3.1.1 Widelane-narrowlane combinations

Principles

As stated in [43], the larger the wavelength, the easier the ambiguity resolution becomes. Therefore we will start our approach from the three most popular widelane combinations, already defined by equations (4.24),(4.25) and (4.26). By using equation (2.70), we can develop the general expression of those three widelane combinations $\varphi_{wl,km}$ [cycles] as follows, with $k, m \in \{\text{L1}, \text{L2}, \text{L5}\}$:

$$\varphi_{wl,km} = \varphi^i_{p,k} - \varphi^i_{p,m} \tag{4.48}$$

$$= \frac{f_k}{c}\rho^i_p + f_k\,\Delta t_p - f_k\left(\Delta t^i + \Delta t^i_{rel}\right) - \frac{f_m}{c}\rho^i_p - f_m\,\Delta t_p + f_m\left(\Delta t^i + \Delta t^i_{rel}\right) \tag{4.49}$$

$$+\frac{f_k}{c}\left(-I^i_{p,k} + T^i_p + d^i_{\Phi,k} + d_{p,\Phi,k} + M^i_{p,\Phi,k} + \varepsilon^i_{p,\Phi,k}\right)$$

$$-\frac{f_m}{c}\left(-I^i_{p,m} + T^i_p + d^i_{\Phi,m} + d_{p,\Phi,m} + M^i_{p,\Phi,m} + \varepsilon^i_{p,\Phi,m}\right)$$

$$-N^i_{p,k} + N^i_{p,m} \tag{4.50}$$

where the combined ambiguity is the widelane ambiguity $N_{wl,km}$ [cycles]:

$$N_{wl,km} = N^i_{p,m} - N^i_{p,k} \tag{4.51}$$

*These concerns the differenced widelane combinations only, which are the only non-IF combination used.

However, this combination is still dependent on the geometry terms, whereas for the needs of the TEC reconstruction technique a GF approach is required. For this purpose, the frequency-weighted average of the related code measurements $P^i_{p,k}$, $P^i_{p,m}$ can be subtracted from equation (4.48) in order to form $c_{wl,km}$ [cycles]:

$$c_{wl,km} = \varphi^i_{p,k} - \varphi^i_{p,m} - \frac{f_k - f_m}{f_k + f_m}\left(\frac{f_k}{c}P^i_{p,k} + \frac{f_m}{c}P^i_{p,m}\right) \tag{4.52}$$

This combination is actually the well-known Melbourne-Wübbena combination [73, 133], whose wavelength is $\lambda_{wl,km}$ [m]

$$\lambda_{wl,km} = \frac{c}{f_k - f_m} \tag{4.53}$$

To express $c_{wl,km}$ in meters, we have to multiply it by its wavelength $\lambda_{wl,km}$:

$$\begin{aligned} C_{wl,km} &= \lambda_{wl,km}\left(\varphi^i_{p,k} - \varphi^i_{p,m}\right) - \frac{c}{f_k + f_m}\left(\frac{f_k}{c}P^i_{p,k} + \frac{f_m}{c}P^i_{p,m}\right) && (4.54)\\ &= \lambda_{wl,km}\left(\varphi^i_{p,k} - \varphi^i_{p,m}\right) - \lambda_{nl,km}\left(\frac{f_k}{c}P^i_{p,k} + \frac{f_m}{c}P^i_{p,m}\right) && (4.55)\\ &= \lambda_{wl,km}\left(\varphi^i_{p,k} - \varphi^i_{p,m}\right) - \frac{f_k P^i_{p,k} + f_m P^i_{p,m}}{f_k + f_m} && (4.56) \end{aligned}$$

From equation (4.55) we understand why this combination is also called the widelane phase minus narrowlane code combination, or simply widelane-narrowlane combination. This latter term will be used from now on.

It can be easily proved that the widelane-narrowlane combination is GF and IF, so that equation (4.52) can be developed as [52, 69]:

$$\begin{aligned} c_{wl,km} = {} & N_{wl,km} \\ & + \frac{f_k}{c}\left(d^i_{\Phi,k} + d_{p,\Phi,k} + M^i_{p,\Phi,k} + \varepsilon^i_{p,\Phi,k}\right) \\ & - \frac{f_m}{c}\left(d^i_{\Phi,m} + d_{p,\Phi,m} + M^i_{p,\Phi,m} + \varepsilon^i_{p,\Phi,m}\right) \\ & - f_{km}\frac{f_k}{c}\left(d^i_{g,k} + d_{p,g,k} + M^i_{p,g,k} + \varepsilon^i_{p,g,k}\right) \\ & - f_{km}\frac{f_m}{c}\left(d^i_{g,m} + d_{p,g,m} + M^i_{p,g,m} + \varepsilon^i_{p,g,m}\right) \end{aligned} \tag{4.57}$$

where the coefficient f_{km} $[-]$ is:

$$f_{km} = \frac{f_k - f_m}{f_k + f_m} \tag{4.58}$$

If the non-ambiguity term is defined as the residual term $\Delta c_{wl,km}$ [cycles], equation (4.57) becomes:

$$c_{wl,km} = N_{wl,km} + \Delta c_{wl,km} \tag{4.59}$$

If we express it in meters, this gives:

$$\begin{aligned} C_{wl,km} &= \lambda_{wl,km}\left(N_{wl,km} + \Delta c_{wl,km}\right) && (4.60)\\ &= \lambda_{wl,km} N_{wl,km} + \Delta C_{wl,km} && (4.61) \end{aligned}$$

From equation (4.57), it comes that this residual term depends on satellite and receiver hardware delays, multipath delays and measurement noise on both code and phase measurements. Moreover, it is worth noticing that the main temporal variability comes from code multipath delays and code measurement noise (see tables 2.7 and 2.8).

By using equations (4.52) to (4.61) we get the particular cases of the widelane-narrowlane combination:

- the extra–widelane–narrowlane (EWLNL) combination c_{EWL} [cycles], whose wavelength (λ_{EWL}) is given by equation (4.27):

$$\begin{aligned} c_{EWL} &= \varphi_{\mathrm{L2}} - \varphi_{\mathrm{L5}} - \frac{f_{\mathrm{L2}} - f_{\mathrm{L5}}}{f_{\mathrm{L2}} + f_{\mathrm{L5}}} \left(\frac{f_{\mathrm{L2}}}{c} P_{\mathrm{L2}} + \frac{f_{\mathrm{L5}}}{c} P_{\mathrm{L5}} \right) && (4.62) \\ &= N_{EWL} + \Delta c_{EWL} && (4.63) \end{aligned}$$

- the widelane–narrowlane (WLNL) combination c_{WL} [cycles], whose wavelength (λ_{WL}) is given by equation (4.28):

$$\begin{aligned} c_{WL} &= \varphi_{\mathrm{L1}} - \varphi_{\mathrm{L2}} - \frac{f_{\mathrm{L1}} - f_{\mathrm{L2}}}{f_{\mathrm{L1}} + f_{\mathrm{L2}}} \left(\frac{f_{\mathrm{L1}}}{c} P_{\mathrm{L1}} + \frac{f_{\mathrm{L2}}}{c} P_{\mathrm{L2}} \right) && (4.64) \\ &= N_{WL} + \Delta c_{WL} && (4.65) \end{aligned}$$

- the middlelane–narrowlane (MLNL) combination c_{ML} [cycles], whose wavelength (λ_{ML}) is given by equation (4.29):

$$\begin{aligned} c_{ML} &= \varphi_{\mathrm{L1}} - \varphi_{\mathrm{L5}} - \frac{f_{\mathrm{L1}} - f_{\mathrm{L5}}}{f_{\mathrm{L1}} + f_{\mathrm{L5}}} \left(\frac{f_{\mathrm{L1}}}{c} P_{\mathrm{L1}} + \frac{f_{\mathrm{L5}}}{c} P_{\mathrm{L5}} \right) && (4.66) \\ &= N_{ML} + \Delta c_{ML} && (4.67) \end{aligned}$$

Resolution

As stated in section 4.2.4.1, the widelane ambiguities are integer ambiguities. Therefore, in order to be able to resolve the EWL, WL and ML ambiguities (i.e. to fix them at the correct integer value), it is critical for the corresponding residual term to be less than half a cycle. It is thus possible to resolve the ambiguities if the following condition (in cycles) is fulfilled:

$$|\Delta c_{wl,km}| < 0.5 \tag{4.68}$$

In meters, the condition becomes:

$$|\Delta C_{wl,km}| < \frac{\lambda_{wl,km}}{2} \tag{4.69}$$

Using table 4.4, we can obtain the maximum value of the residual term $\Delta C_{wl,km}$ that makes the ambiguity resolution possible, i.e. $\frac{\lambda_{wl,km}}{2}$. The values are given in table 4.11. The larger the wavelength, the easier is the ambiguity resolution [43]: a larger wavelength gives more room to errors. To give a simple example, a constant bias of 1 meter on P_{L2} would have an influence on c_{EWL} of 0.087 cycles for GPS and 0.051 cycles for Galileo, and an influence on c_{WL} of 0.508 cycles for GPS and 0.532 cycles for Galileo (see equations (4.62),(4.64)). Therefore, the resolution of EWL ambiguities will be easier for Galileo than for GPS. Moreover, the EWL

Table 4.11 *– Maximum value of the residual term of the widelane-narrowlane combination making it possible to resolve the EWL, WL and ML ambiguities for GPS and Galileo.*

LC	$\frac{\lambda_{wl,km}}{2}$ [m]	
	GPS	Galileo
EWLNL	2.930	4.884
WLNL	0.431	0.407
MLNL	0.376	0.376

ambiguity resolution will be much easier than the WL and ML ambiguity resolution, for both GPS and Galileo systems.

We will now assess the magnitude of the residual term of the widelane-narrowlane combination to see whether or not it is possible to resolve the widelane ambiguities.

In a first step, we consider the influence of measurement noise, multipath delays and hardware delays for all possible cases, i.e. all satellite–receiver–day configurations. This will determine the feasibility of real time ambiguity resolution. For that purpose, we will make several assumptions regarding the distribution of the three types of error. It has to be stressed that we will discuss all these assumptions through chapters 5 and 6. We will put a special emphasis on showing that, even if they cannot be verified, this does not influence the feasibility of the ambiguity resolution.

- As aforementioned in section 2.2.2.11, we assume that code and phase measurement noise are white Gaussian, i.e. that they have a normal distribution with a zero-mean. We assume the standard deviation values from table 2.8. It can be easily justified to assume that code and phase measurement noise follow a normal distribution with a zero-mean [115]. Moreover, since the standard deviation values of measurement noise are retrieved from real GNSS measurements [27, 28, 121, 123], the magnitude of the code and phase measurements noise can be considered as realistic. The standard deviation of code measurement noise for GPS L1/L2 is 25 cm, whereas it is 7 cm for the new L5 signal. The standard deviation of code measurement noise for Galileo L1 is higher (18 cm) than on L2/L5 (5 cm). As far as phase measurement noise is concerned, its standard deviation is smaller than 1 mm for all GPS and Galileo signals.

- Similarly to measurement noise, the code and phase multipath delays will be considered white Gaussian with the standard deviation values from table 2.7. As explained in section 2.2.2.7, the white Gaussian behavior may not be always true for code multipath delays. Nevertheless, over a sufficiently long period, the mean value of code multipath delays becomes low [115]. Since we will make use of a running average filter for combinations which include code measurements, the zero-mean of code multipath delays is a realistic hypothesis in this study. Moreover, since the standard deviation values are partially retrieved from real GNSS measurements, they can be considered as realistic.

- Regarding section 2.2.2.9, the satellite and receiver code and phase hardware delays can generally be assumed as constant in time. Over a satellite pass, they have to be considered as systematic errors. However, when studying all possible cases (satellite–receiver–

day configurations), we may consider hardware delays as random errors. It would probably be better adapted to assume that each type (satellite/receiver, code/phase) of hardware delays follows an uniform distribution on a given interval $[-a, a]$, which means that all values from $-a$ to a have a constant probability. However, assuming that they follow a Gaussian distribution gives nearly the same results* and allows us to apply the law of error propagation. We will assume that 99 % of hardware delays values are below a given threshold, corresponding to a†.

We know that it is possible to obtain an estimation of the undifferenced satellite code hardware delays by the means of T_{GD} or satellite Differential Code Biases (DCB) (see equations (2.48) and (2.43)), which are related to each other by a linear relationship. However, even if receiver DCB values are also available, their relation to the undifferenced receiver code hardware delays is not known. Moreover, the calibration of these undifferenced delays is not straightforward [8]. In a first step, to assess the feasability of the ambiguity resolution, we make the assumption that the magnitude of each type of code hardware delays (satellite and receiver) is smaller than 3 meters. This assumption might not be verified in some cases (see section 6.6). Nevertheless, it is already worth noticing that we will develop a method allowing to calibrate the sum of the satellite and receiver code hardware delays at the decimetric level (see section 4.5). This will enhance the ambiguity resolution process, in the sense that the resolution of widelane ambiguities will not limited anymore by the eventual large code hardware delays.

As far as phase hardware delays are concerned, research aiming at their calibration is ongoing (see section 2.2.2.9). In a first step, we make the assumption that the magnitude of each type of phase hardware delays (satellite and receiver) is smaller than 1 millimeter. Even if this assumption might not be verified, it would only be critical for the resolution of the original ambiguities, but not of the widelane ambiguities. We refer to section 4.4.2.4 for a more extended discussion.

Finally, taking the previous considerations into account, we can thus write:

- $|d^i_{g,k}|$ and $|d_{p,g,k}| < 3$ m (code)
- $|d^i_{\Phi,k}|$ and $|d_{p,\Phi,k}| < 1$ mm (phase)

Considering these assumptions, we can apply the law of error propagation as in section 4.2.3 to estimate the influence of the residual term on the resolution of the widelane ambiguities. We will give the influence of each type of error separately, and then add them up.

Using equation (4.57), the variance of the widelane combination due to code and phase measurement noise $\sigma^2_{\varepsilon_{wl,km}}\left[\text{cycles}^2\right]$ is given by:

$$\sigma^2_{\varepsilon_{wl,km}} = \frac{f_k^2}{c^2}\,\sigma^2_{\varepsilon_{\Phi,k}} + \frac{f_m^2}{c^2}\,\sigma^2_{\varepsilon_{\Phi,m}} + \frac{f_{km}^2 f_k^2}{c^2}\,\sigma^2_{\varepsilon_{g,k}} + \frac{f_{km}^2 f_m^2}{c^2}\,\sigma^2_{\varepsilon_{g,m}} \tag{4.70}$$

Similarly, the variance of the widelane-narrowlane combination due to code and phase multipath delays $\sigma^2_{M_{wl,km}}\left[\text{cycles}^2\right]$ is given by:

$$\sigma^2_{M_{wl,km}} = \frac{f_k^2}{c^2}\,\sigma^2_{M_{\Phi,k}} + \frac{f_m^2}{c^2}\,\sigma^2_{M_{\Phi,m}} + \frac{f_{km}^2 f_k^2}{c^2}\,\sigma^2_{M_{g,k}} + \frac{f_{km}^2 f_m^2}{c^2}\,\sigma^2_{M_{g,m}} \tag{4.71}$$

*This can be justified by the Central Limit Theorem.

†Instead of considering $U(-a, a)$, we will consider $N(0, a/2.58)$.

In our approach, it is also useful to group the influence of multipath delays and measurement noise in $\sigma^2_{E_{wl,km}}$ $\left[\text{cycles}^2\right]$:

$$\sigma^2_{E_{wl,km}} = \sigma^2_{\varepsilon_{wl,km}} + \sigma^2_{M_{wl,km}} \tag{4.72}$$

The variance of the widelane-narrowlane combination due to satellite and receiver hardware delays $\sigma^2_{d_{wl,km}}$ $\left[\text{cycles}^2\right]$ is given by:

$$\sigma^2_{d_{wl,km}} = 2\left(\frac{f_k^2}{c^2}\,\sigma^2_{d_{\Phi,k}} + \frac{f_m^2}{c^2}\,\sigma^2_{d_{\Phi,m}} + \frac{f_{km}^2\, f_k^2}{c^2}\,\sigma^2_{d_{g,k}} + \frac{f_{km}^2\, f_m^2}{c^2}\,\sigma^2_{d_{g,m}}\right) \tag{4.73}$$

The factor "2" accounts for satellite and receiver hardware delays together.
Finally, the variance of the widelane-narrowlane combination due to the total residual term $\sigma^2_{T_{wl,km}}$ $\left[\text{cycles}^2\right]$, i.e. including measurement noise, multipath and hardware delays, is given by:

$$\sigma^2_{T_{wl,km}} = \sigma^2_{\varepsilon_{wl,km}} + \sigma^2_{M_{wl,km}} + \sigma^2_{d_{wl,km}} \tag{4.74}$$

Considering the standard deviation of code/phase multipath delays, measurement noise and hardware delays and using equations (4.70) to (4.74), we have computed the standard deviation of the EWLNL, WLNL and MLNL combination, for each type of error (noise, multipath, hardware), for combined noise and multipath and for all errors together. The results are given in table 4.12 and table 4.13, respectively for GPS and Galileo. Because of the magnitude of code hardware delays, σ_d is at least three times more important that σ_E and is thus the dominant part of σ_T. Moreover, thanks to the larger wavelength σ_T is one order of magnitude smaller for the EWLNL than for the WLNL and MLNL combinations. For the same reasons, σ_T is twice larger for GPS than for Galileo.

Table 4.12 *– Standard deviation of the GPS widelane-narrowlane combinations* [cycles] *due to measurement noise (σ_ε), multipath delays (σ_M), noise/multipath (σ_E), hardware delays (σ_d) and all errors together (σ_T).*

LC	σ_ε	σ_M	σ_E	σ_d	σ_T
EWLNL	0.023	0.057	0.062	0.198	0.208
WLNL	0.207	0.496	0.538	1.359	1.462
MLNL	0.195	0.471	0.510	1.564	1.645

Table 4.13 *– Standard deviation of the Galileo widelane-narrowlane combinations* [cycles] *due to measurement noise (σ_ε), multipath delays (σ_M), noise/multipath (σ_E), hardware delays (σ_d) and all errors together (σ_T).*

LC	σ_ε	σ_M	σ_E	σ_d	σ_T
EWLNL	0.005	0.022	0.023	0.119	0.121
WLNL	0.128	0.298	0.325	1.441	1.477
MLNL	0.140	0.325	0.355	1.564	1.603

Finally, considering their standard deviation due to the total residual term (σ_T), and taking a 99 % level of confidence ($2.58\,\sigma_T$), the widelane-narrowlane combinations (c_{EWL}, c_{WL}, c_{ML})

allow us to obtain, respectively for GPS (left) and Galileo (right):

$$N_{EWL} \pm 0.54/0.31 \tag{4.75}$$
$$N_{WL} \pm 3.77/3.81 \tag{4.76}$$
$$N_{ML} \pm 4.24/4.14 \tag{4.77}$$

This means that in these conditions, we are able to resolve the EWL ambiguities in real time for Galileo, whereas for GPS it might be problematic. However, it is not possible to resolve either the WL or ML ambiguities, for neither GNSS system.

In a second step, we consider the influence of measurement noise, multipath delays and hardware delays on a whole period for all possible satellite-receiver-day configurations. Since the ambiguity remains constant over a satellite pass – as long as there is no cycle slip –, the widelane-narrowlane combination $c_{wl,km}$ can be averaged over time to resolve the widelane ambiguities on a longer period. This smoothing can be done by applying a running average filter [15, 16, 41]. If x_t is the combined observation ($x_t = c_{wl,km}$) at an epoch t, the running mean of x_t is given by:

$$\langle x_t \rangle = \langle x_{t-1} \rangle + \frac{1}{t} \left(x_t - \langle x_{t-1} \rangle \right) \tag{4.78}$$

Considering the previous assumptions, multipath delays and measurement noise average down to zero after this operation. This helps thus to obtain an increasingly precise value of the widelane ambiguities. Nevertheless, as hardware delays are considered to be constant over a satellite pass, their influence remains. Considering their standard deviation due to satellite and receiver hardware delays (σ_d), applying a running average on the widelane-narrowlane combinations (c_{EWL}, c_{WL}, c_{ML}) allows us to obtain for GPS (left) and Galileo (right) (99 % level of confidence):

$$N_{EWL} \pm 0.51/0.30 \tag{4.79}$$
$$N_{WL} \pm 3.51/3.71 \tag{4.80}$$
$$N_{ML} \pm 4.03/4.03 \tag{4.81}$$

We can see that the increase of precision is not sufficient to be able to resolve the WL or the ML ambiguities. Moreover, for the EWL case, the improvement given by the smoothing is negligible. This can be explained by the fact that the residual term is mainly driven by hardware delays, and especially code hardware delays, while the influence of code multipath delays and code measurement noise is negligible. Therefore there is no real benefit to using the running average filter here.

By rounding c_{EWL}, c_{WL}, c_{ML}, or their average filter, to their nearest integer values, we obtain:

- the correct integer values of the EWL ambiguities (N_{EWL}) for Galileo. For GPS the EWL ambiguity resolution could fail depending on the magnitude of code hardware delays.
- the approximated integer values of the WL and ML ambiguities (GPS and Galileo), denoted as $\widetilde{N}_{WL}$ and $\widetilde{N}_{ML}$. The accuracy of this approximation depends on the magnitude of the code hardware delays (see section 6.6).

4.3.1.2 Differenced widelane combinations

Principles

As it is not possible to resolve the WL or ML ambiguities by using widelane-narrowlane combinations, we have investigated another possibility to resolve the WL or ML ambiguities. As EWL ambiguities (N_{EWL}) are resolved, we can subtract them from the extra-widelane combination (φ_{EWL}) and then subtract the result from the widelane combination (φ_{WL}) to obtain the differenced widelane (DWL) combination φ_{DWL} [cycles]:

$$\varphi_{DWL} = \varphi_{WL} - (\varphi_{EWL} - N_{EWL}) \frac{\lambda_{EWL}}{\lambda_{WL}} \tag{4.82}$$

This combination is used by [43] for DD cascaded ambiguity resolution. Alternatively, we could use the equivalent combination to resolve the ML ambiguities, namely the differenced middlelane (DML) combination φ_{DML} [cycles]:

$$\varphi_{DML} = \varphi_{ML} - (\varphi_{EWL} - N_{EWL}) \frac{\lambda_{EWL}}{\lambda_{ML}} \tag{4.83}$$

From now on, we will only consider the DWL combination. The use of the DML combination, and of the ML ambiguities in general, will be considered in appendix A.

The first term of the right-hand side of equation (4.82) contains the WL ambiguity, while its second term is unambiguous. Equation (4.82) can be rearranged to identify the α, β, γ coefficients of the combination:

$$\begin{aligned} \varphi_{DWL} &= \varphi_{\mathrm{L1}} - \left(\frac{\lambda_{EWL}}{\lambda_{WL}} + 1 \right) \varphi_{\mathrm{L2}} + \frac{\lambda_{EWL}}{\lambda_{WL}} \left(\varphi_{\mathrm{L5}} + N_{EWL} \right) && (4.84) \\ &= \alpha\, \varphi_{\mathrm{L1}} + \beta\, \varphi_{\mathrm{L2}} + \gamma\, \varphi_{\mathrm{L5}} + \gamma\, N_{EWL} && (4.85) \end{aligned}$$

It can be demonstrated that this combination is GF but *not* IF, so that equation (4.82) can be developed as:

$$\begin{aligned} \varphi_{DWL} = {} & N_{WL} \\ & + \frac{f_{\mathrm{L1}}}{c} \left(d^i_{\Phi,\mathrm{L1}} + d_{p,\Phi,\mathrm{L1}} + M^i_{p,\Phi,\mathrm{L1}} + \varepsilon^i_{p,\Phi,\mathrm{L1}} - I_{\mathrm{L1}} \right) \\ & + \frac{f_{\mathrm{L2}}}{c} \beta \left(d^i_{\Phi,\mathrm{L2}} + d_{p,\Phi,\mathrm{L2}} + M^i_{p,\Phi,\mathrm{L2}} + \varepsilon^i_{p,\Phi,\mathrm{L2}} - I_{\mathrm{L2}} \right) \\ & + \frac{f_{\mathrm{L5}}}{c} \gamma \left(d^i_{\Phi,\mathrm{L5}} + d_{p,\Phi,\mathrm{L5}} + M^i_{p,\Phi,\mathrm{L5}} + \varepsilon^i_{p,\Phi,\mathrm{L5}} - I_{\mathrm{L5}} \right) \end{aligned} \tag{4.86}$$

The ionospheric delay of the combination can be derived by using equation (4.36), so that equation (4.86) becomes:

$$\begin{aligned} \varphi_{DWL} = {} & N_{WL} \\ & + \frac{f_{\mathrm{L1}}}{c} \left(d^i_{\Phi,\mathrm{L1}} + d_{p,\Phi,\mathrm{L1}} + M^i_{p,\Phi,\mathrm{L1}} + \varepsilon^i_{p,\Phi,\mathrm{L1}} \right) \\ & + \frac{f_{\mathrm{L2}}}{c} \beta \left(d^i_{\Phi,\mathrm{L2}} + d_{p,\Phi,\mathrm{L2}} + M^i_{p,\Phi,\mathrm{L2}} + \varepsilon^i_{p,\Phi,\mathrm{L2}} \right) \\ & + \frac{f_{\mathrm{L5}}}{c} \gamma \left(d^i_{\Phi,\mathrm{L5}} + d_{p,\Phi,\mathrm{L5}} + M^i_{p,\Phi,\mathrm{L5}} + \varepsilon^i_{p,\Phi,\mathrm{L5}} \right) \\ & - \frac{f_{\mathrm{L1}}}{c} I_{\mathrm{L1}} \left(\alpha + \beta \frac{f_{\mathrm{L1}}}{f_{\mathrm{L2}}} + \gamma \frac{f_{\mathrm{L1}}}{f_{\mathrm{L5}}} \right) \end{aligned} \tag{4.87}$$

If the non-ambiguity term (residual term) is divided into two parts: the phase delays $\Delta\varphi_{DWL}$ [cycles] (noise, multipath, hardware) and the ionospheric delays $I_{\varphi_{DWL}}$ [cycles], equation (4.87) becomes:

$$\varphi_{DWL} = N_{WL} + \Delta\varphi_{DWL} + I_{\varphi_{DWL}} \tag{4.88}$$

From equation (4.87), it comes that this combination depends on the WL ambiguity, satellite and receiver phase hardware delays, phase multipath delays, phase measurement noise and on the ionospheric delays.

Resolution

We will now assess the magnitude of the residual term to see whether or not it is possible to resolve the WL ambiguities, which is the case if the following condition (in cycles) is fulfilled:

$$|\Delta\varphi_{DWL} + I_{\varphi_{DWL}}| < 0.5 \tag{4.89}$$

We begin with the phase delays of the DWL residual term ($\Delta\varphi_{DWL}$). To assess the magnitude of $\Delta\varphi_{DWL}$, we can use the same approach as previously to compute the standard deviation of the DWL combination for each type of error (noise, multipath, hardware), for combined noise and multipath and for all errors together. The results are given in table 4.14, respectively for GPS and Galileo. As they are only phase delays (contrary to the widelane-narrowlane case), the influence of hardware delays (σ_d) is one order of magnitude smaller than the influence of combined noise and multipath (σ_E). We can see that here GPS has the advantage thanks to the smaller $\lambda_{EWL}/\lambda_{WL}$ ratio (12 versus 6.8). Considering its standard de-

Table 4.14 *– Standard deviation of the GPS and Galileo DWL combination* [cycles] *due to measurement noise (σ_ε), multipath delays (σ_M), noise/multipath (σ_E), hardware delays (σ_d) and all errors together (σ_T).*

System	LC	σ_ε	σ_M	σ_E	σ_d	σ_T
GPS	φ_{DWL}	0.029	0.126	0.129	0.023	0.131
Galileo	φ_{DWL}	0.049	0.212	0.217	0.039	0.220

viation due to phase delays (σ_T) and taking a 99 % level of confidence, the DWL combination (φ_{DWL}) allows us to obtain, respectively for GPS (left) and Galileo (right):

$$N_{WL} \pm 0.34/0.57 \tag{4.90}$$

Thus, even without the influence of ionospheric delays, this is close to 0.5 cycle for GPS and greater than 0.5 cycle for Galileo. Nevertheless, we can apply a running average filter by using equation (4.78) with $x = \varphi_{DWL}$. As the residual term $\Delta\varphi_{DWL}$ is dominated by noise and multipath delays, this operation will strongly reduce its magnitude (phase multipath delays and phase measurement noise average down to zero). Considering its standard deviation due to phase hardware delays (σ_d), applying a running average on the DWL combination (φ_{DWL}) allows us to obtain for GPS (left) and Galileo (right) (99 % level of confidence):

$$N_{WL} \pm 0.06/0.10 \tag{4.91}$$

It shows that it would have been possible to resolve the WL ambiguities if there was no influence of the ionospheric delays.

The ionospheric delays of the DWL residual term ($I_{\varphi_{DWL}}$) are given in equation (4.87):

$$I_{\varphi_{DWL}} = \kappa_1 \cdot I_{\mathrm{L1}} = \kappa_2 \cdot \mathrm{TEC} \tag{4.92}$$

where
κ_1 [cycles/m] $= -0.5049$ (GPS)/ -0.5437 (Galileo)
κ_2 [cycles/TECU] $= -0.0819$ (GPS)/ -0.0882 (Galileo)

Thus, without taking the influence of $\Delta\varphi_{DWL}$, it can clearly exceed 0.5 cycle: the residual term already reaches 0.5 cycle when the TEC is equal or greater than 6.1 TECU for GPS and 5.6 TECU for Galileo. This means that the DWL combination does not make the resolution of the WL ambiguities possible, unless TEC values are very low.

Nevertheless, we could use an estimation of TEC to resolve the WL ambiguities. As a matter of fact, if we manage to estimate $I_{\varphi_{DWL}}$ accurately enough, the total residual term will be smaller than 0.5 cycle. For that purpose, we can compute "GIM-levelled" calibrated TEC values ($\mathrm{TEC}_{l,GIM}$) by using the carrier-to-GIM levelling process described in section 3.2.3.4. That gives us an estimation of TEC values and therefore of $I_{\varphi_{DWL}}$, denoted as $\widetilde{I}_{\varphi_{DWL}}$:

$$\widetilde{I}_{\varphi_{DWL}} = \kappa_2 \cdot \mathrm{TEC}_{l,GIM} \tag{4.93}$$

By subtracting equation (4.93) from equation (4.88) and taking into account the error on the $\mathrm{TEC}_{l,GIM}$ values (see equation (3.76)), we obtain the DWL combination with the ionospheric delays corrected, i.e. $\varphi_{DWL,c}$ [cycles]

$$\begin{aligned} \varphi_{DWL,c} &= \varphi_{DWL} - \kappa_2 \cdot \mathrm{TEC}_{l,GIM} && (4.94)\\ &= N_{WL} + \Delta\varphi_{DWL} + \Delta I_{\varphi_{DWL}} && (4.95) \end{aligned}$$

where

$$\Delta I_{\varphi_{DWL}} = \kappa_2 \left(\Delta\mathrm{TEC}_{l,GIM} + \Delta\mathrm{TEC}_{l,GIM,model} + E_{l,GIM}\right) \tag{4.96}$$

From previous considerations, it is obvious that we need to apply the running average filter to reduce the influence of $\Delta\varphi_{DWL}$. Equation (4.95) thus becomes:

$$\begin{aligned} \langle\varphi_{DWL,c}\rangle &= N_{WL} + \langle\Delta\varphi_{DWL} + \Delta I_{\varphi_{DWL}}\rangle && (4.97)\\ & && (4.98) \end{aligned}$$

Now the WL can be resolved if the following condition (in cycles) is fulfilled:

$$|\langle\Delta\varphi_{DWL} + \Delta I_{\varphi_{DWL}}\rangle| < 0.5 \tag{4.99}$$

The influence of $\langle\Delta\varphi_{DWL}\rangle$ has been assessed previously. At a 99 % level of confidence, it reaches $\pm$ 0.06 and $\pm$ 0.10 cycles, respectively for GPS and Galileo. That means that, in the worse case, $\langle\Delta I_{\varphi_{DWL}}\rangle$ has to be smaller than 0.4 cycle. Using equation (4.96), this corresponds to an error of about 5 TECU on $\mathrm{TEC}_{l,GIM}$. As stated in section 3.2.3.4, the accuracy of "GIM-levelled" calibrated TEC values is comparable to the accuracy of Global Ionospheric Maps (GIMs). Therefore, regarding their performance discussed in section 3.2.3.3, an accuracy of 5 TECU should be achievable, especially for mid-latitude regions in a period of low solar activity (low TEC values). Nevertheless, for mid-latitudes regions in a period of higher solar activity or for low-latitudes regions in general, an accuracy of 5 TECU might not be achieved. In such conditions, we might thus need a more accuracte estimation of TEC, otherwise the resolution of the WL might not be possible.

Finally, by rounding the average filter of φ_{DWL} – with the ionospheric delays corrected – to their nearest integer values, we obtain the correct values of the WL ambiguities, namely N_{WL}.

This approach constitutes the *a priori* resolution of the WL ambiguities. In appendix B, we explain how the dual frequency estimation of TEC can be used *a posteriori* to resolve the WL ambiguities.

4.3.2 Triple frequency phase multipath combination

4.3.2.1 Principles

The availability of triple frequency phase measurements offers the possibility to form GF and IF combinations of phase measurements, and in particular the triple frequency phase multipath combination $\Phi^3_{M,125}$ $\left[\mathrm{m}^3\right]$ [111]:

$$\Phi^3_{M,125} = \lambda^2_{\mathrm{L5}}\left(\Phi_{\mathrm{L1}} - \Phi_{\mathrm{L2}}\right) + \lambda^2_{\mathrm{L2}}\left(\Phi_{\mathrm{L5}} - \Phi_{\mathrm{L1}}\right) + \lambda^2_{\mathrm{L1}}\left(\Phi_{\mathrm{L2}} - \Phi_{\mathrm{L5}}\right) \tag{4.100}$$

$$= \left(\lambda^2_{\mathrm{L5}} - \lambda^2_{\mathrm{L2}}\right)\Phi_{\mathrm{L1}} + \left(\lambda^2_{\mathrm{L1}} - \lambda^2_{\mathrm{L5}}\right)\Phi_{\mathrm{L2}} + \left(\lambda^2_{\mathrm{L2}} - \lambda^2_{\mathrm{L1}}\right)\Phi_{\mathrm{L5}} \tag{4.101}$$

This combination – which is a generalization of the dual frequency GF phase combination – is formed by using the following principles. First it combines the three dual frequency GF phase combinations $\Phi_{GF,km} = \Phi^i_{p,m} - \Phi^i_{p,k}$, in such a way that each phase measurement appears once with the $+$ sign, once with the $-$ sign:

$$\left(\Phi_{\mathrm{L1}} - \Phi_{\mathrm{L2}}\right) + \left(\Phi_{\mathrm{L5}} - \Phi_{\mathrm{L1}}\right) + \left(\Phi_{\mathrm{L2}} - \Phi_{\mathrm{L5}}\right) \tag{4.102}$$

Each term – i.e. each GF combination – of equation (4.102) contains an ionospheric term $I_{\Phi_{GF,km}}$ [m] which is given by equation (3.52) and equals:

$$I_{\Phi_{GF,km}} = 40.3 \cdot 10^{16} \cdot \left(\frac{1}{f_k^2} - \frac{1}{f_m^2}\right) \mathrm{TEC} \tag{4.103}$$

This term is inversely proportional to $f_k^2 \cdot f_m^2$. Therefore, if we multiply each term of equation (4.102) by the third wavelength component ($\lambda_n^2 = c/f_n^2$), we obtain the triple frequency phase multipath combination of equation (4.100). Its ionospheric term $I_{\Phi_{M,125}}$ [m] can be developed as:

$$I_{\Phi_{M,125}} = 40.3 \cdot 10^{16} \cdot \mathrm{TEC} \cdot c \cdot \left(\frac{f^2_{\mathrm{L1}} - f^2_{\mathrm{L2}} + f^2_{\mathrm{L5}} - f^2_{\mathrm{L1}} + f^2_{\mathrm{L2}} - f^2_{\mathrm{L5}}}{f^2_{\mathrm{L1}}\, f^2_{\mathrm{L2}}\, f^2_{\mathrm{L5}}}\right) = 0 \tag{4.104}$$

This proves that the triple frequency phase multipath combination is IF. As it constitutes a linear combination of three GF combinations, this combination is obviously also GF.

For more convenience, we will normalize triple frequency phase multipath combination to unit of meters. For that purpose, we rearrange the terms of equation (4.100) to obtain equation (4.101), and then we divide equation (4.101) by $\left(\lambda^2_{\mathrm{L2}} - \lambda^2_{\mathrm{L1}}\right)$ [114] to obtain the triple frequency phase multipath combination $\Phi_{M,125}$ [m]:

$$\Phi_{M,125} = \frac{\left(\lambda^2_{\mathrm{L5}} - \lambda^2_{\mathrm{L2}}\right)}{\left(\lambda^2_{\mathrm{L2}} - \lambda^2_{\mathrm{L1}}\right)}\Phi_{\mathrm{L1}} + \frac{\left(\lambda^2_{\mathrm{L1}} - \lambda^2_{\mathrm{L5}}\right)}{\left(\lambda^2_{\mathrm{L2}} - \lambda^2_{\mathrm{L1}}\right)}\Phi_{\mathrm{L2}} + \Phi_{\mathrm{L5}} \tag{4.105}$$

$$= d\,\Phi_{\mathrm{L1}} + e\,\Phi_{\mathrm{L2}} + f\,\Phi_{\mathrm{L5}} \tag{4.106}$$

The coefficients of this combination are :

$$d = 0.226 \quad e = -1.226 \quad f = 1 \quad \text{(GPS)}$$
$$d = 0.128 \quad e = -1.128 \quad f = 1 \quad \text{(Galileo)}$$

Due to the proximity of L2 and L5 frequencies, the d coefficient is one order of magnitude smaller than the e and f coefficients. The combination is thus dominated by L2 and L5 signals.

As it constitutes a linear combination of $\Phi^3_{M,125}$, the $\Phi_{M,125}$ combination is also GF and IF. It means that equation (4.105) satisfies the GF condition ($d + e + f = 0$) and the IF condition given by equation (4.38). Equation (4.106) can therefore be developed as:

$$\begin{aligned} \Phi_{M,125} \quad = \quad & d\left(d^i_{\Phi,\mathrm{L1}} + d_{p,\Phi,\mathrm{L1}} + M^i_{p,\Phi,\mathrm{L1}} + \varepsilon^i_{p,\Phi,\mathrm{L1}}\right) \\ & + e\left(d^i_{\Phi,\mathrm{L2}} + d_{p,\Phi,\mathrm{L2}} + M^i_{p,\Phi,\mathrm{L2}} + \varepsilon^i_{p,\Phi,\mathrm{L2}}\right) \\ & + f\left(d^i_{\Phi,\mathrm{L5}} + d_{p,\Phi,\mathrm{L5}} + M^i_{p,\Phi,\mathrm{L5}} + \varepsilon^i_{p,\Phi,\mathrm{L5}}\right) \\ & - d\,\lambda_{\mathrm{L1}}\,N_{\mathrm{L1}} - e\,\lambda_{\mathrm{L2}}\,N_{\mathrm{L2}} - f\,\lambda_{\mathrm{L5}}\,N_{\mathrm{L5}} \end{aligned} \tag{4.107}$$

If the non-ambiguity term is defined as the residual term $\Delta\,\Phi_{M,125}$ [cycles], equation (4.107) becomes:

$$\Phi_{M,125} = -d\,\lambda_{\mathrm{L1}}\,N_{\mathrm{L1}} - e\,\lambda_{\mathrm{L2}}\,N_{\mathrm{L2}} - f\,\lambda_{\mathrm{L5}}\,N_{\mathrm{L5}} + \Delta\,\Phi_{M,125} \tag{4.108}$$

From equation (4.107), it follows that this combination only depends on the ambiguity of the combined observation, satellite and receiver phase hardware delays, phase multipath delays and phase measurement noise. As the combination is dominated by L2 and L5 signals, the contribution of L2 and L5 delays is prominent in the residual term.

This combination can be used to improve the mitigation of phase multipath delays as well as to improve multi-frequency ambiguity resolution algorithms [111]. In our approach, this combination is used directly after the widelane ambiguity resolution to resolve the original ambiguities N_{L1} , N_{L2} , N_{L5}. This can be achieved by substituting the EWL ambiguities N_{EWL} and WL ambiguities N_{WL} in the triple frequency phase multipath combination of equation (4.108), so that only one ambiguity parameter (N_{L2}) remains unknown. As a matter of fact, substituting N_{EWL} and N_{WL} from equations (4.30) and (4.31) in equation (4.108) gives:

$$\Phi_{M,125} = -d\,\lambda_{\mathrm{L1}}\,(N_{\mathrm{L2}} - N_{WL}) - e\,\lambda_{\mathrm{L2}}\,N_{\mathrm{L2}} - f\,\lambda_{\mathrm{L5}}\,(N_{EWL} + N_{\mathrm{L2}}) + \Delta\,\Phi_{M,125} \tag{4.109}$$

After rearranging equation (4.109) we can isolate N_{L2} [cycles]:

$$N_{\mathrm{L2}} \quad = \quad \frac{\Phi_{M,125} - d\,\lambda_{\mathrm{L1}}\,N_{WL} + f\,\lambda_{\mathrm{L5}}\,N_{EWL} - \Delta\,\Phi_{M,125}}{-\,(d\,\lambda_{\mathrm{L1}} + e\,\lambda_{\mathrm{L2}} + f\,\lambda_{\mathrm{L5}})} \tag{4.110}$$

$$\quad = \quad \frac{\Phi_{M,125} - d\,\lambda_{\mathrm{L1}}\,N_{WL} + f\,\lambda_{\mathrm{L5}}\,N_{EWL}}{-\,(d\,\lambda_{\mathrm{L1}} + e\,\lambda_{\mathrm{L2}} + f\,\lambda_{\mathrm{L5}})} + \Delta\,N_{\mathrm{L2}} \tag{4.111}$$

where $\Delta\,N_{\mathrm{L2}}$ is the influence residual term $\Delta\,\Phi_{M,125}$ on the N_{L2} ambiguities. Its expression can be derived from equations (4.107) and (4.108). We can thus write:

$$\begin{aligned} \Delta\,N_{\mathrm{L2}} \quad = \quad & d'\left(d^i_{\Phi,\mathrm{L1}} + d_{p,\Phi,\mathrm{L1}} + M^i_{p,\Phi,\mathrm{L1}} + \varepsilon^i_{p,\Phi,\mathrm{L1}}\right) \\ & + e'\left(d^i_{\Phi,\mathrm{L2}} + d_{p,\Phi,\mathrm{L2}} + M^i_{p,\Phi,\mathrm{L2}} + \varepsilon^i_{p,\Phi,\mathrm{L2}}\right) \\ & + f'\left(d^i_{\Phi,\mathrm{L5}} + d_{p,\Phi,\mathrm{L5}} + M^i_{p,\Phi,\mathrm{L5}} + \varepsilon^i_{p,\Phi,\mathrm{L5}}\right) \end{aligned} \tag{4.112}$$

The $d^{'}, e^{'}, f^{'}$ $\left[\mathrm{m}^{-1}\right]$ coefficients are equal to the d, e, f coefficients divided by the denominator of equation (4.110):

$$d^{'} = -143.42 \quad e^{'} = 777.54 \quad f^{'} = -634.11 \quad \text{(GPS)}$$
$$d^{'} = -134.30 \quad e^{'} = 1183.44 \quad f^{'} = -1049.14 \quad \text{(Galileo)}$$

4.3.2.2 Resolution

Following the same approach as in section 4.3.1.1, we will assess the magnitude of the residual term of the triple frequency phase multipath combination ($\Delta\,\Phi_{M,125}$), and more particularly its influence on the resolution of N_{L2} ambiguities ($\Delta\,N_{\mathrm{L2}}$). We have computed the standard deviation of $\Phi_{M,125}$ (in units of meters) for each type of error (noise, multipath, hardware), for combined noise and multipath and for all errors together and then divided them by the denominator of equation (4.110) to obtain the effect on N_{L2} in units of cycles ($\Delta\,N_{\mathrm{L2}}$). The results are given in table 4.15. At 99 % level of confidence ($2.58\,\sigma_T$), $\Delta\,N_{\mathrm{L2}}$ reaches more than 8 cycles for GPS and almost 13 cycles for Galileo. Regarding equation (4.125), this does not allow us to reconstruct TEC with a sufficient accuracy (see section 4.4.2).

Table 4.15 *– Standard deviation of the GPS and Galileo triple frequency phase multipath combination* [m] *and influence on the derived* N_{L2} *ambiguities* [cycles] *due to measurement noise* (σ_ε)*, multipath delays* (σ_M)*, noise/multipath* (σ_E)*, hardware delays* (σ_d) *and all errors together* (σ_T)*.*

System	LC	σ_ε	σ_M	σ_E	σ_d	σ_T
GPS	$\Phi_{M,125}$	0.0011	0.0048	0.0049	0.0008	0.0050
	N_{L2}	0.71	3.04	3.12	0.55	3.17
Galileo	$\Phi_{M,125}$	0.0010	0.0045	0.0049	0.0008	0.0047
	N_{L2}	1.11	4.76	4.89	0.87	4.97

Nevertheless, as for the DWL combination σ_E (noise + multipath) is one order of magnitude more important than σ_d (hardware delays), we would benefit from averaging the combination on a whole satellite pass. If we apply a running average filter given by equation (4.78) on $\Phi_{M,125}$, equation (4.110) becomes:

$$N_{\mathrm{L2}} = \frac{\langle\Phi_{M,125}\rangle - d\,\lambda_{\mathrm{L1}}\,N_{WL} + f\,\lambda_{\mathrm{L5}}\,N_{EWL}}{-\left(d\,\lambda_{\mathrm{L1}} + e\,\lambda_{\mathrm{L2}} + f\,\lambda_{\mathrm{L5}}\right)} + \langle\Delta\,N_{\mathrm{L2}}\rangle \tag{4.113}$$

where $\langle\Phi_{M,125}\rangle$ is the recursive mean of $\Phi_{M,125}$

In those conditions, the residual term averages to $\langle\Delta\,N_{\mathrm{L2}}\rangle$. Considering our assumptions, phase multipath delays and phase measurement noise average down to zero. This helps to obtain an increasingly precise value of the ambiguities, with an improvement of one order of magnitude in comparison with the procedure without average filtering (see σ_d versus σ_T). Taking a 99 % level of confidence we obtain, respectively for GPS (left) and Galileo (right):

$$N_{\mathrm{L2}} \pm 1.43/2.25 \tag{4.114}$$

Finally, by rounding the values obtained with equation (4.113) to their nearest integer, we obtain approximated integer values of N_{L2} ambiguities, namely $\widetilde{N}_{\mathrm{L2}}$. The accuracy of this

approximation depends on the magnitude of the phase hardware delays. The influence of this error on the reconstructed TEC values will be considered in section 4.4.2.

4.3.3 Summary

The results of the ambiguity resolution process can be summarized as follows*:

1. The EWLNL combination c_{EWL} makes it possible to resolve the EWL ambiguities N_{EWL} in real time for Galileo. For GPS however, the EWL ambiguity resolution could fail, depending mainly on the magnitude of code hardware delays.
2. The WLNL (MLNL) combination c_{WL} (c_{ML}) does not allow us to resolve the WL (ML) ambiguities N_{WL} (N_{ML}) due to the influence of code hardware delays.
3. The DWL combination φ_{DWL} makes the resolution of WL ambiguities possible if a dual frequency estimation of TEC is used.
4. By substituting the EWL and WL ambiguities in the triple frequency phase multipath combination ($\Phi_{M,125}$), we obtain approximated values of the N_{L2} ambiguities. The accuracy of this approximation depends on the magnitude of the phase hardware delays.

4.4 TEC reconstruction

4.4.1 Principles

Regarding the summary given in section 4.3.3, the EWL (N_{EWL}) and WL (N_{WL}) ambiguities are resolved†, whereas only an approximation of N_{L2} is obtained. For more convenience, in this section we consider that the N_{L2} ambiguities are resolved. The influence of the error on N_{L2} on TEC will be studied in the section 4.4.2.4.

Considering that the ambiguities N_{EWL} , N_{WL} and N_{L2} are resolved, it is straightforward to obtain N_{L1} and N_{L5} by using equations (4.31) and (4.30). Once the original ambiguities are resolved, it is possible to reconstruct the GF ambiguities ($N_{GF,km}$) by using equation (3.58). For triple frequency GNSS, there are three possible GF ambiguities, which are computed as follows:

$$N_{GF,25} = -N_{\mathrm{L2}} + \frac{f_{\mathrm{L2}}}{f_{\mathrm{L5}}} N_{\mathrm{L5}} \tag{4.115}$$

$$N_{GF,12} = -N_{\mathrm{L1}} + \frac{f_{\mathrm{L1}}}{f_{\mathrm{L2}}} N_{\mathrm{L2}} \tag{4.116}$$

$$N_{GF,15} = -N_{\mathrm{L1}} + \frac{f_{\mathrm{L1}}}{f_{\mathrm{L5}}} N_{\mathrm{L5}} \tag{4.117}$$

*Unless mentioned, otherwise the statement is valid for both GPS and Galileo systems.
†We have shown previously that it is at least the case for Galileo.

Since we have reconstructed the GF ambiguities ($N_{GF,km}$), we can add them to the GF phase combination ($\Phi_{GF,km}$) and divide by α_{km} to obtain TEC values (see equation (3.62)). The reconstructed TEC values TEC_r [TECU] are thus given by:

$$\text{TEC}_r = \frac{1}{\alpha_{km}} \left(\Phi_{GF,km} + \lambda_k \, N_{GF,km} \right) \tag{4.118}$$

$$= \text{TEC} + \frac{1}{\alpha_{km}} \left(IFB_{\Phi,km} + E_{\Phi,km} \right) \tag{4.119}$$

4.4.2 Precision and accuracy assessment

Equation (4.119) shows that the reconstructed TEC values are affected by satellite and receiver phase hardware delays or phase IFB ($IFB_{\Phi,km}$), phase multipath delays and phase measurement noise ($E_{\Phi,km}$). Besides, reconstructed TEC values are also affected by the error on the N_{L2} ambiguities. Additionally, the influence of uncorrected phase wind-up effect, uncorrected satellite and receiver antenna PCOs and PCVs and high-order ionospheric effects on the reconstructed TEC values have to be taken into account.

To assess the precision and accuracy of the reconstructed TEC values, we have thus to consider:

- the influence of uncorrected phase wind-up effect, satellite and receiver antenna PCOs and PCVs (see section 4.4.2.1),
- the influence of higher-order ionospheric terms (see section 4.4.2.2),
- the influence of phase IFB, multipath delays and measurement noise on the GF phase combination (see section 4.4.2.3),
- the influence of the error on the N_{L2} ambiguities on the GF ambiguities (see section 4.4.2.4).

All these effects will be considered in detail in the following sections.

4.4.2.1 Uncorrected effects

Phase wind-up

As stated in section 2.2.2.12, GNSS phase measurements are affected by the phase wind-up effect ω_p^i [cycles]. Since it has a non-negligible influence on undifferenced measurements, this effect needs to be corrected. The algorithm which is given by equations (2.63) to (2.66) allows us to obtain a correction of this effect at the cm-level accuracy [19]. Once the correction is computed, we subtract the phase wind-up effect from the phase measurements, following equations (2.70) and (2.71).

As the phase wind-up effect has an identical effect on each carrier wave frequency in cycles, the uncorrected (residual) phase wind-up effect does not depend on the carrier frequency. We can reasonably assume that the residual phase wind-up effect is 1 cm (i.e. 0.05 cycle) for

each frequency [19]. We will now have a thorough look into the TEC reconstruction steps to assess the influence of this residual effect.

- As the phase wind-up effect has an identical effect on each carrier wave frequency in cycles, it cancels out in the widelane combinations (see equation (4.48)), and therefore in the widelane-narrowlane combinations (see equation (4.52)) and differenced widelane combinations (see equations (4.82) and (4.83)). As a consequence, the widelane ambiguity resolution is not affected by the (residual) phase wind-up effect.

- In the triple frequency phase multipath combination the phase wind-up effect is $\omega_{\Phi_{M,125}}$ [m] (see equation (4.106)):

$$\omega_{\Phi_{M,125}} = \omega_p^i \ (d\,\lambda_{\mathrm{L1}} + e\,\lambda_{\mathrm{L2}} + f\,\lambda_{\mathrm{L5}}) \tag{4.120}$$

  Regarding equation (4.110), the phase wind-up effect on N_{L2} is thus equal to ω_p^i. Therefore, the residual phase wind-up effect has an influence of about 0.05 cycle on N_{L2}, N_{L5} and N_{L1}. As the influence of phase hardware delays cause an error of 1 or 2 cycles on the original ambiguities (see section 4.3.2.2), this additional effect does not have an influence on the final ambiguities. Therefore, we can consider that there is no additionnal error induced in the GF ambiguities.

- The phase wind-up effect in the GF phase combination is $\omega_{\Phi_{GF,km}}$ [cycles] (see equation (4.118)):

$$\omega_{\Phi_{GF,km}} = (\lambda_m - \lambda_k)\ \omega_p^i \tag{4.121}$$

  where $k, m \in \{\mathrm{L1}, \mathrm{L2}, \mathrm{L5}\}$

  By dividing equation (4.121) by α_{km} we find that the residual phase wind-up effect has an influence of about 0.025 TECU on the reconstructed TEC values whatever the combination of frequencies is used. This contribution has the same order of magnitude as the error caused by phase hardware delays ($IFB_{\Phi,km}$) and will be included in the $\Delta\,\mathrm{TEC}_r$ term (see section 4.4.2.3).

PCO and PCV

As stated in section 2.2.2.10, the position of the antenna instantaneous phase centers of the satellite and receiver (i.e. the point which the code and phase measurements refer to), are modeled by a consistent set of antenna PCOs and PCVs. For precise positioning applications, adequate corrections of these satellite and receiver antenna PCO and PCV need to be applied [7, 67]. Since the TEC reconstruction methodology presented here is a GF approach, we do not deal with positioning. Nevertheless, regarding their description given in section 2.2.2.10, the satellite antenna PCVs and the receiver antenna PCOs/PCVs are frequency-dependent effects and have thus an influence on TEC reconstruction. Therefore, these effects need to be corrected coherently with the International GNSS Service (IGS) conventions previously defined. We can reasonably assume that the code and phase measurements can be corrected at the cm-level accuracy [106]. Furthermore, to derive the influence of the uncorrected effects, we assume that the accuracy of the correction is independent of the frequency. Since we made the same assumption for the phase wind-up effect, we refer to the previous paragraph for the detailed developments. It comes thus that the residual PCOs and PCVs creates an error of about 0.025 TECU on the reconstructed TEC values. This contribution will be included in the $\Delta\,\mathrm{TEC}_r$ term (see section 4.4.2.3).

4.4.2.2 Higher-order ionospheric terms

As stated in section 3.2.1, the computation of TEC from the GF phase combination relies on the first-order approximation of the ionospheric index of refraction. In this section, we discuss the influence of higher-order ionospheric terms on the reconstructed TEC values. Taking higher-order terms into account, equation (3.62) becomes:

$$\Phi_{GF,km} = \alpha_{km}\,\mathrm{TEC} + I^{i,(2)}_{p,\Phi,m} - I^{i,(2)}_{p,\Phi,k} + I^{i,(3)}_{p,\Phi,m} - I^{i,(3)}_{p,\Phi,k} + IFB_{\Phi,km} - \lambda_k\,N_{GF,km} + E_{\Phi,km} \quad (4.122)$$

If we group the higher-order ionospheric terms of the GF phase combination in a $I^{(2),(3)}_{\Phi,GF}$ term, equation (4.119) is written as:

$$\mathrm{TEC}_r = \mathrm{TEC} + \frac{1}{\alpha_{km}}\left(I^{(2),(3)}_{\Phi,GF} + IFB_{\Phi,km} + E_{\Phi,km}\right) \quad (4.123)$$

The magnitude of the $I^{(2),(3)}_{\Phi,GF}$ term, and therefore its influence on TEC_r (dividing by α_{km}) can be estimated by using equations (3.37) and (3.39) in the "worst-case" scenario. We refer to section 3.1.4.3 for more details.

Figure 4.1 shows the influence of higher-order ionospheric terms on the reconstructed TEC values in the "worst-case" scenario for GPS and Galileo GF phase combinations and for vertical incidence. It can be observed that for TEC values smaller than 50 TECU and 100 TECU, this effect does not exceed 0.1 TECU and 0.2 TECU, respectively. Since these values are computed in the "worst-case" scenario, we can assume that for mid-latitude regions in a period of low solar activity, this effect will not exceed 0.05 TECU.

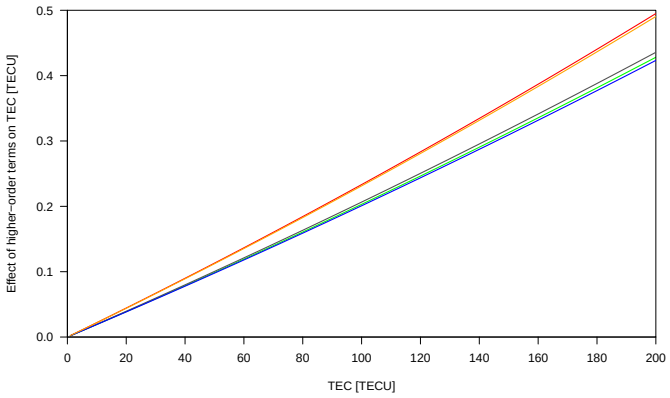

Figure 4.1 *– Influence of higher-order ionospheric terms on the reconstructed TEC values in the "worse-case" scenario (orange = GPS L2/L5, red = Galileo L2/L5, blue = GPS L1/L2, green = Galileo L1/L2, grey = L1/L5).*

4.4.2.3 GF phase combination

To assess the precision and accuracy of GF phase combination, we follow the approach used in section 4.3.1.1. We have computed the standard deviation of GF phase combination for

each type of error (noise, multipath, hardware), for combined noise and multipath and for all errors together. It is worth noting that it is more adequate to give the standard deviation values in units of TECU (thus dividing by α_{km}). The results are given in tables 4.16 and 4.17, respectively for GPS and Galileo.

Table 4.16 *– Standard deviation of the GPS reconstructed TEC values* [TECU] *due to measurement noise (σ_ε), multipath delays (σ_M), noise/multipath (σ_E), hardware delays (σ_d) and all errors together (σ_T).*

LC	σ_ε	σ_M	σ_E	σ_d	σ_T
$GF, 25$	0.042	0.178	0.183	0.033	0.186
$GF, 12$	0.008	0.040	0.041	0.007	0.042
$GF, 15$	0.007	0.033	0.033	0.006	0.034

Table 4.17 *– Standard deviation of the Galileo reconstructed TEC values* [TECU] *due to measurement noise (σ_ε) , multipath delays (σ_M), noise/multipath (σ_E), hardware delays (σ_d) and all errors together (σ_T).*

LC	σ_ε	σ_M	σ_E	σ_d	σ_T
$GF, 25$	0.068	0.290	0.298	0.053	0.303
$GF, 12$	0.008	0.037	0.038	0.007	0.038
$GF, 15$	0.007	0.033	0.034	0.006	0.034

All standard deviation values are actually one order of magnitude greater when using $\Phi_{GF,25}$ than when using $\Phi_{GF,12}$ or $\Phi_{GF,15}$, for both GPS and Galileo. As all phase delays have the same order of magnitude on L1, L2 and L5, this can be explained by the α_{km} [TECU/m] coefficients given by equation (3.52). These are a function of the carrier frequencies f_k and f_m and equal :

$$\alpha_{25} = -0.024 \quad \alpha_{12} = -0.105 \quad \alpha_{15} = -0.128 \quad \text{(GPS)}$$
$$\alpha_{25} = -0.015 \quad \alpha_{12} = -0.114 \quad \alpha_{15} = -0.128 \quad \text{(Galileo)}$$

It follows that the best way to reconstruct TEC is to use frequencies that are as far apart from each other as possible. Since the noise of the L2/L5 GF phase combination is the largest, we will exclusively use L1/L2 or L1/L5 GF phase combinations, whose precision and accuracy can be considered as equivalent.

In coherence with the notations used in sections 3.2.2 and 3.2.3.4, equation (4.119) can be written as follows:

$$\text{TEC}_r = \text{TEC} + \Delta\,\text{TEC}_r + E_r \tag{4.124}$$

where
ΔTEC_r is the error on caused by systematic effects (uncorrected effects, higher-order ionospheric terms, phase IFB) TEC_r [TECU]
$E_r = \dfrac{E_{\Phi,km}}{\alpha_{km}}$ is the observational error on TEC_r [TECU]

The precision of TEC_r is determined by the observational error (E_r), which is a function of phase multipath delays and phase measurement noise. From tables 4.16 and 4.17, it comes that

E_r has a standard deviation of about 0.04 TECU for $\Phi_{GF,12}$ and $\Phi_{GF,15}$ in both GNSS systems. At a 99 % level of confidence, the observational error is thus confined to -0.1 and 0.1 TECU.

Moreover, reconstructed TEC values are affected by systematic errors ($\Delta\,\mathrm{TEC}_r$), which are a function of satellite and receiver phase hardware delays or phase IFB ($IFB_{\Phi,km}$) as well as of uncorrected effects and higher-order ionospheric terms. These effects can be characterized as follows:

- following the results given in tables 4.16 and 4.17, the influence of phase IFB is about 0.02 TECU at a 99 % level of confidence ($2.58\,\sigma_d$),
- the combined influence of the uncorrected effects (phase wind-up and PCO, PCV) is about 0.05 TECU (see section 4.4.2.1),
- the influence of higher-order ionospheric effects does not exceed 0.05 TECU (see section 4.4.2.2).

In total, the error on TEC_r caused by these systematic effects ($\Delta\,\mathrm{TEC}_r$) is about 0.12 TECU at 99% level of confidence. This means that, without considering the fact that we only have approximated values of the N_{L2} ambiguities, we could obtain very precise and accurate reconstructed TEC values.

4.4.2.4 GF ambiguities

We will now assess the contribution of the error on the N_{L2} ambiguities on the reconstructed GF ambiguities and TEC values. We refer to the discussions given in section 4.3.2. The error on N_{L2} is given by equation (4.114). Considering that we round the values obtained with equation (4.113) to their nearest integer, we consider that the error on N_{L2} is an integer, namely Δn_{L2}. This error is also translated in the L1 and L5 ambiguities through equations (4.31) and (4.30), thus $\Delta n_{\mathrm{L1}} = \Delta n_{\mathrm{L5}} = \Delta n_{\mathrm{L2}}$. The error on TEC_r can be derived from equations (4.115) to (4.118) and expressed as a function of a unique Δn_k term:

$$\Delta\,\mathrm{TEC}_{r,N} = \frac{\Delta\,N_{GF,km}}{\alpha_{km}} = \frac{\lambda_m - \lambda_k}{\alpha_{km}}\Delta\,n_k = \eta_{km}\cdot\Delta\,n_k \tag{4.125}$$

where
$\Delta\,\mathrm{TEC}_{r,N}$ is the error on TEC_r caused by the error on the original ambiguities [TECU]
$\Delta\,n_k$ is the error on the N_k ambiguity [cycles], with $\Delta\,n_k \in \mathbb{Z}$)

The η_{km} [TECU/cycles] coefficient is equal to:

$$\begin{aligned} &\eta_{25} = -0.447 \quad \eta_{12} = -0.513 \quad \eta_{15} = -0.501 \quad \text{(GPS)} \\ &\eta_{25} = -0.443 \quad \eta_{12} = -0.508 \quad \eta_{15} = -0.501 \quad \text{(Galileo)} \end{aligned}$$

Integrating the $\Delta\,\mathrm{TEC}_{r,N}$ term, equation (4.124) becomes:

$$\mathrm{TEC}_r = \mathrm{TEC} + \Delta\,\mathrm{TEC}_r + \Delta\,\mathrm{TEC}_{r,N} + E_r \tag{4.126}$$

From equation (4.114), we can consider that $\Delta\,n_{\mathrm{L2}}$ and thus $\Delta\,n_k$ would be 1 cycle for GPS and 2 cycles for Galileo (at a 99 % level of confidence). Regarding equation (4.125), the error on

TEC_r caused by the original ambiguities ($\Delta TEC_{r,N}$) will thus be around 0.5 TECU for GPS and 1 TECU for Galileo.

This result is derived from the law of error propagation, which is based on the assumption that the phase hardware delays are independent between the different frequencies and have a magnitude smaller than 1 millimeter (see section 4.3.1.1). As aforementioned in section 2.2.2.9, the phase hardware delays are actually frequency-dependent effects. We can therefore reasonably assume that they have the same sign and are barely proportional to the frequency. In these conditions, even though they might be larger than 1 millimeter, their influence on the triple frequency phase multipath combination (and thus on the original ambiguities) will be less important than when considering them being independent (as it is done in section 4.3.2.2). This is thanks to the fact that the triple frequency phase multipath combination is a GF combination, whose coefficients fulfills the condition $d + e + f = 0$. A more detailed analysis of how phase hardware delays may affect the accuracy of the N_{L2} ambiguities and therefore of the TEC will be given in section 5.4.

In conclusion, we have to consider that the final reconstructed TEC values could be biased by a larger error than aforementioned. Nevertheless, since calibration procedures of the satellite and receiver phase delays are currently in development, we might soon be able to use the phase hardware delay calibration to reduce the error caused on the N_{L2} ambiguities.

4.4.2.5 Summary

In sections 4.4.2.1 to 4.4.2.4, we have done a detailed analysis of all the effects which have an influence on the precision and accuracy of the reconstructed TEC values. These effects are reported in table 4.18. Table 4.19 summarizes the precision and accuracy of the reconstructed TEC values for GPS and Galileo. These values are given for the L1/L2 GF phase combination, which can be considered equivalent to the L1/L5 GF phase combination.

***Table 4.18** – Overview of the effects determining the precision (E_r) and accuracy (ΔTEC_r , $\Delta TEC_{r,N}$) of the reconstructed TEC values.*

Precision and accuracy	Effects
E_r	phase noise phase multipath
ΔTEC_r	uncorrected phase wind-up uncorrected PCO/PCV higher-order ionospheric terms phase IFB
$\Delta TEC_{r,N}$	error on N_{L2}

The precision and accuracy assessment of the reconstructed TEC values can be summarized as follows:

- Their precision depends on the magnitude of phase measurement noise and phase multipath delays and is about 0.1 TECU for GPS and Galileo.

Table 4.19 *– Precision and accuracy of the reconstructed TEC values for GPS and Galileo (99 % confidence interval).*

Precision and accuracy	TEC_r	
[TECU]	GPS	Galileo
E_r	$[-0.11, 0.11]$	$[-0.10, 0.10]$
ΔTEC_r	$[-0.12, 0.12]$	$[-0.12, 0.12]$
$\Delta TEC_{r,N}$	$[-0.51, 0.51]$	$[-1.02, 1.02]$
$\sum$	$[-0.8, 0.8]$	$[-1.3, 1.3]$

- Their accuracy depends on the influence of uncorrected effects, higher-order ionospheric terms and phase hardware delays*. The accuracy is also and mainly determined by the influence of phase hardware delays on the original ambiguities, which leads to an error of 0.5 TECU for GPS and to an error of 1 TECU for Galileo.
- In total, the error on the reconstructed TEC values are confined to -0.8 and 0.8 TECU for GPS and to -1.3 and 1.3 TECU for Galileo.

Since with dual frequency GNSS techniques, systematic errors are confined to at least -2.5 and 2.5 TECU for a mid-latitude site, and to at least -5.5 and 5 TECU for a low-latitude site (see section 3.2.2.3), we can conclude that this triple frequency TEC reconstruction methodology has succeeded to improve the accuracy of the TEC. However, this might no be the case anymore if the influence of phase hardware delays and therefore the error on the original ambiguities is larger than expected.

4.5 Calibration of satellite and receiver code hardware delays

4.5.1 Principles

This section presents an innovative methodology which allows us to extract information about satellite and receiver code hardware delays by using the results of the ambiguity resolution and TEC reconstruction procedures.

With dual frequency GNSS measurements, it may be necessary† to calibrate the code IFB to compute the TEC (see sections 2.2.2.9 and 3.2.2.1). In our triple frequency approach, the calibration of the code IFB is not required, but can be done as an ancillary product of the TEC reconstruction. Moreover, thanks to the various linear combinations formed, we can obtain additional information on code hardware delays. Especially, we will show that it is possible to calibrate the sum of the satellite and receiver code hardware delays on each carrier frequency, which will be denoted as $D_{g,k}$.

From previous sections, we have obtained:

*through the GF phase combination (phase IFB) as well as through the resolution of the original ambiguities
†for the "carrier-to-code" levelling process

- the widelane ambiguities (N_{EWL} and N_{WL}),
- the reconstructed TEC values (TEC_r).

Regarding equation (4.63), if we subtract the EWL ambiguities from the mean value of c_{EWL} over a satellite pass (i.e. $\langle c_{EWL} \rangle$), we obtain the mean value of the EWLNL residual term (i.e. $\langle \Delta c_{EWL} \rangle$):

$$\langle c_{EWL} \rangle - N_{EWL} = \langle \Delta c_{EWL} \rangle \tag{4.127}$$

As stated in section 4.3.1.1, it can be easily justified that code and phase measurement noise, as well as phase multipath delays have a zero-mean. Moreover, we can consider that the average of code multipath delays over a satellite pass is sufficiently low to be neglected. This assumption will be discussed in section 4.5.2. With these hypotheses, $\langle \Delta c_{EWL} \rangle$ is a function of the code and phase hardware delays on L2 and L5 (see equation (4.57)). We can thus write:

$$\begin{aligned} \langle \Delta c_{EWL} \rangle &= \left(d^i_{\Phi,\text{L2}} + d_{p,g,\text{L2}} \right) - \left(d^i_{\Phi,\text{L5}} + d_{\Phi,g,\text{L5}} \right) \\ &\quad - f_{25} \left[\frac{f_{\text{L2}}}{c} \left(d^i_{g,\text{L2}} + d_{p,g,\text{L2}} \right) + \frac{f_{\text{L5}}}{c} \left(d^i_{g,\text{L5}} + d_{p,g,\text{L5}} \right) \right] \end{aligned} \tag{4.128}$$

For more convenience in the following developments, we define the following quantities:

$$D_{g,k} = d^i_{g,k} + d_{p,g,k} \tag{4.129}$$

$$D_{\Phi,k} = d^i_{\Phi,k} + d_{p,\Phi,k} \tag{4.130}$$

where
$D_{g,k}$ is the sum of the satellite and receiver code hardware delays on k carrier frequency [m]
$D_{\Phi,k}$ is the sum of the satellite and receiver phase hardware delays on k carrier frequency [m]

Using this definition, equation (4.128) becomes:

$$\langle \Delta c_{EWL} \rangle = D_{\Phi,\text{L2}} - D_{\Phi,\text{L5}} - f_{25} \left[\frac{f_{\text{L2}}}{c} D_{g,\text{L2}} + \frac{f_{\text{L5}}}{c} D_{g,\text{L5}} \right] \tag{4.131}$$

Similarly to equation (4.127), if we subtract the WL ambiguities from the mean value of c_{WL} over a satellite pass, we obtain the mean value of the WLNL residual term (see equation (4.65)):

$$\langle c_{WL} \rangle - N_{WL} = \langle \Delta c_{WL} \rangle \tag{4.132}$$

Considering the previous assumptions, $\langle \Delta c_{WL} \rangle$ is a function of the code and phase hardware delays on L1 and L2 (see equation (4.57)):

$$\begin{aligned} \langle \Delta c_{WL} \rangle &= \left(d^i_{\Phi,\text{L1}} + d_{p,g,\text{L1}} \right) - \left(d^i_{\Phi,\text{L2}} + d_{\Phi,g,\text{L2}} \right) \\ &\quad - f_{12} \left[\frac{f_{\text{L1}}}{c} \left(d^i_{g,\text{L1}} + d_{p,g,\text{L1}} \right) + \frac{f_{\text{L2}}}{c} \left(d^i_{g,\text{L2}} + d_{p,g,\text{L2}} \right) \right] \\ &= D_{\Phi,\text{L1}} - D_{\Phi,\text{L2}} - f_{12} \left[\frac{f_{\text{L1}}}{c} D_{g,\text{L1}} + \frac{f_{\text{L2}}}{c} D_{g,\text{L2}} \right] \end{aligned} \tag{4.133}$$

Moreover, considering their magnitude with respect to code hardware delays, the influence of phase hardware delays can be neglected in the WLNL combination. We can thus write:

$$\langle \Delta c_{WL} \rangle = -f_{12} \left[\frac{f_{\text{L1}}}{c} D_{g,\text{L1}} + \frac{f_{\text{L2}}}{c} D_{g,\text{L2}} \right] \tag{4.134}$$

Apart from ionospheric delays, the GF code combination ($P_{GF,km}$) contains the same type of code delays as the WLNL combination (c_{WL}). Since we have reconstructed the TEC values, we can remove the ionospheric delays from $P_{GF,km}$ to obtain $P_{GF,km,c}$ [m] (see equation (3.50)):

$$\begin{aligned} P_{GF,km,c} &= P_{GF,km} - \alpha_{km}\,\mathrm{TEC}_r && (4.135)\\ &= IFB_{g,km} + E_{g,km} && (4.136)\\ &= D_{g,k} - D_{g,m} + E_{g,km} && (4.137) \end{aligned}$$

where TEC_r [TECU] are the TEC values reconstructed with the L1/L2 or L1/L5 GF phase combination. By doing so, this combination only depends on code multipath delays, code measurement noise and code hardware delays. Considering the previous assumptions, the mean of $P_{GF,km,c}$ only depends on code IFB ($IFB_{g,km}$). We can thus write:

$$\langle P_{GF,25,c}\rangle = IFB_{g,25} = D_{g,\mathrm{L2}} - D_{g,\mathrm{L5}} \quad (4.138)$$

$$\langle P_{GF,12,c}\rangle = IFB_{g,12} = D_{g,\mathrm{L1}} - D_{g,\mathrm{L2}} \quad (4.139)$$

$$\langle P_{GF,15,c}\rangle = IFB_{g,15} = D_{g,\mathrm{L1}} - D_{g,\mathrm{L5}} \quad (4.140)$$

This operation allows us to obtain an estimation of code IFB as an ancillary product of the TEC reconstruction. Furthermore, we can use these code IFB together with the $\langle \Delta c_{WL}\rangle$ quantity (see equation (4.134)) to calibrate the sum of the satellite and receiver code hardware delays on each carrier frequency (D_k). Substituting the $D_{g,\mathrm{L2}}$ quantity by $D_{g,\mathrm{L1}} - \langle P_{GF,12,c}\rangle$ from equation (4.139) in equation (4.134) makes it possible to extract the $D_{g,\mathrm{L1}}$ quantity. After several developments, we obtain the expression of $D_{g,\mathrm{L1}}$ [m]:

$$D_{g,\mathrm{L1}} = \frac{f_{\mathrm{L2}}}{f_{\mathrm{L1}} + f_{\mathrm{L2}}} \cdot \langle P_{GF,12,c}\rangle - \lambda_{WL} \cdot \langle \Delta c_{WL}\rangle \quad (4.141)$$

Then if we substitute $D_{g,\mathrm{L1}}$ in equations (4.139) and (4.140), we obtain $D_{g,\mathrm{L2}}$ and $D_{g,\mathrm{L5}}$, respectively. The accuracy of D_k will be assessed in the next section.

It has to be noted that, as for TEC reconstruction, we could have used the MLNL combination instead of the WLNL combination (see appendix A) to extract $D_{g,\mathrm{L5}}$ [m]:

$$D_{g,\mathrm{L5}} = \frac{f_{\mathrm{L1}}}{f_{\mathrm{L1}} + f_{\mathrm{L5}}} \cdot \langle P_{GF,15,c}\rangle - \lambda_{ML} \cdot \langle \Delta c_{ML}\rangle \quad (4.142)$$

It comes from equation (4.142) that this requires the use of the L1/L5 GF code combination.

This innovative calibration method will allow us to improve the ambiguity resolution procedure. We have seen in section 4.3.1.1 that the magnitude of satellite and receiver code hardware delays prevent the resolution of the WL ambiguities through the WLNL combination. These ambiguities are thus resolved by using the DWL combination together with a dual frequency TEC estimation. Since we are now able to calibrate the D_k quantities, these can be used to reduce the influence of the WLNL residual term. It consists of applying the following correction to $\langle c_{WL}\rangle$ to obtain $\langle c_{WL,c}\rangle$ (see equation (4.64)) [m]:

$$\langle c_{WL,c}\rangle = \langle c_{WL}\rangle + f_{12}\left(\frac{f_{\mathrm{L1}}}{c}\,D_{g,\mathrm{L1}} + \frac{f_{\mathrm{L2}}}{c}\,D_{g,\mathrm{L2}}\right) \quad (4.143)$$

It is worth noting that this will be valid for a given time period under which D_k delays can be considered constant, or at least not varying more than the limit imposed by the WLNL ambiguity resolution. By doing so, the WL ambiguities can be resolved with the WLNL combination, and the dual frequency estimation of the TEC is not required anymore. This alleviates the ambiguity resolution and TEC reconstruction procedures.

4.5.2 Accuracy assessment

We will now assess the accuracy of the calibrated sum of satellite and receiver code hardware delays (D_k). Regarding the combinations used for the calibration and to the assumptions on which it relies, we have to take the following effects into account:

- the non-zero average of code multipath delays,
- the accuracy of the reconstructed TEC values.

In the previous section, we made the assumption that code multipath delays have a zero-mean. However, we know from that it may not be always the case (section 2.2.2.7). To derive the influence of the non-zero mean of code multipath delays on the calibrated delays, we have to derive the multipath delays which would be contained in equation (4.141). After several developments, we obtain thus $M_{D_{g,\mathrm{L1}}}$ [m]:

$$M_{D_{g,\mathrm{L1}}} = -f_{12} \cdot \langle M^i_{p,g,\mathrm{L1}} \rangle - \frac{2}{f_{\mathrm{L1}} + f_{\mathrm{L2}}} \cdot \langle M^i_{p,g,\mathrm{L2}} \rangle \quad (4.144)$$

$$= c_1 \cdot \langle M^i_{p,g,\mathrm{L1}} \rangle + c_2 \cdot \langle M^i_{p,g,\mathrm{L2}} \rangle \quad (4.145)$$

Since for GPS and Galileo the sum of c_1 and c_2 coefficients is equal to -1, $M_{D_{g,\mathrm{L1}}}$ must be smaller than $\langle M^i_{p,g,k} \rangle$. Regarding the amplitude of code multipath delays, we can reasonably consider that their non-zero average would be smaller than a few decimeters. Therefore, we can assume that the influence of the non-zero average of code multipath delays on D_k is decimetric.

The calibration of D_k also relies on the use of reconstructed TEC values (TEC_r). To derive the influence of the accuracy of TEC_r on the calibrated delays, we have to derive the ionospheric delays which are contained in equation (4.141). After several developments, we obtain $I_{D_{g,\mathrm{L1}}}$ [m]:

$$I_{D_{g,\mathrm{L1}}} = \frac{f_{\mathrm{L2}}}{f_{\mathrm{L1}} + f_{\mathrm{L2}}} \cdot \alpha_{12} \cdot \mathrm{TEC}_r \quad (4.146)$$

$$= c_3 \cdot \mathrm{TEC}_r \quad (4.147)$$

where c_3 [m/TECU] $= -0.046$ (GPS)/ -0.049 (Galileo)

As stated in section 4.4.2.5, the accuracy of TEC_r is about 0.8 TECU for GPS and 1.3 TECU for Galileo. Thus, from equation (4.146), the influence on the calibrated hardware delays is smaller than 4 cm for GPS and 7 cm for Galileo.

Taking into account the influence of non-zero code multipath delays and the accuracy of the reconstructed TEC values, we find that the accuracy of the calibrated satellite and receiver hardware delays (D_k) is at the decimetric level.

4.6 Conclusions

This chapter was dedicated to the development of an innovative TEC reconstruction methodology using the three civil frequencies of the GPS and Galileo systems.

We have driven the conceptual development based on the strengths and weaknesses of dual frequency techniques. After investigation of the characteristics (wavelength, noise and multipath amplification) of various linear combinations, we put a special emphasis on searching GF combinations of undifferenced measurements making it possible to resolve the integer ambiguities on each frequency. By doing so, the GF ambiguity can thus be reconstructed from the original integer ambiguities without the need for TEC modeling. The TEC values are then obtained from the usual dual frequency GF phase combination.

We performed an in-depth analysis of the widelane-narrowlane, differenced widelane and triple frequency phase multipath combinations. In particular, we assessed the magnitude of the non-ambiguity term to see whether or not is is possible to resolve the original ambiguities. Since all of these combinations are GF and IF*, the non-ambiguity (or residual) term contains all frequency-dependent GNSS errors affecting code and/or phase measurements†, i.e. satellite and receiver hardware delays, multipath delays, measurement noise, satellite and receiver antenna PCOs and PCVs and phase wind-up effect.

The assessment of the ambiguity resolution feasibility was based on several assumptions about the distribution and magnitude of measurement noise, multipath delays and hardware delays:

- Code and phase measurement noise, as well as code and phase multipath delays are white Gaussian. We assume realistic standard deviation values retrieved from real GNSS measurements. Even if the white Gaussian behavior might not be always true for code multipath delays, the use of a running average filter combined with the widelane character of the ambiguity resolution makes it a realistic hypothesis in this study.
- Satellite and receiver code and phase hardware are assumed to constant in time. Moreover, we make the assumption that the magnitude of each type (satellite and receiver) of code/phase hardware delays is smaller than 3 meters/1 millimeter, respectively.

Furthermore, we consider the adequate corrections for the phase wind-up effect and satellite and receiver antenna PCOs and PCVs to have been applied.

Through this in-depth analysis of the different combinations, we built an ambiguity resolution scheme based on a promising set of combinations. The following summarizes the ambiguity resolution procedure:

- Thanks to its large wavelength, the EWLNL combination allows us to resolve the EWL ambiguities for Galileo. For GPS however, the EWL ambiguity resolution could fail depending on the magnitude of satellite and receiver code hardware delays.
- Since the WLNL combination has a smaller wavelength, the influence of the code hardware delays prevents us from resolving the WL ambiguities with the WLNL combination. Therefore, the WL ambiguities are resolved through the DWL combination, which is a phase-only combination. Nevertheless, this requires an estimation of dual frequency ionospheric delays with an accuracy better than 5 TECU. This is shown to be achievable, especially for mid-latitude regions in period of low solar activity. Nevertheless, for mid-latitudes regions in a period of higher solar activity, or for low-latitudes regions

*except the differenced widelane combination
†depending on the type of combination used

in general, an accuracy of 5 TECU might not be achieved and the resolution of the WL ambiguities might not be possible.

- By substituting the EWL and WL ambiguities in the triple frequency phase multipath combination, we obtain approximated values of the original integer ambiguities. Their accuracy depends on the magnitude of satellite and receiver phase hardware delays.

Since the computation of TEC is based on the use of the GF phase combination, the next step after ambiguitiy resolution is the reconstruction of the GF ambiguities from the original ambiguities. These GF ambiguities are then added to the dual frequency GF phase combination to obtain the TEC values. In order to avoid noise amplification, the best way to reconstruct the TEC is to use frequencies that are as far apart from each other as possible. Therefore we exclusively use L1/L2 or L1/L5 GF phase combination.

We performed a detailed assessment of the precision and accuracy of the reconstructed TEC values TEC_r [TECU]

$$\mathrm{TEC}_r = \mathrm{TEC} + \Delta\,\mathrm{TEC}_r + \Delta\,\mathrm{TEC}_{r,N} + E_r \tag{4.148}$$

The precision of the TEC_r (E_r) depends on the magnitude of phase multipath delays and phase measurement noise and is about 0.1 TECU for GPS and Galileo. As far as the accuracy of the TEC is concerned, it depends on the uncorrected effects (phase wind-up, PCO, PCV), higher-order ionospheric terms as well as on phase IFB on the GF phase combination ($\Delta\,\mathrm{TEC}_r$). The accuracy of the TEC is also and mainly determined by the influence of phase hardware delays on the original ambiguities ($\Delta\,\mathrm{TEC}_{r,N}$), which leads to an error of 0.5 TECU for GPS and to an error of 1 TECU for Galileo. In total, the error on the reconstructed TEC values are confined to -0.8 and 0.8 TECU for GPS and to -1.3 and 1.3 TECU for Galileo. Finally, this triple frequency TEC reconstruction methodology has succeeded to improve the accuracy of the TEC with regards to existing dual frequency techniques. However, this might no be the case anymore if the influence of phase hardware delays and therefore the error on the original ambiguities is larger than expected.

We also developed an innovative technique to calibrate the satellite and receiver code hardware delays. Actually, this method uses the results of the ambiguity resolution and TEC reconstruction procedures to compute the sum of the satellite and receiver code hardware on each carrier frequency. Taking into account the non-zero average of code multipath delays and the accuracy of the reconstructed TEC values, we found that the accuracy of the calibrated satellite and receiver hardware delays (D_k) is at the decimetric level.

These calibrated delays can thus be used to reduce the influence of the WLNL residual term, making it possible to resolve the WL ambiguities without the need for a dual frequency estimation of the TEC*. This alleviates the ambiguity resolution and TEC reconstruction procedures.

*which is required by the DWL combination

Chapter 5

Triple frequency TEC reconstruction using simulated data

THIS chapter is dedicated to triple frequency TEC reconstruction with simulated GNSS measurements. The first section (5.1) introduces the main objectives of the chapter. The second section (5.2) describes the triple frequency GNSS simulation software in detail. The third (5.3) and fourth (5.4) sections present the results of the ambiguity resolution and TEC reconstruction procedures based on triple frequency GPS and Galileo simulated data. Finally, we give the conclusions of the chapter in section 5.5.

5.1 Introduction

The aim of this work is to develop a Total Electron Content (TEC) reconstruction methodology based on triple frequency Global Navigation Satellite System (GNSS) measurements. Since it is well known that using simulations has always facilitated the development of new techniques, and since at the beginning of our research real triple frequency data were not available yet, we have developed a simulation software providing triple frequency GNSS measurements.

Even if it can not be shown here, this software has been an essential tool to conceive the TEC reconstruction methodology. However, the main concrete objectives of this chapter can be described as follows:

1. The first objective is to develop a simulation software able to generate realistic triple frequency code and phase measurements that will be emitted by the Galileo and modernized Global Positioning System (GPS) systems (see section 5.2).

   It is worth noticing that the simulation software is designed in a way that takes our final goal into account. Therefore this software aims to simulate as realistically as possible the geometric distance between the satellite and the receiver (and thus the orbital motion of satellites), as well as all error sources which have an influence on the ambiguity resolution and TEC reconstruction procedures. As described in section 4.3, the concerned

error sources are the frequency-dependent errors. We will thus put a special emphasis on the simulation of measurement noise, multipath delays and hardware delays.

2. The second objective to use the simulation software as a tool for testing and validating the concepts of the TEC reconstruction technique which have been developed theoretically in chapter 4.

   Once we are able to provide realistic GNSS measurements, we can test the triple frequency TEC reconstruction methodology developed, and in particular:

   - the feasibility of the ambiguity resolution process (see section 5.3),
   - the precision and accuracy of the reconstructed TEC (see section 5.4).

5.2 Triple frequency GNSS simulation software

The objective of this software is to simulate triple frequency code and phase GNSS measurements. Before describing how the GPS and Galileo satellite coordinates are obtained, we briefly discuss the orbital motion of GPS and Galileo satellites (section 5.2.1.1). Given a receiver position (section 5.2.1.2), we explain how to obtain the geometric distance and other geometric parameters (section 5.2.1.3). In section 5.2.2 we explain in detail how phase ambiguities and all error sources are simulated. We insist particularly on error sources which have an influence on the ambiguity resolution and TEC reconstruction procedures. Section 5.2.3 deals with the generation of raw simulated data.

5.2.1 Geometric distance

5.2.1.1 Satellite position

Orbital motion

The orbital motion of a satellite is a result of the Earth's gravitational attraction, as well as a number of disturbing forces (attraction of the sun and moon, solar radiation pressure, etc.) [69]. We will first focus on the so-called "normal orbits": the satellite moves in an orbital plane that is fixed in space; its path is an ellipse sensu stricto, of which one focal point is at the Earth's center. For using the normal orbital theory, there are several assumptions to fulfill:

- the mass of artificial satellites is negligible compared to the the mass of the Earth,
- the Earth is considered as a sphere with spherically symmetric density distribution, and can thus be treated as point mass,
- the satellite motion takes place in a vacuum,
- there is no disturbing force on the satellite.

Based on the above mentioned assumptions, Kepler's three laws can be used to describe the orbital motion of satellites around the Earth. Derived from those laws, six Kepler elements

are generally used to describe the position of satellites in space [69]. Two figures will help us to introduce them. Figure 5.1 shows the geometry of an orbital plane and gives the position of the satellite ($\mathbf{q}$) in the orbital plane coordinate system $(q_1\,, q_2\,, q_3)$ – whose origin is the focal point F that coincides with the center of the Earth – as:

$$\mathbf{q} = r \begin{bmatrix} \cos f \\ \sin f \\ 0 \end{bmatrix} \tag{5.1}$$

where r is the geocentric distance from the center of the Earth to the satellite and f is the true anomaly.

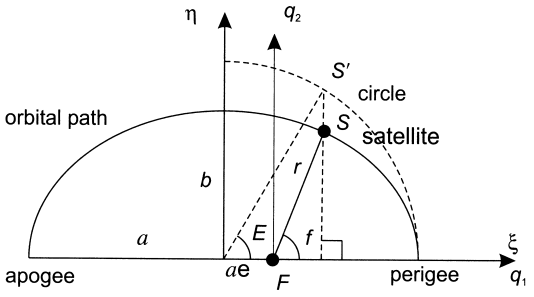

Figure 5.1 *– Geometry of the orbital plane. From [69].*

Figure 5.2 shows the orbital plane with respect to the true celestial coordinate system. Its origin is the focal point F; the X-axis points towards the vernal equinox and the Z-axis towards the celestial ephemeris pole; the Y-axis is located in the equator and completes the right-handed coordinate system. The six Kepler elements which are illustrated in figures 5.1 and 5.2 are:

1. the semimajor axis of the ellipse a,
2. the eccentricity of the ellipse e,
3. the inclination i, i.e. the angle between the orbital plane and the equator,
4. the right ascension of the ascending node Ω, with the ascending node the point at which the satellite ascends the equator,
5. the argument of perigee ω, i.e. the angle between the nodal line (intersection of the orbital plane with the equator) and the line of absides (connect the focal point F and the perigee),
6. the true anomaly f or eccentric anomaly E.

It is worth noticing that f is the only element that is a function of time, while the five other parameters remain constant.

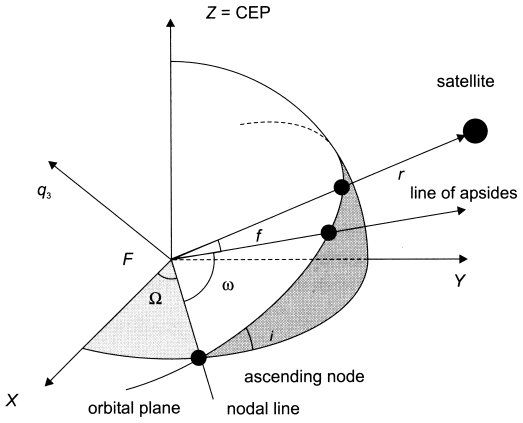

Figure 5.2 *– Orbital plane with respect to the true celestial coordinate system. From [69].*

It is also possible to derive Kepler's laws analytically by integrating Newton's laws of gravitation and motion. By coupling Newton's law of gravitation and Newton's second law, we can retrieve Kepler's third law in the following form [107]:

$$a^3 n^2 = GM \tag{5.2}$$

where $n = \frac{2\pi}{T}$ is the mean angular motion $\left[\text{rad} \cdot \text{s}^{-1}\right]$, i.e. the average angular velocity of the satellite.

After several developments we can obtain what is called Kepler's equation [107]:

$$\overline{M} = n\,(t - t_0) = E - e\,\sin E \tag{5.3}$$

where
$\overline{M}$ is the mean anomaly [rad]
E is the eccentric anomaly [rad]
t_0 is the time of perigee passage of the satellite [s]

As it can be interpolated linearly, one usually uses the mean anomaly $\overline{M}$. To obtain E as a function of M, equation (5.3) has to be transformed into an elliptical series expansion [107]:

$$\begin{aligned} E = \overline{M} \quad &+ \quad \left(e - \frac{1}{8}\,e^3 + \frac{1}{192}\,e^5 - \frac{1}{9216}\,e^7\right)\,\sin\,\overline{M} \\ &+ \quad \left(\frac{1}{2}\,e^2 - \frac{1}{6}\,e^4 + \frac{1}{48}\,e^6\right)\,\sin 2\,\overline{M} \\ &+ \quad \left(\frac{3}{8}\,e^3 - \frac{27}{128}\,e^5 + \frac{243}{5120}\,e^7\right)\,\sin 3\,\overline{M} \\ &+ \quad \left(\frac{1}{3}\,e^4 - \frac{4}{15}\,e^6\right)\,\sin 4\,\overline{M} + \left(\frac{125}{384}\,e^5 - \frac{3125}{9216}e^7\right)\,\sin\,5\overline{M} \\ &+ \quad \frac{27}{80}\,e^6\,\sin 6\,\overline{M} - \frac{16807}{46080}\,e^7\,\sin 7\,\overline{M} + ... \end{aligned} \tag{5.4}$$

$$\tag{5.5}$$

All three anomalies are zero when the satellite passes at the perigee. It has to be noted that by replacing f by $\overline{M}$ or E we have two alternative sets of Kepler elements.

Using the geometry of the orbital plane given in figure 5.1, we can adapt equation (5.1) so that the position of the satellite is a function of Kepler's elements a, e, and f:

$$\mathbf{q} = \begin{bmatrix} a\,(\cos E - e) \\ a\sqrt{1-e^2}\,\sin E \\ 0 \end{bmatrix} \tag{5.6}$$

The transformation from the Kepler elements to the satellite coordinates expressed in the true celestial coordinate system can then be achieved by [52]:

$$\mathbf{X^i_{cel}} = \mathbf{R}\,\mathbf{q} \tag{5.7}$$

where the matrix $\mathbf{R}$ is composed of three successive rotation matrices $\mathbf{R_i}$ around axis i:

$$\begin{aligned} \mathbf{R} &= \mathbf{R_3}(-\Omega)\mathbf{R_1}(-i)\mathbf{R_3}(-\omega) && (5.8)\\ &= \begin{bmatrix} \cos\Omega\cos\omega - \sin\Omega\sin\omega\cos i & -\cos\Omega\sin\omega - \sin\Omega\cos\omega\cos i & \sin\Omega\sin i \\ \sin\Omega\cos\omega + \cos\Omega\sin\omega\cos i & -\sin\Omega\sin\omega + \cos\Omega\cos\omega\cos i & -\cos\Omega\sin i \\ \sin\omega\sin i & \cos\omega\sin i & \cos i \end{bmatrix} \end{aligned}$$

By neglecting polar motion, i.e. considering that the Celestial Ephemeris Pole (CEP) is identical to the Conventional Terrestrial Pole (CTP), the transformation to Earth-Centered-Earth-Fixed (ECEF) coordinate system is given by [52, 69]:

$$\begin{aligned} \mathbf{X^i} &= \mathbf{R_3}(\mathrm{GAST})\,\mathbf{X^i_{cel}} && (5.9)\\ &= \begin{bmatrix} \cos(\mathrm{GAST}) & \sin(\mathrm{GAST}) & 0 \\ -\sin(\mathrm{GAST}) & \cos(\mathrm{GAST}) & 0 \\ 0 & 0 & 1 \end{bmatrix} \mathbf{X^i_{cel}} && (5.10) \end{aligned}$$

where GAST is the Greenwich Apparent Sideral Time, i.e. the true Greenwich hour angle of the true vernal equinox.

"Homogeneous" orbit

To simulate the orbital motion of GNSS satellites, it is possible to follow two approaches: either the "real orbit" one, or the "homogeneous orbit" one. In the former, real broadcast or precise ephemeris are used. The principles of "homogeneous" orbit is to locate the orbital planes regularly, and then to distribute the satellites equally on each orbital plane. Here we will only apply the "homogeneous orbit" approach.

For GPS, we simulate a constellation of 30 satellites, distributed on 6 orbital planes as in the real constellation described in section 2.1.1.1. Each one is characterized by an angle Ω going from 0° to 300°, with a 60° increment. On each orbital plane, five satellites are distributed equally by increasing ω from 0° to 288° with a 72° increment. We give realistic value to the remaining constant Kepler elements a, e and i. As in practice their values do not differ significantly from satellite to satellite, we take the same values for all satellites [118]. We also realize an iteration on t_0 on a whole day to compute the mean anomaly $\overline{M}$ with equation (5.3) and consequently the eccentric anomaly E with equation (5.4). We have then set the six Kepler elements. The satellite coordinates in the ECEF coordinate system can thus be obtained with equations (5.6) to (5.9).

For Galileo, we also simulate a constellation of 30 satellites, distributed on three orbital planes as in the real constellation described in section 2.1.2.1. Each orbital plane is characterized by the Ω angle going from 0° to 240°, with a 120° increment. On each orbital plane, five satellites are distributed equally by increasing ω from 0° to 324° with a 36° increment. Given the values of section 2.1.2.1 we use:

$$\begin{aligned} a &= 29600\ [\text{km}] \\ e &= 0 \\ i &= 56\,[^\circ] \end{aligned}$$

The procedure to obtain E is the same as for the GPS. Finally, equations (5.6) to (5.9) are used to obtain the satellite coordinates in the ECEF system.

We have shown in [117] that the "homogeneous orbit" approach allows us to properly reproduce the mean properties of a satellite constellation. In the TEC reconstruction technique, the satellite coordinates are used either to compute the geometric distance ρ_p^i, or to compute several angles (satellite zenith and azimuth angles at the receiver, satellite zenith angle at IP). As stated in chapter 4, all combinations which are used are Geometric-Free (GF) and thus independent of the geometric distance. Moreover, the different angles are used in secondary processing steps of the TEC reconstruction. Consequently, we can assume that the satellite coordinates obtained will meet the accuracy requirements regarding their use in our TEC reconstruction technique.

5.2.1.2 Receiver position

Since we simulate GNSS measurements at a given station, we need to have the position of the receiver in the ECEF coordinate system. For that purpose, we use the coordinates given either in the Receiver Independent Exchange (format) (RINEX) observation data (*.O file) or on the International Terrestrial Reference Frame (ITRF) website [35]. As in both cases these receiver coordinates correspond to the position of the marker on the ground, we have to take the antenna height (h_{ant}) into account to obtain the position of the Antenna Reference Point (ARP), This is done by using the tranformation routine between cartesian coordinates X, Y, Z and ellipsoidal coordinates φ, λ, h, which are the geodetic latitude, longitude and height, respectively [52].

5.2.1.3 Geometric distance and other geometric parameters

Since we know the satellite ($\mathbf{X^i}$) and receiver ($\mathbf{X_p}$) positions in the ECEF coordinate system, we can compute the geometric distance between the satellite and the receiver (ρ_p^i) by using:

$$\rho_p^i = \|\mathbf{X^i} - \mathbf{X_p}\| \tag{5.11}$$

It has to be stressed that, as we compute the satellite coordinates in an Earth-fixed reference frame, they normally need to be corrected for the Earth rotation effect described in section 2.2.2.4. However, when computing simulations, there is no physical transmission of the signal thus no physical rotation of the Earth, so that the position of the satellite does not change with regards to the position of the receiver in the ECEF coordinate system. Unless if

we wish to test the correction algorithm, there is thus no need to simulate the Earth rotation effect.

We also derive other quantities from the satellite and receiver positions, namely the satellite zenith/azimuth angle at the receiver and the ionospheric pierce point (IP) parameters (position, zenith angle, local time).
The satellite zenith angle at the receiver χ [rad] is the angle between the local zenith and the line of sight to the satellite. It can be computed by using the scalar product of the vector "position of the station" $\mathbf{X_p}$ (whose norm is the Earth radius R_E) – and the vector "relative position station-satellite" $\mathbf{X^i} - \mathbf{X_p}$ (whose norm is ρ_p^i), as illustrated in figure 5.3:

$$\chi = \arccos\left(\frac{\mathbf{X_p} \cdot (\mathbf{X^i} - \mathbf{X_p})}{R_E \cdot \rho_p^i}\right) \tag{5.12}$$

The satellite elevation angle at the receiver e [rad] is equal to $\pi - \chi$. Equation (5.12) is nearly equivalent to the formula given by [135]; the latter applies to an ellipsoidal Earth, whereas ours considers the Earth as a sphere. However, as this is only used for angle computation, it does not make a significant difference.
The satellite azimuth angle at the receiver A [rad] can be computed from [135] and is illustrated in figure 2.10:

$$A = \arctan\left(\frac{-\sin\lambda\left(X^i - X_p\right) + \cos\lambda\left(Y^i - Y_p\right)}{-\sin\varphi\cos\lambda\left(X^i - X_p\right) - \sin\varphi\sin\lambda\left(Y^i - Y_p\right) + \cos\varphi\left(Z^i - Z_p\right)}\right) \tag{5.13}$$

For the needs of ionospheric delays processing we have to compute the parameters of the ionospheric points (IP) along the satellite path: position, satellite zenith angle and local time at IP. As stated in section 3.1.4.4, the ionospheric point is the intersection of the line of sight with the 1-layer ionosphere. Mathematically, this is the solution of the intersection between a sphere (i.e. the spherical ionosphere) and a straight line (i.e. the line-of-sight to the satellite), which is rather straightforward. Given that solution, we obtain the cartesian coordinates of the corresponding ionospheric point in the ECEF coordinate system ($\mathbf{X_{IP}}$) for each satellite observed at a given station. Using the adequate routine [52], we can also obtain the ellipsoidal coordinates of the ionospheric point ($\varphi_{IP}, \lambda_{IP}$). The satellite zenith angle at the ionospheric point (χ_{IP}) can be directly computed from equation (3.45). Finally, the local time at the ionospheric point (h) can be simply derived from GPS/Galileo time and λ_{IP}.

5.2.2 Error sources and phase ambiguities

5.2.2.1 Integer phase ambiguities

The simulation of integer phase ambiguities is rather straightforward. We have implemented an algorithm that simulates a random integer number constant for each satellite pass and – independently – for each frequency, namely N_{L1}, N_{L2}, N_{L5}.

As seen in section 4.3, ambiguity resolution is required for TEC reconstruction. Therefore, in our particular case, we will be able to study whether it is possible to retrieve the ambiguities that have been simulated.

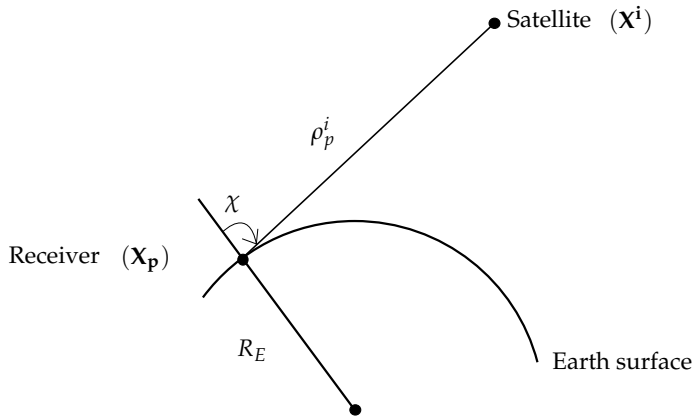

Figure 5.3 *– Satellite zenith angle at the receiver (χ).*

5.2.2.2 Satellite clock bias and relativistic effects

The satellite clock biases can be simulated by using real data, either broadcast ephemerides or precise ephemerides. We refer to section 2.2.2.2 for more details, e.g. the accuracy of each clock product. In both cases, the values have to be linearly interpolated to match the sample interval of the measurements (30 s/1 s), causing interpolation errors. We refer to section 2.2.2.2 for more details.

As far as relativistic effects are concerned, they can also be simulated by using broadcast ephemerides or precise ephemerides (section 2.2.2.3).

It is worth noticing that satellite clocks and relativistic effects cancel out in all combinations which are used for the TEC reconstruction. As a consequence, it is not important whether we use broadcast or precise ephemerides. For GPS, both broadcast and precise ephemerides are available anytime [56]. For Galileo, we can either use Giove broadcast ephemeris – not available every time – or choose not to include those effects, since they have no impact on our method.

5.2.2.3 Receiver clock bias

As stated in section 2.2.2.8, the receiver clock bias is a parameter to be solved for in most GNSS applications. Therefore, one way of simulating realistic clock bias is to generate white noise on frequency. This is implemented in [2]. Another solution is to use the receiver clock bias from the International GNSS Service (IGS) clock RINEX files.

As receiver clock biases cancel out in all combinations which are used in for TEC reconstruction, the simulation of receiver clock bias is not a critical point, and not even a necessity.

5.2.2.4 Ionospheric delays

Since several types of ionospheric models exist (see section 2.2.2.5), there are several ways to simulate realistic ionospheric delays. Since the main goal is to show how accurately the method is able to reconstruct the TEC values that have been simulated, the choice of the simulation method does not have any influence on the results.

We choose to simulate ionospheric delays by using the broadcast ionospheric model, i.e. the well-known Klobuchar model [61]. The eight coefficients of the Klobuchar model are provided in the broadcast ephemerides (α_i, β_i = 0,1,2,3). In addition, other input parameters are the geodetic latitude and longitude of the receiver, the satellite elevation (e) and azimuth angle (A) at the receiver, and the time of observation. The Klobuchar algorithm is described in detail in [23, 69, 135]. This model is based on the 1-layer model of the ionosphere described in section 3.1.4.4 and assumes that the zenithal ionospheric delay is maximum at 2 pm (local time) and constant during the night. The eight coefficients are updated daily. The Klobuchar ionospheric delay on L1 in units of meters is given by $I^i_{p,\mathrm{L1,klobu}}$ [m] [69]:

$$\begin{cases} I^i_{p,\mathrm{L1,klobu}} = c\,F\left[DC + A\left(1 - \frac{x^2}{2} + \frac{x^4}{25}\right)\right] & \text{if } |x| < 1.57 \\ I^i_{p,\mathrm{L1,klobu}} = c\,F\,DC & \text{if } |x| > 1.57 \end{cases} \tag{5.14}$$

with

$$x = \frac{2\pi\,(h - 50400)}{P} \tag{5.15}$$

where
F is the Klobuchar mapping function $[-]$
$DC = 5.10^{-9}$ [s] is the constant night-day offset
A is the amplitude [s]
P is the period [s]
h is the local time at the ionospheric point [s]

From this, it is possible to also obtain the ionospheric delays on L2 and L5 by:

$$I^i_{p,\mathrm{L2,klobu}} = \frac{f^2_{\mathrm{L1}}}{f^2_{\mathrm{L2}}}\, I^i_{p,\mathrm{L1,klobu}} \tag{5.16}$$

$$I^i_{p,\mathrm{L5,klobu}} = \frac{f^2_{\mathrm{L1}}}{f^2_{\mathrm{L5}}}\, I^i_{p,\mathrm{L1,klobu}} \tag{5.17}$$

The Klobuchar model makes it possible to compensate between 50 and 60% of the ionospheric delay at mid-latitudes [69].

5.2.2.5 Tropospheric delays

As stated in sections 4.3 and 4.4, tropospheric delays cancel out in all combinations which are used in our method. We can thus simulate tropospheric delays in a simple way by using a constant zenithal tropospheric delay ($vT^i_{p,d}$) together with the Niell's dry (MF_d) and wet

(MF_w) mapping functions [80]. As stated in section 2.2.2.6, we obtain the total tropospheric delay T_p^i [m] by:

$$T_p^i = MF_d \cdot vT_{p,d}^i + MF_w \cdot vT_{p,w}^i \tag{5.18}$$

5.2.2.6 Measurement noise

According to section 2.2.2.11, measurement noise can be simulated as Gaussian white noise. White noise is a random signal with a flat uniform spectral density. In statistical sense, this corresponds to a series of uncorrelated random variables with zero mean and finite variance σ^2. In particular, if the random variables are normally distributed with zero mean and variance σ^2, we talk about Gaussian white noise. In our case we need to simulate Gaussian white noise with a variance of $\sigma^2_{\varepsilon_{g,k}}$ for code measurements, and a variance of $\sigma^2_{\varepsilon_{\Phi,k}}$ for phase measurements (see section 2.2.2.11). The standard deviation of code and phase measurement noise for GPS and Galileo L1, L2 and L5 measurements are given in table 2.8.

The measurement noise of GNSS observations is simulated through several steps:

- Generation of random numbers

  We generate pseudo-random numbers from a continuous uniform distribution. This can be done by using the linear congruence method [88]. This method has the advantage to be fast, but is not free of sequential correlation on successive calls. To avoid this problem, we use a C routine called *ran1* that is based on three linear congruential generators [88] and returns random numbers which are uniformly distributed on [0,1]. Note that such a routine requires the specification of an initial number to start. This so-called *seed number* needs to be different to obtain different sequences.

  $\Longrightarrow$ we obtain random numbers $x \sim \mathrm{U}(0,1)$

- Box-Muller transformation

  We apply the Box-Muller transformation [128]. This algorithm is dedicated to the transformation of a two-dimensional continuous uniform distribution to a two-dimensional bivariate normal distribution. In particular, if x_1 and x_2 are random numbers which are uniformly and independently distributed on [0,1] (generated in the previous step), the Box-Muller transformation returns random numbers which are normally distributed (μ=0, σ^2=1). In our work, the C routine called *gasdev()* is used to apply the Box-Muller transformation [88].

  $\Longrightarrow$ we obtain Gaussian white noise $z \sim \mathrm{N}(0,1)$

- Standard deviation of measurement noise

  Code (phase) measurement noise is obtained by multiplying z by the standard deviation of code (phase) measurement noise given in table 2.8:

$$\varepsilon_{g,k}^i = z \cdot \sigma_{\varepsilon_{g,k}} \tag{5.19}$$

$$\varepsilon_{\Phi,k}^i = z \cdot \sigma_{\varepsilon_{\Phi,k}} \tag{5.20}$$

$\Longrightarrow$ we obtain Gaussian white noise $\varepsilon^i_{g,k} \sim \mathrm{N}(0, \sigma^2_{\varepsilon_{g,k}})$ and $\varepsilon^i_{\Phi,k} \sim \mathrm{N}(0, \sigma^2_{\varepsilon_{\Phi,k}}, 1)$

- Elevation-modulated noise

  To be more realistic, it is also possible to generate elevation-dependent measurement noise. We multiply the Gaussian white noise by the following factor:

  $$\cdot \cos\left(\frac{e}{1.69}\right) \tag{5.21}$$

  where e is the satellite elevation angle [rad]

  From equation (5.21) it comes that for $e = \pi/2$ the elevation-modulation factor equals 0.6, which means that there remains 60 % of the noise amplitude at high elevations. Despite the elevation modulation, we can consider that over a satellite pass the effects have a zero-mean. This constitutes an important point for the ambiguity resolution process (see section 5.3).

  $\Longrightarrow$ we obtain elevation-dependent Gaussian white noise

It has to be stressed that we have insured the independence of measurement between the different frequencies by setting a specific *seed number* for each carrier frequency. This is mandatory to obtain a realistic assessment of the standard deviation of measurement noise for a combined measurement, i.e. for the combinations used for TEC reconstruction.

Figure 5.4 shows examples of simulated code and phase measurement noise for both GPS and Galileo systems. As the simulation is based on the standard deviation values given in table 2.8, we can retrieve the different characteristics discussed in section 2.2.2.11. We can observe that GPS L1 code measurements are the noisiest, while GPS L5 has the same level of noise as Galileo L2/L5 observables. As far as phase measurement noise is concerned, it has the same magnitude on GPS and Galileo observables. Moreover, due to the larger wavelength L2 and L5 phase measurement are slightly noisier.

Finally, we can assume that this algorithm is able to realistically simulate code and phase measurement noise. It enables us thus to study the propagation of measurement noise in the combinations used for TEC reconstruction.

5.2.2.7 Multipath delays

According to the description given in section 2.2.2.7, multipath delays can be simulated as a pseudo-random error. The used algorithm considers multipath delays as a time-correlated Gaussian noise modulated by several factors (amplitude, environment, receiver sensitivity, elevation). Code and phase multipath delays are simulated according to the routine described in [2]:

$$M^i_{p,g,k} = A_g \, K_{env} \, K_{rec} \, K_{ran} \, \cos(\omega \, e) \tag{5.22}$$

$$M^i_{p,\Phi,k} = A_\Phi \, K_{env} \, K_{rec} \, K_{ran} \, \cos(\omega \, e) \tag{5.23}$$

where
A_g, A_Φ is the amplitude of the code and phase multipath delays, respectively [m]
K_{env} is the environment factor $[-]$, equal to 0.1/0.6/0.7 respectively for rural, suburban and

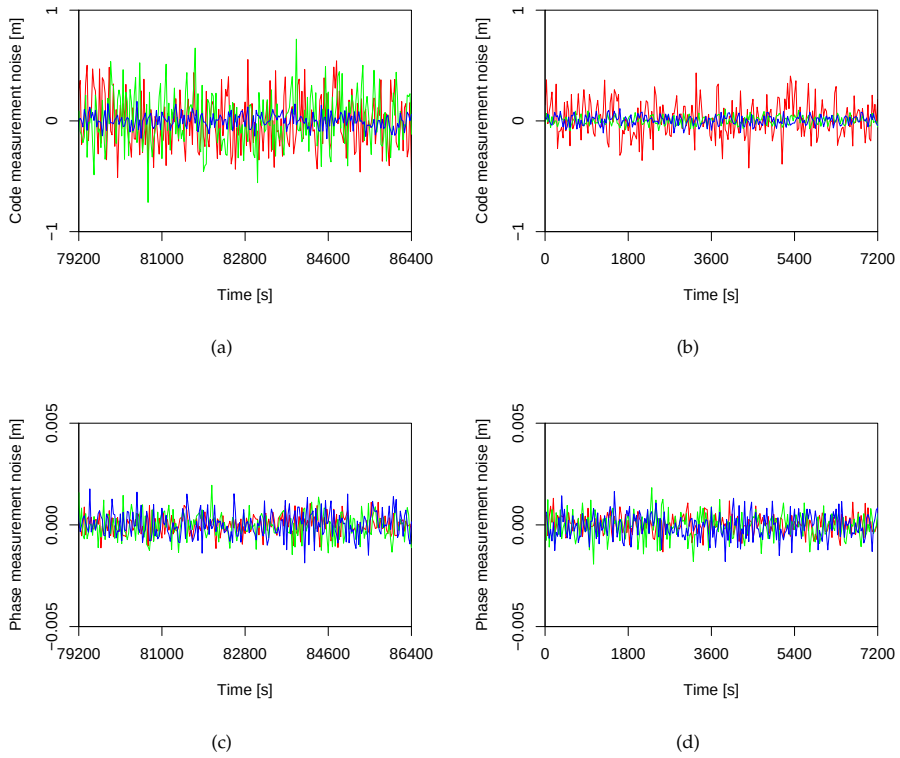

Figure 5.4 *– Examples of simulated code (a,b) and phase (c,d) measurement noise on GPS (left) and Galileo (right) L1, L2 and L5 observables (red = L1, green = L2, blue = L5).*

urban environment
K_{rec} is the receiver sensivity factor $[-]$, varying from 0 to 1
$K_{ran} \sim \mathrm{N}(0, 1, \tau)$ is a time-correlated Gaussian white noise $[-]$
ω is the multipath frequency [cycles/rad]
e is the satellite elevation angle [rad]

The simulation of the time-correlated Gaussian noise (K_{ran}) is done in several steps. First, as explained in section 5.2.2.6, the routines *ran1* and *gasdev()* are used sequentially to obtain Gaussian white noise ($z_0 \sim \mathrm{N}(0, 1)$). Then, we apply the following recursive algorithm to obtain $K_{ran,i}$ at t_i from z_i [2, 85]:

$$K_{ran,0} = \sigma\, z_0 \tag{5.24}$$

$$K_{ran,i} = T_i\, K_{ran,i-1} + \sqrt{1 - T_i^2}\, \sigma\, z_i \tag{5.25}$$

where $T_i = e^{-|t_i - t_{i-1}|/\tau}$ and τ is the correlation time [s].

As far as the multipath factors are concerned, we will use the typical values of $K_{rec} = 1$, $\omega = 0.8$ cycles/rad and $\tau = 100$ s [2]. Moreover, it is generally suitable to use K_{env} equal to

0.6 or 0.7. Finally, we take σ equal to 1 and adapt the values of A_g and A_Φ so that the standard deviation of simulated code and phase multipath delays with equations (5.22) and (5.23) fit the values given in table 2.7.

As for measurement noise, we have insured the independence of multipath delays between the different frequencies, as well as the independence with regards to the measurement noise which is also simulated by Gaussian white noise.

Figure 5.5 shows examples of simulated code and phase multipath delays for both GPS and Galileo systems. As the simulation is based on the standard deviation values given in table 2.7, we can retrieve the different characteristics discussed in section 2.2.2.7. We can observe that GPS L1 and L2 code observables are much more affected by multipath delays than any other code observable, whereas Galileo L1 code measurements are more affected than L2 and L5 codes. As far as phase multipath delays are concerned, they have the same order of magnitude on GPS and Galileo observables.

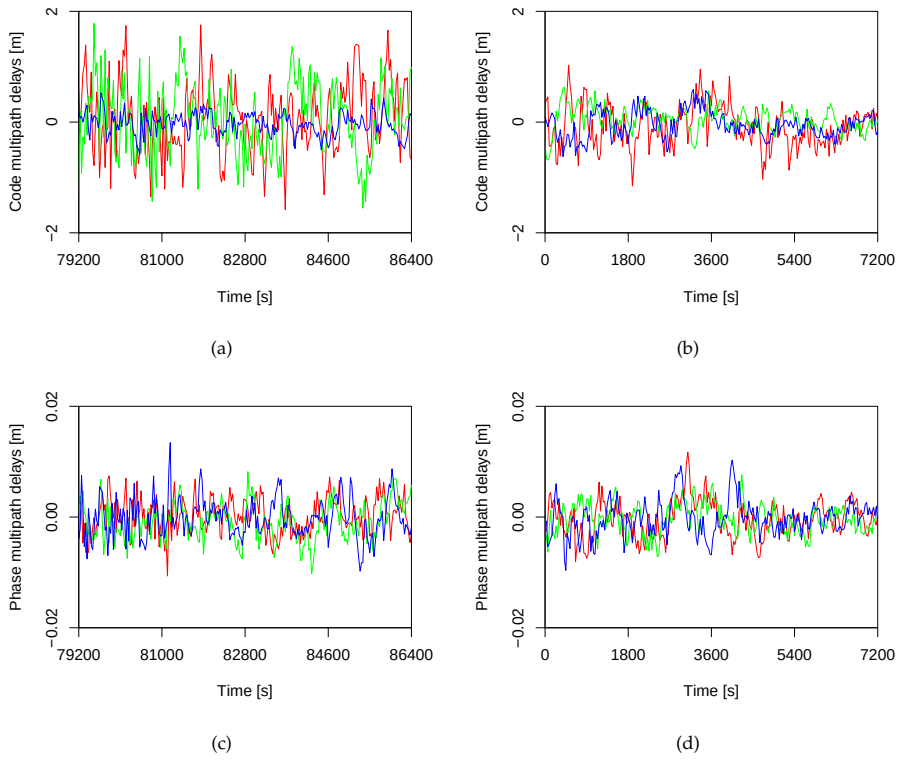

Figure 5.5 *– Examples of simulated code (a,b) and phase (c,d) multipath delays on GPS (left) and Galileo (right) L1, L2 and L5 observables (red = L1, green = L2, blue = L5).*

Finally, we can assume that this multipath simulation algorithm is able to reproduce the general characteristics of code and phase multipath delays in typical environment conditions. It enables us thus to study the propagation of multipath delays in the combinations used for

TEC reconstruction.

5.2.2.8 Satellite and receiver hardware delays

According to section 2.2.2.9 and 4.3.1.1, we have simulated the code and phase hardware delays as follows:

- constant values over a satellite pass
- random values in the following range

$$\begin{aligned} |d^i_{g,k}| \text{ and } |d_{p,g,k}| &< 3\,\text{m (code)} \\ |d^i_{\Phi,k}| \text{ and } |d_{\Phi,g,k}| &< 1\,\text{mm (phase)} \end{aligned}$$

In chapter 4, we showed that even if the influence of code hardware delays can sometimes prevent us from resolving the widelane ambiguities, this can be overcome by the use of the differenced widelane (DWL) combination and/or by using the code hardware delay calibration methodology. However, we found that the accuracy of the reconstructed TEC values is mainly determined by the influence of phase hardware delays on the original ambiguities. In this context, only the latter influence will be deepened in this chapter (see section 5.4).

5.2.2.9 Satellite and receiver antenna phase center offset and variations

As aforementioned in section 2.2.2.10, the position of the antenna instantaneous phase centers of the satellite and receiver are modeled by a consistent set of antenna Phase Center Offsets (PCOs) and Phase Center Variations (PCVs). Since the IGS provides the PCOs and PCVs corrections, allowing us to correct the code and phase measurements at the cm-level accuracy [106], we do not simulate these effects. The influence of the uncorrected effects on the reconstructed TEC values has been estimated in section 4.4.2.1.

However, these effects need to be corrected when processing real measurements (see section 6.3.1.2).

5.2.2.10 Phase wind-up effect

As stated in section 2.2.2.12, GNSS phase measurements are affected by the phase wind-up effect (ω^i_p), which is a geometric effect related to the emission/reception of GNSS electromagnetic waves. Since it is possible to obtain a correction of this effect at the cm-level accuracy [19], we do not simulate this effect. The influence of the uncorrected effects on the reconstructed TEC values has been estimated in section 4.4.2.1.

A correction of this effect will however be necessary when processing real measurements (see section 6.3.1.3).

5.2.3 Generation of triple frequency GNSS data

In section 5.2.1 we have simulated the geometric distance between the satellite and the receiver in the ECEF receiver coordinate system. In section 5.2.2 we have generated the phase ambiguities and the error sources affecting GNSS code and phase observables. Altogether it enables us to generate triple frequency GNSS measurements, whose mathematical model is given by:

$$\begin{aligned} P_{k,sim} &= \rho^i_p + c\,\Delta t_p - c\left(\Delta t^i + \Delta t^i_{rel}\right) + I^i_{p,k} + T^i_p + d^i_{g,k} + d_{p,g,k} \\ &\quad + M^i_{p,g,k} + \varepsilon^i_{p,g,k} \end{aligned} \tag{5.26}$$

$$\begin{aligned} \Phi_{k,sim} &= \rho^i_p + c\,\Delta t_p - c\left(\Delta t^i + \Delta t^i_{rel}\right) - I^i_{p,k} + T^i_p + d^i_{\Phi,k} + d_{p,\Phi,k} \\ &\quad + M^i_{p,\Phi,k} + \varepsilon^i_{p,\Phi,k} - \lambda_k\, N^i_{p,k} \end{aligned} \tag{5.27}$$

where
$k \in \{\mathrm{L1}, \mathrm{L2}, \mathrm{L5}\}$
$P_{k,sim}$ is the simulated code measurement on k carrier frequency [m]
$\Phi_{k,sim}$ is the simulated phase measurement on k carrier frequency [m]

It is worth noticing that our simulation software has been designed to simulate either 1-second or 30-second GNSS data. Moreover, we apply an elevation mask which keeps only the observation data where:

$$\chi < 70^\circ \tag{5.28}$$

This criterion helps to have an average value of code multipath delays sufficiently close to zero over a satellite pass. It will also be applied in section 6.3.3 for the processing of real data.

To summarize, the triple frequency GNSS simulation software is able to provide:

- ▷ triple frequency measurements (L1, L2, L5)
- ▷ with a 1-second or 30-second sampling rate
- ▷ for a constellation of 30 GPS and/or Galileo satellites
- ▷ at any given receiver position

This constitutes the observation dataset which is available for testing the TEC reconstruction technique developed in chapter 4, and in particular:

- the feasibility of the ambiguity resolution process (see section 5.3),
- the precision and accuracy of the reconstructed TEC (see section 5.4).

5.3 Ambiguity resolution

As stated in section 4.3, the ambiguity resolution procedure follows two main steps:

1. resolution of the widelane ambiguities using the widelane-narrowlane and differenced widelane combinations (see section 5.3.1),
2. resolution of original integer ambiguities by substituting the widelane ambiguities in the triple frequency phase multipath combination (see section 5.3.2).

For each type of combination used, we address a quick review of their characteristics.

The main objective is then to assess the feasibility of the ambiguity resolution process. For that purpose, we will estimate the influence of the frequency-dependent effects (i.e. residual term) on the ambiguity resolution, and in particular the influence of the following effects:

- measurement noise (code/phase),
- multipath delays (code/phase),
- hardware delays (phase*).

It has to be stressed that the simulation software will allow us to analyze the influence of each error source individually, as well as to combine (e.g. multipath and noise) or compare (e.g. code versus phase) the different types of error sources. As mentioned earlier, in this chapter we do not analyze the influence of these effects:

- code hardware delays,
- (uncorrected) satellite/receiver antenna PCOs/PCVs,
- (uncorrected) phase wind-up effect.

5.3.1 Widelane ambiguity resolution

5.3.1.1 Widelane-narrowlane combinations

The widelane-narrowlane combination ($c_{wl,km}$) is a dual frequency combination of code and phase measurements which is GF and Ionospheric-Free (IF). The general expression of $c_{wl,km}$ [cycles] is:

$$c_{wl,km} = N_{wl,km} + \Delta c_{wl,km} \tag{5.29}$$

By definition its wavelength is greater than the wavelength of L5 carrier frequency. Given L1, L2 and L5 frequencies, we have defined the extra–widelane–narrowlane (EWLNL), widelane–narrowlane (WLNL) and WLNL combinations in section 4.3.1.1. Their wavelength is given in table 4.2 and 4.3, respectively for GPS and Galileo. As stated in section 4.3.1.1, the widelane ambiguities can be resolved if the following condition is fulfilled:

$$\Delta c_{wl,km} < 0.5 \tag{5.30}$$

Equation (4.57) shows that this residual term depends on satellite and receiver hardware delays, multipath delays and measurement noise on both code and phase measurements.

*We study the influence of phase hardware delays on the reconstructed TEC values in section 5.4.

In order to study the feasibility of the ambiguity resolution, we will assess the magnitude of multipath and noise in the residual term. We consider the effect of multipath delays and measurement noise together, and compare the contribution of code delays with the contribution of phase delays.

Figure 5.6 shows the part of Δc_{EWL} due to multipath delays and measurement noise for a whole satellite pass, respectively for GPS and Galileo. It is worth noticing that for GPS the influence of code delays is dominant, while for Galileo the influence of phase delays has the same order of magnitude. In total, the influence is also more than twice as large for GPS than for Galileo. This difference between GPS and Galileo can be explained by the fact that – especially on L2 – code multipath delays and measurement noise are larger for GPS than for Galileo (tables 2.7 and 2.8), but also and mainly by the fact that the f_{km} coefficient is twice as great for GPS ($f_{25} = 0.0212$) than for Galileo ($f_{25} = 0.0128$). This coefficient is directly linked to the wavelength and is given by equation (4.58).

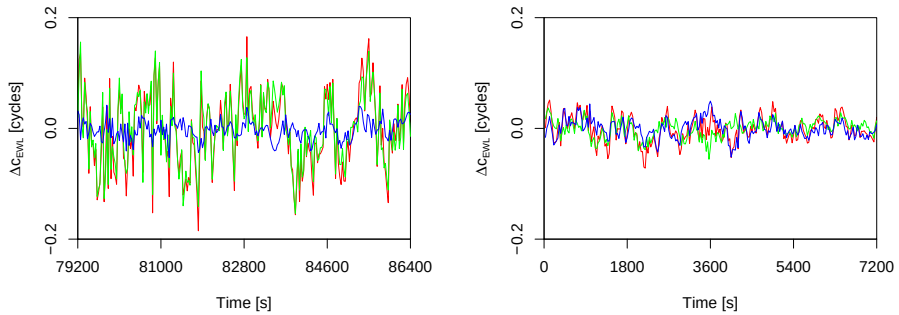

(a) (b)

Figure 5.6 *– Influence of multipath delays and measurement noise on GPS (a) and Galileo (b) EWLNL combination (red = total, green = codes only, blue = phases only).*

Figure 5.7 shows the part of Δc_{WL} due to multipath delays and measurement noise for a whole satellite pass, respectively for GPS and Galileo. For both GPS and Galileo, the influence of phase delays is negligible with regards to the influence of code ones*, which is linked to the wavelength of the combination, or in particular to the f_{km} coefficient. This coefficient is one order of magnitude larger than in the EWLNL case, and is approximately the same for GPS ($f_{12} = 0.1240$) and Galileo ($f_{12} = 0.1323$). In total, the influence is two times larger for GPS than for Galileo, which is due to the higher code multipath and noise level on L1/L2 observables.

As stated in section 4.3.1.1, the use of a running average filter allows us to obtain an increasingly precise value of the widelane ambiguities. Since the magnitude of the residual term is mainly driven by code hardware delays, the improvement of precision is not significant.

*and therefore with regards to the total influence

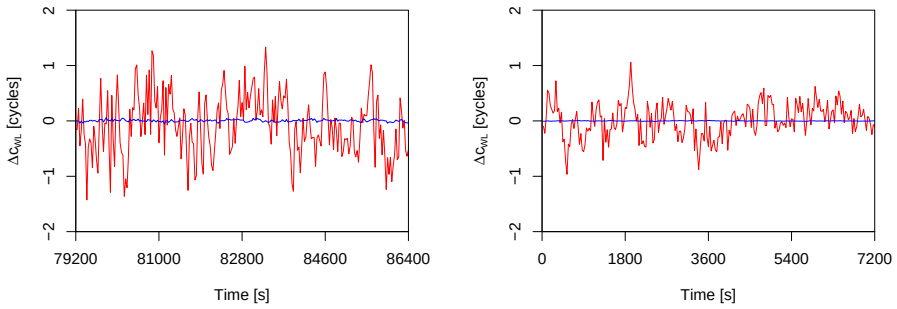

(a) (b)

Figure 5.7 *– Influence of multipath delays and measurement noise on GPS (a) and Galileo (b) WLNL combination (red = total, blue = phases only).*

5.3.1.2 Differenced widelane combinations

The differenced widelane combination (φ_{DWL}) is a GF but not IF phase combination which uses the extra–widelane (EWL) ambiguities to resolve the widelane (WL) ambiguities. Equation (4.87) shows that the non-ambiguity term can be divided into two parts: the phase delays (noise, multipath, hardware) and the ionospheric delays. As stated in section 4.3.1.2, the resolution of the WL ambiguities is feasible if we use an estimation of the ionospheric delays or TEC together with a running average filter. The accuracy of TEC has to be better than 5 TECU, which is generally feasible for mid-latitude regions in period of low solar activity. We will thus only assess the magnitude of the multipath and noise of the residual term.

We consider the influence of phase multipath delays and phase measurement noise together. Figure 5.8 shows the part of $\Delta\varphi_{DWL}$ due to multipath delays and measurement noise respectively for GPS and Galileo. It can be observed that the effect is smaller for GPS than for Galileo: this is due to the $\lambda_{EWL}/\lambda_{WL}$ coefficient that is 6.8 for GPS and 12 for Galileo (see equation (4.82)). In both cases, the influence is smaller than 1 cycle, and even smaller than 0.5 cycle for GPS. Therefore the use of a running average filter is useful to obtain an increasingly precise value of the WL ambiguities. As a matter of fact, it can be observed in figure 5.9 (a) that the effect of noise and multipath averages down to zero after several epochs.

5.3.2 Triple frequency phase multipath combination

The triple frequency phase multipath combination ($\Phi_{M,125}$) is a triple frequency combination of phase measurements which is GF and IF. As stated in section 4.3.2, this combination is used to resolve the original ambiguities N_{L2} (and thus N_{L1} and N_{L5}). The residual term ΔN_{L2} depends on phases delays only, namely satellite and receiver hardware delays, multipath delays and measurement noise (see equation (4.112)). In order to determine the feasibility of the ambiguity resolution, we will assess the magnitude of this residual term.

We will consider the influence of phase multipath delays and phase measurement noise

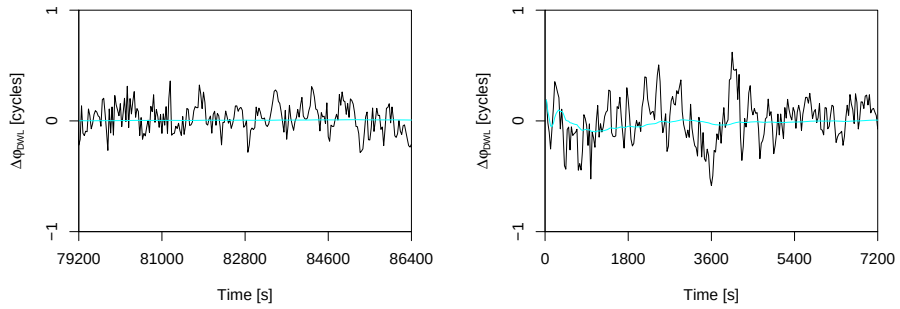

(a) (b)

Figure 5.8 *– Influence of multipath delays and measurement noise on GPS (a) and Galileo (b) DWL combination (cyan = running average).*

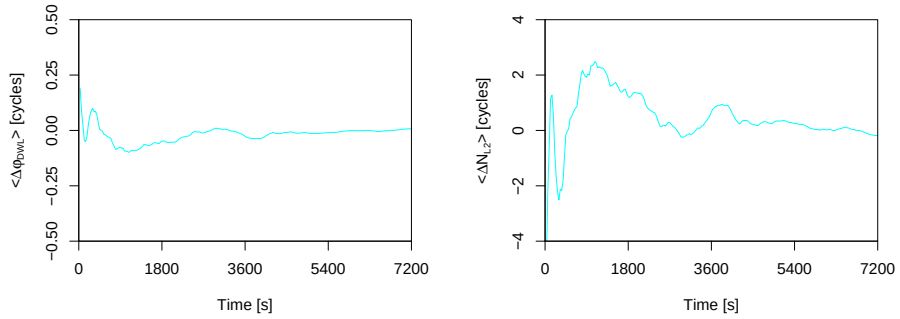

(a) (b)

Figure 5.9 *– Running average of the influence of multipath delays and measurement noise on Galileo DWL combination (a) and triple frequency phase multipath combination (b).*

together. Figure 5.10 shows the part of ΔN_{L2} due to multipath delays and measurement noise, respectively for GPS and Galileo. We can see that in both cases the total influence is much larger than one cycle, which is not acceptable for ambiguity resolution. Moreover, due to the combinations of frequencies*, GPS performs here better than for Galileo.

To reduce the influence of the residual term, we have to apply a running average filter on triple frequency phase multipath combination to obtain $\langle \Phi_{M,125} \rangle$. The corresponding remaining part of the residual term due to multipath delays and measurement noise ($\langle \Delta N_{L2} \rangle$) is shown in figure 5.10. It can be observed in figure 5.9 (b) that the influence averages down to zero over a short time.

The influence of the satellite and receiver phase hardware delays on the original ambigui-

*The denominator of equation (4.110) is equal to $1.5 \cdot 10^{-5}$ m for GPS and to $9 \cdot 10^{-4}$ m for Galileo.

ties (and therefore on the TEC) will be discussed in the next section.

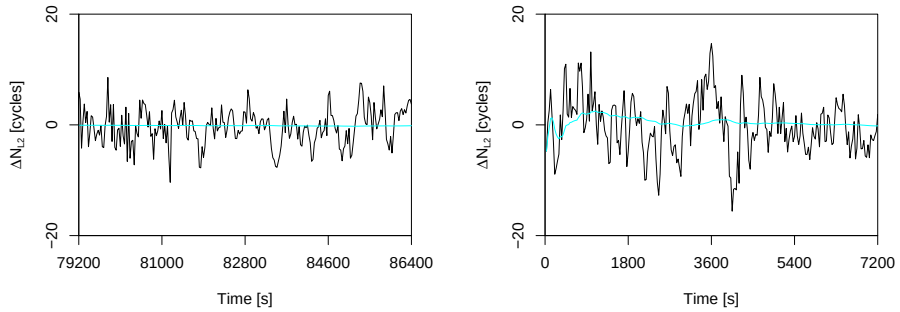

(a) (b)

Figure 5.10 *– Influence of multipath delays and measurement noise on GPS (a) and Galileo (b) triple frequency phase multipath combination (cyan = running average).*

5.4 TEC reconstruction

As seen in section 3.2.1, once we obtain the original ambiguities, it is possible to reconstruct the GF ambiguities $N_{GF,km}$ by using equation (3.58), and then to reconstruct the TEC by using equation (4.118). The objective is now to assess the precision and accuracy of the reconstructed TEC values.

Regarding the conclusions given in section 4.6, the precision of the TEC values (E_r) depends on the magnitude of phase multipath delays and phase measurement noise. Figure 5.11 shows the influence of multipath and measurement on the reconstructed TEC values using the three possible GF phase combinations. As already stated in theory (section 4.4), it can be observed that the influence is one order of magnitude larger when using $\Phi_{GF,25}$ than when using $\Phi_{GF,12}$ or $\Phi_{GF,15}$. Since phase multipath delays and phase measurement noise have the same magnitude on L1, L2 and L5, this difference is only due to the α_{km} coefficient. Moreover, the influence of multipath and noise has the same magnitude for GPS and Galileo, except for $\Phi_{GF,25}$, which can also be explained by the α_{km} coefficient values.

In total, when using L1/L2 or L1/L5 GF phase combination, the precision of the reconstructed TEC values from simulated data is about 0.1 TECU for GPS and Galileo.

As far as the accuracy of the reconstructed TEC is concerned, it is mainly determined by the influence of phase hardware delays on the original ambiguities ($\Delta \mathrm{TEC}_{r,N}$). We simulate the satellite and receiver phase hardware delays on each frequency as random values smaller than a given threshold (see section 5.2.2.8). The hardware delays are thus different and independent between the different frequencies. However, we know that hardware delays are actually frequency-dependent effects. For this reason, we compare the influence of phase hardware delays on the original ambiguities in two extreme cases, both assuming constant delays over a satellite pass:

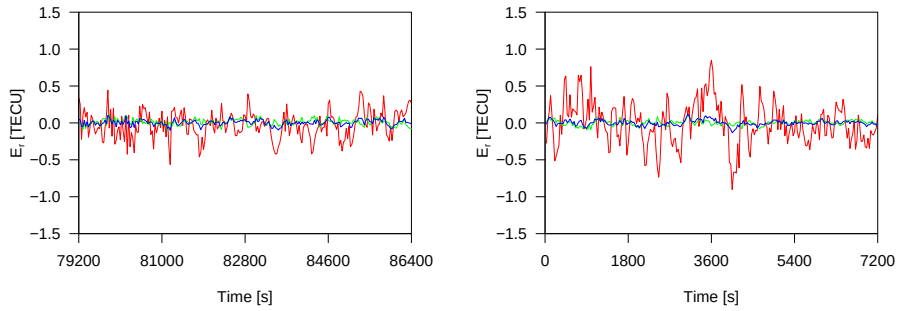

(a) (b)

Figure 5.11 *– Influence of multipath delays and measurement noise on GPS (a) and Galileo (b) reconstructed TEC values with L2/L5 (red), L1/L2 (green) and L1/L5 (blue) GF phase combination.*

- in one case, we simulate phase hardware delays as random values (frequency-independent),
- in the other case, we simulate phase hardware delays as being directly proportional to the carrier frequency (frequency-dependent).

Figure 5.12 shows the error caused by phase hardware delays on the GPS and Galileo reconstructed TEC values ($\Delta \mathrm{TEC}_{r,N}$) in these two cases as a function of the magnitude of the phase hardware delays. We can retrieve the results obtained in section 4.4.2.4, i.e. the error on TEC_r caused by frequency-independent phase hardware delays with a magnitude of 1 mm is around 0.5 TECU for GPS and 1 TECU for Galileo. It has also to be noted that the error induced by phase hardware delays on the reconstructed TEC values is significantly reduced when the phase hardware delays are considered to be directly proportional to the carrier frequency. However, the real behavior of phase multipath delays might be in-between the two cases considered here. Therefore, even though phase hardware delays might be larger than 1 mm, their influence on the resolution of the original ambiguities, and therefore on the reconstructed TEC values might be smaller than 1-2 TECU for GPS and Galileo. In these conditions, the accuracy of the reconstructed TEC is improved in regards with existing dual frequency techniques. Nevertheless, if the phase delays are larger than 1 mm and are not proportional to the frequency, the accuracy of the reconstructed TEC could be strongly degraded to a level of several TECU. Once calibration procedures of the phase hardware delays will be available, this probem will be overcome.

5.5 Conclusions

This chapter was dedicated to triple frequency TEC reconstruction with simulated GNSS measurements.

First we developed a simulation software to provide triple frequency GPS and Galileo code and phase measurements. Since at the beginning of our research, real triple frequency

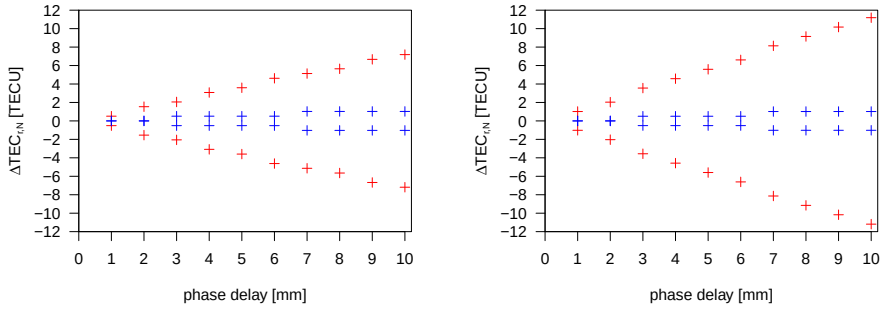

Figure 5.12 *– Error caused by phase hardware delays on GPS (a) and Galileo (b) reconstructed TEC values at a 99 % level of confidence (red = frequency-independent, blue = frequency-proportional)*

data were not available yet, this software has been an essential tool to conceive the TEC reconstruction methodology. We put an emphasis on simulating the error sources which have an influence on the ambiguity resolution and TEC reconstruction procedures as realistically as possible. For that purpose, advanced simulation tools were developed to generate multipath delays and measurement noise:

- measurement noise is simulated as Gaussian white noise,
- multipath delays are simulated as time-correlated Gaussian white noise.

Finally, the software allowed us to constitute a observation dataset for testing the TEC reconstruction methodology developed in chapter 4.

Then we used a dataset of simulated GPS and Galileo measurements to test the feasibility of the ambiguity resolution procedure, i.e.:

- resolution of the widelane ambiguities using the widelane-narrowlane and differenced widelane combinations,
- resolution of original integer ambiguities by substituting the widelane ambiguities in the triple frequency phase multipath combination.

For each combination used, we addressed a quick review of their characteristics and estimated the influence of the frequency-dependent effects (residual term) on the ambiguity resolution, and in particular the influence of measurement noise and multipath delays. Since the influence of code hardware delays can be overcome by the use of the DWL combination and/or by using the code hardware delay calibration methodology (see chapter 4), we have only studied the influence of phase hardware delays on the accuracy of the TEC values. Moreover, since these effects can actually be corrected at the cm-level accuracy, the influence of satellite/receiver antenna PCOs/PCVs and phase wind-up effect was not considered in this chapter.

Finally, the dataset was also used to assess the precision and accuracy of the reconstructed TEC values. The precision of the reconstructed TEC values from simulated data is about 0.1 TECU for GPS and Galileo. We tested the influence of phase hardware delays on the reconstructed TEC values. We concluded that even though phase hardware delays might be larger than 1 mm, their influence on the resolution of the original ambiguities, and therefore on the reconstructed TEC values might be smaller than 1-2 TECU for GPS and Galileo. In these conditions, the accuracy of the reconstructed TEC is improved in regards with existing dual frequency techniques. Nevertheless, if the phase delays are larger than 1 mm and are not proportional to the frequency, the accuracy of the reconstructed TEC could be strongly degraded to a level of several TECU. This problem will be overcome once estimated phase delays are available.

Chapter 6

Triple frequency TEC reconstruction using real data

THIS chapter is dedicated to triple frequency TEC reconstruction with real GNSS measurements. After a short introduction (6.1), the second section (6.2) describes the GIOVE dataset which will be used for TEC reconstruction. The third section (6.3) deals with the preprocessing of the observation and navigation data. The fourth (6.4) and fifth (6.5) sections present the results of the ambiguity resolution process and TEC reconstruction. The sixth section (6.6) addresses the results of the satellite and receiver code hardware delay calibration. Finally, we provide the conclusions of the chapter in section 6.7.

6.1 Introduction

Since the launch of the two Galileo In-Orbit Validation Element (GIOVE) satellites, real triple frequency code and phase measurements are available and can be used to validate the Total Electron Content (TEC) reconstruction technique developed theoretically in chapter 4 and tested on simulated data in chapter 5. Besides, since one Global Positioning System (GPS) satellite already emits the third civil signal (L5), we could also test the TEC reconstruction on real GPS data. The presence of thermally induced line bias variations were detected on this satellite [78]. Since theses variations appear to be non-negligible and frequency-dependent, TEC reconstruction would not give reliable results. For this reason, we choose to test the method on GIOVE data only.

6.2 GIOVE dataset

As already seen in section 2.1.2.3, a global network of 13 sensor stations, referred to as Galileo Experimental Sensor Stations (GESS) has been settled for the needs of GIOVE in-orbit validation activities. Table 6.1 gives an overview of the GESS network, while figure 6.1 shows GESS locations.

Table 6.1 *– Overview of the GESS network [86].*

Station name	Location	Country
GIEN	INRiM, Turin	Italy
GKIR	Kiruna	Sweden
GKOU	Kourou	French Guyana
GLPG	La Plata	Argentina
GMAL	Malindi	Kenya
GMIZ	Mizusawa	Japan
GNNO	New Norcia	Australia
GNOR	ESA, Noordwijk	The Netherlands
GOUS	Dunedin	New Zealand
GTHT	Tahiti	French Polynesia
GUSN	USNO, Washington	USA
GVES	Vesleskarvet	Antarctica
GWUH	Wuhan	China

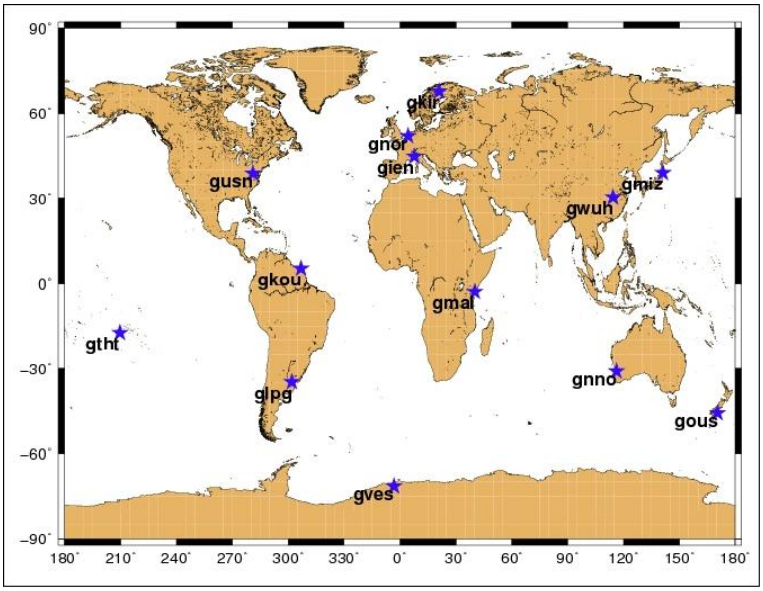

Figure 6.1 *– GESS locations [86].*

The Galileo Experimental Test Receiver (GETR) developed by Septentrio [113] with which each GESS station is equipped is a dual-constellation (GPS and Galileo) multi-frequency receiver that includes 35 channels, with 7 channels dedicated to Galileo. GETR is configured to generate the GIOVE code and phase observables shown in table 6.2.

As stated in chapter 4, code and phase measurements on L1, E5b and E5a are required for triple frequency TEC reconstruction (see table 4.1). The GIOVE-A/-B dataset used for the

Table 6.2 *– GIOVE code and phase observables available from GETR [113].*

Signal	Frequency [MHz]	Pilot/Data	Code	Phase
L1	1575.42	Data	C1A	L1A
		Data	C1B	L1B
		Pilot	C1C	L1C
E5b	1207.14	Pilot	C7Q	L7Q
E5a	1176.45	Data	C5I	L5I
		Pilot	C5Q	L5Q
E5a+b	1191.795	Pilot	C8Q	L8Q

research has been provided by the European Space Agency (ESA). Considering that GIOVE-A satellites only transmit two frequency bands at a time (L1+E5 or L1+E6), we need a period where the satellite transmits on L1+E5. The dataset consists thus of a set of L1+E5 GIOVE-A/-B data for four stations in 2008. We use the pilot dataless component of each signal, defined in section 2.1.2.2. Table 6.3 presents the GIOVE code and phase observables which are used for TEC reconstruction. As previously, L1, E5b and E5a, are more conveniently named L1, L2 and L5, respectively.

Table 6.3 *– GIOVE code and phase observables for triple frequency TEC reconstruction.*

Signal	GIOVE observable	
	code	phase
L1	C1C	L1C
L2	C7Q	L7Q
L5	C5Q	L5Q

Table 6.4 gives all information about the dataset, i.e. the satellite, station, Day of Year (DOY), number of period of each study case, associated to a study case number for more convenience. For GIEN, GKOU and GNOR stations we only have GIOVE-A data, and for GMIZ only GIOVE-B data. Unfortunately, for a given station, the data are not always consecutive days. We have at our disposal observation data (*.O files) in Receiver Independent Exchange (format) (RINEX) [39] at 1 s sample interval and navigation data in Standard Product # 3 Orbit (format) (SP3) [119] at 15 min sample interval. Before being able to process those data for any application, and particularly for TEC reconstruction, some preprocessing is required for both observation (e.g. cycle slip detection) and navigation (e.g. orbit interpolation) data. This is explained in detail in the next section.

Table 6.4 *– GIOVE post-processed dataset.*

Satellite	Station	DOY 2008	Period	Study case
GIOVE-A	GIEN	013	1	1
		013	2	2
		016	1	3
		017	1	4
		020	1	5
GIOVE-A	GKOU	015	1	6
		018	1	7
GIOVE-A	GNOR	013	1	8
		013	2	9
		016	1	10
		017	1	11
		019	1	12
		020	1	13
GIOVE-B	GMIZ	337	1	14
		338	1	15
		341	1	16
		344	1	17
		345	1	18

6.3 Data preprocessing

6.3.1 Observation data

6.3.1.1 Cycle slip detection

In order to attain high precision in applications using Global Navigation Satellite System (GNSS) phase measurements, it is necessary to detect and handle cycle slips.

A cycle slip can be defined as a sudden jump in the phase measurement that is always an integer number of cycles. This integer may be small (1 or a few cycles) or could be millions of cycles. A cycle slip is schematically represented in figure 6.3.

A cycle slip occurs – independently on each carrier frequency – if the receiver loses the phase lock loops of the satellite signal. There are three main sources for that loss of lock. Firstly – and most frequently –, a cycle slip can be due to an obstruction of the satellite signal by some obstacles (trees, buildings...). Secondly, it can be due to a low Signal-to-Noise Ratio (SNR) caused by low elevation angle, bad ionospheric conditions, multipath delays, etc. Thirdly, a failure in the receiver software can cause a cycle slip [52, 69, 107].

A lot of different methods dealing with cycle slips have been discussed in the literature. First of all, two solutions have to be distinguish: either cycle slips are detected at a given epoch t, and from t a new ambiguity parameter has to be determined (*cycle slip detection*), or

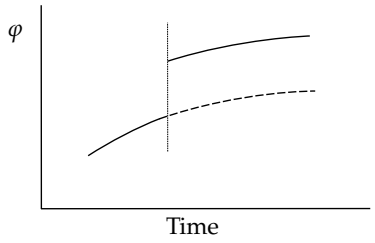

Figure 6.2 *– Representation of a cycle slip.*

cycle slips are detected and then repaired (*cycle slip fixing*). In this work, we will apply the first approach only. As GNSS phase measurements are used to monitor the state of the ionosphere, it is critical to deal reliably with cycle slips in order to have correct and continuous phase and thus TEC measurements. It is particularly true during disturbed ionospheric conditions (see section 3.1.3.5), when receivers are more prone to cycle slip effect [6], and when it is essential to obtain reliable TEC values.

All cycle slip detection processes are based on quantities derived from the observations, namely on linear combinations of the undifferenced code and phase measurements (test quantities). Once the times series of the derived quantities have been computed, the cycle slip detection process consists in detecting discontinuities in those times series. For that purpose, there are four main methods in use; it is possible to:

- compute higher order Time Differences (TDs) of the times series [52, 60],
- fit a low degree polynomial over the time series [52],
- use a dynamic model to predict the subsequent observations in the time series (Kalman filtering [10], wavelets [21]),
- apply a running average filter to the times series [15, 16].

The first test quantity that may be used is the code-phase combination $r_{CP,k}$ [m] [10, 107]:

$$r_{CP,k} = P^i_{p,k} - \Phi^i_{p,k} \tag{6.1}$$

where $k \in \{\text{L1}, \text{L2}, \text{L5}\}$

Using equations (2.69) and (2.71), and neglecting hardware delays, equation (6.1) becomes:

$$r_{CP,k} = \lambda_k N^i_{p,k} + 2\, I^i_{p,k} + M^i_{p,g,k} - M^i_{p,\Phi,k} + \varepsilon^i_{p,g,k} - \varepsilon^i_{p,\Phi,k} \tag{6.2}$$

It comes from equation (6.2) that this combination is Geometric-Free (GF), so that it slowly changes between consecutive epochs. That allows cycle slips to be detected as sudden jumps in the times series. One drawback of the code-phase combination is that it depends on the ionosphere: in case of high ionopsheric activity it is difficult to distinguish between the variations in the combinations due to cycle slips and the variations due to the ionosphere. Another limitation of this combination is its noise level, preventing the detection of small cycle slips.

A second combination used for cycle slip detection is the GF phase combination $\Phi_{GF,km}$ [m] (which is also used for TEC reconstruction):

$$\Phi_{GF,km} = \Phi^i_{p,m} - \Phi^i_{p,k} \tag{6.3}$$

This combination was initially used on L1/L2 carrier frequencies [10, 38] but in triple frequency GNSS processing, it can obviously be used on L1/L5 or on L2/L5. As stated in section 3.2.1, this combination is a function of frequency-dependent effects. Equation (3.51) shows that the main variability with time is caused by ionospheric delays. In other words, this combination has the advantage of varying slowly with time and, in normal ionospheric conditions, cycle slips are detected as sudden jumps in the time series. In [15] this combination has been used in the form of TDs [60]. The median of the four TDs is compared with the TD to be tested, and if the difference is greater than a given threshold, a cycle slip is detected.

However, in period of high ionospheric activity, there is a risk to interpret abrupt variations in the ionosphere as cycle slips. Note that we had the opportunity to experience that problem with the data corresponding to the severe geomagnetic storms of October 29-30 and November 20 2003, associated to TEC temporal gradients of 9 TECU/min [70].

Moreover, if cycle slips occur on both frequencies, and for some combinations of cycle slips, the effect on $\Phi_{GF,km}$ is small and the detection is therefore not possible. Thus, there are some specific cycle slip pairs which cannot be detected [25].

In [25] the cycle slip detection has been extended to the triple frequency case. The study shows that by properly choosing two triple frequency GF phase combination it is possible to detect all cycle slip groups, except the so-called *most insensitive* cycle slips – which are proportional to the carrier frequency. The concerned combinations are named *first optimal phase combination* ($\Phi_{cs,1}$) and *second optimal phase combination* ($\Phi_{cs,2}$):

$$\Phi_{cs,1} = -\Phi^i_{p,\mathrm{L1}} - \Phi^i_{p,\mathrm{L2}} + 2\,\Phi^i_{p,\mathrm{L5}} \tag{6.4}$$

$$\Phi_{cs,2} = -\Phi^i_{p,\mathrm{L1}} + 4\,\Phi^i_{p,\mathrm{L2}} + 3\,\Phi^i_{p,\mathrm{L5}} \tag{6.5}$$

More than just being GF, these combinations minimize the non-ambiguity term, i.e. ionospheric delays and measurement noise in order to be able to detect the possible cycle slips. Therefore, these combinations fulfill the ionosphere- and noise-reduced criteria given in section 4.2.4.2 and 4.2.4.3, respectively. Even if this triple frequency approach performs better than the dual frequency one (the number of insensitive cycle-slips is decreased), it is still sensitive to disturbed ionospheric conditions.

In the case of differential positioning, the data of the two stations can be combined to form Single Difference (SD), Double Difference (DD) and triple differences that can be used as testing quantities for cycle slip detection. As we only use undifferenced data, we refer to [107] for more details.

More recently, in response to the drawbacks of the other methods, several authors have proposed to use the widelane-narrowlane combination $c_{wl,km}$ [cycles] which is defined in section 4.3.1.1:

$$c_{wl,km} = \varphi^i_{p,k} - \varphi^i_{p,m} - \frac{f_k - f_m}{f_k + f_m}\left(\frac{f_k}{c}P^i_{p,k} + \frac{f_m}{c}P^i_{p,m}\right) \tag{6.6}$$

Initially this combination was used on L1/L2 [15, 16]. For triple frequency GNSS, it can be extended to L1/L5 and L2/L5. These combinations are defined by equations (4.64), (4.66) and (4.62). As already stated in section 4.3.1.1, the widelane-narrowlane combination is GF and Ionospheric-Free (IF). Equation (4.57) shows that the main variability with time comes from code multipath delays and code measurement noise. Those fluctuations make cycle slip detection impossible. Therefore, it is adequate to apply a running average filter to the combination, so that multipath and noise terms average down to more or less constant values, making cycle slip detection likely [16]. As with the Kalman filtering approach, this method has the advantage of using statistical information from the observation data themselves. However, the initial parametrization – the choice of the *a priori* variance – is not critical here.

This low pass-filter cycle slip detection process is applied as follows:

1. We compute the running mean $\langle x_t \rangle$ and the running standard deviation σ_t^2 of the combination, defined as [15]:

$$\langle x_t \rangle = \langle x_{t-1} \rangle + \frac{1}{t} \left(x_t - \langle x_{t-1} \rangle \right) \tag{6.7}$$

$$\sigma_t^2 = \sigma_{t-1}^2 + \frac{1}{t} \left[\left(x_t - \langle x_t \rangle \right)^2 - \sigma_{t-1}^2 \right] \tag{6.8}$$

   where x_t is the observation ($x_t = c_{wl,km}$) and σ_t the standard deviation of the observation at epoch t.
   This is a recursive approach: the mean and the standard deviation are computed and updated epoch by epoch.

2. We calculate the corresponding confidence interval $\langle x_t \rangle \pm 4\,\sigma_t$

3. If the current value of the combination is outside that interval, i.e.

$$x_t > \langle x_t \rangle \pm 4\,\sigma_t \tag{6.9}$$

   then the observation x_t is declared to be an "outlier".

4. If there are two consecutives outliers, and if the previous (x_{t-1}) and subsequent (x_{t+1}) observations lie outside and within one cycle, respectively:

$$x_{t-1} - x_t > 1 \tag{6.10}$$

$$x_{t+1} - x_t < 1 \tag{6.11}$$

   then we declare that a cycle slip has occurred at t, and we re-initialize all parameters. We start a new period and define a new ambiguity term, implying that a new ambiguity parameter will have to be determined.

5. If there is just one isolated outlier, it is removed from the dataset, but the parameters are kept.

Figure 6.3 shows the widelane–narrowlane (WLNL) combination (x_t), its running mean ($\langle x_t \rangle$) and confidence interval (at $\pm 4\,\sigma_t$) for one study case. Since the combination remains inside the confidence interval, no cycle slip is detected.

One drawback of this method is that it does not allow the detection of cycle slips whose values would be equal on f_k and f_m frequency (equation (6.6)). However even though this is known to be rare [16], it could be better to use a second combination to avoid this issue.

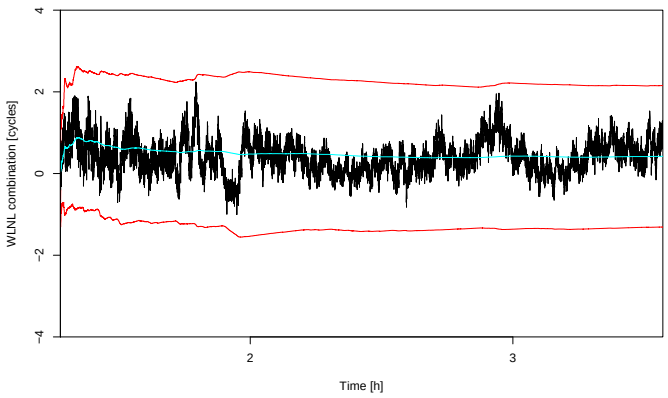

Figure 6.3 *– WLNL combination, running mean (cyan) and confidence interval (red) for GNOR DOY 013/08.*

Another weakness of the method is its lack of robustness. The statistical parameters, and therefore the detection of eventual cycle slips can be influenced by several particular conditions, e.g. at the beginning of a period and/or in presence of strong code multipath delays. To avoid this problem, it is possible to add test conditions in the algorithm. Another solution could be to use a moving average filter algorithm (instead of running) in order to better fit the raw data and thus follow the effects of code multipath delays. Nevertheless, the use of a second test quantity allows us to compensate for this lack of robustness.

In the present study, we need to tackle the triple frequency detection problem. In coherence with the combinations used for TEC reconstruction, we have implemented the following cycle slip detection algorithm:

- A running average filter is applied on the three widelane-narrowlane combinations (c_{EWL} , c_{WL} and c_{ML}).
- A complementary cycle slip detection is processed with the so-called *first and second optimal phase combinations* ($\Phi_{cs,1}$ and $\Phi_{cs,2}$) by the means of time differencing. This allows us to overcome the drawbacks of the first detection step.

6.3.1.2 Antenna PCO and PCV corrections

As aforementioned in section 2.2.2.10, the satellite antenna Phase Center Variations (PCVs) and the receiver antenna Phase Center Offsets (PCOs) and PCVs are frequency-dependent effects. Therefore, they have an influence on TEC reconstruction and need to be corrected coherently with the International GNSS Service (IGS) conventions previously defined.

However, the antenna PCO and PCV corrections are not available yet for the GIOVE data (neither for the satellites or the stations). The code and phase measurements of the GIOVE dataset used for TEC reconstruction can thus not be corrected. This will affect the TEC values by unknown error. In order to have an idea of what would be the error on the reconstructed TEC values, we will use an example of antenna corrections and propagate their influence in

the TEC reconstruction methodology. Actually, since the satellite antenna PCV corrections are provided for the IF linear combination and not for L1 and L2 separately, it is only possible to estimate the influence of the receiver antenna PCOs and PCVs on L1 and L2 measurements. It has to be stressed that we do not have antenna corrections values for the L5 frequency at our disposal.

In practice, we use the absolute receiver antenna PCO and PCV corrections provided for the common antenna "LEIAR25.R3" and radome "LEIT" in the *igs08.atx* file. We have computed their effect on code and phase measurements (i.e. the $pco_{p,k}$ and $pcv_{p,k}$ terms) corresponding to one GIOVE study case (#3, see table 6.4). It is rather straightforward to obtain the $pco_{p,k}$ term by using equations (2.56) to (2.59). To obtain the $pcv_{p,k}$ term, the scalar values provided in the IGS antenna file need to be interpolated* to match the values of elevation and azimuth angles of the study case. Figure 6.4 shows the $pco_{p,k}$ and $pcv_{p,k}$ terms for L1 and L2 frequencies in the considered study case. It is worth noting that the $pcv_{p,k}$ terms are one order of magnitude smaller than the $pco_{p,k}$ terms.

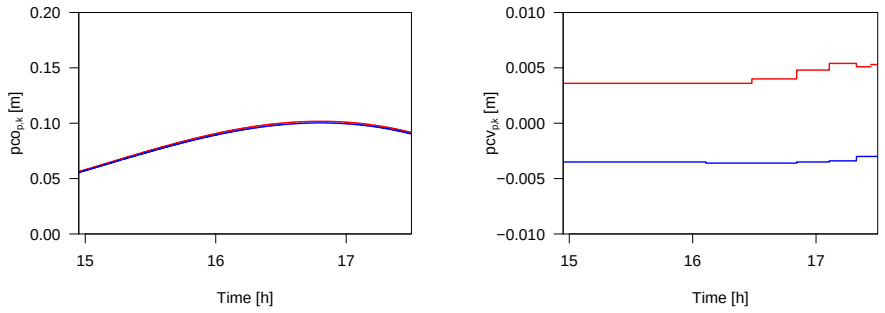

(a) (b)

Figure 6.4 *– Receiver antenna PCO (a) and PCV (b) on L1 (red) and L2 frequencies (blue) for GIEN DOY 016/08.*

Once we have computed the $pco_{p,k}$ and $pcv_{p,k}$ terms for L1 and L2 frequencies, we sum them and propagate their combined influence on the TEC reconstruction methodology.
Since we have no antenna correction for L5 frequency, it is not possible to estimate properly the error caused by the receiver antenna PCOs and PCVs on the extra–widelane–narrowlane (EWLNL) combination (c_{EWL}). Nevertheless, using the values for L1 and L2 frequencies, we can attribute approximated values to $pco_{p,k}$ and $pcv_{p,k}$ terms for L5. By doing so, we found that this error has the same magnitude as on the WLNL combination (c_{WL}), which is found to be smaller than 0.04 cycles (see figure 6.5). We have to use the same trick to estimate the effect on the differenced widelane (DWL) combination (φ_{DWL}), which is found to be about 0.2 cycles. This might cause a problem for the widelane (WL) ambiguity resolution, depending on the accuracy of the dual frequency TEC estimation (see section 4.3.1.2). However, the receiver PCOs and PCVs will not have an influence on the ambiguity resolution if we use c_{EWL} and c_{WL} combination together with the code hardware delay information, as explained in section 4.5.1. Following the same procedure, the error caused by the receiver antenna PCOs and PCVs on

*We use the bivariate interpolation algorithm defined in section 3.2.3.2.

the N_{L2} ambiguities causes an error about 5 TECU on TEC_r , while the error on the L1/L2 GF phase combination induces an error smaller than 0.1 TECU on TEC_r (see figure 6.5).

Finally, we will have to consider that the final reconstructed TEC values could be biased by a non-negligible error caused by the satellite antenna PCVs and by the receiver antenna PCOs and PCVs. Nevertheless, once the GIOVE corrections will be available, the influence of these effects will be reduced to about 0.025 TECU (see section 4.4.2.1).

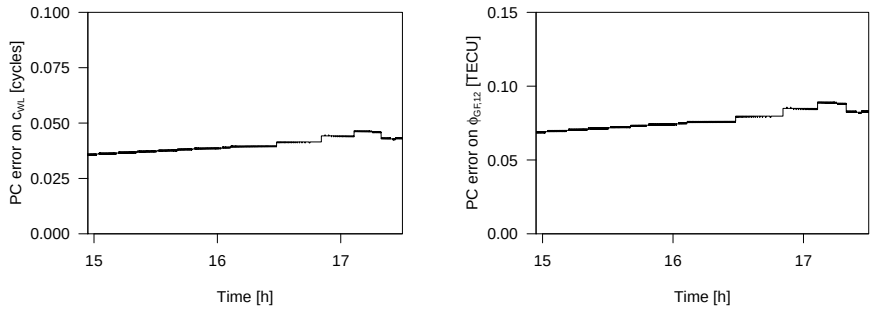

Figure 6.5 *– Error caused by the receiver antenna PCOs and PCVs on the WLNL combination (a) and on the L1/L2 GF phase combination (b) for GIEN DOY 016/08.*

6.3.1.3 Phase wind-up correction

As stated in section 2.2.2.12, GNSS phase measurements are affected by the phase wind-up effect ω_p^i [cycles]. Since it has a non-negligible influence on undifferenced measurements, this effect needs to be taken into account in the data preprocessing. We have applied the algorithm given by equations (2.63) to (2.66). Once the correction is computed, we subtract the phase wind-up effect from the phase measurements, following equations (2.70) and (2.71):

$$\varphi_{p,k}^i \quad - \quad \omega_p^i \tag{6.12}$$

$$\Phi_{p,k}^i \quad - \quad \lambda_k \, \omega_p^i \tag{6.13}$$

The influence of the non-corrected phase wind-up effect has been assessed in section 4.4.2.1. We have concluded that the phase wind-up correction is accurate enough for the triple frequency TEC reconstruction. From now on, we can thus assume that the phase measurements are free from phase wind-up effect.

6.3.2 Navigation data

As stated in section 6.2, GIOVE precise orbits are given in SP3 format at 15 min sample interval, from 00:00:00 through 23:45:00 for a single day. Therefore the preprocessing involves

interpolating these ephemeris to obtain the satellite position at any considered epoch between the 15 min given positions. In our case, we need to match the observation data given at the 1 s sample interval. The satellite coordinates are given in the Earth-Centered-Earth-Fixed (ECEF) coordinate system in units of kilometers.

There are several mathematical functions and software available which are suitable for such orbit interpolation: Lagrange, Neville or Chebyshev polynomial methods, and trigonometric function methods. Contrary to Lagrange and Neville's algorithms, the two other algorithms allow the use of n-term polynomials to fit more than n data points (least-square estimation), which generally leads to better interpolation results.

In [34] the authors compare the performance of each interpolator in four different schemes. The basic test procedure consists of interpolating a given *source* ephemeris at the 15 min sample interval to produce satellite coordinates at shorter interval (5 min or 30 s), and then compare it to a *control* ephemeris given at the shorter interval. The primary requirement is that the interpolation process may not degrade the original information, which means the interpolation errors have to be smaller than the ephemeris accuracy, i.e. 5 cm (see table 2.4). Since a common problem of all algorithms is the performance degradation near the ends of the interpolation interval, particular attention was paid to this issue in that study. Interpolation results show that the 9-term trigonometric polynomial method is the optimal method for a 2 h GPS orbit arc (9 data points), especially with regards to the endpoints. Nevertheless, the performance of the other methods with the 9-term polynomial is just slightly lower.

In [103], the same basic test procedure is applied. Here, only two interpolation strategies are considered: the Neville polynomial and the trigonometric function. As the Neville algorithm is a simple recursive algorithm [87], it can be associated with the use of the so-called Walk-Along interpolation strategy. This strategy consists of producing the polynomial successively, i.e. to select the source ephemeris data point at each interpolation epoch. The associated code for comparing different techniques for interpolating precise ephemerides in SP3 format is given in [104]. This study shows that both interpolation strategies are more than adequate (interpolation errors smaller than 5 cm) if the 9-term to 13-term polynomial are used.

We have tested the interpolation strategies by applying the same test procedure to several sets of precise GPS ephemerides. The results show that the 12-term Neville polynomial (with Walk-Along strategy) appears to be the best choice. This strategy is therefore applied to interpolate the GIOVE source ephemeris data.

The Neville interpolation algorithm allows us to evaluate the polynomial $P_{ij}(x)$ at a given point x with a recursive approach. Given a set of $n+1$ data points (x_i, y_i), we can write $P_{ii}(x_i) = y_i$ for all $i = 0, ...n$. If P_{ij} is the polynomial of degree $j-i$ evaluated through the points (x_k, y_k) for $k = i, i+1, ...j$, we have the following recurrence [87]:

$$P_{ii}(x) = y_i \qquad 0 \leq i \leq n \tag{6.14}$$

$$P_{ij}(x) = \frac{(x - x_j)P_{i,j-1}(x) + (x_i - x)P_{i+1,j}(x)}{x_i - x_j} \qquad 0 \leq i < j \leq n \tag{6.15}$$

For satellite orbit interpolation, $P_{ij}(x)$ represents the X^i, Y^i or Z^i interpolated satellite coordinate value at the time x, while y_i is the X^i, Y^i or Z^i satellite coordinate from the source ephemeris. It has to be stressed that the Neville algorithm evaluates the polynomial directly without computation of polynomial coefficients.

As stated in section 2.2.2.4, those satellite coordinates still need to be corrected for the Earth rotation effect. Since this correction requires the computation of the geometric distance (ρ_p^i), this is performed in the next section.

6.3.3 Post-processed GIOVE dataset

Since the preprocessing of both observation and navigation data is accomplished, we can compute the geometric distance between the satellite and the receiver (ρ_p^i) by using equation (2.10). This geometric distance is then corrected the Earth rotation effect using the algorithm described in section 2.2.2.4.

The satellite zenith angle at the receiver (χ) and the satellite azimuth angle at the receiver (A) are obtained by using equation (5.12) and (5.13), respectively. We also derive the parameters of the ionospheric points along the satellite path: cartesian ($\mathbf{X_{IP}}$) and ellipsoidal ($\varphi_{IP}, \lambda_{IP}$) coordinates, satellite zenith angle (χ_{IP}) and local time (h).

We apply a elevation mask which keeps only the observation data where:

$$\chi < 70^\circ \leftrightarrow e > 20^\circ \tag{6.16}$$

This criterion helps to have an average value of code multipath delays sufficiently close to zero over a satellite pass. We have thus constituted the observation GIOVE dataset which is available for testing the TEC reconstruction technique.

The skyplots for GIEN, GKOU, GNOR and GMIZ stations are shown in figure 6.6. A skyplot usually represents the satellites which are visible for a given period, in the aim of analyzing the geometry of the constellation. Here these satellite visibility diagrams give a simple illustration of the GIOVE trajectory over each station for the given days (identified by their DOY number). The position of the satellite is plotted as a function of the elevation (e) and azimuth (A), with the elevation mask of 20°. As GIEN and GNOR stations are relatively close to each other, their skyplot shows approximately the same pattern.

6.4 Ambiguity resolution

As stated in section 4.3, the ambiguity resolution procedure follows two main steps:

- resolution of the widelane ambiguities using the widelane-narrowlane and differenced widelane combinations (see section 6.4.1),
- resolution of original integer ambiguities by substituting widelane ambiguities in the triple frequency phase multipath combination (see section 6.4.2).

For each type of combination used, we present the results obtained with the post-processed GIOVE dataset. Moreover, we test the assumptions given in section 4.3.1.1 about the distribution of code and phase multipath delays and measurement noise.

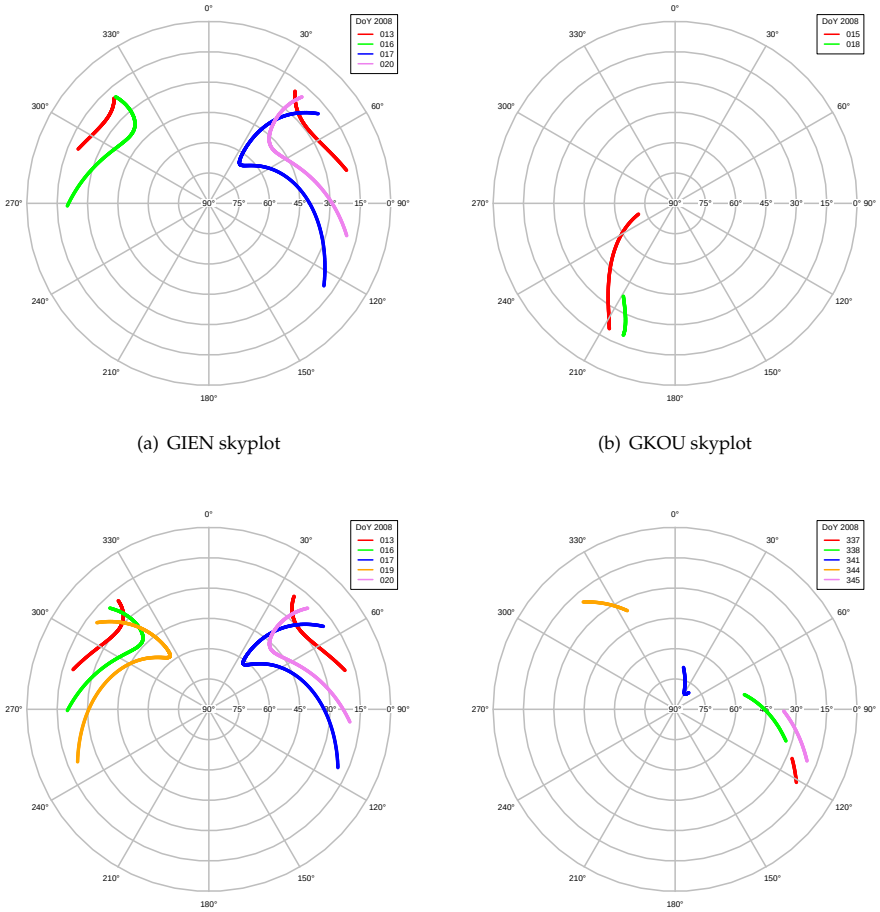

(a) GIEN skyplot

(b) GKOU skyplot

(c) GNOR skyplot

(d) GMIZ skyplot

Figure 6.6 *– Skyplots for GIEN (a), GKOU (b), GNOR (c) and GMIZ (d) stations, giving the position of GIOVE-A or GIOVE-B satellite as a function of the satellite elevation angle (from 0° to 90°) and the satellite azimuth angle (from 0° to 360°).*

6.4.1 Widelane ambiguity resolution

6.4.1.1 Widelane-narrowlane combinations

EWLNL combination

By using equation (4.62) we have computed the EWLNL combination (c_{EWL}) for the whole dataset given in table 6.4. In sections 4.3.1.1 and 5.3.1.1, we have concluded that the extra–widelane (EWL) ambiguities should be correctly resolved for Galileo. Moreover, it is demon-

strated in appendix B.2 that an error on the EWL ambiguities would have lead to unrealistic TEC values and would have therefore been noticeable. Since we did not notice such an effect in our dataset, we may state that the following condition (in cycles) is fulfilled:

$$|\Delta c_{EWL}| < 0.5 \tag{6.17}$$

This means that the fractional part of c_{EWL} is equal to the residual term Δc_{EWL}.

Figure 6.7 shows an example of Δc_{EWL} for two study cases*. As predicted in section 4.3.1.1, the variability of the EWLNL combination is very low. Therefore, the average filtering is not helpful to obtain increasingly precise values of the ambiguities.

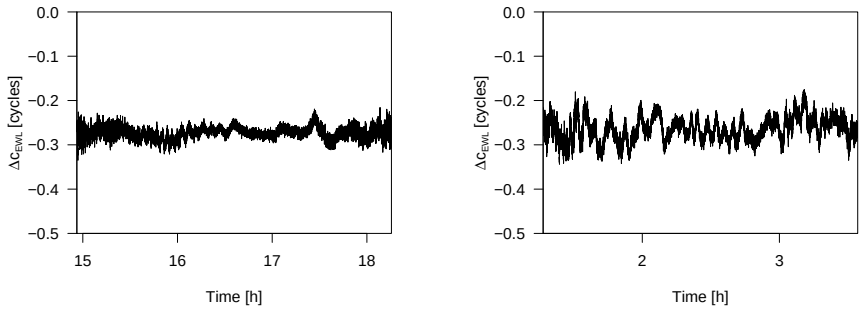

Figure 6.7 *– Residual term of the EWLNL combination (Δc_{EWL}) for GIEN DOY 016/08 (a) and GNOR DOY 013/08 (b).*

We will now test the assumptions given in section 4.3.1.1 about the distribution of code and phase multipath delays and measurement noise. They are supposed to have a normal distribution with a zero-mean (white Gaussian) with the standard deviation values given in tables 2.7 and 2.8. Since we can reasonably assume that code and phase hardware delays are constant over a satellite pass (see section 2.2.2.9), the variability of c_{EWL} (or the variability of Δc_{EWL}) is due to code/phase multipath delays and measurement noise. Therefore, the quantity Δc_{EWL} is used to test the distribution of multipath delays and measurement noise on L2 and L5. This statistical study will make use of graphic descriptive statistics, statistical test of normality and numerical descriptive statistic.

- Graphic descriptive statistics

  We will first make use of empirical – especially graphic – techniques to see whether the distribution of Δc_{EWL} is normal. A first view of the distribution of Δc_{EWL} is given by the density plot surimposed over the histogram. Figure 6.8 shows the histogram–density plot of Δc_{EWL} for two study cases. Visually, the compatibility with a normal distribution cannot be rejected. Note that these two examples are representative of the whole dataset.

  Furthermore, a Quantile-Quantile (QQ)-plot can be used to compare the quantile function of the dataset (sample quantiles) to the quantile function of a theoretical distribution

*Detailed results for the whole dataset will be presented in section 6.6.

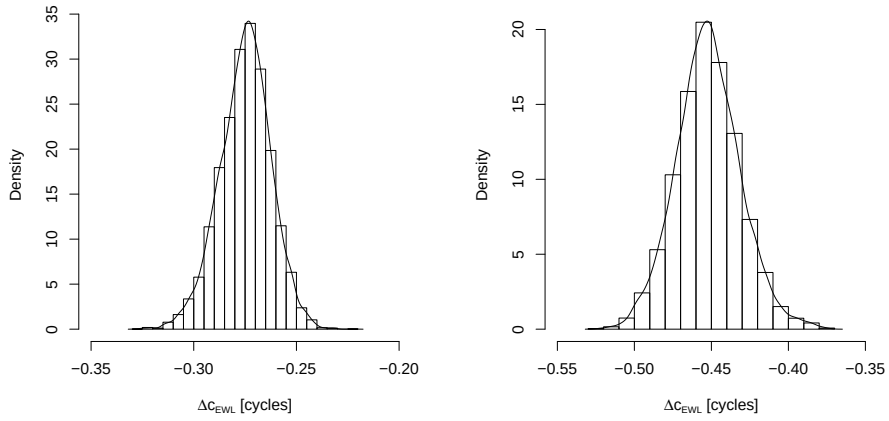

Figure 6.8 *– Histogram–density plot of Δc_{EWL} for GIEN DOY 013/08 (a) and GKOU DOY 015/08 (b).*

(theoretical quantiles), the latter being the standard normal distribution $N(0,1)$. This particular QQ-plot is called *normal probability plot*. An important property of a QQ-plot is that if the two distributions being compared are identical, the QQ-plot follows the straight line $y = x$ (zero origin, slope 1). If the distributions are linearly related, the QQ-plot still lies on a straight line $y = ax + b$. Figure 6.9 shows the QQ-plot for the same two study cases than in figure 6.8 representing the quantile function of Δc_{EWL} versus the quantile function of $N(0,1)$. The straight line (*"droite de Henry"*) passes through the first and third quartiles. Each QQ-plot actually fits quite well to the straight line, at least in the middle region. There is thus a good correspondence between the quantiles of the dataset and the quantiles of the standard normal distribution. As Δc_{EWL} is not supposed to have a zero-mean or a unit standard deviation, it is normal that the straight line does not have zero origin or unit slope. Moreover, the correspondence is high in the middle region, whereas it is lower in the extremities (which correspond to the tails of the distribution).

Finally, this empirical graphic analysis was instructive: we could see that the data distribution deviated from normal on the tails, but it can be observed for samples coming from a normal distribution. Nevertheless, it would be helpful to have a quantitative approach by using a statistical test procedure.

- Statistical test of normality

  A statistical test procedure can be appplied to find out whether a sample comes from a normal distribution or not. The *Shapiro–Wilkinson* test is a non-parametric variation of the *Kolmogorov-Smirnov* test [108]. Other statistical tests of normality are the *Lilliefors* test, which is also a variation of *Kolmogorov-Smirnov* test, and the *Jarque-Bera* test which is based on the classical measure of skewness and kurtosis. Since most authors agree that the *Shapiro–Wilkinson* test is the most reliable test of normality for small to medium size sample sets [96, 108], we will use the R statistics* routine *shapiro.test()* to test the

*R statistics is a free software environment for statistical computing and graphics.

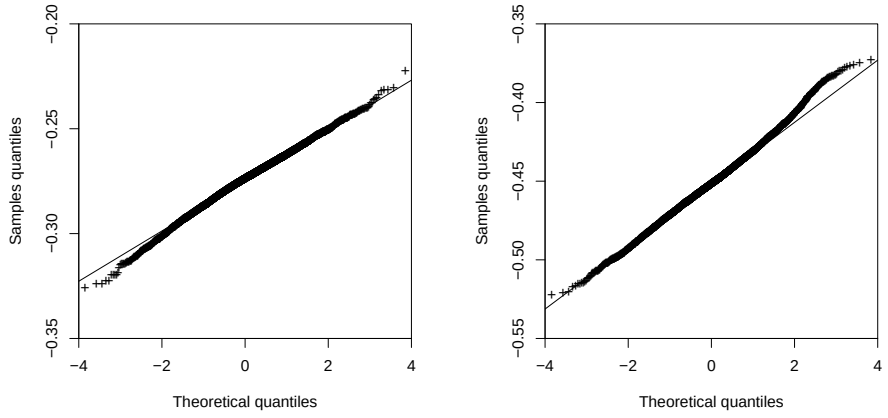

(a) (b)

Figure 6.9 *– QQ–plot of Δc_{EWL} versus $N(0,1)$ for GIEN DOY 013/08 (a) and GKOU DOY 015/08 (b).*

normality of Δc_{EWL}. The basic test procedure is divided into six steps [3]:

1. Definition of the null-hypothesis H_0: the data are sampled from a normal distribution
2. Constitution of the dataset: Δc_{EWL} times series (for each study case)
3. Decide the significance level of the test: $\alpha = 5\,\%$
4. Computation of the test statistic (W)
5. Computation of the associated p-value (p)
6. Decision: reject H_0 if $p \leq \alpha$

It is well-known that the results of such a test depend on the sample size. The incompatibility with the normal distribution is quasi-systematically decided with large samples, even if the differences with normal distribution are small [90]. If we take the whole time series of each study case into account (the number of data n is given in table 6.5), the null-hypothesis has to be rejected ($p < 0.05$). However, if we randomly take smaller samples (n=120), we do not reject the null hypothesis ($p > 0.05$). Therefore we can reasonably assume that Δc_{EWL} follows a normal distribution.

- Numerical descriptive statistics

  We compute the mean (m) and standard deviation (s) of Δc_{EWL} for each study case. It is worth noticing that by definition the standard deviation of Δc_{EWL} is equal to the standard deviation of c_{EWL}. The computed standard deviation values are given in table 6.5. For more convenience, the theoretical standard deviation values are given in the first line. The standard deviation values are compatible with the standard deviation of c_{EWL} due to noise/multipath ($\sigma_E = 0.023$ cycles) given in table 4.13. This means that the influence of code/phase multipath delays and measurement noise does not exceed the predicted influence and should stay negligible with respect to the influence of code

hardware delays. As far as the mean of Δc_{EWL}, it includes (the mean of) the code/phase hardware delays as well as the eventual non-zero mean of code multipath delays*. Since the hardware delays are supposed to be relatively stable from day to day, we have tested the homogeneity of the means with a Student's *t*-test (two study cases at a time) and with an ANOVA-1 (all study cases together). In each case, the null-hypothesis (which is that all means are equal) had to be rejected. Nevertheless, it cannot be distinguished if this is due to the non-zero average of code multipath delays, or to the variability of hardware delays.

Table 6.5 *– Standard deviation of the EWLNL, WLNL, corrected DWL and triple frequency phase multipath combinations.*

Study case	n	$s_{c_{EWL}}$ [cycles]	$s_{c_{WL}}$ [cycles]	$s_{\varphi_{DWL,c}}$ [cycles]	$s_{\Phi_{M,125}}$ [m]
theory		0.023	0.325	0.219	0.0049
1	8514	0.012	0.292	0.191	0.0040
2	6130	0.025	0.424	0.247	0.0052
3	12336	0.013	0.250	0.233	0.0050
4	18828	0.011	0.210	0.199	0.0042
5	15078	0.014	0.217	0.227	0.0048
6	8221	0.093	0.284	0.189	0.0040
7	4356	0.186	0.396	0.247	0.0052
8	1228	0.017	0.373	0.219	0.0046
9	3599	0.011	0.259	0.228	0.0048
10	3599	0.007	0.198	0.089	0.0019
11	2967	0.017	0.338	0.165	0.0035
12	3035	0.017	0.335	0.175	0.0037
13	9068	0.027	0.433	0.291	0.0061
14	9157	0.026	0.322	0.285	0.0060
15	13542	0.023	0.315	0.227	0.0048
16	17958	0.019	0.304	0.199	0.0042
17	17059	0.018	0.334	0.176	0.0037
18	14602	0.024	0.407	0.168	0.0035

To summarize, we have tested the assumptions given in section 4.3.1.1 about the distribution of code/phase multipath delays and measurement noise L2 and L5 carrier frequencies by using the residual term of the EWLNL combination (Δc_{EWL}) as test quantity. The conclusions are:

- we can reasonably assume that Δc_{EWL}, and therefore the code/phase multipath delays and measurement noise on L2 and L5 can be approximated by a normal distribution,
- the zero-mean hypothesis of code multipath delays was tested, but it is not possible to distinguish between variations of code multipath delays or hardware delays,

*We have assumed that the mean of code/phase measurement noise and the mean of phase multipath delays are equal to zero (see section 4.3.1.1).

- the standard deviation of Δc_{EWL} was found to be in agreement with the theoretical values*.

Finally, even if all assumptions cannot be verified, we achieve the same result as in section 4.3.1.1 in terms of EWL ambiguity resolution feasibility. As a matter of fact, we have demonstrated that the EWL ambiguities are correctly resolved.

WLNL combination

By using equation (4.64) we have computed the WLNL combination (c_{WL}) for the whole dataset given in table 6.4. In sections 4.3.1.1 and 5.3.1.1 we have concluded that, because of the influence of code hardware delays, the WL ambiguities cannot be correctly resolved by using the WLNL combination. Nevertheless, if we apply a running average filter to the WLNL combination and round the resulting value ($\langle c_{WL} \rangle$) to its nearest integer value, we obtain the approximated integer values of the WL ambiguities ($\widetilde{N}_{WL}$). Figure 6.10 shows an example of c_{WL} and its running mean $\langle c_{WL} \rangle$†. For more convenience, we have removed the quantity $\widetilde{N}_{WL}$ to represent $c_{WL} - \widetilde{N}_{WL}$. As the WL ambiguities are not supposed to be correctly resolved, this quantity is not equal to the residual term Δc_{WL}, but to the residual term plus or minus an integer number of cycles. The latter corresponds to the difference between N_{WL} and $\widetilde{N}_{WL}$). It is already worth noticing that $\widetilde{N}_{WL}$ are much different from the WL ambiguities computed with the DWL combination (see section 6.6). The difference is about 200 cycles and is larger than expected with regards to the aforementioned considerations about the magnitude of the WLNL residual term. These results will be discussed in section 6.6. Besides, the variability of $c_{WL} - \widetilde{N}_{WL}$ is equal to the variability of Δc_{WL} and appears to be as large as expected.

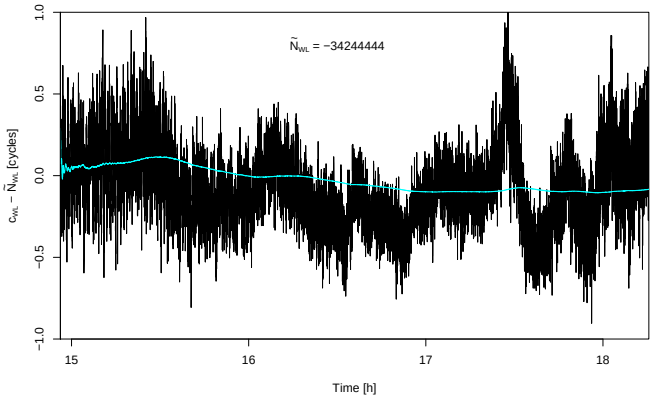

Figure 6.10 *– WLNL combination and its running average (cyan) for GIEN DOY 016/08.*

Since we can reasonably assume that code and phase hardware delays are constant on a satellite pass (see section 2.2.2.9), the variability of c_{WL} is due to code/phase multipath delays and measurement noise. Therefore, the quantity c_{WL} is used to test the distribution of multipath delays and measurement noise on L1 and L2. Similarly to the EWLNL case, we

*except for the study case #7, which concerns GKOU station

†Detailed results for the whole dataset will be presented in section 6.6.

use graphic, numerical descriptive statistics and the *Shapiro-Wilkinson* test of normality. The results and conclusions reached are similar:

- we can reasonably assume that c_{WL}, and therefore the code/phase multipath delays and measurement noise on L1 and L2, follow a normal distribution,
- the computed standard deviation values of c_{WL} reported in table 6.5 are rather close to the theoretical value given in table 4.13 ($\sigma_E = 0.325$ cycles).

Finally, even if the influence of code/phase multipath and measurement noise can be overcome with a running average filter, it is not possible to resolve the WL ambiguities.

6.4.1.2 Differenced widelane combinations

By using equation (4.82) we have computed the differenced widelane combination (φ_{DWL}) for the whole dataset given in table 6.4. Using the results from section 4.3.1.2, we can assume that by rounding the average filter of the DWL combination – with the ionospheric delays corrected – to their nearest integer values, we obtain the correct values of the WL ambiguities, namely N_{WL}. As stated before, the results show that N_{WL} value differ from $\widetilde{N}_{WL}$ of about 200 cycles (see section 6.6).

Using the methodology explained in section 3.2.3.4, we use global final IGS Global Ionospheric Maps (GIMs) to level the GF phase combination and obtain an estimation of the TEC ($\text{TEC}_{l,GIM}$). To be able to resolve the WL ambiguities, their accuracy has to be better than about 5 TECU. As stated in section 3.2.3.4, the accuracy of $\text{TEC}_{l,GIM}$ is comparable to the accuracy of GIMs. The required accuracy should thus be achievable, especially in periods of low solar activity (low TEC values) like 2008. We can thus correct the DWL combination from the ionospheric delays ($\varphi_{DWL,c}$) by substituting $\text{TEC}_{l,GIM}$ in equation (4.94). Figure 6.11 shows an example of $\varphi_{DWL,c}$ and its running mean, for the same study case as in figure 6.10. For more convenience, we have represented $\varphi_{DWL,c} - N_{WL}$. This figure shows that the running average filter is indeed useful.

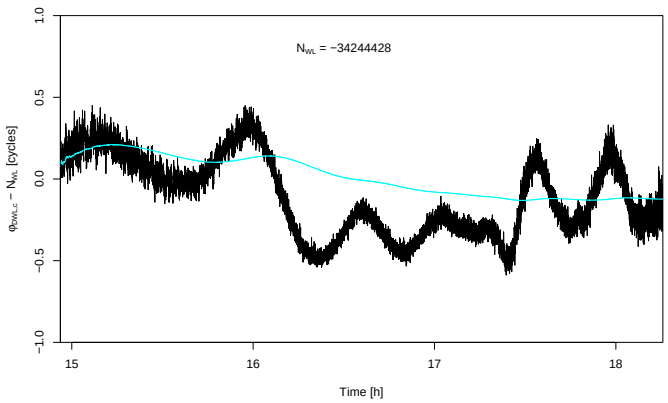

Figure 6.11 *– Corrected DWL combination and its running average (cyan) for GIEN DOY 016/08.*

Since we can reasonably assume that phase hardware delays are constant on a satellite pass (see section 2.2.2.9), the variability of $\varphi_{DWL,c}$ is due to phase multipath delays and measurement noise. Therefore, the quantity $\varphi_{DWL,c}$ is used to test the distribution of multipath delays and measurement noise on L1, L2 and L5. As for the EWLNL combination, we use graphic, numerical descriptive statistics and the *Shapiro-Wilkinson* test of normality. The results and conclusions reached are similar:

- we can reasonably assume that $\varphi_{DWL,c}$, and therefore the phase multipath delays and measurement noise on L1, L2 and L5, can be approximated by a normal distribution,
- the computed standard deviation values of $\varphi_{DWL,c}$ reported in table 6.5 are compatible with the theoretical value given in table 4.14 ($\sigma_E = 0.219$ cycles).

6.4.2 Triple frequency phase multipath combination

By using equation (4.105) we have computed the triple frequency phase multipath combination ($\Phi_{M,125}$) for the whole dataset given in table 6.4. Then, if we substitute the EWL and WL ambiguities resolved in the previous steps and apply a running average filter, we can extract the N_{L2} ambiguities (see equation (4.113)).

Figure 6.12 shows an example of the triple frequency phase multipath combination. For more convenience, we have removed the mean over a satellite pass. This allows us to remove the impact of the unknown ambiguities. Due to its coefficients, this combination is dominated by the L2 and L5 signals: phase multipath delays and phase measurement noise on L2 and L5 are thus prominently seen in the combination. This combination has thus helped to detect the presence of the line bias variations in the GPS L5 signal [78].

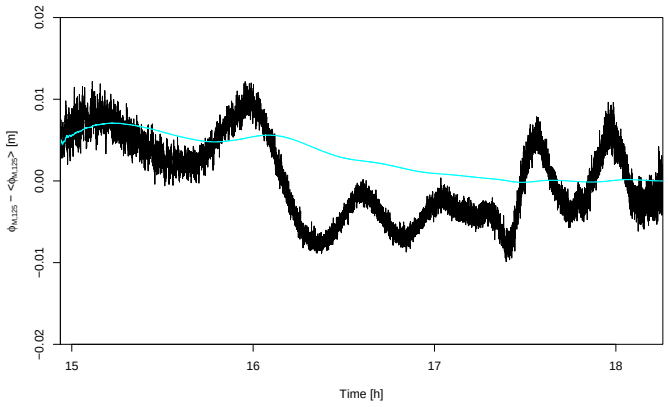

Figure 6.12 *– Triple frequency phase multipath combination and its running average (cyan) for GIEN DOY 016/08.*

Since we can reasonably assume that phase hardware delays are constant on a satellite pass (see section 2.2.2.9), the variability of $\Phi_{M,125}$ is due to phase multipath delays and measurement noise. Therefore, the quantity $\Phi_{M,125}$ is used to test the distribution of multipath delays and measurement noise on L1, L2 and L5. Similarly to the EWLNL case, we use graphic,

numerical descriptive statistics and the *Shapiro-Wilkinson* test of normality. The results and conclusions achieved are similar:

- we can reasonably assume that $\Phi_{M,125}$, and therefore the phase multipath delays and measurement noise on L1, L2 and L5, follow a normal distribution,
- the computed standard deviation values of $\Phi_{M,125}$ reported in table 6.5 are compatible with the theoretical value given in table 4.15 ($\sigma_E = 0.0049$ m).

6.5 TEC reconstruction

Considering that N_{EWL}, N_{WL} and N_{L2} are resolved, it is straightforward to obtain N_{L1} and N_{L5} and to reconstruct the GF ambiguities by using equations (4.115) to (4.117). Finally, the reconstructed TEC values are obtained by equation (4.118). As already stated before, the best way to reconstruct TEC is to use frequencies that are as far apart from each other as possible, i.e. L1/L2 or L1/L5. When using L2/L5 GF combination, the multipath delays and measurement noise ($E_{\Phi,km}$ term) are increased by the α_{km} coefficient. This is illustrated in figure 6.13, which shows the TEC reconstructed with each of the three GF phase combinations. As expected, the TEC computed with L2/L5 is much less precise, whereas the TEC computed with L1/L2 and L1/L5 has the same level of precision.

Figure 6.14 shows the reconstructed TEC values for GIEN, GMIZ and GNOR stations. We obtain relatively low TEC values, which can be explained by the low solar activity. Besides, the day-to-day variations in each station can be explained by the differences of local time and the changes in the satellite position which determines the position of the Ionospheric (Piercing) Point (IP).

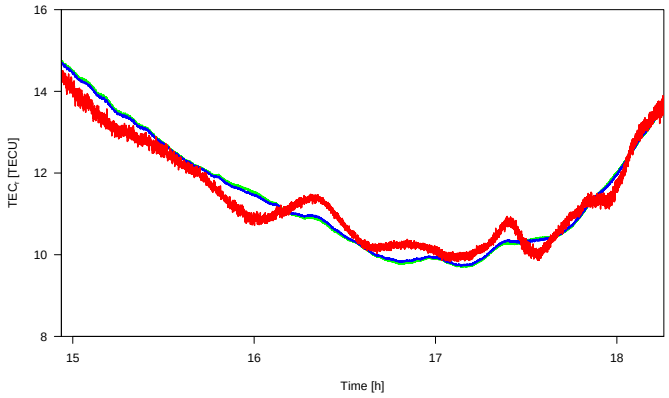

Figure 6.13 *– Reconstructed TEC values with L2/L5 (red), L1/L2 (green) and L1/L5 (blue) GF phase combinations for GIEN DOY 016/08.*

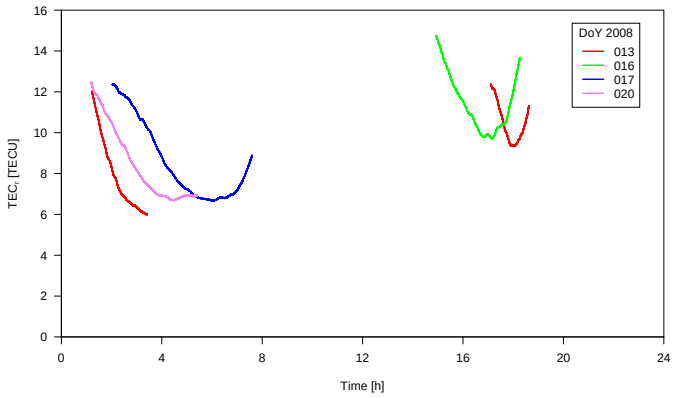

(a)

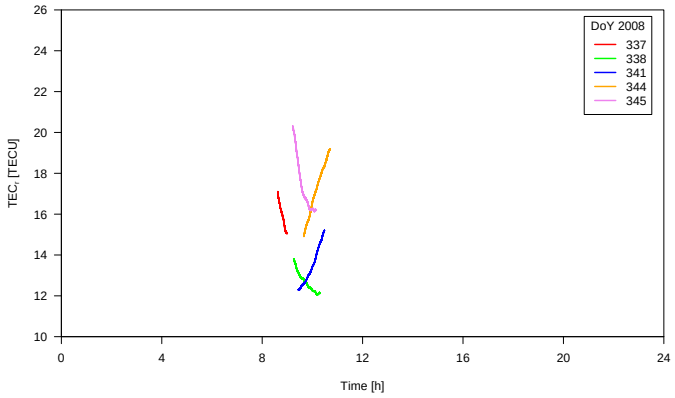

(b)

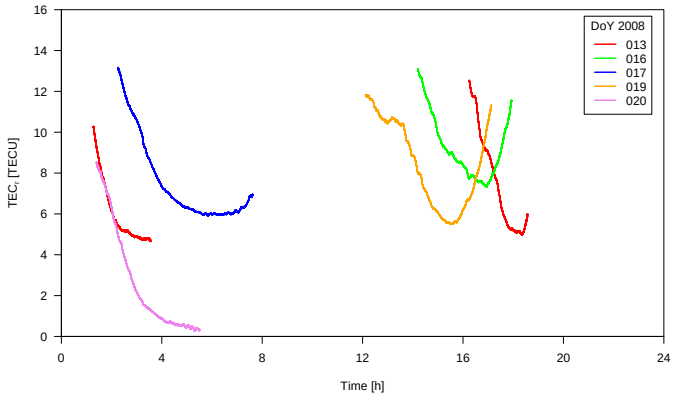

(c)

Figure 6.14 *– Reconstructed TEC values for GIEN (a), GMIZ (b) and GNOR (c) stations.*

6.6 Calibration of satellite and receiver code hardware delays

This section presents the results of the code hardware delay calibration following the methodology explained in section 4.5 and using the results of the ambiguity resolution and TEC reconstruction procedures.

Regarding equation (4.63), if we subtract the EWL ambiguities from the mean value of c_{EWL} over a satellite pass, we obtain the mean value of the residual term Δc_{EWL}. Following equation (4.131), that gives:

$$\langle \Delta c_{EWL} \rangle = \langle c_{EWL} \rangle - N_{EWL} \tag{6.18}$$

$$= D_{\Phi,\mathrm{L2}} - D_{\Phi,\mathrm{L5}} - f_{25} \left[\frac{f_{\mathrm{L2}}}{c} D_{g,\mathrm{L2}} + \frac{f_{\mathrm{L5}}}{c} D_{g,\mathrm{L5}} \right] \tag{6.19}$$

where
$D_{g,k}$ is the sum of the satellite and receiver code hardware delays on k carrier frequency [m]
$D_{\Phi,k}$ is the sum of the satellite and receiver phase hardware delays on k carrier frequency [m]

We have computed $\langle \Delta c_{EWL} \rangle$ for the whole dataset, and the results are shown in figure 6.15. We can observe that this quantity is smaller than 0.5 cycles, as it has been established earlier (see equation (6.17)).

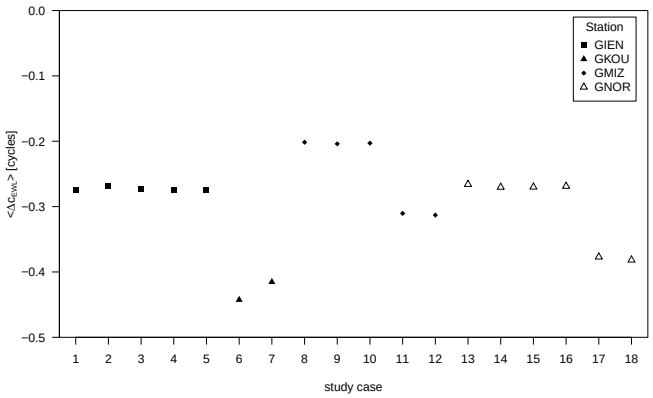

Figure 6.15 *– Mean value of the EWLNL combination residual term for all study cases.*

In the previous sections we have obtained some interesting results to discuss: the approximated values of the WL ambiguities ($\tilde{N}_{WL}$) computed from the WLNL combination significantly differ from the N_{WL} resolved with the DWL combination. The difference is about 200 cycles. Regarding the way to compute these ambiguities (see sections 4.3.1.1 and 4.3.1.2), this must be explained by a difference in the residual term. Since the DWL combination is phase combination, whereas the WLNL combination is a code/phase combination, this difference probably comes from satellite and/or receiver code hardware delays. The code hardware delay calibration methodology will thus be useful to see whether this assumption can be confirmed.

The WL ambiguities could not be resolved with the WLNL combination but well with the DWL combination (see sections 6.4.1.1 and 6.4.1.2). We can thus subtract the WL ambiguities from the mean value of the WLNL combination over a satellite pass to obtain the mean of the residual term Δc_{WL}. Regarding equation (4.134), we can write:

$$\langle \Delta c_{WL} \rangle = \langle c_{WL} \rangle - N_{WL} \tag{6.20}$$

$$= -f_{12} \left[\frac{f_{\mathrm{L1}}}{c} D_{g,\mathrm{L1}} + \frac{f_{\mathrm{L2}}}{c} D_{g,\mathrm{L2}} \right] \tag{6.21}$$

The values of $\langle \Delta c_{WL} \rangle$ for each study case are presented in figure 6.16. The magnitude of this residual term varies from -191 to -198 cycles.

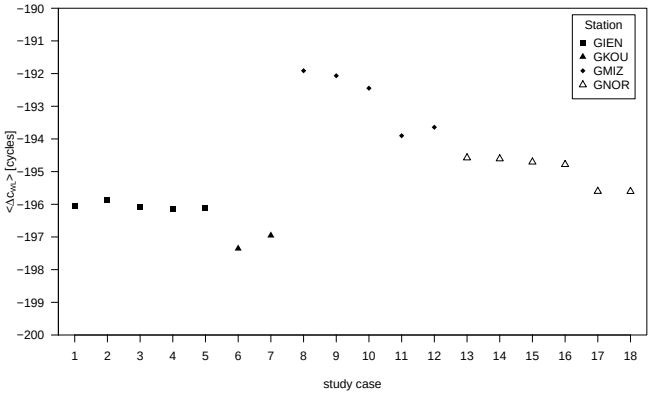

Figure 6.16 *– Mean value of the WLNL combination residual term for all study cases.*

Besides to $\langle \Delta c_{WL} \rangle$, we need to compute the GF code combination given by equation (3.50). Apart from ionospheric delays, this combination contains the same type of code delays as the WLNL combination (c_{WL}). Since we now have reconstructed the TEC values, we can remove the ionospheric delays from the GF code combination and apply a running average filter to obtain $\langle P_{GF,km,c} \rangle$ [m]:

$$\langle P_{GF,km,c} \rangle = \langle P_{GF,km} - \alpha_{km} \, \mathrm{TEC}_r \rangle \tag{6.22}$$

$$= IFB_{g,km} \tag{6.23}$$

$$= D_{g,k} - D_{g,m} \tag{6.24}$$

where TEC_r [TECU] are the TEC values reconstructed with L1/L2 or L1/L5 GF phase combination (see equation (4.118)). This gives an estimation of code Inter-Frequency Biases (IFB).

Figure 6.17 and figure 6.18 show the mean value of the three GF code combinations with the ionospheric delays corrected ($P_{GF,km,c}$) which give an estimation of the code IFB. The values of $\langle P_{GF,25,c} \rangle$ or $IFB_{g,25}$ vary around between -1 and $+1$ m, while the values of $\langle P_{GF,12,c} \rangle$ or $IFB_{g,12}$ and $\langle P_{GF,15,c} \rangle$ or $IFB_{g,15}$ vary between 272 and 278 m. As $\langle P_{GF,25,c} \rangle \simeq 0$ and $\langle P_{GF,25,c} \rangle << \langle P_{GF,12,c} \rangle$ and $\langle P_{GF,15,c} \rangle$ it comes that $D_{g,\mathrm{L2}}$ and $D_{g,\mathrm{L5}}$ delays are rather equal, while different from $D_{g,\mathrm{L1}}$.

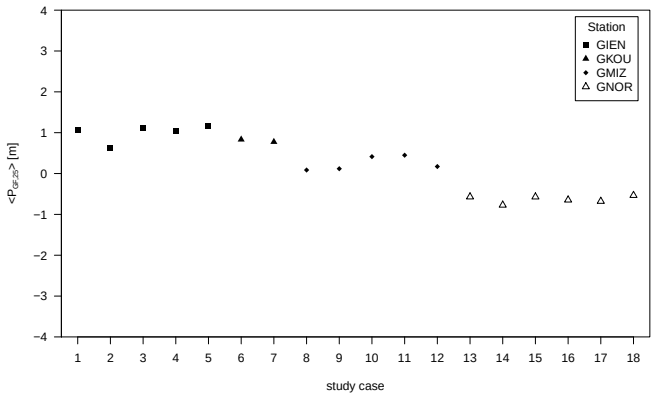

Figure 6.17 *– Mean value of the corrected L2/L5 GF code combination for all study cases.*

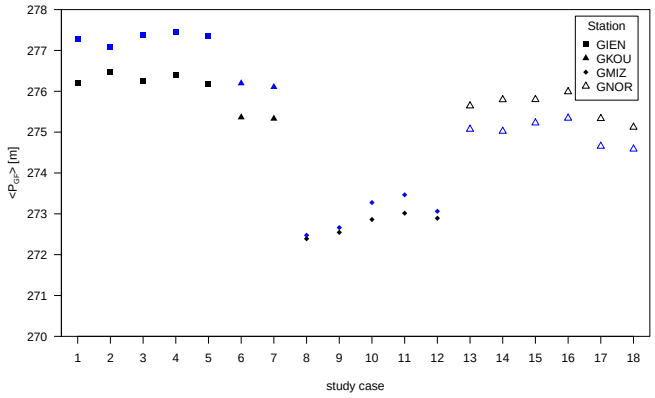

Figure 6.18 *– Mean value of the corrected L1/L2 (black) and L1/L5 (blue) GF code combination for all study cases.*

In [72] dual frequency (L1/L2) GIOVE code and phase measurements from GESS stations are processed to determine the code IFB and calibrate the TEC . In this study, the methodology used consists of smoothing the GF code combination with the GF phase combination [42] and is actually similar to the carrier-to-code levelling process. For GIEN and GNOR stations, the code IFB on L1/L2 for May 25, 2009 are found to be -2386.24 TECU and -2393.80 TECU, which corresponds to 305.44 m and 306.22 m, respectively. These values actually have the same order of magnitude as the values of $IFB_{g,12}$ obtained with our dataset (see figure 6.18). The authors also show that GIOVE code IFB are very stable: their Root Mean Square (RMS) over a period of one month is found to be about 3 TECU ($\sim$ 1 ns or 30 cm). We do not have enough data to study the stabililty of the computed IFB. Nevertheless, we can observe that for each station the maximal day-to-day variation of $IFB_{g,12}$ or $IFB_{g,15}$ is about 30 cm.

Using the previous results in equation (4.141) makes it possible to compute the sum of the satellite and receiver code hardware delays on L1:

$$D_{g,\mathrm{L1}} = \frac{f_{\mathrm{L2}}}{f_{\mathrm{L1}} + f_{\mathrm{L2}}} \cdot \langle P_{GF,12,c} \rangle - \lambda_{WL} \cdot \langle \Delta c_{WL} \rangle \tag{6.25}$$

Then if we substitute $D_{g,\mathrm{L1}}$ in equations (4.139) and (4.140) we obtain $D_{g,\mathrm{L2}}$ and $D_{g,\mathrm{L5}}$, respectively.

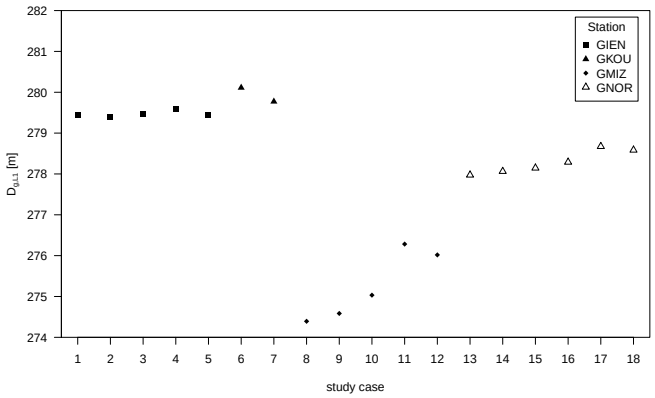

Figure 6.19 *– Sum of the satellite and receiver code hardware delays on L1 carrier frequency.*

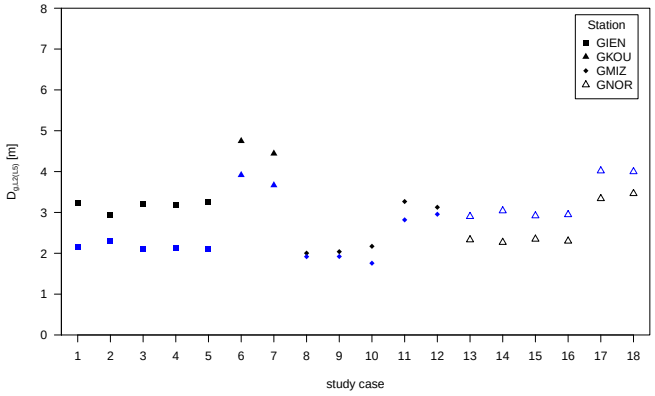

Figure 6.20 *– Sum of the satellite and receiver code hardware delays on L2 and L5 carrier frequency (blue = L5).*

We have calibrated the sum of the satellite and receiver code hardware delays in each frequency ($D_{g,k}$) for each study case. Figure 6.19 shows that the $D_{g,\mathrm{L1}}$ are consistently large in the four stations (varying between 274 m and 281 m), whereas figure 6.20 indicates that $D_{g,\mathrm{L2}}$ and $D_{g,\mathrm{L5}}$ are consistently small in the four stations (varying between 1 and 5 m). It

means that they are consistently large or small either for GIOVE-A or GIOVE-B satellite. It is worth noting that the observed day-to-day variability could be partly or totally due to their inherent accuracy of these delays (which was shown to be at the decimetric level) and not to real variability.

The large $D_{g,\mathrm{L1}}$ values are responsible for the magnitude of the residual term Δc_{WL}. Moreover, they exceed the magnitude considered in section 4.3.1.1. This has no influence of the ambiguity resolution, since the WL ambiguities were resolved through the DWL combination. Moreover, as stated in section 4.5.1, these calibrated delays can be use to reduce the influence of the WLNL residual term. It makes it possible to resolve the WL ambiguities with the WLNL combination without the need for a dual frequency TEC estimation (which was associated to the use of the DWL combination).

It is interesting to ask ourselves whether the satellite or receiver hardware delays on L1 are large. It is stated in [6] that the code hardware delays are similar between different satellites. Moreover, code IFB are similar for the three stations observing GIOVE-A with a small variation with respect to their mean. From these elements, we can guess that the magnitude L1/L2 IFB would be caused by large satellite code hardware delays. The same affirmation has actually been drawn in [72] after calibration of GIOVE IFB over a month period on several GESS stations (included GIEN and GNOR stations). However, a larger dataset would be needed to confirm this realistic assumption.

6.7 Conclusions

This chapter was dedicated to triple frequency TEC reconstruction with real GIOVE measurements.

In order to test the triple frequency TEC reconstruction methodology on real GNSS measurements, we used a dataset consisting of GIOVE-A/-B data for a few days in 2008 in four GESS stations. As a prerequisite, we performed the preprocessing of the observation and navigation data, including:

- detection of cycle slips

  We implemented a two-step cycle slip detection algorithm. First a running average filter was applied on the three widelane-narrowlane combinations, and then a complementary cycle slip detection was processed with the so-called *first and second optimal phase combinations* by the means of time differencing.

- correction of the satellite ans receiver antenna PCOs and PCVs

  Since the antenna PCO and PCV corrections are not available yet for the GIOVE data, we used an example of antenna corrections and propagate their influence on the reconstructed TEC values. We found out that the final TEC values could be biased by a non-negligible error (5 TECU) caused by the satellite PCOs and by the receiver antenna PCOs and PCVs. Nevertheless, once the correction will be available, the influence will be reduced to about 0.025 TECU (see section 4.4.2.1).

- correction of the phase wind-up effect

  We applied the phase wind-up correction algorithm given by [132]. It has been shown in section 4.4.2.1 that the influence of the non-corrected phase wind-up effect on the reconstructed TEC is about 0.025 TECU.

- interpolation of the satellite ephemeris

  To obtain the satellite position at any considered epoch between the precise orbits given at 15 min sample interval, we used the 12-term Neville polynomial interpolation strategy. With such an algorithm, the interpolation errors are smaller than 5 cm.

Finally, after correcting the Earth rotation effect and applying an elevation mask, we constituted the observation GIOVE dataset for testing the TEC reconstruction methodology developed in chapter 4.

We first tested the ambiguity resolution procedure. For each type of combination used, we presented the results obtained with the post-processed GIOVE dataset.

- We showed that the EWL ambiguities can be resolved with the EWLNL combination.
- We corrected the DWL combination from the ionospheric delays in order to resolve the WL ambiguities. For that purpose, we used global final IGS maps to compute "GIM-levelled" calibrated TEC values. Since the solar activity in the concerned period (i.e. 2008) was low, their required accuracy of 5 TECU should be achieved.
- The differences between the approximated WL ambiguities computed with the WLNL combination and the resolved WL ambiguities computed with the DWL combination are about 200 cycles. This indicates the presence of large code hardware delays.

Furthermore, we performed several statistical tests aimed at validating the assumptions about the distribution and magnitude of code and phase multipath delays and measurement noise. The conclusions achieved are the following.

- Since we can reasonably assume that the code and phase hardware delays are constant over a satellite pass, the variability of the combinations is due to multipath delays and measurement noise. After analyzing the distribution of the various combinations through histogram–density plots and a QQ-plots, and after compiling the results of the *Shapiro-Wilkinson* statistical test of normality, we can reasonably assume that the code/phase multipath delays and measurement noise on L1, L2 and L5 frequencies can be approximated by a normal distribution.
- We tested the zero-mean hypothesis of code multipath delays with Student's *t-test* and with an ANOVA-1. However, since it is not possible to distinguish between variations of multipath delays and hardware delays, we could not validate this hypothesis.
- Finally, we computed the standard deviations of the various combinations. These are generally in agreement with the theoretical standard deviation values given in chapter 4.

Using the results of the ambiguity resolution procedure, we computed the final reconstructed TEC values for the whole dataset. These values confirm the low solar activity period,

and the fact that the best way to reconstruct TEC is to use frequencies that are as far apart from each other as possible, i.e. L1/L2 or L1/L5. It has to be stressed that, as mentioned earlier, these TEC values might be biased by a non-negligible error (5 TECU) caused by the satellite PCOs and by the receiver antenna PCOs and PCVs.

Finally, we calibrated the sum of the satellite and receiver code hardware delays on each frequency ($D_{g,k}$) by using the methodology developed in chapter 4. This method required the computation of the mean value of the GF code combination with the ionospheric delays corrected, which gives an estimation of the code IFB. This combination vary between 272 and 278 m for L1/L2 and L1/L5, and between -1 and $+1$ m for L2/L5, which implies that code hardware delays on L2 and L5 are rather equal, while different from code hardware delays on L1. Actually, the results show that $D_{g,\mathrm{L1}}$ are consistently large in the four stations (varying between 274 m and 281 m), whereas $D_{g,\mathrm{L2}}$ and $D_{g,\mathrm{L5}}$ are consistently small in the four stations (varying between 1 and 5 m). Since their accuracy is at the decimetric level (see section4.5.2), the observed day-to-day variability could be due to their inherent accuracy and not to real variability. Moreover, even if a larger dataset would be needed to confirm this assumption, the large $D_{g,\mathrm{L1}}$ values are probably due to large GIOVE code hardware delays.

Once we have calibrated the sum of the satellite and receiver code hardware delays on each frequency, it is possible to reduce the influence of the WLNL residual term, making it possible to resolve the WL ambiguities without the need for a dual frequency estimation of the TEC*. This alleviates the ambiguity resolution and TEC reconstruction procedures.

Acknowledgments

The GIOVE datasets used for the work presented in this chapter have been provided by the European Space Agency (ESA). The views presented in the text represent solely the opinions of the authors and should be considered as research results not strictly related to Galileo Project design.

The authors would like to thank the European Space Agency for kindly providing the GIOVE datasets.

*which is required by the DWL combination

Chapter 7

Conclusions and recommendations

THIS work is exclusively dedicated to the development of an innovative Total Electron Content (TEC) reconstruction methodology using triple frequency Global Positioning System (GPS) and Galileo measurements and aimed at improving the accuracy of the final TEC values with regards to existing dual frequency techniques. We investigated how it is possible to improve the accuracy of the TEC by using triple frequency Global Navigation Satellite System (GNSS) measurements, and which level of accuracy can be reached.

The literature review showed that the computation of TEC is based on the use of the Geometric-Free (GF) phase combination and requires the computation of its non-integer GF ambiguity. With dual frequency GNSS measurements, this can be achieved by the carrier-to-code levelling process (code/phase) or the unlevelled carrier phase process (phase only). In both techniques, the resolution of the GF ambiguities requires the slant TEC (TEC) to be modeled by means of a mathematical expansion using the vertical TEC (VTEC) and a mapping function to convert VTEC into TEC. This induces non-negligible model errors which affect the accuracy of the TEC values. In total, even if the calibrated TEC values are very precise, their accuracy is thus limited to a few TECU. For a mid-latitude site, the error effects are confined to -4.6 and 3.6 TECU for the code/phase technique, and to -2.5 and 2.5 TECU for the phase only technique. For a low-latitude site, the performance deteriorates: the error effects are confined to -5.5 and 5 TECU for the code/phase process, and to -5.5 and 7.5 TECU for the phase only process.

We built an ambiguity resolution scheme based on a promising set of combinations of undifferenced measurements, making it possible to resolve the integer ambiguities on each frequency. By doing so, the GF ambiguity can thus be reconstructed from the original integer ambiguities without the need for TEC modeling. The ambiguity resolution feasibility depends on the magnitude of the non-ambiguity term. Since all of these combinations are GF and Ionospheric-Free (IF)*, the non-ambiguity (or residual) term contains all frequency-dependent GNSS errors affecting code and/or phase measurements†, i.e. satellite and receiver hardware delays, multipath delays, measurement noise, satellite and receiver antenna Phase Center Offsets (PCOs) and Phase Center Variations (PCVs) and phase wind-up effect. In this context, since we consider the adequate corrections for the phase wind-up effect and satellite

*except the differenced widelane combination
†depending on the type of combination used

and receiver antenna PCOs and PCVs to have been applied, we based the assessment of the ambiguity resolution feasibility on several assumptions about the distribution and magnitude of measurement noise, multipath delays and hardware delays:

- Code and phase measurement noise, as well as code and phase multipath delays are white Gaussian. We assume realistic standard deviation values retrieved from real GNSS measurements. Even if the white Gaussian behavior might not be always true for code multipath delays, the use of a running average filter combined with the wide-lane character of the ambiguity resolution makes it a realistic hypothesis in this study.
- Satellite and receiver code and phase hardware delays are assumed to be constant in time. Moreover, we make the assumption that the magnitude of each type (satellite and receiver) of code/phase hardware delays is smaller than 3 meters/1 millimeter, respectively.

Finally, the ambiguity resolution procedure can be summarized as follows:

- Thanks to its large wavelength, the extra–widelane–narrowlane (EWLNL) combination allows us to resolve the extra–widelane (EWL) ambiguities for Galileo. For GPS however, the EWL ambiguity resolution could fail depending on the magnitude of satellite and receiver code hardware delays.
- Since the widelane–narrowlane (WLNL) combination has a smaller wavelength, the influence of the code hardware delays prevents us from resolving the widelane (WL) ambiguities with the WLNL combination. Therefore, the WL ambiguities are resolved through the differenced widelane (DWL) combination, which is a phase-only combination. Nevertheless, this requires an estimation of dual frequency ionospheric delays with an accuracy better than 5 TECU. This is shown to be achievable, especially for mid-latitude regions in period of low solar activity. Nevertheless, for mid-latitudes regions in a period of higher solar activity, or for low-latitudes regions in general, an accuracy of 5 TECU might not be achieved and the resolution of the WL ambiguities might not be possible.
- By substituting the EWL and WL ambiguities in the triple frequency phase multipath combination, we obtain approximated values of the original integer ambiguities. Their accuracy depends on the magnitude of satellite and receiver phase hardware delays.

The next step after the ambiguitiy resolution process is the reconstruction of the GF ambiguities from the original ambiguities. These GF ambiguities are then added to the dual frequency L1/L2 or L1/L5 GF phase combination to obtain the absolute TEC values. We performed a detailed assessment of the precision and accuracy of the reconstructed TEC values. Let us stress here that the quality of this assessment depends on the validity of our hypotheses about measurement noise, multipath and hardware delays. The precision of the TEC depends on the magnitude of phase multipath delays and phase measurement noise and is about 0.1 TECU for GPS and Galileo. As far as the accuracy of the TEC is concerned, it depends on the uncorrected effects (phase wind-up, PCO, PCV), higher-order ionospheric terms as well as on phase Inter-Frequency Biases (IFB) on the GF phase combination. The accuracy of the TEC is also and mainly determined by the influence of phase hardware delays on the original ambiguities which leads to an error of 0.5 TECU for GPS and to an error of 1 TECU for Galileo.

In total, the error on the reconstructed TEC values are confined to -0.8 and 0.8 TECU for GPS and to -1.3 and 1.3 TECU for Galileo.

In parallel with the TEC reconstruction methodology, we also developed an innovative technique which allows us to calibrate the sum of the satellite and receiver code hardware delays on each carrier frequency based on the results of the ambiguity resolution and TEC reconstruction procedures. Taking into account the non-zero average of code multipath delays and the accuracy of the reconstructed TEC values, we found that the accuracy of the calibrated satellite and receiver hardware delays is at the decimetric level. These calibrated delays can thus be used to reduce the influence of the WLNL residual term, making it possible to resolve the WL ambiguities without the need for a dual frequency estimation of the TEC*. This alleviates the ambiguity resolution and TEC reconstruction procedures.

We developed a simulation software to provide triple frequency GPS and Galileo code and phase measurements. Since at the beginning of our research, real triple frequency data were not available yet, this software has been an essential tool to conceive the TEC reconstruction methodology. We put an emphasis on simulating the error sources which have an influence on the ambiguity resolution and TEC reconstruction procedures as realistically as possible. For that purpose, advanced simulation tools were developed to generate multipath delays and measurement noise.

A simulated observation dataset of triple frequency GNSS measurements was then used to test the feasibility of the ambiguity resolution procedure as well as the precision and accuracy of the reconstructed TEC values. For each combination used in the ambiguity resolution process, we addressed a quick review of their characteristics and estimated the influence of the frequency-dependent effects (residual term) on the ambiguity resolution, and in particular the influence of measurement noise and multipath delays. Finally, the dataset was also used to assess the precision and accuracy of the reconstructed TEC values. The precision of the reconstructed TEC values from simulated data is about 0.1 TECU for GPS and Galileo. We also tested the influence of phase hardware delays on the reconstructed TEC values. We concluded that if the phase hardware delays are barely proportional to the frequency of the signal, their influence on the resolution of the original ambiguities, and therefore on the reconstructed TEC values might be smaller than 1-2 TECU for GPS and Galileo. However, if the phase delays are larger than 1 mm and are not proportional to the frequency, the accuracy of the reconstructed TEC could be strongly degraded to a level of several TECU. This problem will be overcome once estimated phase delays are available.

We have also tested the triple frequency TEC reconstruction methodology on real GNSS measurements. We used a dataset consisting of Galileo In-Orbit Validation Element (GIOVE)-A/-B data for a few days in 2008 in four Galileo Experimental Sensor Stations (GESS) stations. As a prerequisite, we performed the preprocessing of the observation and navigation data, including the detection of cycle slips, the interpolation of the satellite ephemeris and the correction of the satellite and receiver antenna PCOs and PCVs, phase wind-up effect and Earth rotation effect.

We utilized the post-processed GIOVE dataset to test the ambiguity resolution procedure. We showed that the EWL ambiguities can be resolved with the EWLNL combination, and that the DWL combination corrected from the ionospheric delays allows us to resolve the WL ambiguities. Moreover, the differences between the approximated WL ambiguities computed

*which is required by the DWL combination

with the WLNL combination and the resolved WL ambiguities computed with the DWL combination are about 200 cycles, which indicates the presence of large code hardware delays. Furthermore, we performed several statistical tests aimed at validating the assumptions about the distribution and magnitude of code and phase multipath delays and measurement noise. As a result, we can reasonably assume that the code/phase multipath delays and measurement noise on L1, L2 and L5 frequencies can be approximated by a normal distribution. However, since it is not possible to distinguish between variations of multipath delays and hardware delays, we could not validate the zero-mean hypothesis of code multipath delays. Finally, the standard deviations of the various combinations are generally in agreement with the theoretical standard deviation values.

The reconstructed TEC values computed with the GIOVE dataset confirm the low solar activity period. It has to be stressed that, as mentioned earlier, these TEC values might be biased by a non-negligible error (5 TECU) caused by the satellite PCOs and by the receiver antenna PCOs and PCVs. Indeed, corrections for these effects are not yet available for Galileo satellites and receivers. We calibrated the sum of the satellite and receiver code hardware delays on each frequency. The results actually show that the delays on L1 are consistently large in the four stations (varying between 274 m and 281 m), whereas the delays on L2 and L5 are consistently small in the four stations (varying between 1 and 5 m). We can reasonably assume that the large L1 delays are probably due to large GIOVE code hardware delays.

Finally, based on the theoretical considerations developed in chapter 4 as well as on the tests performed on simulated data in chapter 5, we can reasonably assume that the innovative triple frequency TEC reconstruction methodology developed in this work has successfully improved the accuracy of the TEC with regards to existing dual frequency techniques. This improvement has been made possible thanks to the enhanced ambiguity resolution scheme, based on linear combinations of dual and triple frequency GNSS measurements, which allows us to resolve the original ambiguities without the need of TEC modeling. However, depending on the magnitude of the phase hardware delays, as well as on their behavior between the frequencies, the accuracy of the reconstructed TEC might be degraded to a level of a few TECU. This limitation will be overcome once the calibration of phase hardware delays is possible.

We will now address the recommendations for this research. In a short-term horizon, we could test other ambiguity resolution schemes, e.g. the high performance Galileo E5-Alternative Binary Offset Carrier (AltBOC) signal together with L1 and L2 (or L5). Furthermore, we could plan to perform further investigations concerning the calibration of the satellite and receiver code hardware delays. Since our method was developed exclusively on undifferenced measurements, allowing us to reconstruct the absolute TEC, it would also be interesting to adapt it for Double Differences (DDs). In this case, we obtain the DD ionospheric delays, which need to be accurately corrected for the needs of differential positioning applications. In a long-term horizon, it would also be necessary to investigate the possibilities of calibrating the satellite and receiver phase hardware delays, which might limit the accuracy of the reconstructed TEC.

With regards to the limitations encountered for this work, it is worth noticing that we were limited by the small size of the GIOVE dataset. If we had had a larger triple frequency dataset, e.g. a few months for several GESS stations as well as more available GIOVE satellites, additional tests could have been performed. We could have tested the stability and the origin of the large code hardware delays. Since our method was developed exclusively on undifferenced measurements, a larger dataset would have allowed us to apply it on DDs, and

therefore analyze the benefit of the improved TEC reconstruction in differential positioning applications. Finally, with a large dataset, we could have tested the benefits of using triple frequency measurements from a network of GNSS receivers to determine the three dimensional distribution (latitude, longitude, time) of vertical TEC.

Since this work promises accurate reconstructed TEC values, this would obviously be beneficial for multiple applications.
Firstly, ionospheric studies, and in particular the detection of short-term ionospheric variability (e.g. TID, scintillations, geomagnetic storms) based on GNSS observations would benefit from an increased TEC accuracy. Moreover, more accurately reconstructed TEC values could make it possible to distinguish between the ionospheric and plasmaspheric TEC, and to calibrate the plasmaspheric TEC.
From another point of view, since the ionospheric delay constitutes one of the major error sources in space geodetic techniques, GNSS applications will highly benefit from an improved TEC reconstruction. For example, a better estimation of the first-order ionospheric delays could enhance single frequency positioning applications. Similarly, the correction of the higher-order ionospheric effects, and therefore the accuracy of Precise Point Positioning (PPP) applications, could be improved.

Appendix A

Use of the middlelane ambiguities

In the triple frequency Total Electron Content (TEC) reconstruction methodology described in chapter 4, the ambiguity resolution procedure is performed by:

- resolving the extra–widelane (EWL) ambiguities with the extra–widelane–narrowlane (EWLNL) combination (see section 4.3.1.1),
- resolving the widelane (WL) ambiguities with the differenced widelane (DWL) combination (see section 4.3.1.2),
- substituting the EWL and WL ambiguities in the triple frequency phase multipath combination to resolve the original integer ambiguities (see section 4.3.2).

It is worth noting that only two of the three widelane ambiguities given in equations (4.30) to (4.32) are independent. Therefore the methodology could make use of the middlelane (ML) ambiguities instead of the WL ambiguities.

In this appendix we derive the equations of the ambiguity resolution procedure which uses the ML ambiguities instead of the WL ambiguities. The aim is to show whether this alternative would have an impact on the ambiguity resolution and on the accuracy of the reconstructed TEC values.

A.1 Differenced middlelane combination

The DWL combination φ_{DML} [cycles] is given by equation (4.83):

$$\varphi_{DML} = \varphi_{ML} - (\varphi_{EWL} - N_{EWL}) \frac{\lambda_{EWL}}{\lambda_{ML}} \tag{A.1}$$

Similarly to equation (4.84), equation (A.1) can be rearranged to identify the α, β, γ coefficients of the combination:

$$\varphi_{DML} = \varphi_{\mathrm{L1}} - \left(\frac{\lambda_{EWL}}{\lambda_{ML}}\right) \varphi_{\mathrm{L2}} + \left(\frac{\lambda_{EWL}}{\lambda_{ML}} + 1\right) (\varphi_{\mathrm{L5}} + N_{EWL}) \tag{A.2}$$

$$= \alpha\, \varphi_{\mathrm{L1}} + \beta\, \varphi_{\mathrm{L2}} + \gamma\, \varphi_{\mathrm{L5}} + \gamma\, N_{EWL} \tag{A.3}$$

As this equation has exactly the same coefficients values than the DWL combination given by equation (4.84), the two combinations are not independent and we can write:

$$I_{\varphi_{DML}} = I_{\varphi_{DWL}} \tag{A.4}$$

$$\Delta\varphi_{DML} = \Delta\varphi_{DWL} \tag{A.5}$$

Therefore, similarly to the DWL combination, by rounding the average filter of φ_{DML} – with the ionospheric delays corrected – to their nearest integer values, we obtain the correct values of the ML ambiguities, namely N_{ML}.

A.2 Triple frequency phase multipath combination

If we substitute the ML ambiguities (N_{ML}) instead of the WL ambiguities (N_{WL}) in the triple frequency phase multipath combination (see equation 4.108), N_{L5} is the only unknown ambiguity. The equation corresponding to equation (4.113) is thus:

$$N_{\mathrm{L5}} = \frac{\langle\Phi_{M,125}\rangle - d\,\lambda_{\mathrm{L1}}\,N_{ML} + f\,\lambda_{\mathrm{L5}}\,N_{EWL}}{-(d\,\lambda_{\mathrm{L1}} + e\,\lambda_{\mathrm{L2}} + f\,\lambda_{\mathrm{L5}})} + \langle\Delta N_{\mathrm{L5}}\rangle \tag{A.6}$$

Since equation (A.6) is equivalent to equation (4.113), we can conclude that the error on N_{L5} would be equivalent to the error on N_{L2} , which is assessed in equation (4.114).

A.3 TEC reconstruction

As stated in section 4.4.2, the error on N_{L5} is translated in the ambiguities on L2 and L1, so that we can write:

$$\Delta n_{\mathrm{L1}} = \Delta n_{\mathrm{L5}} = \Delta n_{\mathrm{L2}} \tag{A.7}$$

where $\Delta n_k \in \mathbb{Z}$. When using the ML ambiguities instead of the WL ambiguities, the error on the reconstructed TEC values ($\Delta\mathrm{TEC}_{r,N}$) given by equation (4.125) is thus equivalent.

Finally, we can conclude that the use of the middlelane ambiguities – instead of the widelane ambiguities – leads to the same results in terms of ambiguity resolution and accuracy of the reconstructed TEC.

Appendix B

Resolution of the WL ambiguities a posteriori

The first section (B.1) of this appendix explains how the dual frequency estimation of Total Electron Content (TEC) can be used *a posteriori* (instead of being used *a priori*) to resolve the widelane (WL) ambiguities. The second section (B.2) derives the error on the reconstructed TEC values which would be caused by an error on the extra–widelane (EWL) ambiguities when using this *a posteriori* resolution procedure.

B.1 Principles

In the triple frequency TEC reconstruction methodology described in chapter 4, a dual frequency estimation of the TEC is used to resolve the WL ambiguities *a priori*. The term *a priori* supposes that the WL ambiguities are resolved before the TEC reconstruction. As a matter of fact, it is established that the ionospheric delays of the differenced widelane (DWL) residual term $I_{\varphi_{DWL}}$ are given by [cycles]:

$$I_{\varphi_{DWL}} = \kappa_2 \cdot \text{TEC} \tag{B.1}$$

where κ_2 [cycles/TECU] $= -0.0819$ (GPS)/ -0.0882 (Galileo) is derived from equation (4.87). Therefore "GIM-levelled" calibrated TEC values are used to correct the DWL combination from the ionospheric delays. Then, rounding the average filter of the corrected DWL combination allows to resolve the WL ambiguities *a priori*.
If we assume that the EWL ambiguities have been resolved by using the extra–widelane–narrowlane (EWLNL) combination (see section 4.3.1.1), the EWL and WL ambiguities can be substituted in the triple frequency phase multipath combination to resolve the original ambiguities (see section 4.3.2), which are then used to reconstruct the Geometric-Free (GF) ambiguities and the TEC values (see section 4.4.1).

An alternative to this procedure would be to resolve the WL ambiguities *a posteriori*, i.e after TEC reconstruction. The idea is to use the approximated widelane ambiguities ($\widetilde{N}_{WL}$) obtained with the widelane–narrowlane (WLNL) combination (see section 4.3.1.1) directly in the triple frequency phase multipath combination and then follow the usual procedure to reconstruct the TEC. Since it is possible to establish a direct relationship between the error on the WL ambiguities (denoted as δN_{WL}) and the error induced by δN_{WL} on the reconstructed

TEC values (denoted as δTEC_r), the dual frequency estimation of TEC can be used *a posteriori* to resolve the WL ambiguities.

The error on the WL ambiguities (δN_{WL}) is defined as the difference between the approximated values of the widelane ambiguities and the correct values of the WL ambiguities, i.e.:

$$\delta N_{WL} = \widetilde{N}_{WL} - N_{WL} \tag{B.2}$$

As $\widetilde{N}_{WL}$ are used to reconstruct the TEC, we can derive the error which is induced on the original ambiguities (δN_k), on the GF ambiguities ($\delta N_{GF,k}$) and on the reconstructed TEC values (δTEC_r). The relationship between δN_{WL} and δTEC_r can be established in four steps. Firstly, considering the error δN_{WL} , δN_{L2} can be computed from equation (4.110):

$$\delta N_{\text{L2}} = \frac{-d\,\lambda_{\text{L1}}\,\delta N_{WL}}{-\left(d\,\lambda_{\text{L1}} + e\,\lambda_{\text{L2}} + f\,\lambda_{\text{L5}}\right)} = \kappa \cdot \delta N_{WL} \tag{B.3}$$

where $\kappa\ [-] = -27.29$ (GPS) and -25.55 (Galileo).

Secondly, using equations (4.30) and (4.31), we obtain δN_{L5} and δN_{L1} as a function of δN_{L2} (and therefore of δN_{WL}):

$$\begin{aligned} \delta N_{\text{L5}} &= N_{EWL} + \Delta N_{\text{L2}} = \kappa \cdot \delta N_{WL} && \text{(B.4)} \\ \delta N_{\text{L1}} &= \delta N_{\text{L2}} - \delta N_{WL} = (\kappa - 1) \cdot \delta N_{WL} && \text{(B.5)} \end{aligned}$$

It is worth noticing that, since the EWL ambiguites are supposed to be correctly resolved, we write N_{EWL} and not δN_{EWL}. Thirdly, substituting equations (B.3) to (B.5) in equations (4.115) to (4.117), we obtain:

$$\begin{aligned} \delta N_{GF,25} &= \kappa \left(1 + \frac{f_{\text{L2}}}{f_{\text{L5}}}\right) \delta N_{WL} = \gamma_{25} \cdot \delta N_{WL} && \text{(B.6)} \\ \delta N_{GF,12} &= \left(1 + \frac{f_{\text{L1}}}{f_{\text{L2}}}\,\kappa - \kappa\right) \delta N_{WL} = \gamma_{12} \cdot \delta N_{WL} && \text{(B.7)} \\ \delta N_{GF,15} &= \left(1 + \frac{f_{\text{L1}}}{f_{\text{L5}}}\,\kappa - \kappa\right) \delta N_{WL} = \gamma_{15} \cdot \delta N_{WL} && \text{(B.8)} \end{aligned}$$

where γ_{25}, γ_{12} and γ_{15} are unitless coefficients.
Fourthly, substituting equations (B.6) to (B.8) in equation (4.118), we obtain:

$$\begin{aligned} \delta\text{TEC}_r &= \frac{\gamma_{25}}{\alpha_{25}} \cdot \lambda_{\text{L2}} \cdot \delta N_{WL} && \text{(B.9)} \\ \delta\text{TEC}_r &= \frac{\gamma_{12}}{\alpha_{12}} \cdot \lambda_{\text{L1}} \cdot \delta N_{WL} && \text{(B.10)} \\ \delta\text{TEC}_r &= \frac{\gamma_{15}}{\alpha_{15}} \cdot \lambda_{\text{L1}} \cdot \delta N_{WL} && \text{(B.11)} \end{aligned}$$

It turns out that the multiplying coefficient of δN_{WL} is the same in the three previous equations, which means that δTEC_r is independent of the GF phase combination used. Finally, the relationship between the error on the WL ambiguities and the error on the reconstructed TEC values may be written as follows:

$$\delta\text{TEC}_r = K \cdot \delta N_{WL} \tag{B.12}$$

where $K\ [\text{TECU/cycles}] = 12.19$ (GPS)$/11.33$ (Galileo).

For example, an error of 1 cycle on the WL ambiguities causes an error on TEC of 12.19 TECU for GPS and of 11.33 TECU for Galileo. Note that the K coefficient is the reciprocal of the κ_2 coefficient given in equation (B.1).

When used together with a dual frequency estimation of TEC ($\mathrm{TEC}_{l,GIM}$), the relationship given in equation (B.12) allows to correct $\widetilde{N}_{WL}$ and thus the reconstructed TEC values. As a matter of fact, the error made on the WL ambiguities (δN_{WL}) can be estimated by y [cycles]:

$$y = \frac{1}{K}\left(\widetilde{\mathrm{TEC}}_r - \mathrm{TEC}_{l,GIM}\right) \tag{B.13}$$

where $\widetilde{\mathrm{TEC}}_r$ [TECU] are the approximated reconstructed TEC values.

By rounding y to its nearest integer value, we obtain δN_{WL} and thus the correct the WL ambiguities by using equation (B.2):

$$N_{WL} = \widetilde{N}_{WL} - \delta N_{WL} \tag{B.14}$$

It has to be stressed that the WL ambiguities will be correctly resolved if the following condition is fullfilled (in cycles):

$$\frac{1}{K}\left|\mathrm{TEC}_r - \mathrm{TEC}_{l,GIM}\right| < 0.5 \tag{B.15}$$

This condition implies that the accuracy of $\mathrm{TEC}_{l,GIM}$ has to be better than 6.1 TECU for GPS and 5.6 TECU. It has to be emphasized that this condition leads to the equivalent accuracy requirements than for the *a priori* WL ambiguity resolution process (see section 4.3.1.2). As stated in section 3.2.3.4, the accuracy of "GIM-levelled" calibrated TEC values is comparable to the accuracy of Global Ionospheric Maps (GIMs). Therefore, regarding to their performance discussed in section 3.2.3.3, an accuracy of 5-6 TECU should be achievable, especially for mid-latitude regions in period of low solar activity (low TEC values).

From this, we can assume that the WL have been resolved *a posteriori*. We can thus apply the usual procedure to reconstruct the TEC.

B.2 Influence of an error on the EWL ambiguities

The *a posteriori* ambiguity resolution procedure relies on the fact that the EWL ambiguities are correctly resolved (see appendix B.1). In this section, we will derive the error on the reconstructed TEC values which would be caused by an error on the EWL ambiguities when using this *a posteriori* ambiguity resolution procedure.

Considering that there is an error in the EWL ambiguities (δN_{EWL}) and in the WL ambiguities (δN_{WL}), equation B.3 becomes:

$$\delta N_{\mathrm{L2}} = \frac{-d\,\lambda_{\mathrm{L1}}\,\delta N_{WL} + f\,\lambda_{\mathrm{L5}}\,\delta N_{EWL}}{-\left(d\,\lambda_{\mathrm{L1}} + e\,\lambda_{\mathrm{L2}} + f\,\lambda_{\mathrm{L5}}\right)} \tag{B.16}$$

$$= \kappa \cdot \delta N_{WL} + \kappa^{'} \cdot \delta N_{EWL} \tag{B.17}$$

Deriving equations (B.4) to (B.11), we find:

$$\delta\mathrm{TEC}_r = K \cdot \delta N_{WL} + K^{'} \cdot \delta N_{EWL} \tag{B.18}$$

where $K^{'}$ [TECU/cycles] $= (\lambda_{EWL}/\lambda_{WL}) \cdot K = 82.94$ (GPS)/135.93 (Galileo).
Equation (B.18) thus becomes:

$$\delta \text{TEC}_r = K \left(\delta N_{WL} + \frac{\lambda_{EWL}}{\lambda_{WL}} \delta N_{EWL} \right) \tag{B.19}$$

Since we use equation (B.13) to resolve the WL ambiguities (supposing that the EWL ambiguities are resolved), the error on the EWL ambiguities induces an error of $-(\lambda_{EWL}/\lambda_{WL})\,\delta N_{EWL}$ on the WL ambiguities. It can be derived from equations (B.3) to (B.11) that the error induced on final reconstructed TEC values is:

$$\delta \text{TEC}_r = C \cdot \delta N_{EWL} \tag{B.20}$$

where C [TECU/cycles] $= -229.30$ (GPS)/ -271.85 (Galileo). Regarding to the value of the C coefficient, an error on the EWL ambiguities would lead to unrealistic TEC values.

Finally, we have shown that if we use the *a posteriori* ambiguity resolution procedure, an error on the EWL ambiguities leads to unrealistic TEC values and is therefore noticeable.

List of acronyms and abbreviations

AGW . . . . . Atmospheric Gravity Wave

AltBOC . . . . . Alternative Binary Offset Carrier

ANOVA . . . . . Analysis of variance

ANTEX . . . . . Antenna Exchange format

ARP . . . . . Antenna Reference Point

BIPM . . . . . Bureau International des Poids et Mesures

BPSK . . . . . Binary Phase Shift Keying

C/N_0 . . . . . Carrier-to-Noise density ratio

C/A . . . . . Coarse Acquisition

CCIR . . . . . Comité Consultatif International des Radios Communications

CEP . . . . . Celestial Ephemeris Pole

CM . . . . . Center of Mass

CME . . . . . Coronal Mass Ejection

CODE . . . . . Center for Orbit Determination in Europe

CS . . . . . Commercial Service

CTP . . . . . Conventional Terrestrial Pole

DCB . . . . . Differential Code Biases

DD . . . . . Double Difference

DML . . . . . differenced middlelane

DoD . . . . . Department of Defense

DOY . . . . . Day of Year

DWL . . . . . differenced widelane

EC . . . . . European Commission
ECEF . . . . . Earth-Centered-Earth-Fixed
EPN . . . . . EUREF Permanent Network
ESA . . . . . European Space Agency
ESTEC . . . . . European Space Research and Technology Center
EUV . . . . . Extreme Ultraviolet
EWL . . . . . extra–widelane
EWLNL . . . . . extra–widelane–narrowlane

GAST . . . . . Greenwich Apparent Sideral Time
GCC . . . . . Ground Control Center
GCS . . . . . Ground Control Segment
GESS . . . . . Galileo Experimental Sensor Stations
GETR . . . . . Galileo Experimental Test Receiver
GF . . . . . Geometric-Free
GIM . . . . . Global Ionospheric Map
GIOVE . . . . . Galileo In-Orbit Validation Element
GISM . . . . . Global Ionospheric Scintillation Model
GLONASS . . . . Global'naya Navigatsionnaya Sputnikkovaya Sistema
GMS . . . . . Ground Mission Segment
GNSS . . . . . Global Navigation Satellite System
GPS . . . . . Global Positioning System
GSS . . . . . Galileo Sensor Station
GST . . . . . Galileo System Time
GTRF . . . . . Galileo Terrestrial Reference Frame

IAAC . . . . . Ionosphere Associate Analysis Centers
IF . . . . . Ionospheric-Free
IFB . . . . . Inter-Frequency Biases
IGS . . . . . International GNSS Service

IONEX . . . . . Ionosphere Map Exchange (format)

IOV . . . . . In-Orbit Validation

IP . . . . . Ionospheric (Piercing) Point

IRI . . . . . International Reference Ionosphere

ITRF . . . . . International Terrestrial Reference Frame

ITRF08 . . . . . International Terrestrial Reference Frame of 2008

ITRS . . . . . International Terrestrial Reference System

ITU . . . . . International Telecommunications Union

JPL . . . . . Jet Propulsion Laboratory

LAMBDA . . . . . Least-Squares Ambiguity Decorrelation Adjustment

LSTID . . . . . large-scale TID

MEO . . . . . Medium Earth Orbit

ML . . . . . middlelane

MLNL . . . . . middlelane–narrowlane

MSTID . . . . . medium-scale TID

OS . . . . . Open Service

P . . . . . Precise

PC . . . . . Phase Center

PCO . . . . . Phase Center Offset

PCV . . . . . Phase Center Variation

PPP . . . . . Precise Point Positioning

PPS . . . . . Precise Positioning System

PRN . . . . . Pseudorandom Noise

PRS . . . . . Public Regulated Service

QQ . . . . . Quantile-Quantile

RINEX . . . . . Receiver Independent Exchange (format)

RMS . . . . . Root Mean Square

SB . . . . . Short Baseline

SD . . . . . Single Difference

SIP . . . . . Sub-Ionospheric Point

SISRE . . . . . Signal-In-Space-Range-Error

SLR . . . . . Satellite Laser Ranging

SMR . . . . . Signal-to-Multipath Ratio

SNR . . . . . Signal-to-Noise Ratio

SoL . . . . . Safety-of-Life Service

SP3 . . . . . Standard Product # 3 Orbit (format)

SPS . . . . . Standard Positioning Service

SSTID . . . . . small-scale TID

TD . . . . . Time Difference

TEC . . . . . Total Electron Content

TID . . . . . Travelling Ionospheric Disturbance

TTC . . . . . telemetry, tracking and command

UPC . . . . . Universitat Politècnica de Catalunya

WGS84 . . . . . World Geodetic System of 1984

WL . . . . . widelane

WLNL . . . . . widelane–narrowlane

ZB . . . . . Zero Baseline

Bibliography

[1] CCIR foF2 and M(3000)F2 model maps (1982). *Planetary and Space Science*, 40(4):546–546, 1992. 22

[2] *GSSF Operations Manual, Volume 2 – Algorithms and Models* , May 2005. 110, 113, 114

[3] A. Albert. *Biostatistique*. Céfal & EULg, Liège, Belgique, 2005. 142

[4] J. Artru. *Observations au sol ou par satellite et modélisation des signaux ionosphériques post-sismiques*. PhD thesis, Institut de Physique du Globe de Paris, France, 2001. 29

[5] F. Azpilicueta, C. Brunini, and S. M. Radicella. Global ionospheric maps from GPS observations using modip latitude. *Advances in Space Research*, 38:2324–2331, 2006. 53

[6] B. Banville, R. B. Langley, S. Saito, and T. Yoshihara. Handling cycle slips in GPS data during ionospheric plasma bubble events. *Radio Science*, 45(RS6007), 2010. doi: 10.1029/2010RS004415. 131, 153

[7] S. Banville. Aspects liés à la résolution des ambiguités de phase dans le positionnement ponctuel de précision (PPP) par GPS. Master's thesis, Université Laval, Québec, Canada, 2007. 19, 23, 24, 29, 30, 92

[8] S. Banville, R. Santerre, M. Cocard, and R. B. Langley. Satellite and Receiver Phase Bias Calibration for Undifferenced Ambiguity Resolution. In *Proc. ION NTM*, San Diego, CA, United States, January 28-30 2008. 28, 30, 81

[9] S. Bassiri and G. A. Hajj. Higher-order ionospheric effects on the global positioning system observables and means of modeling them. *Manuscripta Geodaetica*, 18:280–289, 1993. 21, 51

[10] L. Bastos and H. Landau. Fixing cycle slips in dual-frequency kinematic GPS applications using Kalman filtering. *Manuscripta Geodaetica*, 13(4):249–256, 1988. 131, 132

[11] Y. Béniguel. Global Ionospheric Propagation Model (GIM): A propagation model for scintillations of transmitted signals. *Radio Science*, 37(3), 2002. 47

[12] Y. Béniguel, J.-P. Adam, A. Bourdillon, and P. Lassudrie-Duschene. Ionospheric scintillation effects on navigation effects. *Comptes Rendus Physique*, 12:186–191, 2011. 47

[13] B. Bidaine and R. Warnant. Measuring Total Electron Content with GNSS: Investigation of Two Different Techniques. In *Proc. IRST*, Edinburgh, United Kingdom, 2009. 61

[14] D. Bilitza. International reference ionosphere 2000. *Radio Science*, 36(2):261–275, 2001. 22, 61

[15] S. B. Bisnath. Efficient, Automated Cycle-Slip Correction of Dual-frequency Kinematic GPS Data. In *Proc. ION GPS*, pages 145–154, Salt Lake City, United States, September 19-22 2000. 83, 131, 132, 133

[16] G. Blewitt. An automatic editing algorithm for GPS data. *Geophysical Research Letters*, 17 (3):199–202, 1990. 83, 131, 133

[17] C. Brunini and F. Azpilicueta. Accuracy assessment of the GPS-based slant total electron content. *Journal of Geodesy*, 83(8):773–785, 2009. 53, 56, 57, 58, 59

[18] C. Brunini, M. A. Van Zele, A. Meza, and M. Gende. Quiet and perturbed ionospheric representation according to the electron content from GPS signals. *Journal of Geophysical Research*, 108(A2):1056, 2003. 53

[19] K. Chen and Y. Gao. Real-Time Precise Point Positioning Using Single Frequency Data. In *Proc. ION GNSS*, pages 1514–1523, Long Beach, California, United States, September 13-16 2005. 37, 91, 92, 116

[20] L. Ciraolo, F. Azpilicueta, C. Brunini, A. Meza, and S. M. Radicella. Calibration errors on experimental slant total electron content (TEC) determined with GPS. *Journal of Geodesy*, 81(2):111–120, 2007. 55, 56

[21] F. Collin and R. Warnant. Application of the wavelet transform for GPS cycle slip correction and comparison with Kalman filter. *Manuscripta Geodaetica*, 20(3):161–172, 1995. 131

[22] P. Collins. An Overview of inter-frequency carrier phase combinations. Available online at `http://gauss.gge.unb.ca/papers.pdf/L1L2combinations.collins.pdf`, 1999. 70

[23] ARINC Research Corporation. *Interface Control Document ICD-GPS-200 : Navstar GPS Space Segment and Navigation User Interfaces*. CA, United States, April 12 2000. 14, 16, 17, 28, 111

[24] ARINC Research Corporation. *Interface Control Document ICD-GPS-705*. CA, United States, March 29 2002. 29

[25] Z. Dai, S. Knedlik, and O. Loffeld. Instantaneous Triple-Frequency GPS Cycle-Slip Detection and Repair. *International Journal of Navigation and Observation*, 2009. doi: 10.1155/2009/407231. 132

[26] K. Davies. *Ionospheric radio*. Institution of Electrical Engineers, London, United Kingdom, 1997. 2, 48

[27] P. F. De Bakker, H. van der Marel, and C. C. J. M. Tiberius. Geometry-Free undifferenced, single and double difference analysis of single-frequency GPS, EGNOS and GIOVE-A/B measurements. *GPS Solutions*, 13:305–214, 2009. doi: 10.1007/s10291-009-0123-6. 35, 36, 80

[28] P. F. De Bakker, C. C. J. M. Tiberius, H. van der Marel, and R. J. P. van Bree. Short and zero baseline analysis of GPS L1 C/A, L5Q, GIOVE E1B and E5aQ signals. *GPS Solutions*, 2011. doi: 10.1007/s10291-011-0202-3. 35, 36, 80

[29] W. Dieminger, G. K. Hartmann, and R. Leitinger. *The upper atmosphere. Data analysis and interpretation*. Springer-Verlag, Berlin (Germany), 1996. 19, 39

[30] ESA. `http://www.esa.int/esaNA/SEM86CSMD6E_galileo_0.html`, 2007. 9

[31] EUREF. Minutes of EUREF Analysis Workshop, Padua, March 15-16, 2006. `http://www.epncb.oma.be/_newsmails/workshops/EPNLACWS_2006/minutes.php`. 34

[32] M. Fantino, P. Mulassano, F. Dovis, and L. Lo Presti. Performance of the Proposed Galileo CBOC Modulation in Heavy Multipath Environment. *Wireless Personal Communications*, 44:323–339, 2008. 26

[33] J. Feltens and S. Schaer. IGS products for the ionosphere. In *Proc. of the IGS Analysis Center Workshop*, ESOC, Darmstadt, Germany, February 9-11 1998. 59

[34] Y. Feng and Y. Zheng. Efficient interpolation to GPS orbits for precise wide area applications. *GPS Solutions*, 9:273–282, 2005. 137

[35] The International Terrestrial Reference Frame. `http://itrf.ensg.ign.fr/`, 2011. 108

[36] M. Ge, G. Gendt, and M. Rothacher. Integer ambiguity resolution for precise positioning: applied to fast integrated estimation of very huge GNSS networks. In *Proc. of VI Hotine-Marussi Symposium of Theoretical and Computational Geodesy*, Wuhan, China, May 29 - June 2 2006. 30

[37] M. Ge, G. Gendt, M. Rothacher, C. Shi, and J. Liu. Resolution of GPS carrier-phase ambiguities in Precise Point Positioning (PPP) with daily observations. *Journal of Geodesy*, 82:389–399, 2008. 12, 30

[38] C. Goad. Precise positioning with the Global Positioning System. In *Proc. of the Third International Symposium on Inertial Technology for Surveying and Geodesy*, pages 745–756, Banff, Canada, September 16-20 1988. 132

[39] W. Gurtner. RINEX: The Receiver Independent Exchange Format, Version 3.00. `http://igscb.jpl.nasa.gov/data/format/rinex300.pdf`, 2007. 31, 129

[40] G. K. Hartmann and R. Leitinger. Range Errors due to Ionospheric and Tropospheric Effects for Signal Frequencies Above 100 MHz. *Bulletin Géodésique*, 58:109–136, 1984. 48, 50

[41] R. R. Hatch. A New Three-Frequency, Geometry-Free, Technique for Ambiguity Resolution. In *Proc. ION GNSS*, pages 309–316, Forth Worth, United States, September 26-29 2006. 83

[42] R. R. Hatch. The Synergism of Code and Carrier Measurements. In *Proceedings of the Third International Geodetic Symposium on Satellite Doppler Positioning*, pages 1213–1232, Las Cruces, N.M.,New Mexico State University, 1982. 151

[43] R. R. Hatch, J. Jung, P. Enge, and B. Pervan. Civilian GPS: The Benefits of Three Frequencies. *GPS Solutions*, 3(4):1–9, 2000. 65, 66, 77, 79, 84

[44] G. W. Hein, J. Godet, J. L. Issler, J. C. Martin, P. Erhard, R. Lucas-Rodriguez, and T. Pratt. Status of Galileo Frequency and Signal Design. In *Proc. ION GPS*, Portland, United States, 2002. 9

[45] P. Henkel. *Reliable Carrier Phase Positioning*. PhD thesis, Technische Universität München, Germany, 2010. 36

[46] P. Henkel and C. Gunther. Three frequency linear combinations for Galileo. In *Proc. of 4th Workshop on Positioning, Navigation and Communication (WPNC'07)*, pages 239–245, Hannover, Germany, March 22 2007. 70

[47] M. Hernandez-Pajares, J. M. Juan, and J. Sanz. New approaches in global ionospheric determination using ground GPS data. *Journal of Atmospheric and Solar-Terrestrial Physics*, 61:1237–1247, 1999. 59, 61

[48] M. Hernandez-Pajares, J. M. Juan, and J. Sanz. Medium-scale traveling ionospheric disturbances affecting GPS measurements: Spatial and temporal analysis. *Journal of Geophysical Research*, 111(A07S11), 2006. 46

[49] M. Hernandez-Pajares, J. M. Juan, J. Sanz, and R. Orus. Second-order ionospheric term in GPS: Implementation and impact on geodetic estimates. *Journal of Geophysical Research*, 112(B08417), 2007. 21, 50, 51

[50] P. Héroux and J. Kouba. GPS Precise Point Positioning Using IGS Orbit Products. *Physics and Chemistry of the Earth (A)*, 26(6-8):573–578, 2001. 36, 54

[51] G. Hochegger, B. Nava, S. M. Radicella, and R. Leitinger. A family of ionospheric models for different uses. *Physics and Chemistry of the Earth (C)*, 25(4):307–210, 2000. 21

[52] B. Hofmann-Wellenhof, H. Lichtenegger, and J. Collins. *GPS: Theory and Practice*. Springer-Verlag, Wien New-York, 1997. 12, 14, 78, 107, 108, 109, 130, 131

[53] H. S. Hopfield. Two-quartic Tropospheric Refractivity Profile for Correcting Satellite Data. *Journal of Geophysical Research*, 74(18):4487–4499, 1969. 23

[54] M. M. Hoque and N. Jakowski. Higher order ionospheric effects in precise GNSS positioning. *GPS Solutions*, 81:259–268, 2007. 48

[55] M. M. Hoque and N. Jakowski. Mitigation of higher order ionospheric effects on GNSS users in Europe. *GPS Solutions*, 12:87–97, 2008. 21, 51

[56] IGS. IGS Products. `http://igscb.jpl.nasa.gov/components/prods.html`, 2009. 14, 15, 16, 28, 61, 110

[57] M. Irsigler, J. A. Avila-Rodriguez, and G. W. Hein. Criteria for GNSS multipath performance assessment. In *Proc. ION GNSS*, Long Beach, California, United States, September 13-16 2005. 26

[58] O. Julien. Carrier-Phase Tracking of future Data/Pilot Signals. In *Proc. ION GNSS*, Long Beach, California, United States, September 13-16 2005. 8

[59] E. D. Kaplan and C. J. Hergarty. *Understanding GPS: Principles and Applications*. Artech House, Boston London, 2006. 28, 29

[60] A. Kleusberg, Y. Georgiadou, F. van den Heuvel, and P. Heroux. GPS data preprocessing with DIDOP 3.0. Internal technical memorandum, University of New Brunswick, Fredericton, NB, Canada, 1993. 131, 132

[61] J. Klobuchar. Ionospheric time-delay algorithm for single-frequency GPS users. *IEEE Transactions on Aerospace and Electronic Systems*, AES-23(3):325–331, 1987. 21, 111

[62] J. Kouba. Relativistic Time Transformations in GPS. *GPS Solutions*, 5(4):1–9, 2002. 18

[63] J. Kouba. Improved relativistic transformation in GPS. *GPS Solutions*, 8(3):170–180, 2004. 18

[64] J. Kouba. A Guide to Using International GNSS Service (IGS) Products. `http://acc.igs.org/UsingIGSProductsVer21.pdf`, 2009. 32, 36, 37

[65] R. B. Langley. GPS, the ionosphere, and the solar maximum. *GPS World*, 11(7):44–49, 2000. 46

[66] R. B. Langley. GPS Receiver System Noise. *GPS World*, 8(6):40–45, 1997. 34

[67] R. F. Leandro. *Precise Point Positioning with GPS: A New Approach for Positioning, Atmospheric Studies, and Signal Analysis*. PhD thesis, University of New Brunswick, Fredericton, NB, Canada, 2009. 12, 30, 92

[68] R. F. Leandro and M. C. Santos. Wide Area Based Precise Point Positioning. In *Proc. ION GNSS*, pages 2272–2278, Forth Worth, Texas, United States, September 26-29 2006. 30

[69] A. Leick. *GPS Satellite Surveying*. John Wiley & Sons, New Jersey, 2004. 10, 14, 21, 22, 23, 24, 25, 32, 34, 37, 78, 104, 105, 106, 107, 111, 130

[70] S. Lejeune, G. Wautelet, and R. Warnant. Ionospheric effects on relative positioning within a dense network. *GPS Solutions*, 2011. doi: 10.1007/s10291-011-0212-1. 46, 132

[71] A. J. Manucci, B. D. Wilson, D. N. Yuan, C. H. Ho, U. J. Lindqwister, and T. F. Runge. A global mapping technique for GPS-derived ionospheric total electron content measurements. *Radio Science*, 33:565–582, 1998. 29

[72] C. Mayer, C. Becker, N. Jakowski, and M. Meurer. Ionosphere monitoring and interfrequency bias determination using Galileo: First results and future prospects. *Advances in Space Research*, 47(5):859–866, 2011. 151, 153

[73] W. G. Melbourne. The Case for Ranging in GPS Based Geodetic Systems. In *Proc. of 1st International Symposium on Precise Positioning with the Global Positioning System*, pages 373–386, Rockville, Maryland, United States, April 15-19 1985. 78

[74] Y. Memarzadeh. *Ionospheric Modeling for Precise GNSS Applications*. PhD thesis, Delft University of Technology, Netherlands, 2009. 42, 45

[75] V. B. Mendes. *Modeling the neutral-atmosphere propagation delay in radiometric space techniques*. PhD thesis, University of New Brunswick, Fredericton, NB, Canada, 1999. 22, 24

[76] P. Misra and P. Enge. *Global Positioning System: Signals, Measurements and Performance*. Ganga-Jamuna Press, Lincoln, Massachusetts, 2nd edition, 2006. 23

[77] O. Montenbruck, E. Gill, and R. Kroes. Rapid orbit determination of LEO satellites using IGS clock and ephemeris products. *GPS Solutions*, 9:226–235, 2005. 16, 17

[78] O. Montenbruck, P. Steigenberger, E. Schonemann, A. Hauschild, U. Hugentobler, R. Dach, and R. Becker. Flight Characterization of New Generation GNSS Satellite Clocks. In *Proc. ION GNSS*, Portland, Oregon, United States, September 21-23 2011. 127, 146

[79] B. Nava, S. M. Radicella, R. Leitinger, and P. Coisson. Use of total electron content data to analyze ionosphere electron density gradients. *Advances in Space Research*, 39:1292–1297, 2007. 53

[80] A. E. Niell. Global mapping functions for the atmosphere delay at radio wavelengths. *Journal of Geophysical Research*, 101(b2):3227–3246, 1996. 24, 112

[81] D. Odijk. *Fast precise positioning in the presence of ionospheric delays*. PhD thesis, Delft University of Technology, Netherlands, 2002. 13, 28, 40

[82] R. Orus. *Contributions on the improvement, assessment and application of the Global Ionospheric VTEC Maps computed with GPS data*. PhD thesis, Universitat Politecnica de Catalunya, Spain, 2005. 52, 53, 60

[83] R. Orus, M. Hernandez-Pajares, J. M. Juan, J. Sanz, and M. Garcia-Fernandez. Performance of different TEC models to provide GPS ionospheric corrections. *Journal of Atmospheric and Solar-Terrestrial Physics*, 64:2055–2062, 2002. 61

[84] R. Orus, L. R. Cander, and M. Hernandez-Pajares. Testing regional vertical total electron content maps over Europe during the 17-21 January sudden space weather event. *Radio Science*, 42(RS3004), 2007. doi: 10.1029/2006RS003515. 60, 61, 62

[85] B. W. Parkinson and J. J. Spilker. *Global Positioning System: Theory and Applications Volume 1*, chapter 14. Multipath effects. AIAA, 1996. 114

[86] Earth Observation Portal. `http://events.eoportal.org/presentations/182/11874.html`, 2007. 128

[87] W. H. Press, S. A Teukolsky, W. T. Vetterling, and B. P. Flannery, editors. *Numerical Recipes in C. The Art of Scientific Computing*, chapter 3.1. Polynomial Interpolation and Extrapolation, pages 108–110. Cambridge University Press, 2nd edition, 1992. 137

[88] W. H. Press, S. A Teukolsky, W. T. Vetterling, and B. P. Flannery, editors. *Numerical Recipes in C. The Art of Scientific Computing*, chapter 7. Random numbers, pages 274–328. Cambridge University Press, 2nd edition, 1992. 112

[89] S. M. Radicella and R. Leitinger. The evolution of the DGR approach to model electron density profiles. *Advances in Space Research*, 27(1):35–40, 2001. 21

[90] Rakotomalala. Tests de normalité – Techniques empiriques et tests statistiques – Version 2.0. `http://eric.univ-lyon2.fr/~ricco/cours/cours/Test_Normalite.pdf`, 2008. 142

[91] K. Rawer, editor. *Encyclopedia of Physics*, chapter Geophysics III, Part VII, pages 389–391. Springer-Verlag, 1984. 53

[92] T. Richert and N. El-Sheimy. Low-Noise Linear Combinations of Triple-Frequency Carrier Phase Measurements. *Journal of The Institute of Navigation*, 53(1):61–67, 2005. 66

[93] T. Richert and N. El-Sheimy. Optimal linear combinations of triple frequency carrier phase data from future global navigation satellite systems. *GPS Solutions*, 11:11–19, 2007. 66, 75

[94] M. Rothacher and R. Schmid. Antex: The Antenna Exchange Format, Version 1.4. `http://igscb.jpl.nasa.gov/igscb/station/general/antex14.txt`, 15 September 2010. 32, 34

[95] A. Roulston, N. Talbot, and K. Zhang. An Evaluation of Various GPS Satellite Ephemerides. In *Proc. ION GNSS*, pages 44–54, Salt Lake City, Utah, United States, September 19-22 2000. 15

[96] P. Royston. An extension of Shapiro and Wilk's W test for normality to large samples. *Applied Statistics*, 31:115–124, 1982. 141

[97] J. Saastamoinen. Contribution to the theory of atmospheric refraction. *Bulletin Géodésique*, 105(1):279–298, 1972. 23

[98] M. C. Santos. personal communication, 2011. 28

[99] G. Sasibhushana Rao. GPS satellite and receiver instrumental biases estimation using least squares method for accurate ionosphere modelling. *Journal of Earth System Science*, 116(5):407–411, 2007. 53

[100] S. Schaer. *Mapping and Predicting the Earth's Ionosphere Using the Global Positioning System*. PhD thesis, University of Bern, 1999. 29

[101] S. Schaer and W. Gurtner. IONEX: The IONosphere Map EXchange Format, Version 1. `http://igscb.jpl.nasa.gov/pub/data/ionex1.pdf`, 15 September 2010. 29, 59

[102] S. Schaer, W. Gurtner, and J. Feltens. IONEX : The IONosphere Map EXchange Format Version 1. In *Proceedings of the IGS Analysis Center Workshop*, ESOC, Darmstadt, Germany, February 9-11 1998. 59

[103] M. Schenewerk. A brief review of basic GPS orbit interpolation strategies. *GPS Solutions*, 6:265–267, 2003. 16, 137

[104] M. Schenewerk. The GPS Toolbox: A Brief Review of Basic GPS Orbit Interpolation Strategies. `http://www.ngs.noaa.gov/gps-toolbox/sp3intrp.htm`, 2003. 137

[105] R. Schmid. How to Use IGS Antenna Phase Center Corrections. `http://www.gpsworld.com/tech-talk-blog/how-use-igs-antenna-phase-center-corrections-11369`, February 3rd, 2010. 32

[106] R. Schmid, P. Steigenberger, G. Gendt, G. Maorong, and M. Rothacher. Generation of a consistent absolute phase center model for GPS receiver and satellite antennas. *Journal of Geodesy*, 81:781–798, 2007. 32, 34, 92, 116

[107] G. Seeber. *Satellite Geodesy*. Walter de Gruyter, Berlin, New York, 2nd edition, 2003. 18, 22, 24, 28, 34, 35, 40, 106, 130, 131, 132

[108] S. S. Shapiro and M. B. Wilkinson. An analysis of variance test for normality (complete samples). *Biometrika*, 52(3-4):591–611, 1965. 141

[109] Solar Influences Data Analysis Center (SIDC). Sunspot data. `http://www.sidc.be/sunspot-data`, 2010. 44, 45

[110] Solar Influences Data Analysis Center (SIDC). User guide. `http://www.sidc.be/educational/classification.php`, 2010. 46

[111] A. Simsky. Three's the Charm - Triple frequency Combinations in Future GNSS. *Inside GNSS*, 1(5):38–41, 2006. 25, 26, 87, 88

[112] A. Simsky and J.-M. Sleewagen. Performance Assessment of Galileo Ranging Signals Transmitted by GSTB-V2 Satellites. In *Proc. ION GNSS*, Forth Worth, Texas, United States, September 26-29 2006. 26

[113] A. Simsky, J.-M. Sleewagen, W. De Wilde, and F. Wilms. Galileo Receiver Development at Septentrio. In *Proc. ENC-GNSS*, Munich, Germany, 2005. 8, 26, 35, 128, 129

[114] A. Simsky, D. Mertens, J.-M. Sleewagen, M. Hollreiser, and M. Crisci. Experimental Results for the Multipath Performance of Galileo Signals Transmitted by GIOVE-A Satellite. *International Journal of Navigation and Observation*, 2008. doi: 10.1155/2008/416380. 26, 27, 87

[115] J.-M. Sleewagen. *Modeling, Quality Analysis and Management of GPS data: an Instrumental Approach*. PhD thesis, Université Libre de Bruxelles, Belgium, 1999. 25, 26, 27, 35, 80

[116] J.-M. Sleewagen, W. De Wilde, and M. Hollreiser. Galileo AltBOC receiver. In *Proc. ENC-GNSS*, Rotterdam, Netherlands, May 17 2004. 8

[117] J. Spits. Dévelopement d'un logiciel pour la simulation de mesures de pseudo-distances Galileo et validation sur base de données GPS. Master's thesis, Université de Liège, Belgique, 2004. 108

[118] J. Spits. Dévelopement d'un logiciel pour la simulation de mesures de codes et de phases GPS. Master's thesis, Université de Liège, Belgique, 2005. 107

[119] P. R. Spofford and B. W. Remondi. The National Geodetic Survey Standard GPS Format SP3 (SP3-a format). `http://igscb.jpl.nasa.gov/igscb/data/format/sp3_docu.txt`, 1994. 129

[120] P. J. G. Teunissen. [Invited lecture] Least-square estimation of the integer GPS ambiguities. In *Section IV Theory and Methodology, IAG General Meeting*, Beijing, China, 1993. 66

[121] C. C. J. M. Tiberius, P. F. de Bakker, H. van der Marel, and R. J. P. van Bree. Geometry-Free Analysis of GIOVE-A/B E1-E5a and GPS L1-L5 measurements. In *Proc. ION GNSS*, pages 2911–2925, Savannah, GA, United States, September 22-25 2009. 28, 35, 36, 80

[122] L. Urquhart. An Analysis of Multi-Frequency Carrier Phase Linear Combinations for GNSS. Technical Report No. 263, University of New Brunswick, Fredericton, NB, Canada, 2009. 70, 73

[123] H. van der Marel, P. F. de Bakker, and C. C. J. M. Tiberius. Zero, single and double difference analysis of GPS, EGNOS and GIOVE-A/-B pseudorange anf carrier phase measurements. In *Proc. ENC GNSS*, Naples, Italy, 2009. 35, 36, 80

[124] M. Wang and Y. Gao. An Investigation on GPS Receiver Initial Bias and Its Determination. In *Proc. ION NTM*, pages 873–880, San Diego, CA, United States, January 22-24 2007. 30

[125] Z. Wang, Y. Wu, K. Zhang, and Y. Meng. Triple-Frequency Method for High-Order Ionospheric Refractive Error Modelling in GPS Modernization. *Journal of Global Positioning Systems*, 4(1-2):291–295, 2005. 21

[126] R. Warnant. *Etude du comportement du Contenu Electronique Total et de ses irrégularités dans une région de latitude moyenne. Application aux calculs de positions relatives par le GPS*. PhD thesis, Université Catholique de Louvain, Belgium, 1996. 53

[127] D. L. M. Warren and J. F. Raquet. Broadcast vs. precise GPS ephemerides: a historical perspective. *GPS Solutions*, 7:151–156, 2003. 15, 16

[128] E. W. Weisstein. Box-Muller Transformation, From *MathWorld*–A Wolfram Web Resource. `http://mathworld.wolfram.com/Box-MullerTransformation.html`, 2011. 112

[129] P. Wessel and W. H. F. Smith. Generic Mapping Tools (GMT). `http://gmt.soest.hawaii.edu`, 2010. 59

[130] B. D. Wilson and A. J. Mannucci. Instrumental Biases in Ionospheric Measurements Derived from GPS Data. In *Proc. ION GPS*, Salt Lake City, United States, 1993. 29

[131] B. D. Wilson, C. H. Yinger, W. A. Feess, and Cpt. C. Shank. New and improved: The Broadcast Interfrequency Biases. *GPS World*, USA, 1999. 28

[132] J. T. Wu, S. C. Wu, G. A. Hajj, W. I. Bertiger, and S. M. Lichten. Effects of antenna orientation on GPS carrier phase. *Manuscripta Geodaetica*, 18:91–98, 1993. 36, 37, 154

[133] Wübbena, G. Software Developments for Geodetic Positioning with GPS Using TI 4100 Code and Carrier Measurements. In *Proc. of 1st International Symposium on Precise Positioning with the Global Positioning System*, pages 403–412, Rockville, Maryland, United States, April 15-19 1985. 78

[134] Wübbena, G. and Schmitz, M. GPS Block II/IIA Satellite Antenna Testing using the Automated Field Calibration with Robot. In *Proc. ION GNSS*, Forth Worth, Texas, United States, September 25-28 2007. 32

[135] G. Xu. *GPS: Theory, Algorithms and Applications*. Springer-Verlag, Berlin Heidelberg New York, 2nd edition, 2007. 18, 19, 21, 31, 32, 109, 111

[136] J.F. Zumberge and G. Gendt. The demise of selective availability and implications for the international GPS service. *Physics and Chemistry of the Earth (A)*, 26(6-8):637–644, 2001. 17